UNIVERSITEIT VAN PRETORIA
UNIVERSITY OF PRETORIA
YUNIBESITHI YA PRETORIA

Denkleiers • Leading Minds • Dikgopolo tša Dihlalefi

A Computational Fluid Dynamics Approach to Selecting a Concentrating Solar Thermal Plant Site Location Around a Ferromanganese Smelter Based on Heliostat Soiling Potential

By

Milan André Swart

Submitted in partial fulfilment of the requirements for the degree of

Master of Engineering (Mechanical Engineering)

In the

Department of Mechanical and Aeronautical Engineering

Faculty of Engineering, Built Environment and Information Technology

Supervisor: Professor K.J. Craig

Co-supervisors: S.A.C. Hockaday; Q.G. Reynolds, Ph.D

University of Pretoria

December 2021

Abstract

A Computational Fluid Dynamics Approach to Selecting a Concentrating Solar Thermal Plant Site Location Around a Ferromanganese Smelter Based on Heliostat Soiling Potential

by

Milan André Swart

Supervisor:	Professor K.J. Craig
Co-supervisors:	S.A.C. Hockaday; Q.G. Reynolds, Ph.D
Department:	Mechanical and Aeronautical Engineering
University:	University of Pretoria
Degree:	Master of Engineering (Mechanical Engineering)
Keywords:	Concentrating solar thermal (CST), energy-intensive industry (EII), computational fluid dynamics (CFD), heliostat soiling, ANSYS Fluent

There is a need to reduce the share of process heat generated by fossil fuels in energy-intensive industries. One proposed solution in the iron and steel sector is to introduce high temperature solar thermal heat energy into a pre-heating stage of the ferromanganese smelting process. In principle, this is an idea that can work, but there are unknowns related to concentrating solar thermal (CST) solar field performance in the vicinity of an industrial smelting operation. This dissertation adopts a two-part approach to addressing the unknowns related to solar field performance.

First, a field experimental campaign is carried out at a ferromanganese smelter in South Africa, where mirror soiling data, dust characterisation data, and on-site meteorological data are collected. A clear change in rainfall was observed during the summer and winter period, with the dry winter period being the period where the most mirror soiling was observed. Results from the 8-month mirror soiling measurement campaign showed that proximity of the mirror sampling set to the smelter dust source is the primary driver of mirror soiling rates, with dust concentrations decreasing further away from the source. The secondary drivers for mirror soiling rates were observed to be wind direction and wind speed, for reflectance sampling locations at roughly equal distances from the smelter dust source. A 13 % relative improvement in mirror reflectance loss rate was observed by simply considering an adjacent mirror sampling location through the dry season.

The second part of this dissertation demonstrates the use of a large-scale atmospheric flow computational fluid dynamics (CFD) modelling based approach to selecting an appropriate CST solar field site in the vicinity of an industrial smelter. The k-ϵ turbulence model is adapted to be more suitable to modelling neutral atmospheric boundary layer (ABL) flows, along with other modelling strategies. The tailored modelling approach is validated against wind tunnel and on-site wind mast data. On-site wind mast data is also used to derive priority wind speed and direction simulation cases. The discrete phase method (DPM) is used to simulate dust dispersion and deposition based on the results of the full-scale neutral ABL CFD simulations for priority wind cases. The dust deposition results for individual cases are then combined and weighted using the on-site wind data for a given sampling period, yielding a dust deposition map that shows the deposition hot spots around the smelter for the given period. The weighted dust deposition pattern is validated against experimental mirror soiling data for the same

period. Some minor discrepancies are observed, but the simulation approach correctly predicted the experimentally observed soiling pattern for the studied period. The CFD-based CST solar field site-selection approach is thus successfully demonstrated and validated as an approach that can be used to identify a candidate solar field site relative an industrial dust source.

Acknowledgements

This work was done as a part of a European Union's Horizon 2020 research and innovation project called PREMA under grant agreement No 820561. The author would like to thank the EU Horizon program for continued support of this work and other research and development projects working towards a sustainable future. My thanks also go to Mintek for providing me with financial support and giving me a place to call my work home.

This work in this dissertation would not have been possible without a number of people.

The experimental component of this work would not have been possible at all without the assistance of Derek Griffith at the CSIR. In the true spirit of research collaboration, he trained and gave the use of custom-made reflectometer device used to carry out the reflectance measurement campaign. My sincerest thanks to you, Derek.

The experimental campaign was carried out at the Transalloys smelter. Thank you, Kobus and Quintin, for always making yourself available, even though you actually have a plant to run. The personal tours you both gave me of the plant have made a lasting impression. Thank you, Eugene, for providing me with the CAD models of the plant and making yourself available to assist a fellow engineer.

My special thanks go to Prof. Alessandro Parente, and Prof. David Hargreaves for assisting me with the implementation of numerical methods described in your published works. Thank you for the detailed feedback you gave me on my code snippets and for even sending me versions of your own to compare with.

The simulation component of this work required 65,000 CPU-hours on the CHPC's high performance compute resource under the MINTEK776 project. Thank you for providing and maintaining this crucial resource and being very quick to respond to any queries submitted through the help desk.

To my supervisors at Mintek. Thank you, Lina, for giving me the freedom to steer my part of the PREMA research as I saw fit and backing my choices. Thank you, Quinn, for the countless coffees, discussions about CFD and sometimes work. Thank you both for always being available to talk and for boosting me when needed. I certainly would not have made it through if it were not for you.

To my mentor and supervisor, Prof. Ken Craig. I feel deeply grateful to have had the opportunity to be taught and guided by you. Your command of your domain, combined with your calm and ease, is inspiring. Thank you for inspiring me to be better. I have been a student of yours since my undergraduate days and I hope to remain one, even if informally, into the future.

Most importantly, thank you to my brothers Lucca and Benito, my parents Tina and André, my Ouma Kay, and my partner Anke, for sticking with me and motivating me through the roller coaster that has been the last two years of our lives. A person is only as good as their support system, thank you for being mine. I dedicate this dissertation to my Oupa Schu[2].

Publications

- SASEC conference paper and presentation (2019)
- HiTEMP conference poster (2020)
- Blog posts for the PREMA website
- Milestone 9 PREMA Dust management protocol technical report (2020)
- SAIMM Renewables in metallurgy conference presentation (2021)
- Journal paper under preparation

Contents

List of figures

List of tables

Nomenclature

Latin symbols

U	Free stream velocity	[m/s]
$\dot{C}$	Cleanliness loss rate	[-]
a	Particle drag constants	[-]
A_N	Dimensionless constant	[-]
d	Diameter	[m]
E	Empirical constant	[-]
F	Body force	[N]
f	Coriolis parameter	[-]
g	Gravitational acceleration	[m/s^2]
h	Height	[m]
L	Length scale	[m]
m	Mass	[kg]
r	Uniform random number	[-]
T	Integral time scale	[s]
Y	Mass fraction	[-]
C	Cleanliness factor, coefficient, constant	[-]; [-]
G	Energy production term	[-]
S	Source term, particle deposition flux	[-]; [kg/m^2 s]
c	Concentration	[kg/m^3]
k	Turbulent kinetic energy, sand-grain roughness	[m^2/s^2]; [m]
p	Pressure	[N/m^2]
t	Time	[s]
u, v, w	Velocity components in the x, y, and z directions	[m/s]
v	Particle deposition velocity	[m/s]
x, y, z	Coordinates	[m]

Greek symbols

α	Absorptance	[-]
θ	Beam angle, general flow variable	[°]; [-]
μ	Dynamic viscosity	[N s/m^2]
ν	Kinematic viscosity	[m^2/s]
δ	Delta function	[-]
φ	Polar angle; scalar field	[mrad]; [-]
σ	Prandtl number	[-]
ϕ	Radiant flux	[W]
ρ	Reflectance; material density	[-]; [kg/m^3]
γ	Scaling parameter	[-]
τ	Transmittance; shear stress, relaxation time	[-]; [N/m^2]; [s]
ϵ	Turbulent dissipation rate	[m^2/s^3]
ξ	Uniformly distributed random number	[-]

κ	Von Karman constant	[-]
λ	Wavelength	[μm]

Subscripts

s	Solar, sand-grain roughness
a	Air
b	Body force indicator
d	Diffuse
i, j, k	Direction indicators for Cartesian tensor notation
D	Drag
e	Eddy
$cross$	Eddy crossing indicator
ft	Fluid (static) threshold
h	Hemispherical
i	Incident
$*$	Indicating friction velocity
t	Indicator of turbulent (eddy) viscosity
L	Lagrangian
m	Mirror
$soil$	Mirror soiling indicator
p	Particle, first cell centroid value
0	Reference value
r	Reflected, relaxation time indicator
S	Spots
ϵ	Turbulent dissipation rate
k	Turbulent kinetic energy
μ	Viscosity constant indicator
$wall$	Wall function value indicator
ref	Reference
$local$	Indicating a cell local value

Abbreviations and acronyms

ABL	Atmospheric boundary layer
AGL	Above ground level
AOI	Area of interest
ASL	Atmospheric surface layer
BC	Boundary condition
BOI	Body of influence
CAD	Computer aided design
CFD	Computational fluid dynamics
CS	Concentrating solar
CSP	Concentrating solar power

CST	Concentrating solar thermal
DEM	Digital elevation model
DMRE	South African Department of Mineral Resources and Energy
DNI	Direct normal irradiance
DPM	Discrete phase method
DTM	Digital terrain model
EDS	Energy dispersive spectroscopy
EII	Energy-intensive industry
EPSG	European petroleum survey group (geodetic datum)
EU	European Union
GHG	Green-house gasses
GIS	Geographic information system
IEA	International Energy Association
IPCC	Inter-governmental panel on climate change
IPPPP	Independent power producers procurement programme
LES	Large eddy simulation
MDRL	Mean daily reflectance loss
NASA	National Aeronautics and Space Administration
NEF	Nikon electronic format
N-E-S-W	North-east-south-west
O&M	Operation and maintenance
PBL	Planetary boundary layer
PI	Pixel intensity
PM	Particulate matter
PREMA	EU Horizons 2020 project
PSD	Particle size distribution
PV	Photovoltaic
RANS	Reynolds-averaged Navier-Stokes
RGB	Red-green-blue
SANBI	South African National Biodiversity Institute
SEM	Scanning electron microscopy
SolarPACES	Solar power and chemical energy systems
SRTM	Shuttle radar topography mission
TDR	Turbulent dissipation rate
TES	Thermal energy storage
TI	Turbulence intensity
TKE	Turbulent kinetic energy
UDF	User defined function
UDM	User defined memory
UDS	User defined scalar
UN	United Nations
UTM	Universal Transverse Mercator
WMO	World meteorological organisation
WRF	Weather research and forecasting model
XRD	X-ray diffraction

1 Introduction

1.1 Context

As of 2021, the global rise in renewable energy generation capacity is still falling short of the rise of global energy demand (IEA, 2021). Renewable energy power generation through utility-scale solar photovoltaics (PV) and wind farms have come to the fore, with it currently being cheaper to add new generation capacity using renewable generation than it is to add fossil fuel-based generation (DMRE, 2021). Continuing on the path of decarbonizing the electricity grid is only a part of the solution to the goal of reaching a 'net-zero' carbon emission world by 2050 (European Commission, 2020). However, renewable electricity supplies only solve a part of the challenge. Most of the energy demand in industry is for process heat, of which almost half of the demand is for materials transformation processes in energy intensive industry (EII) (IEA and Philibert, 2017). The current sources of heat are all fossil fuels, therein lies the challenge. New ways of supplying the heat source demanded by EIIs are required for deep decarbonisation to be realised (Bataille *et al.*, 2018).

A European Union Horizons 2020 funded project is currently investigating the energy efficient, primary production of manganese ferroalloys through the application of novel energy systems in the drying and pre-heating of furnace feed materials, also known as PREMA. Amongst other project objectives, the PREMA project aims to demonstrate the application of concentrating solar thermal (CST) heat energy for pre-heating of furnace feed materials to reduce energy consumption and carbon-dioxide (CO_2) emissions. The author forms a part of work package two of the PREMA project, which is investigating the *Development of solar thermal technologies*, tasked specifically with the development of a *Dust management protocol* for potential solar thermal plant siting. The development of the *Dust management protocol* is the starting point for this dissertation and provides context for all further investigations. Transalloys smelters, which produce ferromanganese alloys, are a PREMA project consortium partner and have made their smelter complex available for experimental work.

1.2 Concentrating solar thermal (CST) heat energy for ferromanganese smelting

Concentrating solar thermal (CST) plants that supply a renewable heat source to low and medium temperature ($\leq 400\ °C$) industrial processes have been trialled in industry, however, the integration of CST with EII processes that require high temperatures ($> 400\ °C$) have not (IEA and Philibert, 2017). The technical challenges posed by the high temperature requirements of most EIIs, continuity of thermal energy supply and the unknowns associated with locating a CS type plant close to an EII, have all contributed to integration concepts not being further developed until now. One of the unknowns associated with locating a CST plant in the vicinity of a ferromanganese smelter is the unknown impacts of industrially-generated dust on the optical performance of the heliostat field.

The unknown impacts of industrial dust on the performance of a heliostat field can be broken down in the following way:

- What are heliostat soiling rates like in the vicinity of a ferromanganese smelter, and given these soiling rates, would it be feasible to locate a heliostat field in the vicinity of a ferromanganese smelter?

- Is there any particulate matter of aerosol present in the atmosphere immediately surrounding a ferromanganese smelter that could result in enhanced physical degradation of a heliostat?
- Is there a location around the smelter complex that will have a lower heliostat soiling potential in comparison to other locations around the smelter?

It is unacceptable to have these listed unknowns when considering the development of a potential CST plant, since the CST plant efficiencies are largely dependent on the optical efficiency of the heliostat field, and the heliostat field's cleaning cost accounts for a large portion of the total CST plant operational and maintenance costs. Unknowns regarding the predicted heliostat field performance and lifetime operation and maintenance (O&M) costs could result in underperformance and financial infeasibility of the proposed CST plant.

1.3 Objectives

A two-pronged experimental and modelling approach is adopted to explore the three listed unknowns associated with the performance of a heliostat field in the vicinity of a ferromanganese smelter.

The experimental part of this dissertation aims to design and conduct a heliostat soiling study, at the ferromanganese smelter, over the period of a few months. Mirror samples placed at different locations around the smelter will be used as proxies for heliostats, and their reflectance loss rates will be monitored, which will assist in addressing the question of heliostat performance. The reflectance loss behaviour at the different sampling locations will be used to help understand if a variation in reflectance performance can be expected at different locations around the smelter. Dust characterisation work of samples collected from the mirrors will assist in addressing the question of enhanced heliostat degradation and in identifying important dust sources. In addition to the mirror soiling study, wind speed and direction data will also be collected to assess how these two variables influence the dust dispersion and soiling experienced at the different reflectance sampling locations.

Experimental campaigns can be time consuming and expensive. The ability to use simulation as a predictive tool to identify a location(s) where there is less potential for heliostat soiling relative to another location, if there is such a location, would be valuable. The objective is to validate and demonstrate a computational fluid dynamics (CFD) based approach to predict a location around the smelter where there is the least potential for heliostat soiling. Wind and dust characterisation data from the experimental campaign will be required to derive appropriate boundary conditions for the CFD simulations.

1.4 Dissertation structure

This dissertation consists of eight chapters. The body of the dissertation is followed by the references made and the appendices that provide auxiliary information. Table 1 provides the structure breakdown of this thesis.

Table 1. Chapters and content of this thesis.

Chapter	Contents
Chapter 1: Introduction	Context is provided for the subject of this thesis. The objectives and structure of the dissertation are also provided.

Chapter 2: Literature Review	A literature review covering all of the subjects that are required to investigate heliostat soiling experimentally and numerically.
Chapter 3: Experimental Campaign	The experimental investigation of the experimental campaign conducted at the Transalloys ferromanganese smelter. The equipment, experimental methods, and outcomes of the experimental campaign are detailed. Dust characterisations, meteorological measurements, and reflectance loss measurements are the results featured.
Chapter 4: CFD Model Description and Validation	Modifications to the standard k-ϵ turbulence models required to model ABL flow more realistically are described. Different methods for prescribing boundary conditions are evaluated, the preferred method is validated against experimental wind tunnel data for ABL flow around an isolated building.
Chapter 5: CFD Investigation of Neutral ABL Flow at the Transalloys Smelters	A full-scale CFD investigation is carried out of the neutral ABL flow at and around the Transalloys smelter. Best practice guidelines are followed to arrive at a reliable computational mesh and to validate the resultant flow field against experimentally obtained wind mast data. Simulations are then performed for the identified priority wind conditions for a selected period.
Chapter 6: Dust Dispersion at the Transalloys Smelters	Dust dispersion and deposition are simulated in this chapter using the discrete phase method (DPM), which uses flow field results from the CFD simulations. Dust dispersion simulations are performed for all the identified priority wind conditions and the deposition results combined to form a cumulative weighted map of dust deposition around the Transalloys smelter for the studied period. Comparisons are then made between simulation and mirror soiling experimental results for the studied period.
Chapter 7: Demonstration of CST Site Selection	This chapter pulls together all the information from previous chapters, making it practical.
Chapter 8: Conclusions and Recommendations	This chapter provides the limitations of the investigations, the recommendations for future work of this nature, and the conclusions that can be drawn from the various results.

2 Literature Review

This literature review highlights previous research performed on the experimental and numerical investigation of solar reflector soiling. An overview of the important concepts is also provided. Each sub-section in this review is a field worthy of investigation in its own right. For that reason, the information given is only discussed as thoroughly as needed, no more and no less.

2.1 Climate and energy

The Intergovernmental Panel on Climate Change (IPCC) have investigated the link between global warming and greenhouse gases (GHGs) for three decades (IPCC, 1990), confirming beyond any doubt that the observed rate of climate change is a direct result of humans burning fossil fuels (IPCC, 2021). Limiting the global mean surface temperature rise to 1.5 °C is what is required for human society to function in its current state, anything more than 2 °C of warming will lead to irreversible climate change (IPCC, 2018). Irreversible climate change implies changes and the potential breakdown of certain aspects of human society that are hard to predict. The focus on global mean surface temperature, although an important indicator to scientists, subtracts from more relatable region-specific threats such as the risk of increased duration and intensity of dry spells and heat waves that can lead to crop failure and food shortages in a region, to name one example (IPCC, 2018). It is thus incumbent on us to take the steps necessary to limit global warming below 2 °C by all means possible.

In 2014, industrial activities accounted for about one-third (36 %) of global total final energy consumption and were directly and indirectly responsible for about one-third (24 % CO_2 emissions) of GHG emissions (IEA, 2017). Modelling done by the IPCC suggests that emission reduction of 65 % to 95 % by 2050 compared to 2010 emissions is required in the industry sector to limit global warming to below 2 °C (IPCC, 2018). Apart from the technology developments required to achieve these reductions, heavily trade-exposed industries such as iron and steel are challenging to reform through individual country policy action because of the competitive nature of these industries and the cost involved in implementing new technologies (IEA and Philibert, 2017; Nabernegg *et al.*, 2017; Bataille *et al.*, 2018)

Industrial activities with high energy demands, or Energy-Intensive Industries (EIIs), are a subset of broader industrial activities discussed above in general. Industries classified as EIIs are iron and steel, basic chemicals, cement, aluminium, glass, ceramics, and pulp and paper (IEA and Philibert, 2017). The focus industry in this research is the manganese ferroalloy beneficiation industry, which falls under the iron and steel industry categorisation, but the findings and recommendations are expected to be mostly generalisable to other dust-emitting EII activities.

2.2 CST technology application to EII

CST technology emerged from concentrating solar (thermal) power (CSP) technology, where the thermal energy absorbed in the heat transfer medium at the receiver is used to generate electricity through a Rankine (steam) power cycle. At the system level, there are three components to a CSP system, namely the reflector field, the receiver, and the thermal cycle. The lifetime O&M outlook for the central receiver and the thermal cycle side of the CST system is not expected to be sensitive to a different environment, whereas the lifetime O&M outlook for the solar reflector field is expected to be more sensitive to the environmental condition. Most recent operational CSP plants have thermal storage integrated into the thermal cycle, allowing these CSP plants to dispatch power on demand during peak

electricity demand hours when the sun is not necessarily shining. The ability to dispatch power means that CSP plants can have a stabilising effect on the electricity grid. The central receiver, or point focus, tower type CST technology is being investigated for the PREMA project because point focus receivers achieve the highest solar concentration ratios compared to other CS technologies and are thus able to generate high temperatures (i.e., > 400 °C) (Lovegrove and Pye, 2012).

Recently, Ebert *et al.* (2018, 2019) demonstrated reaching receiver outlet temperatures upwards of 900 °C using a central tower setup with a particle receiver to collect capture the solar energy. The development of particle receivers represents a breakthrough in CST technology because the particles (bauxite as an example (Ebert *et al.*, 2018)) have a high heat capacity, which makes high-temperature heat transport and storage possible. Furthermore, the particles are also cheap and easy to come by and resist thermal cycle degradation. The solar thermal integration concept proposed by the PREMA project is depicted in Figure 1.

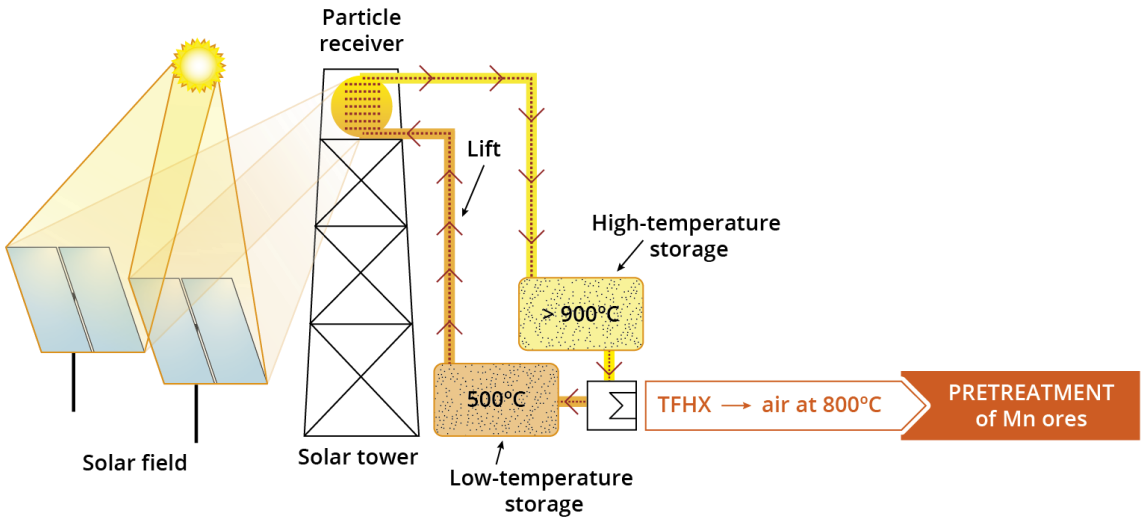

Figure 1. PREMA project CST integration concept with the manganese ferroalloy smelting process. Image credit: produced for PREMA by Mateusz Korcz, adapted from Buck and Giuliano (2019) with permission.

Figure 1 shows that the PREMA project is proposing to use solar thermal heat for pre-treatment (preheating) of the smelter feedstock. A trickle flow heat exchanger (TFHX) is being investigated to perform the heat exchange between the particles and the air that will be used to heat the feedstock (Reichart *et al.*, 2021). The major benefits predicted by this project are a 25 % reduction in energy demand, a 15 % reduction in CO_2 emissions, and a 10 % reduction in the operating cost of the smelter (Ringdalen, 2018).

Other proposed applications for solar thermal process heat are summarised by Hockaday (2019) as:

- Solar thermal preheating of smelter feed materials to reduce electricity and fossil fuel demand
- Re-melting and casting of scrap and low melting point metals
- Hot dip galvanisation
- Hydrometallurgical zinc production
- Zinc distillation

- Copper electrolytic refining
- Electrowinning of manganese metals

The findings of the investigation conducted in this work are expected to be adaptable to the above-listed applications.

2.3 Solar Reflector Soiling – from a dust source and receiver perspective

2.3.1 Dust and dust sources

Dust accumulation adversely affects the performance of all solar energy systems, whether they are PV or CS type systems, but not to the same extent, as explained in section 2.3.4. The scenario under investigation is that of a CST plant situated in the vicinity of a ferromanganese smelter complex in a heavily industrialised region. Near-field pollution dispersion acts at distances up to 10 km (Vervoort et al., 2019), which means that the presence of particulate matter (PM) and aerosols arising from industrial activities at any distance up to 10 km away from the smelter complex under consideration are expected.

Any particle suspended in the atmosphere is known as an aerosol (Hewitt and Jackson, 2020). Gas is not an aerosol but can chemically transform into a particle, through oxidation for example. Hewitt and Jackson (2020) categorise aerosols as primary or secondary aerosols. Primary aerosols are typically larger than 2 μm in diameter (coarse), are directly emitted into the atmosphere, and are mechanically produced. Secondary aerosols are smaller than 2 μm in diameter (fine) and are chemically produced. Hewitt and Jackson (2020) provide a summary of the different aerosol types. Table 2 summarises the different aerosol types.

Table 2. Summary of aerosol types and descriptions (Hewitt and Jackson, 2020).

Origin	Classification	Type	Description
Natural	Primary	Mineral dust	Oxides and carbonates of Si, Al, Ca, Fe. Although naturally occurring, disturbances of soil by humans contribute to a large portion of the atmospheric burden.
	Primary	Biological matter	Plant fragments, pollen, spores, fungi, and other decaying plant matter.
Anthropogenic	Primary	Biomass burning	Fires for agricultural clearing and cooking; releasing soot, sulphate, nitrate and products of incomplete combustion. Natural fires have the same characteristics.
	Primary	Industrial aerosols	Mining activities that release coal and mineral dust, stone crushing, cement manufacturing, metal smelters, black carbon (soot).
	Secondary	Sulphate and nitrate aerosol	Oxidation of SO_2 and NO_X is a significant source of secondary particles. Anthropogenic sources of these components are from fossil fuel combustion.

Petavratzi et al. (2005) studied dust sources from mineral processing operations in general. They concluded that coarse particles are generated by crushing and raw materials preparation and that fine

particles are generated by loading and dumping activities, draglines, and haulage roads. Notably, windblown dust from storage piles at a mine was a minor contributor to the overall dust emissions.

A life cycle assessment focusing on manganese-bearing PM was conducted on the manganese alloy supply chain by a group in the neurotoxicology field (Davourie *et al.*, 2017). They studied the emissions produced from seven mining operations and nine smelters. Most PM-related studies are carried out from an occupational health and safety perspective, which means that the particle size fractions studied are at the crossover between the fine and coarse particle sizes (1 to 10) μm, in the respirable size range, usually 2.5 μm or 10 μm in size. The study found that 66 % of the aerosol emissions associated with the production of manganese ferroalloy are indirect and happen outside of the smelter facility, mostly resulting from fossil-fuel combustion and the mining and materials processing required for fossil-fuelled power plants and furnace consumables. The other 34 % of aerosol emissions are directly emitted, with the process contributions given in Figure 2.

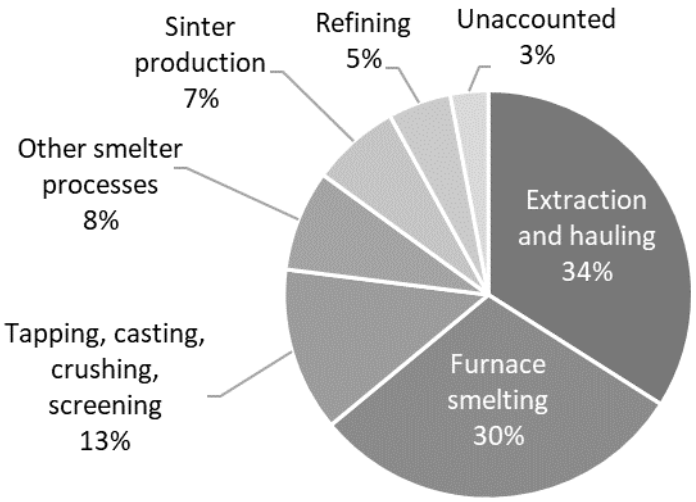

Figure 2. Process contributions to the direct aerosol emissions associated with ferromanganese production (Davourie *et al.*, 2017).

Based on the outcomes of their analysis, Davourie *et al.* (2017) developed a framework meant to help the industry prioritise their emission abatement plans for the following process areas (in order of highest to lowest priority): extraction and hauling; furnace emissions; tapping, casting, crushing and screening; general smelter; sinter plant. The controlled furnace emissions go through baghouse filters (for open furnaces) and wet scrubbers (for closed furnaces). The uncontrolled furnace emissions bypass these dust control measures during abnormal operating conditions. The study found that 64 % of stack furnace emissions are controlled, and 34 % are uncontrolled, implying a 10.2 % direct uncontrolled furnace emission contribution based on the above-mentioned direct emissions breakdown. The authors suggest that improved regulation of furnace operating conditions will significantly reduce uncontrolled emissions by limiting the amount of time the furnace spends operating abnormally. The highest contributors to ground-level emissions are the tapping, casting, crushing and screening processes, most of which can be captured or suppressed.

A particle's emission, entrainment, and deposition behaviours are described by the set of aerodynamic forces, gravitational forces and inter-particle forces acting on it. Smaller particles are primarily influenced by molecular forces, whereas gravitational and inertial forces primarily influence larger particles. Dust particles in the range of (10 to 30) μm travel up to 500 m from their source, and dust

particles larger than 30 μm tend to deposit within 100 m from their source (Petavratzi, Kingman and Lowndes, 2005).

2.3.2 Soiling studies - past to present

In a recently published conference paper, poetically entitled *"Dust in the Wind: An Historical Timeline of Soiling R&D for Solar Technologies"*, (Kazmerski, Diniz and Costa, 2020) present a succinct overview of the past seven decades of research investigations into the soiling of solar components; highlighting and contextualising the different paths of investigation followed over the years. This historical account also shows the vast difference in the number of publications dedicated to PV panel soiling compared to CS reflector soiling, reflecting the cost advantage of PV over CS technology; Figure 3 presents the data.

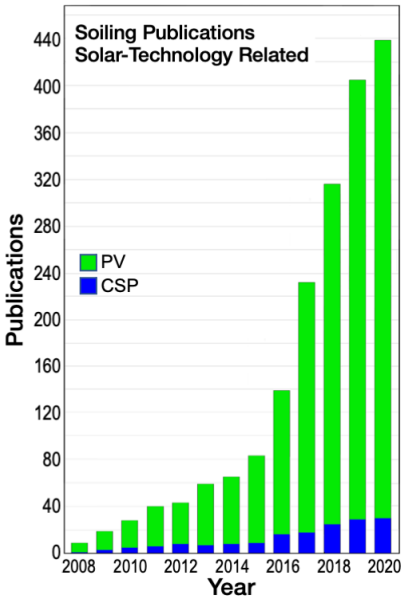

Figure 3. Solar technology-related soiling publications from 2008-2020. Unpublished data at the time of writing: Image used with permission of and provided by Kazmerski (2021).

The soiling components of the two fields represented in Figure 3 are mostly the same; the difference lies in what happens to the sun's light when it encounters a soiled surface, as detailed in sub-section 2.3.4. Updated records of all the soiling literature as it relates to solar technologies, first published by Sarver et al. (2013), then again by Costa et al. (2016), with the latest update by Costa et al. (2018), are invaluable. One trend that emerges is the increased focus on modelling and simulation in the past five years. The literature also reveals that an appropriate CST plant dust mitigation response can only be developed with a complete understanding of all the factors influencing solar reflector soiling. The following elements related to solar reflector soiling are essential to consider:

- Solar reflector performance monitoring, including climate conditions and effects
- Dust particle size and morphology
- Dust particle composition and chemistry
- Dust transport behaviour
- Dust deposition and accumulation on the surface

- Existing solar reflector soiling mitigation and prevention methods

2.3.3 Reflectance measurement

The Solar Power and Chemical Energy Systems (SolarPACES) group is an international cooperative network of experts focusing on the development and marketing of CSP systems. One of their working groups develops *Reflectance Guidelines* for use in industry and academia. These guidelines enable the collection of relevant and comparable results for solar reflector soiling studies. The latest version of these guidelines is used to elaborate on key concepts used throughout this investigation; see Meyen *et al.* (2018) for the complete set of guidelines.

Light's interaction with any surface is described with knowledge of the wavelength of the incident light and the material properties of the surface. There are three material properties, namely absorptance α, transmittance τ, and reflectance ρ; the law of conservation of energy applies, therefore $\alpha + \tau + \rho = 1$. Transmittance is assumed to be zero for an opaque surface, which is the case for solar reflectors. There is always a small component of absorptance which means that a reflector will never have perfect reflectivity. The material property of reflectance ρ, is the ratio of the reflected radiant flux ϕ_r, to the incident radiant flux ϕ_i, expressed as

$$\rho = \frac{\phi_r}{\phi_i} \qquad \text{Eq. 1}$$

Reflectance is a function of the wavelength λ of the incident ray and its angle of incidence θ_i. The spectral hemispherical reflectance $\rho_{\lambda,h}(\lambda, \theta_i, h)$, is used to describe the reflected intensity integrated over the possible hemisphere of reflection centred at the point of incidence. The hemispherical reflectance has a diffuse and a specular component. The reflectance of concern for CSP is the near-specular (or specular) reflectance $\rho_{\lambda,\varphi}(\lambda, \theta_i, \varphi)$, where φ is the polar angle indicating the maximum allowable deviation of the reflected beam (or bundle of incident rays) from the ideal specularly reflected beam. The maximum allowable beam deviation is determined by the acceptance aperture of the CS receiver, given by 2φ. A perfectly planar surface would therefore be ideal for solar reflectors, where the roughness is much less than the wavelength of the incoming solar radiation. Reflected beam deviation is caused by surface imperfections (i.e. roughness, machine marks, abrasions, scattering effects, and so on), giving the diffuse reflectance component$\rho_{\lambda,d}(\lambda, \theta_i, d)$; which is summarised by

$$\rho_{\lambda,h}(\lambda, \theta i, h) = \rho_{\lambda,\phi}(\lambda, \theta i, \phi) + \rho_{\lambda,d}(\lambda, \theta i, d) \qquad \text{Eq. 2}$$

For CS applications, proper material selection of the solar reflector results in anisotropic scattering, yielding a reflectance peak in the specular direction and scattered rays still reflected within the acceptance aperture of the receiver (or measuring device), with a slightly lower intensity; Figure 4 shows this effect.

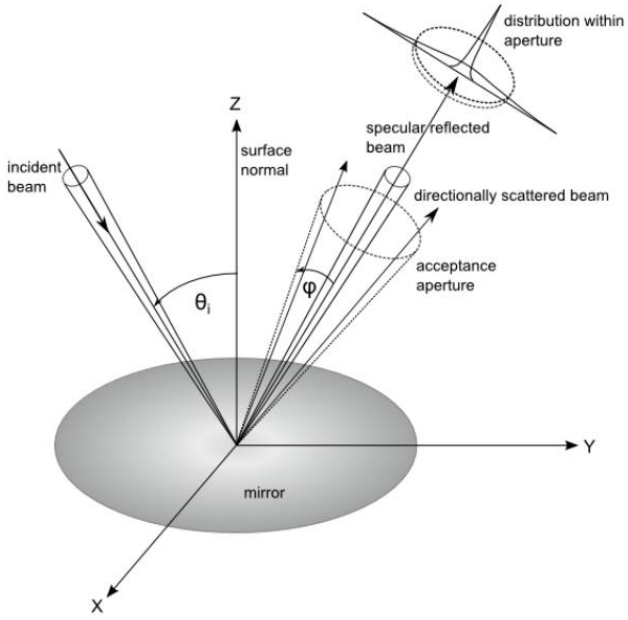

Figure 4. Specularly reflected beam, showing directional scatter within the acceptance aperture. Source: (Meyen *et al.*, 2018).

A measure of how clean a reflector is can be given by a cleanliness factor C_s, defined in Eq. 3 as the ratio of the reflectance of the soiled reflector to that of the clean reflector.

$$C_s = \frac{\rho_{\lambda,\phi,soil}(\lambda, \theta_i, \phi)}{\rho_{\lambda,\phi}(\lambda, \theta_i, \phi)} \quad \text{Eq. 3}$$

The soiling rate is defined as the change in cleanliness factor over the change in time Δt, as given by Eq. 4.

$$\dot{C}_s = \frac{\Delta C_s}{\Delta t} \quad \text{Eq. 4}$$

2.3.4 Solar reflector soiling and degradation

Most of the soiling studies conducted have been undertaken in desert or semi-desert regions, or simulated to mimic those conditions, because of the favourable solar conditions (i.e., high direct normal irradiation (DNI)) typically found there. The dry conditions result in higher dust concentrations in the atmosphere, posing a challenge for CS systems in general, especially because the performance of a CS system is sensitive to small losses in reflector performance. This is explained by the fact that a particle on the reflector's surface acts doubly by shading and blocking the incident solar rays, relative to PV soiling, where only shading is relevant. Figure 5 illustrates the blocking and shading mechanism of solar reflector soiling.

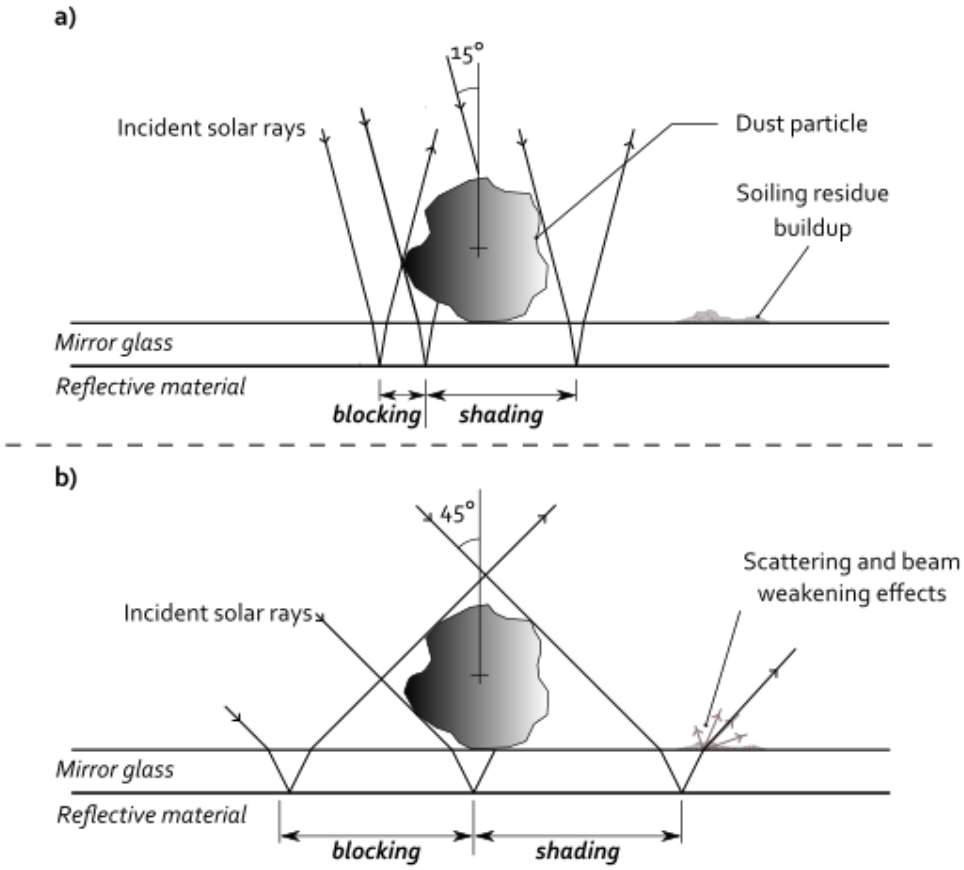

Figure 5. Diagram representation of shading and blocking effects particles have on a reflective surface for a beam incidence angle of a) 15° and b) 45°.

Sandia National Laboratories, in the United States, funded and drove most of the major early investigations into CSP systems, with many efforts focused on dust and heliostat reflective performance (Sarver et al., 2013). This is mentioned because these studies provide the underpinnings for understanding the impact of dust on heliostat reflector performance and how to clean these reflective surfaces at scale.

Early on, Blackmon and Curcija (1978) observed that optical losses caused by particles on the reflective surface are directly related to the particle size, dust density and thickness of the dust layer on the reflector's surface. Dielectric properties of a particle were also found to be of importance; this is attributed to the different adhesion properties of the particles and their surface interactions, according to Sarver et al. (2013). Pettit and Freese (1980) found that the primary effect of dust accumulation is the weakening of intensity of the specularly reflected beam while retaining the same beam profile, confirming earlier studies by Pettit et al. (1978) and Freese (1979). Specular reflectance was reduced by five times that of hemispherical reflectance, implying that the particles accumulated on the reflective surface are more likely to scatter than absorb solar radiation. Continuous dust analysis also found a higher percentage of larger particles (> 10 μm) relative to smaller particles (< 1 μm) on the studied reflector surface shortly after cleaning, and as time passed, smaller particles became more prevalent until they surpassed the number of large particles.

In locations where dust storms occur, particle damage as a result of bombardment and abrasion occurs. Zakhidov and Ismanzhanov (1980) showed wind speed to be the governing parameter for damage caused to a reflector's surface by particles. Intuitively, the damage potential depends on the particle's dimensions. Winds flowing at 6 m/s, carrying particles equal to and smaller than 5 μm, were not found to damage the reflector's surface, but larger particles were found to cause damage. It was also found

that wind speeds above 15 m/s damage the mirrors, no matter the particle size. A preventative action would be to avoid situating concentrating solar fields in regions with loose soil and frequent wind events above 15 m/s.

The beneficial effects of rain in cleaning dust off reflectors have been found in multiple studies, e.g., Costa et al. (2018), where the performance of solar reflectors are usually restored to nearly original capacities if the intensity and duration of the rain are sufficient (Roth and Pettit, 1980). Light rains and morning dews can become problematic in some cases. A light rain that does not last long enough to wash the dust off a reflector can leave dirt spots on its surface, while morning dew can collect atmospheric dust and deposit it on a reflector's surface as it condenses and evaporates. Both of these precipitation and evaporation processes are known as cementation. Cementation, and other such mechanisms, is mainly influenced by dust particle and reflector surface topologies. Cementation most often occurs in coastal environments where salt precipitation is a primary cause (Ilse *et al.*, 2018). Cementation processes also occur when the relative humidity is above 80 % and the temperature above 0 °C.

2.3.5 Dust prevention and mitigation

A general rule of thumb for reflectance drop at a CSP site is 0.8% per day, with reflectance values allowed to drop as low as 72 % before the cost of power loss exceeds the cost of cleaning, but these are very site-specific (Wang, 2019b). It is typical for heliostat fields in commercial operations to require cleaning twice per month. Macro site selections are made by considering a number of factors, including (Schlecht and Meyer, 2012): site-specific solar resource and meteorological patterns, terrain topography and surroundings, infrastructure connectivity, water resource, natural risks, labour availability and land permissions. Consideration of dust prevention does not feature in the typical recommendations outlined above because it does not make sense in the context of an area dust source (i.e., a semi-desert region), but preventative actions could play an important role when considering the siting of a CST plant close to a 'point' dust source (i.e., a smelter).

In the context of this study, where a dust emitting smelter is the source of dust, one way to prevent heliostat soiling would be through dust emissions source control. Comprehensive coverage of dust emissions source control is provided in the *Pollution prevention and abatement handbook* published by the World Bank Group (World Bank, 1999). Authors Jain et al. (2016) also discuss the prevention of particulate matter pollution from industrial mining and minerals processing activities in some detail. Source control is not expanded on here because the methods advocated for industry are widely understood and documented in handbooks and textbooks. Another way to prevent heliostat soiling would be to locate the prospective CST plant such that it avoids most of the wind blown dust for most of the year.

If heliostat soiling cannot be prevented, it must be mitigated to limit the potential heliostat performance loss. A heliostat's surface material resistance to dust accumulation is a crucial consideration in heliostat design. Once dust particles have deposited on the heliostat's surface, they are held there by a charge-double layer, surface energy, and capillary effects in addition to the electrostatic and gravitational forces (Berg, 1977). The various forces involved in dust accumulation are potentially adaptable to dust removal or mitigation (Berg, 1978). There are a few studies that attempt to understand these forces to develop soiling mitigation methods for solar PV panels and CS reflectors (Costa, Diniz and Kazmerski, 2018). The following relates six general methods for cleaning of flat surface solar reflector surfaces or PV panels (Ghazi, Sayigh and Ip, 2014):

- Water jet washing, which is expensive in areas where water is scarce and it is labour intensive relative to passive methods

- Compressed air jetting, where there is a risk that dislodged dust gets suspended into the air and resettles onto a recently cleaned surface
- Tilting of the surface to an elevation of 90° in the morning so that accumulated dust falls off, which is a low-cost, high impact method but only works for larger particles
- Automated dry mechanical wiping systems, which do not remove bird droppings or cemented particles
- Anti-soiling coatings, an example of which would be a TiO_2 super-hydrophilic film
- Electrostatic methods, developed for extra-terrestrial rover exploration purposes

Fernández-García et al. (2014) studied various cleaning methods under outdoor conditions in the semi-desert climate at the Platforma Solar de Almeria testing facility in South Spain. The study was conducted over two years, batched into phases of three-month periods, and different cleaning methods compared. Cleaning methods were applied every two weeks. They tested a variety of cost-effective cleaning approaches to find the best one. The cleaning methods consisted of a combination of these variables: contact device type (brush and soft tissue), water quality (demineralized and tap), water pressure, additives, and water state (liquid and steam). They found that the simple application of demineralized water and brushing with a horsehair brush was the most effective cleaning method. Detergents were not found to aid the cleaning. Furthermore, the authors found this method to be the only effective one in very dry periods. During the rainy season, a high-pressure demineralised water spray was shown to be just as effective as the brush with the demineralised water method.

Wette, Sutter and Fernández-García (2019) evaluated anti-soiling coatings in outdoor conditions. Anti-soiling coatings can be divided into three types categorized by working mechanisms, namely: hydrophobic coatings, hydrophilic coatings, and ultraviolet organic matter degradation enhancement coatings. For a coating to be effective, it needs to have a negligible effect on the reflectance properties of the reflector's initial state, withstand degradation and keep its optical properties, and reduce dust accumulation on the surface of the reflector enough to see a bankable reflectance difference between a coated and uncoated reflector can be measured. Fernández-García et al. (2019) performed durability tests that address the first two of the above-mentioned points, concluding that the anti-soiling coating does not have a noticeable effect on the reflectivity of the reflector, and it showed good durability in outdoor and mechanical wear testing. It was observed that the coated mirrors perform better relative to uncoated mirrors as the soiling conditions worsen. The behaviour and performance of the coatings are strongly dependent on environmental conditions and cleaning strategy.

This concludes the review of important points regarding dust prevention and dust mitigation as they relate to heliostat soiling. With a physical understanding of heliostat soiling and the factors that influence it, we can now develop the understanding required for modelling dust dispersion.

2.4 Modelling atmospheric boundary layer (ABL) flow

This sub-section seeks to develop a basic intuition of ABL flows and highlights the core concepts needed to model microscale flows and near field particle dispersion. A good basic understanding of the relevant meteorological processes and analysis techniques is gained by considering books by Stull (1988), Zhang (2015) and Landberg (2016).

2.4.1 Scales of atmospheric motion

Energy exchange between the atmosphere and the Earth's surface, driven by solar irradiation, cause winds to blow. Rotation of the Earth causes winds to veer. The combination of these two effects result in continuous global scale circulation processes, all the way down to the microscale. The spatial and temporal scales observed in the atmosphere are shown in Figure 6.

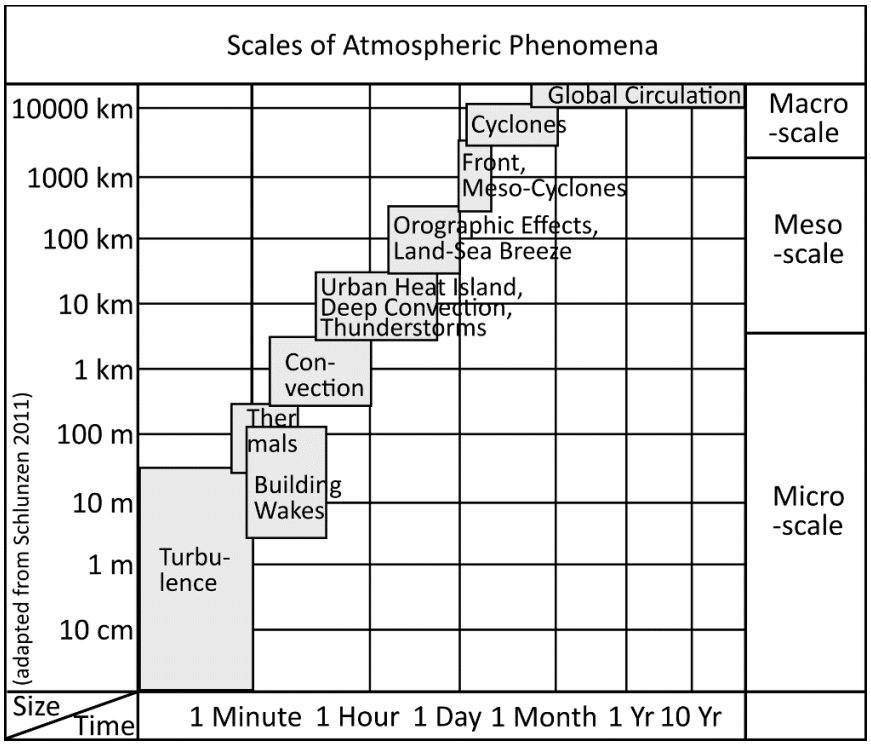

Figure 6. Spatial and temporal scales of phenomena observed in the atmosphere, adapted from Schlünzen *et al.* (2011) with permission, based on work originally done by Orlanski (1975) and Randerson (1976).

Dispersion and deposition of dust and pollution processes occur at all atmospheric scales, but the micro-scale, as classified in Figure 6, is where these processes can be thought of as 'near-field' and is the focus of this research (Vervoort, Blocken and van Hooff, 2019a).

2.4.2 Vertical structure of the ABL

The atmosphere is vertically divided into layers. The bottom layer where dispersion occurs, and the one we inhabit, is the troposphere which extends about ten kilometres upwards. As with any flow over a surface, the troposphere has a boundary layer called the atmospheric boundary layer (ABL), extending about 1 km upwards (Stull, 1988). ABL flows have steep velocity gradients near the ground and are turbulent, with Reynolds numbers in excess of $\sim 10^6$ (Zhang, 2015). The ABL is subdivided into the atmospheric surface layer (ASL), the Ekman layer, and the free atmosphere. The ASL is where the logarithmic wind velocity profile holds, with its height depending on the time of day and stability conditions, but is typically a few 100 m. The Ekman layer above is characterised by a three-component force balance between Coriolis forces, pressure gradient and friction forces. Where the surface frictional forces become negligible, the free atmosphere is found. The change of the vertical structure of the ABL with the time of day is illustrated in Figure 7.

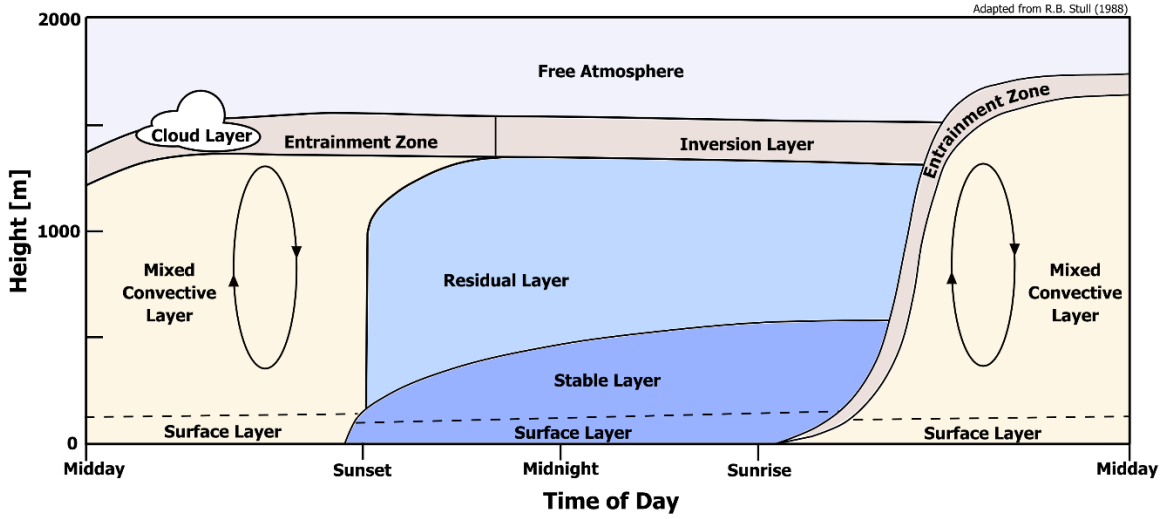

Figure 7. Evolution of the vertical structure of ABL flow with the time of day, adapted from Stull (1988).

Figure 7 shows the unstable and stable ABL stability classes, with the neutral stability class implied. The vertical motion of air in the atmosphere is driven by heat fluxes to and from the Earth's surface, which causes localised upwards or downward movements of an air parcel. When the ASL is positively heated by the terrain, the air becomes buoyant and rises, resulting in unstable conditions. The opposite is true at night times when the surface temperature is lower than the air above it. Unstable conditions promote turbulent mixing, whereas stable conditions dampen turbulent mixing. The neutral condition is not so common as it mainly occurs at the crossover time between day and night or when cloud cover suppresses surface heating (Svensson *et al.*, 2011).

Starting from the free atmosphere and going down, frictional forces become more noticeable, and wind speed reduces, causing the wind to veer towards the low pressure inside the Ekman layer. The wind does not veer in the ASL, with frictional forces dominating its behaviour. The vertical wind velocity profile of the ASL can be described by a logarithmic profile or equivalently by a power-law profile, depending on the requirement. Microscale models seeking to represent the flow close to the surface more realistically use the logarithmic profile, given by Eq. 5 for neutral ABL stability conditions,

$$\frac{u(z)}{u_*} = \frac{1}{\kappa}\ln\left(\frac{z}{z_0}\right) \qquad \text{Eq. 5}$$

with κ the von Karman constant, usually taken as $\kappa = 0.4$, the friction velocity u_* (Stull, 1988), indicating the boundary layer velocity gradient

$$u_* = \sqrt{|\tau|/\rho} \qquad \text{Eq. 6}$$

and τ the shear stress. The surface aerodynamic roughness length z_0, is the lower boundary or height where the velocity profile disappears (i.e., forest canopy tops, suburban housing rooftops, grass tops in grassy fields) (Wieringa, 1992). Surface roughness has a delayed effect on the wind profile shape. As an equilibrium wind profile blows over land that changes from one roughness to another in a discrete manner, an internal boundary layer forms. It takes a few kilometres for the effect of the roughness to traverse the entire height of the profile. This means that sufficient upstream length is required when modelling ABL flow to allow for the realistic development of wind profiles before the area of interest (AOI) is reached. A roughness classification reference is given in Appendix A for later use.

Since this research is only interested in micro-scale dust dispersion in the ASL, the vertical structure of the ABL is simplified and assumed to carry the characteristics of the ASL throughout. Reference to the ABL modelling from here onwards will carry this simplification. The modelling will be termed ABL modelling because any simulation domain will necessarily extend vertically into the Ekman layer region (for reasons that will become clear later), even though the physics of the Ekman layer can be neglected since they are minor over the micro-scale investigated.

It has been established that ABL flows are mostly stable or unstable (Svensson *et al.*, 2011), with the neutral stability conditions only represented for shorter periods throughout a day. However, the neutral ABL stability condition is suitable for modelling most wind engineering applications (Franke *et al.*, 2007). Joseph, Lowndes and Hargreaves (2018) clarify that the approach of only investigating neutral conditions when considering dust dispersion can lead to overestimations of ground particle concentrations since the upwards convective mixing is not included in the modelling approach. From the referenced literature, it is concluded that if the goal is to simulate exact conditions over time, then stability must be accounted for, and if the goal is to study dust dispersion behaviour in a cumulative relative manner, then the well-known Reynolds-averaged Navier-Stokes (RANS) with $k-\epsilon$ turbulence models are sufficient. The following two sub-sections consider the RANS equations and the $k-\epsilon$ turbulence models.

2.4.3 The Reynolds-averaged Navier-Stokes (RANS) equations

The discussion in this chapter is aided by consultation of the books written by Moukalled, Mangani and Darwish (2016) and Nieuwstadt, Westerweel and Boersma (2016), both containing a thorough exposition of turbulence modelling and its underlying physics, each with their own focus.

The Navier-Stokes (N.S.) equations describe fluid motions for laminar and turbulent flows. They are based on the laws of conservation of mass, conservation of linear momentum, and the conservation of energy for a given fluid element or material volume. Time averaging of the N.S. equations is achieved through Reynolds decomposition, which separates the mean flow components ($\overline{\theta_i}$) from the fluctuating flow components (θ_i'), shown in Eq. 7, resulting in the RANS equations, where θ represents any flow component. Time averaging is required to obtain a steady-state flow field solution.

$$\theta_i(x,y,z,t) = \overline{\theta_i(x,y,z)} + \theta_i'(x,y,z,t) \qquad \text{Eq. 7}$$

The RANS equations for continuity and conservation of momentum, absent of mass sources and sinks, are given by Eq. 8 and Eq. 9.

$$\frac{\partial(\rho\overline{u_i})}{\partial x_i} = 0 \qquad \text{Eq. 8}$$

and

$$\frac{\partial(\rho\overline{u_i})}{\partial t} + \frac{\partial(\rho\overline{u_i}\overline{u_j})}{\partial x_j} = -\frac{\partial\bar{p}}{\partial x_i} + \frac{\partial}{\partial x_j}\left[\mu\frac{\partial\overline{u_i}}{\partial x_j} - \rho\overline{u_i'u_j'}\right] + F_b \qquad \text{Eq. 9}$$

with μ the dynamic viscosity and F_b representing body forces acting on the fluid volume. The energy conservation equation usually makes up the third equation in the system but is not given here since no energy sources or sinks will be modelled. The terms that emerge after the decomposition are the Reynolds stresses, $-\rho\overline{u_i'u_j'}$, the averaged fluctuating components of the non-linear terms. These Reynolds stresses add six more unknowns to the momentum equations. The process of solving these Reynolds stresses is referred to as turbulence modelling. Turbulence models close the system of equations by expressing the non-linear averaged fluctuating components in terms of the mean flow. The

Reynolds stresses are modelled by relating the Reynolds stresses to the mean velocity gradient via the Boussinesq hypothesis, as follows for incompressible flows

$$-\rho\overline{u_i'u_j'} = \mu_t\left(\frac{\partial\overline{u}_i}{\partial x_j}+\frac{\partial\overline{u}_j}{\partial x_i}\right)-\frac{2}{3}\rho k\delta_{ij}\,, \qquad \text{Eq. 10}$$

where k is the turbulent kinetic energy and μ_t is the turbulent eddy viscosity, noting that these two terms are purely dependent on the flow and are not material properties of the fluid. The two-equation $k-\epsilon$ turbulence model, appropriate for modelling ABL flows (Franke *et al.*, 2007), is used to solve for the turbulent eddy viscosity in this work.

2.4.4 The k - ϵ turbulence model

The $k-\epsilon$ turbulence model introduced by Jones and Launder (1972) is widely used in industry because it is economical, reasonably accurate, and applicable to a wide range of common turbulent industrial flows (Wilcox, 1993). The $k-\epsilon$ turbulence transport equations, as they are implemented in ANSYS Fluent (ANSYS Inc., 2020), are described in this section. The equations for turbulence kinetic energy (TKE) and turbulence dissipation rate (TDR) are given by

$$\frac{\partial\rho k}{\partial t}+\overline{u_j}\frac{\partial\rho k}{\partial x_j}=G_k-\epsilon+\frac{\partial}{\partial x_j}\left[(\mu+\mu_t/\sigma_k)\frac{\partial k}{\partial x_j}\right]+S_k \qquad \text{Eq. 11}$$

and

$$\frac{\partial\rho\epsilon}{\partial t}+\overline{u_j}\frac{\partial\rho\epsilon}{\partial x_j}=C_{\epsilon1}\frac{\epsilon}{k}G_k-C_{\epsilon2}\rho\frac{\epsilon^2}{k}+\frac{\partial}{\partial x_j}\left[(\mu+\mu_t/\sigma_\epsilon)\frac{\partial\epsilon}{\partial x_j}\right]+S_\epsilon \qquad \text{Eq. 12}$$

On the right-hand side of Eq. 11, we have the production, dissipation and diffusion of kinetic energy terms; and on the far right-hand side of both equations are user-defined source terms, S_k and S_ϵ, for later use. The turbulence production term is written in terms of the Boussinesq hypothesis for both equations, as follows

$$G_k=-\rho\overline{u'_iu'_j}\frac{\partial\rho\overline{u}_i}{\partial x_j} \qquad \text{Eq. 13}$$

The turbulent viscosity term is represented by Eq. 14

$$\mu_t=\rho C_\mu\frac{k^2}{\epsilon} \qquad \text{Eq. 14}$$

where C_μ is an added constant. The default values of the closure constants found in Eq. 11 to Eq. 14 are: $C_{\epsilon1}=1.44$, $C_{\epsilon2}=1.92, C_\mu=0.09$, $\sigma_k=1.0$, $\sigma_\epsilon=1.3$.

2.5 Near field particle dispersion modelling

2.5.1 Background

Tracking particle trajectories in the atmosphere has been under development in different forms for more than a century (Thomson and Wilson, 2013). Particle dispersion in the atmosphere is modelled using a Lagrangian approach, whereby particles are tracked as they move through a flow domain by using a moving frame of reference. In this way, information about the particle's trajectory is made available, which is not the case when a Eulerian frame of reference is used.

Lagrangian models of varying approximations to reality have been developed. The most basic form is the mean trajectory model that assumes a tracked air parcel retains its form, which is very unrealistic because turbulent diffusion cannot be ignored for ABL flows (Stull, 1988). Model types that attempt to take the effects of turbulent diffusion into account are the Lagrangian box models (Strong *et al.*, 2010), Gaussian puff models used for regulatory purposes (Scire, Strimaitis and Yamartino, 2000), and the more advanced Lagrangian particle dispersion models (Anfossi *et al.*, 2010).

These dispersion models include the terrain explicitly and can include forest canopies implicitly along with other terrain roughness features. They also make simplifying assumptions about near-building vortex flows in urban canopies, and some include basic building geometries explicitly (Hanna *et al.*, 2011). Separate codes are usually required to solve the flow field and particle tracking. These weaknesses lead to the strength of CFD codes. With the computational power available today, it is possible to calculate atmospheric flows at the meteorological microscale using steady-state RANS-based methods to resolve flows around buildings without any physics parameterisations. It is also possible to solve the near field particle dispersion using built-in Lagrangian Discrete Phase Methods (DPM) (ANSYS Inc., 2021). These are the reasons why researchers and engineers have adopted the Euler-Lagrange (or CFD-DPM) approach to particle dispersion modelling.

2.5.2 CFD-DPM approach

Researchers and engineers interested in near field pollution dispersion acting at the meteorological microscale have adopted the use of one-way coupled CFD-DPM approaches to study how high pollution concentrations can be prevented or mitigated in certain urban settings (Vervoort, Blocken and van Hooff, 2019b). Other examples of near field pollution dispersion studies include the study of cooling-tower particle emission drift (Meroney, 2008), the spread of particulates from mining operations (Joseph, Lowndes and Hargreaves, 2018), and assessing the potential for human and environmental health fallout should industrial chemical leaks or spills occur (Scargiali *et al.*, 2005).

Assessments of near-field particle dispersion for various industrial and urban flows have been carried out through on-site measurement campaigns, experimentation in ABL wind tunnels, and by simulation using a CFD-DPM approach, with varying levels of success. The difficulty with an on-site measurement campaign is that a dense spread of sampling locations are needed over extended periods of time. These two requirements must be met to reasonably capture the effects of varying mass fluxes at the particle source and the short-term variations in wind direction on the particulate concentrations. The lack of proper validation data of dust dispersion has been, and still is, one of the main hurdles to reliable CFD-DPM dust dispersion simulations (Schatzmann and Leitl, 2009, 2011). Difficulties in acquiring suitable data mean that particulate source injection rates into the atmosphere are typically unknown. Modellers, therefore, take a stochastic approach by injecting 10^5 to 10^6 particles at the source such that particle trajectory and deposition statistics can be determined with confidence. It is assumed that the particles do not interact with one another nor with the continuous phase from which their trajectories are determined.

2.5.3 Particle trajectory model description

Particle behaviour as formulated in ANSYS Fluent is given in this section (ANSYS Inc., 2021). The particle's inertial transport, written in a Lagrangian reference frame, is given by

$$m_p \frac{d\boldsymbol{u_p}}{dt} = m_p \frac{\boldsymbol{u} - \boldsymbol{u_p}}{\tau_r} + m_p \frac{\boldsymbol{g}(\rho_p - \rho)}{\rho_p} + \boldsymbol{F} \qquad \text{Eq. 15}$$

where m_p is the particle mass, u the fluid velocity, u_p the particle velocity, ρ_p the particle density, and $\boldsymbol{F}$ is an additional force vector. Additional forces include torque applied to particles, virtual mass forces

(relevant if considering the particles' force on the fluid), fluid pressure gradient force, and forces resulting from moving frames of reference (i.e., Coriolis forces if applicable). The particle relaxation time τ_r, is given by Eq. 16,

$$\tau_r = \frac{\rho_p d_P^2}{18\mu} \frac{24}{C_D Re_p} \quad \text{Eq. 16}$$

with d_p being the effective particle diameter, and C_D the particle drag coefficient for an assumed spherical particle,

$$C_D = a_1 + \frac{a_2}{Re_p} + \frac{a_3}{Re_p^2} \quad \text{Eq. 17}$$

where the constants a_1, a_2 and a_3 vary with the flow Reynolds number in accordance with empirical relationships (Morsi and Alexander, 1972). The particle relaxation time is the particle's response time to changes in fluid velocity, where a faster flow in a denser fluid will cause a particle to respond faster to fluctuations in the flow. Similarly, a heavier particle will be slower to respond to fluid velocity fluctuations. The particle Reynolds Re_p, given in Eq. 18, is the relative Reynolds number.

$$Re_p = \frac{\rho d_p |\boldsymbol{u} - \boldsymbol{u}_p|}{\mu} \quad \text{Eq. 18}$$

The particle deposition flux rate *S*, is a useful measure of a given area of terrain's reflector soiling potential in the flow field, and is given by

$$S = c_{dust} v_d \quad \text{Eq. 19}$$

where c_{dust} is the dust concentration and v_{dust} is the particle deposition velocity.

2.5.4 Stochastic Lagrangian DPM

Each individual particle is tracked by integrating the particle trajectory equations of motion for the instantaneous fluid velocity along the particle path. The RANS equations give the mean fluid velocity component. The fluctuating fluid velocity component must therefore be determined. The fluctuating velocity component is obtained using a stochastic random-walk process, resulting in piecewise-constant velocity fluctuation components that are functions of time, remaining constant for a time equal to the calculated local eddy characteristic lifetime. The integral time scale T, over which the trajectory integration is done, is given by

$$T = \int_0^\infty \frac{u_p'(t) u_p'(t-\tau)}{\overline{u_p'^2}} d\tau \quad \text{Eq. 20}$$

For particles dispersed in a $k-\epsilon$ turbulence field, the integral time becomes

$$T_L = C_L \frac{k}{\epsilon} \quad \text{Eq. 21}$$

the Lagrangian integral time, where the integration time-scale constant is approximated to $C_L = 0.15$, by making the predicted diffusion rate equal to the tracer particle diffusivity $\overline{u_i' u_j'} T_L$. The Lagrangian integral time is used to calculate the eddy lifetime.

The discrete random-walk method models the particle's motion by having it interact with a series of discrete eddies. Eddies are described by their lifetime and fluctuating velocity components. The eddy characteristic lifetime is given by

$$\tau_e = -T_L \ln(r) \qquad \text{Eq. 22}$$

where r is a uniform random number between zero and one. An eddy's fluctuating components (u', v', w') are assumed to exhibit a Gaussian distribution, such that

$$u' = \xi\sqrt{\overline{u'^2}} \qquad \text{Eq. 23}$$

where ξ is a normally distributed random number. The turbulent kinetic energy is available from the calculated flow field, and with the assumption of local isotropic turbulence, the root-mean-squared fluctuating components are

$$\sqrt{\overline{u'^2}} = \sqrt{\overline{v'^2}} = \sqrt{\overline{w'^2}} = \sqrt{2k/3} \qquad \text{Eq. 24}$$

The interaction time of a particle with an eddy is taken as the shorter of the eddy lifetime or the particle eddy crossing time t_{cross}, given by

$$t_{cross} = -\tau_r \ln\left[1 - \left(\frac{L_e}{\tau_r|u - u_p|}\right)\right] \qquad \text{Eq. 25}$$

with L_e the eddy length scale. The particle-eddy interaction time is thus,

$$t_{interaction} = \min\left(t_{cross}, \tau_e\right) \qquad \text{Eq. 26}$$

Once the particle-eddy interaction is complete, a new instantaneous velocity is calculated by generating a new value for ξ. Eq. 20 to Eq. 26 describe the Lagrangian DPM with the internal discrete random-walk model, which mimics the effects of turbulence based on the turbulence values of a steady-state flow-field solution.

It is noted here that the described method starts to perform poorly when particles are less than a few microns (i.e., $d_p \ll 10$ μm). Additionally, Brownian motion and other buoyancy forces acting on the particles need to be included when particles are less than a few microns in size.

Earlier it was stated that it is hard to come by reliable dust dispersion and emissions data (Schatzmann and Leitl, 2009, 2011). It is therefore also hard to know at what wind speeds particles will be entrained and dispersed. Thus, the following section addresses this need such that wind speeds can be empirically matched to particle emissions for use in simulation setups.

2.5.5 Dust emissions

There are different modes of particle emissions which mainly rely on particle size and wind speed (Rabinovich and Kalman, 2007). Larger particles (~ 100 μm) are the first to move as a result of wind-induced shear at the surface, hopping along in a motion known as saltation (Kok *et al.*, 2012). Interparticle cohesive forces, or Van der Waal's forces, are stronger with smaller particles and prevent particles from being directly lifted off a surface. Particles are generally ejected into an airstream as a result of impaction from saltating particles on a group of smaller particles, the repetition of this process leads to dust emissions (Gillette, Blifford and Fryrear, 1974; Shao, Raupach and Findlater, 1993). The threshold wind speed for dust emission is given by the threshold wind speed for saltation initiation, also

known as the static or fluid threshold; which is higher than the dynamic threshold wind speed since it is easier to transfer momentum to static particles through impaction than from fluid drag (Kok *et al.*, 2012). A semi-empirical expression for static threshold friction velocity u_{*ft}, was obtained by Shao and Lu (2000):

$$u_{*ft} = A_N \sqrt{\frac{\rho_p - \rho_a}{\rho_a} g D_p + \frac{\gamma}{\rho_a D_p}} \qquad \text{Eq. 27}$$

where ρ_a is the density of air, the dimensionless constant $A_N = 0.111$, and γ is a parameter that scales the strength of the interparticle forces in the range of 1.65×10^{-4} N m^{-1} $\leq \gamma \leq 5.00 \times 10^{-4}$ N m^{-1}. The particle density ρ_p, and particle equivalent spherical diameter D_p, vary depending on particle material.

This concludes the exposition of all the information and methods required to model near-field particle dispersion acting at a micro meteorological scale.

2.6 Summary

The literature review has expanded on all the various topics and tools required to study near-field dust particle dispersion experimentally and numerically as it relates to solar reflector soiling. The developed understanding will aid the discussions of any findings in future chapters.

The following chapter is focused on the experimental campaign undertaken at the Transalloys smelter complex.

3 Experimental Campaign

This chapter outlines the experimental campaign conducted at the Transalloys ferromanganese smelters over an eight-month period, from 05/02/2020 to 29/10/2020. The campaign involves a soiling study carried out on thirty-two reflector samples, characterisation of dust samples collected at the site and on the mirrors using various analysis techniques, and the measurement of meteorological parameters throughout the period.

The experimental data are used in the development of the *Dust management protocol* for the PREMA project, as well as for validation of the CFD and DPM simulation work that follows this chapter.

3.1 Study domain

The Transalloys ferromanganese smelter is located near Emalahleni, Mpumalanga, South Africa. The plant is one of two ferromanganese producers in South Africa, with an annual production of around 165,000 tonnes per annum. They are the only producers of silicomanganese in the country. Transalloys is situated in the heart of industrial South Africa, with many mining and related activities in the region, as illustrated by Figure 8. An open-source tool named QGIS is used to work with the terrain data (QGIS.org, 2021).

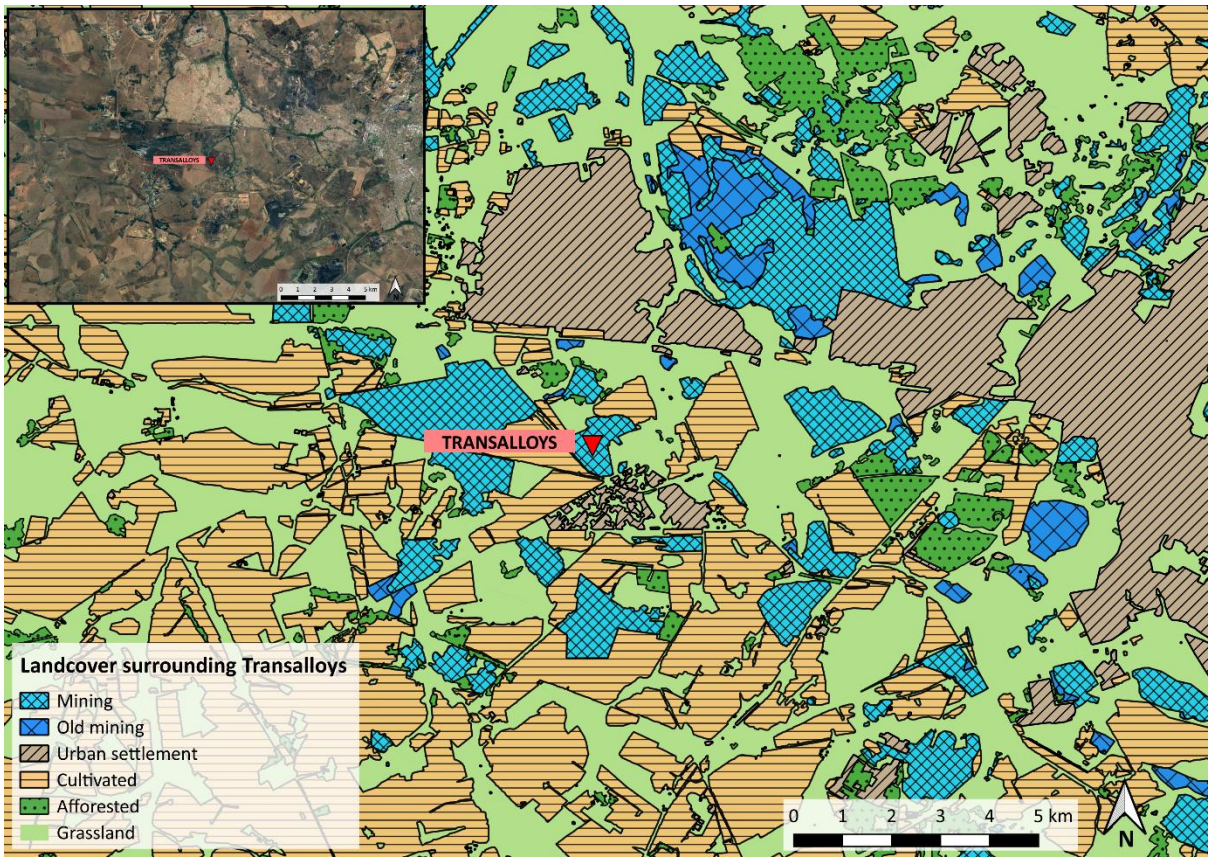

Figure 8. Land-use classification of area immediately surrounding Transalloys ferromanganese smelters (Emalahleni, South Africa). Data source: Lotter (2010) with Google Earth insert.

The numerous coal-fired power plants, coal mines, cement quarries, cement plants, and ferrochrome smelters all make Transalloys the ideal location for studying the effects of industrial dust on solar

reflectors. Figure 9 visually shows the atmospheric dust loads at, and in the region of, the Transalloys smelter on a windy day. A ferrochrome smelter can be seen in the distant background.

Figure 9. A photograph of dust conditions around Transalloys on a windy day. The photograph is taken from the Transalloys site, with the camera aimed in a NE direction, around 10AM in the morning.

The Transalloys smelter is an EII where materials handling (transportation, screening, fines recovery), mechanical breakdown of ores and other reactants, normal smelter reactions, tapping, and casting are expected to be the main dust-producing activities as identified in the literature. An enlarged view of Transalloys is given in Figure 10, showing the areas where grab samples were taken to get a first impression of the most common materials found on site.

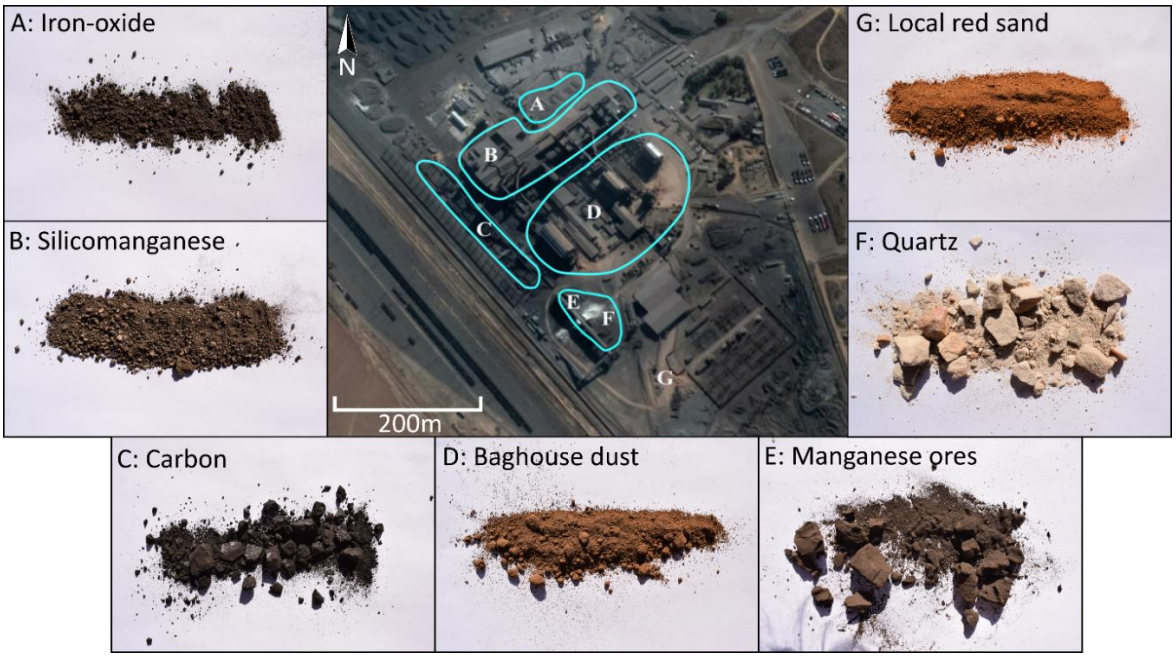

Figure 10. Enlarged view of dust detailing areas at Transalloys, highlighting different potential sources of dust and showing representative grab samples taken from each area. Overview source: Google Earth.

The source materials for potential dust emissions at the Transalloys site, as pictured in Figure 10, are:

A. FeOx – Iron-oxide dust produced during tapping
B. SiMn – Silicomanganese dust produced during casting
C. C – Carbon dust from handling high-carbon charcoal
D. Baghouse dust – Mixture of FeOx, SiMn, and C
E. MnOx – Manganese ore dust resulting from handling
F. SiO2 – Quartz dust from handling
G. Local red sand – dust generated by agricultural, human activities, and natural processes

3.2 Method

The aim of this soiling study is to observe how reflector soiling rates vary with location relative to the plant and with the time of year. Since the goal is not to determine an optimal cleaning frequency but rather to measure reflectance loss between reflector cleaning, a cleaning frequency of 14 (±3) days is chosen. The cleaning frequency is chosen such that the mirrors are cleaned more than once per month, based on a cleaning frequency optimisation case study for a hypothetical CST plant and heliostat field located in Woomera in South Australia (Picotti *et al.*, 2020).

The reflector cleaning method consisted of spraying the samples with demineralized water using a hand-pump pressure sprayer, followed by subsequent wiping with a microfiber cloth to loosen all the dust particles, followed by another spray to wash loosened materials off. The aim of this cleaning method is to clean the mirrors as best possible and not to test cleaning method effectiveness.

Field soiling studies of solar reflectors are conducted using portable reflectometer devices, such as the ones compared by Fernández-García *et al.* (2017). Guidelines have been developed by a SolarPACES working group on reflectance measurement (Meyen *et al.*, 2018), that outline the suggested methods for measuring solar reflectance of solar reflectors. These have been adhered to as far as is possible for this study.

The reflector soiling measurement campaign procedures are summarised as follows:

1. Take reflectivity measurements of calibration mirror in the lab and store mirror in a safe place
2. Install mirrors in the field and take baseline reflectivity measurements of each mirror
3. Let reflectors soil for 14 (±3) days
4. Take reflectivity samples of each mirror sample
5. Wash the mirrors after measuring the reflectivity of soiled mirrors
6. Take reflectivity measurements of cleaned mirrors
7. Repeat steps 3 – 6 for the duration of the campaign

Wind speed, wind direction, and rainfall are monitored for the duration of the study, using a standalone wind mast and a research-grade weather station. The weather station is a South African Universities

Radiometric Network (Brooks *et al.*, 2015) weather station that was relocated to Transalloys site to measure solar radiation data for PREMA project purposes that are not relevant here.

3.3 Equipment

Reflector soiling and dust deposition sampling points are spread out around the plant, along with the standalone wind mast and the weather station. The locations of all measuring equipment are shown in Figure 11.

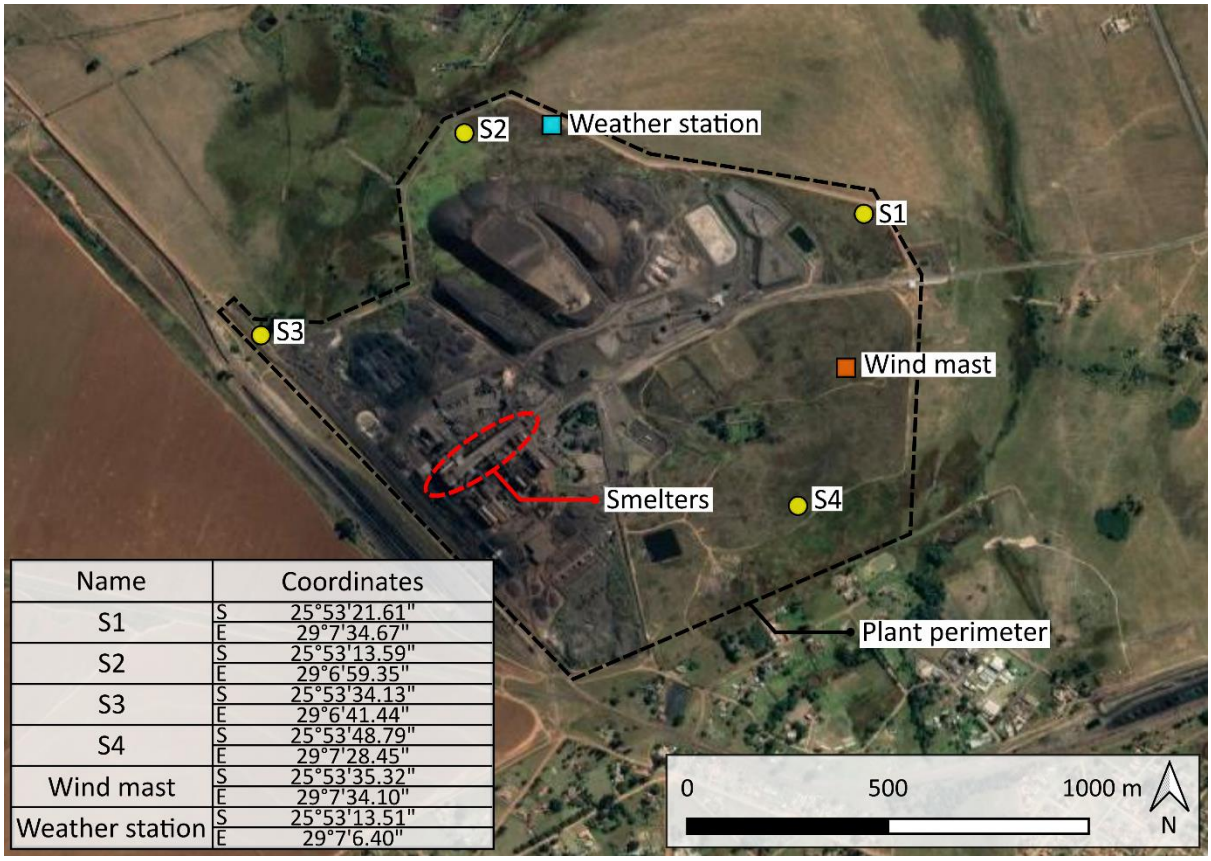

Name	Coordinates	
S1	S	25°53'21.61"
	E	29°7'34.67"
S2	S	25°53'13.59"
	E	29°6'59.35"
S3	S	25°53'34.13"
	E	29°6'41.44"
S4	S	25°53'48.79"
	E	29°7'28.45"
Wind mast	S	25°53'35.32"
	E	29°7'34.10"
Weather station	S	25°53'13.51"
	E	29°7'6.40"

Figure 11. Reflector sampling set and meteorological equipment locations at the Transalloys site. Source: Google Earth.

The reflector set locations were chosen as close as possible to N-E-S-W compass directions relative to the plant as possible. Factors limiting the locations of the sampling sets are the security perimeter location, proximity to operations, and proximity to another sampling set.

The weather station gathers a full set of meteorological data and was located at the Transalloys site to meet other PREMA project requirements (Swart, 2019). The data gathered are used to give an idea of the seasonal weather variations at the Transalloys site.

The standalone wind mast supplied by Campbell Scientific consists of two 2-dimensional Gill Windsonic 1405-PK-100 SDI-12 ultrasonic anemometers. The anemometers are capable of sampling the wind at 4 Hz and have a 0.01 m/s and a 1° resolution on wind speed and direction respectively. The wind mast has an anemometer at (4 and 10) m above ground level (AGL) so that the ABL velocity profile can be deduced from the velocities measured at the two different heights. Care was taken to locate the wind mast at least 10 times the height away from the tallest building in the smelter complex, as per the World Meteorological Organization's (WMO) *Guide to Instruments and Methods of*

Observation recommendation on anemometers over land (WMO, 2018). In this case, the wind mast is in an open field 800 m away from the tallest smelter building, which is equal to 20 times its height, thus in accordance with the WMO's guideline. No correction will be applied to the wind direction data, although the WMO guideline states that the uncorrected measured value can (not will) be erroneous by up to 25 % if the wind is blowing from the direction where the obstacle is found. A photograph of the standalone wind mast is shown in Figure 12.

Figure 12. Wind mast with two 2-dimensional ultrasonic anemometers, one at 4 m and one at 10 m height AGL.

The reflector samples are 5 mm thick, 200 mm by 400 mm, silvered second-surface low-iron glass with a protective vinyl coating applied to the back. Note here that the words 'reflector' and 'mirror' are sometimes used interchangeably in this section to prevent confusion between the words 'reflector' and 'reflectance', the need for which will become clear. The reflectors are installed 2 m AGL and face towards the smelter complex area, assumed to be the main dust source. Each reflector set has eight reflectors, six reflectors at 60° elevation and two at 30° elevation. The reflectors are positioned in four by two arrays, each reflector 2 m apart horizontally and diagonally, as shown in Figure 13. Dust deposition samplers are co-located with each set of reflectors to allow the measurement of atmospheric dust characteristics.

Figure 13. Reflector sampling set four (S4), consisting of eight reflectors, six of which are elevated at 60° and two at 30°. Two collocated dust deposition samplers are seen in the background. The ferrochrome smelter is seen in the far background centre.

The reflectivity measurements of the solar reflectors are made using a custom camera-based reflectometer, developed by Griffith, Vhengani and Maliage (2014) as an alternative to an off-the-shelf handheld reflectometer device such as the ones compared by Merrouni *et al.* (2017), which would have exceeded budget limitations for the project. An advantage this device offers over off-the-shelf reflectometers is that it samples by taking high-resolution images of the sampled reflector area, complementing the information extracted from them by allowing qualitative visual inspection of the sample space. The device and a schematic representation of it are shown in Figure 14.

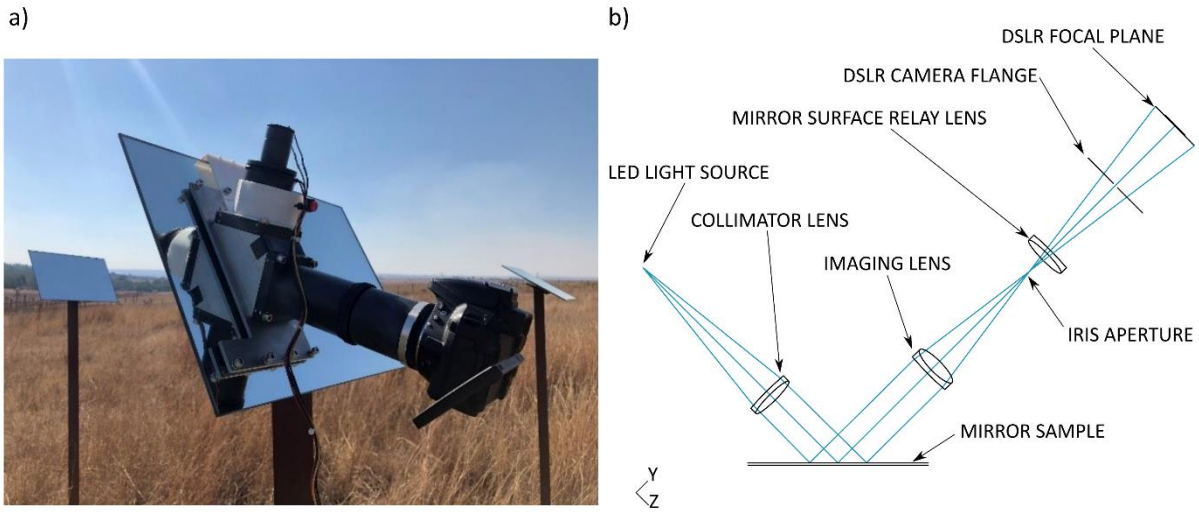

Figure 14. a) Camera-based reflectometer (Griffith, Vhengani and Maliage, 2014) on cleaned mirror sample, b) schematic representation of reflectometer device.

A Nikon D5300 DSLR camera is attached to the custom lens and light system, with a cool white Phillips LumiLEDs Luxeon Rebel Light LED as light source. The camera is built for professional use, thus

having a very high signal-to-noise ratio of 0.2 %. The sampling area is 17.7 mm by 16.8 mm, giving a linear field of view of ~ 300 mm^2. The reflectometer samples at a fixed incidence angle of θ_i = 45°, and an acceptance aperture of φ = 15.7 mrad. The angle of incidence is not considered to be near-normal, with θ_i < 15° usually being recommended as a starting point (Meyen *et al.*, 2018). This is justifiable because there is still a large percentage of heliostats in a CSP field that are reflecting at this range of incidence (Heimsath and Nitz, 2019).

The camera-based reflectometer used in this study does not determine the incident light intensity required to determine reflectance. However, the specular reflectance can still be determined without knowing the incident light intensity. The detected beam intensities are a function of the same components, with different reflectance distribution functions. This allows the specular reflectance to be determined as the ratio of light intensity reflecting specularly from a soiled mirror to the intensity of light reflecting specularly from a reference mirror, measured by the same receiving device. The specular reflectance as a fraction of a reference mirror is thus determined, but for convenience is referred to simply as reflectance from here onwards.

The same method described by Griffith *et al.* (2014) of calculating the reflectance for each reflector is followed. First, a dark photo is taken to subtract from the illuminated photo, cancelling out the camera sensor and background noise. Red-green-blue (RGB) mean channel pixel intensities (PI) are then calculated for the corrected image, yielding PI_{RGB}. These two steps are repeated for a minimum of ten sampling spots N_S, per reflector. The mirror (reflector) mean is then calculated by

$$PI_{RGB} = \frac{\sum PI_{RGB}}{N_S} \qquad \text{Eq. 28}$$

The mean PI for the mirror is then used to calculate the reflectance of the mirror as a fraction of the mean PI of a reference (calibration) mirror as follows

$$mirror\_reflectance = \frac{PI_{RGB;mean;sampled}}{PI_{RGB;mean;reference}} \qquad \text{Eq. 29}$$

The reference mirror is kept in a clean lab environment. A representative reflectance is then calculated for each set of mirrors by

$$Mirror\_set\_reflectance = \frac{\sum mirror\_reflectance}{N_m} \qquad \text{Eq. 30}$$

where N_m is the number of mirrors at the same elevation in the current set. Appendix B shows the code and detailed method used to calculate reflectance from the raw mirror image data.

The camera used captures images in the Nikon Electronic Format (NEF), which is a raw image, and is stored in 14-bit unassigned integer (uint14) arrays in this case. The maximum pixel value depends on the number of bits used to store them. The NEF format allows for 14-bit arrays at most and is, therefore, what is used, the maximum value of which is 16383.

3.3.1 Dispersed dust characterisation

To establish whether the smelter is indeed the main dust source, characterizations of the total atmospheric dust, as well as the dust that tends to soil the reflectors, were performed. Dust was collected from all the dust deposition buckets and from all of the reflector sampling sets on different occasions after being left exposed for more than a month. The dust buckets used were based on SANS 1137, itself based on ASTM D1739 (SANS 1137:2012 and ASTM D1739:1998, 2012). The deposited atmospheric

dust were collected after the extended March to May 2020 sampling period. The reflector soiling dust was collected after the reflectance measurement campaign.

Particle size distributions (PSD) for both samples were determined using a Malvern Mastersizer v3.63, which uses a laser diffraction measurement technique. Two separate composite samples were made for the dust collected from the dust deposition buckets, and for the dust collected from the reflectors, these two samples were then analysed. The PSDs for both composite samples are given on the same graph in Figure 15 for comparison.

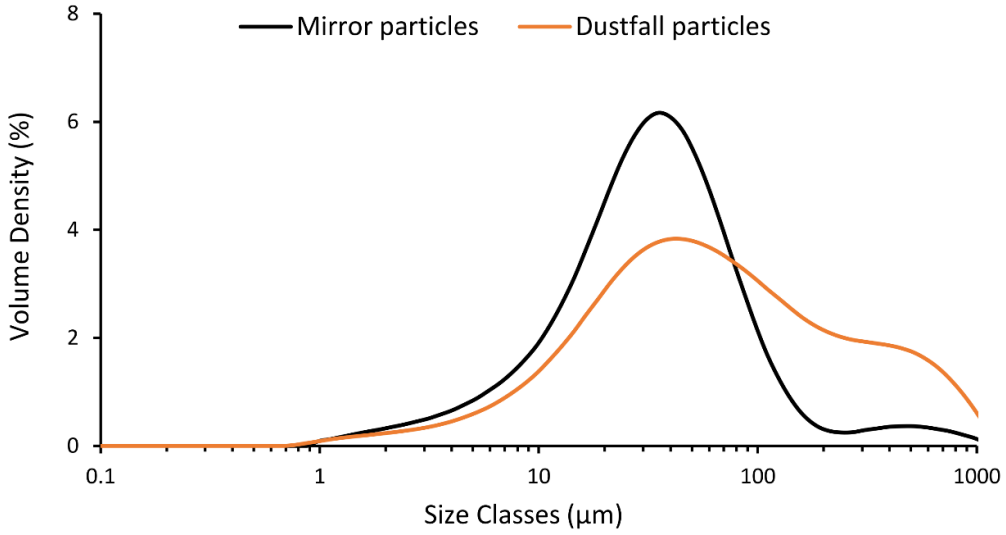

Figure 15. PSD of composite dust samples collected from dust fall samplers and from multiple reflectors at the Transalloys site.

The PSD of the dust collected from the reflectors compared to that collected from the dust fall samplers reveals that the dust present in the atmosphere covers a much larger size range than the dust found on the reflectors. The observation made was that particles larger than 100 µm tend to fall off the mirror and are, for the most part, not transported that far away from the dust source to begin with, shown by the count peak of the atmospheric dust PSD being below 100 µm. The mean of dust particle sizes found on the reflectors is 35.5 µm, with 50 % of the sample being less than 31.1 µm and 90 % of the sample being smaller than 98 µm.

The dust morphology was visually analysed by high-resolution imaging using scanning electron microscopy (SEM) at different magnifications, as revealed by Figure 16.

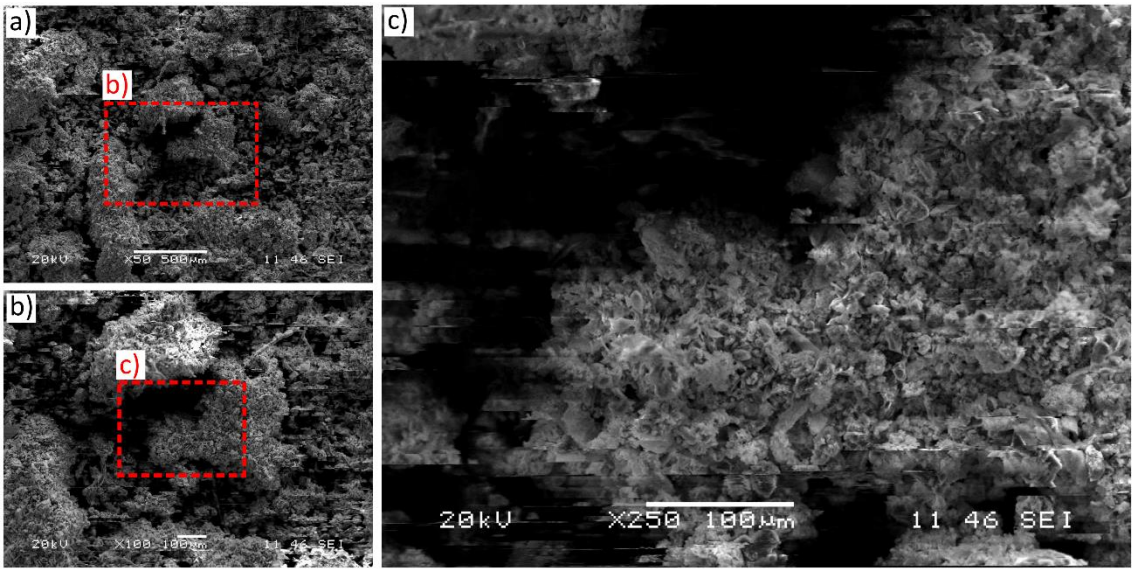

Figure 16. a) x50 magnification b) x100 magnification c) x250 magnification SEM micrographs of dust samples collected from reflectors.

The SEM images show the agglomeration of small particles that occurred as a result of how they were stored and not the state the dust was collected in. The particle shapes become visible at the largest magnification. Some rough edges are visible, but not enough to be called jagged or abrasive.

The quantitative composition analysis is conducted using energy dispersive spectroscopy (EDS). A representative spectra analysis of the reflector dust samples is shown in Figure 17.

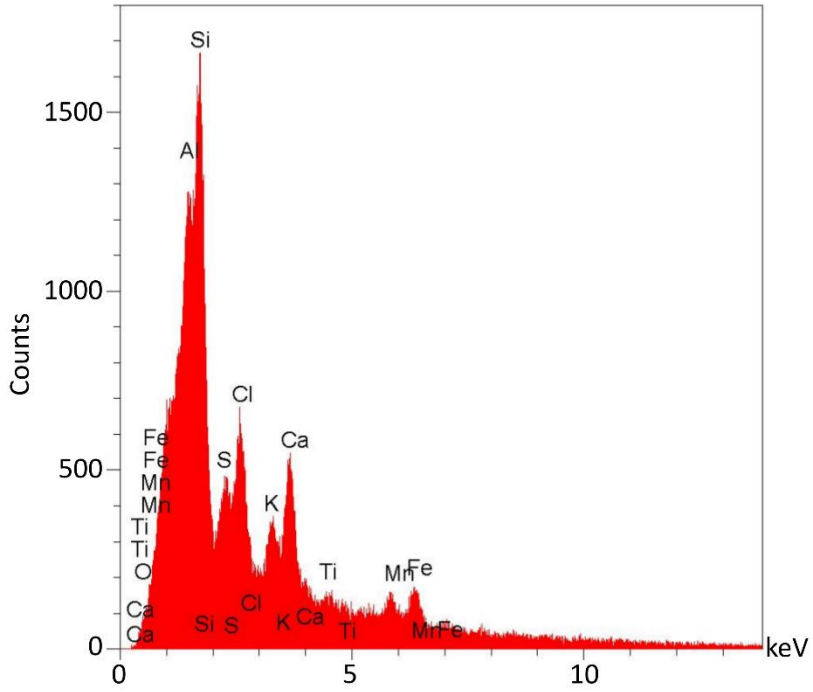

Figure 17. Representative EDS spectra of reflector dust samples.

The results of Figure 17 are summarised in Table 3, with the three dominant elements (in wt. %) being Si (23.5), Al (15.2) and Fe (8.2).

Table 3. Summary of EDS spectra chemical composition of reflector dust sample, in wt. %.

Element (wt. %)	Si	Al	Fe	S	O	Mn
Sample	23.5	15.2	8.2	7.7	7.5	5.8

The crystalline phases present in the sample were extracted using X-ray diffraction (XRD) analysis. Phase matches were made as a part of PREMA, where Silica related phases were dominant, as shown below:

- SiO_2 – Silica-oxide
- Fe_2SiO_4 – Iron-silicate
- $Al_2O_3.SiO_2$ – Kyanite
- $Al_9Fe_2Si_2$ – Ferrosilicon aluminium

The oxide phases are common in sand as well as ores. Routine XRD analysis of coals, ores, and slag at the smelter site shows non-negligible concentrations of alumina (Al_2O_3) in all three of these, thus explaining the most likely source of the aluminium oxide-related phases but not the silica-oxide phase. The alumina present in the coal is typically ~ 1 %, 4 – 5 % in the manganese ores and 3 – 6 % in the slags. An important note made regarding the alumina phase is that even though the concentration in the raw coal is considered low, concentrations of alumina are 3 – 7 % off the 15 % ash content of the reacted coal. The silica-oxide phase can come directly from the raw silica quartz piles and from sand at the site; it is most likely a combination of both. An interesting note to make is that the most common phase (SiO_2) is also the least dense phase, $\rho_{SiO_2} \approx 2.20$ g/cm^3, amongst the other phases identified, confirming that less dense phases are more likely to be present in higher quantities further away from the source than denser phases.

The EDS and XRD results reveal that the sampled dust collected from the reflectors consists mainly of oxidized materials with some metallic aluminium phase also detected. The dominant silica-oxide phase presence suggests a strong soiling source from the raw silica quartz, stored in close proximity to one of the baghouse endpoints. The other common phases found, including the aluminium phases, point towards furnace emissions product, either from fugitive furnace dust or, more likely, from baghouse products.

As the slag heaps are formed by the dumping of liquid and solidified slag, slag particles are likely to be larger in size than dust and ore particles. Slags are also handled less than raw materials. It, therefore, makes sense that dust from the slag products does not seem to significantly contribute to mirror soiling.

3.3.2 Atmospheric conditions

Rainfall data for two full seasons are shown in Figure 18. The dry winter season (June to August) coincides with the decrease in reflectance and rise in soiling trends observed in Figure 20 and Figure 21, respectively.

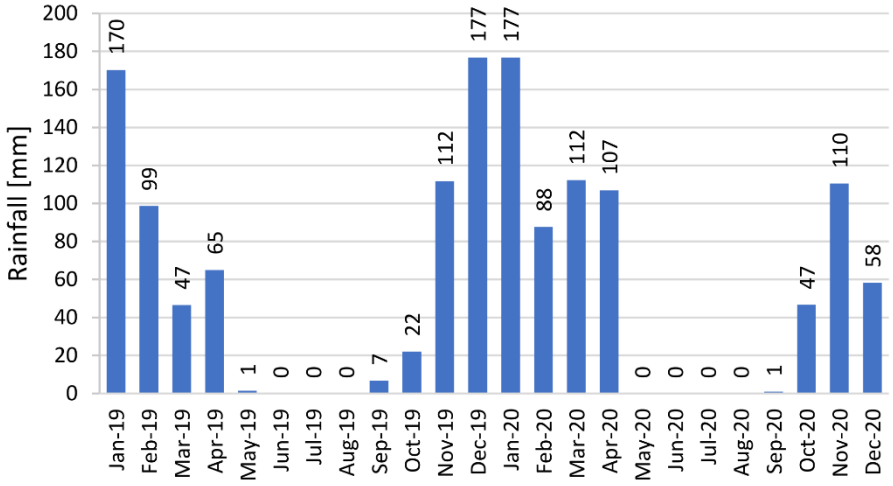

Figure 18. Rainfall measured at Transalloys site from January 2019 to December 2020.

Wind speed and direction data are displayed in Figure 19 for the standalone wind mast, in the form of a wind rose. The displayed wind roses are for seven two-week periods during the dry season when increased loss of reflectance was observed (June to September). The wind roses are displayed to coincide with reflectance sampling dates. All wind data are processed using an open-source python library called *windrose v1.6.8* (Celles *et al.*, 2020).

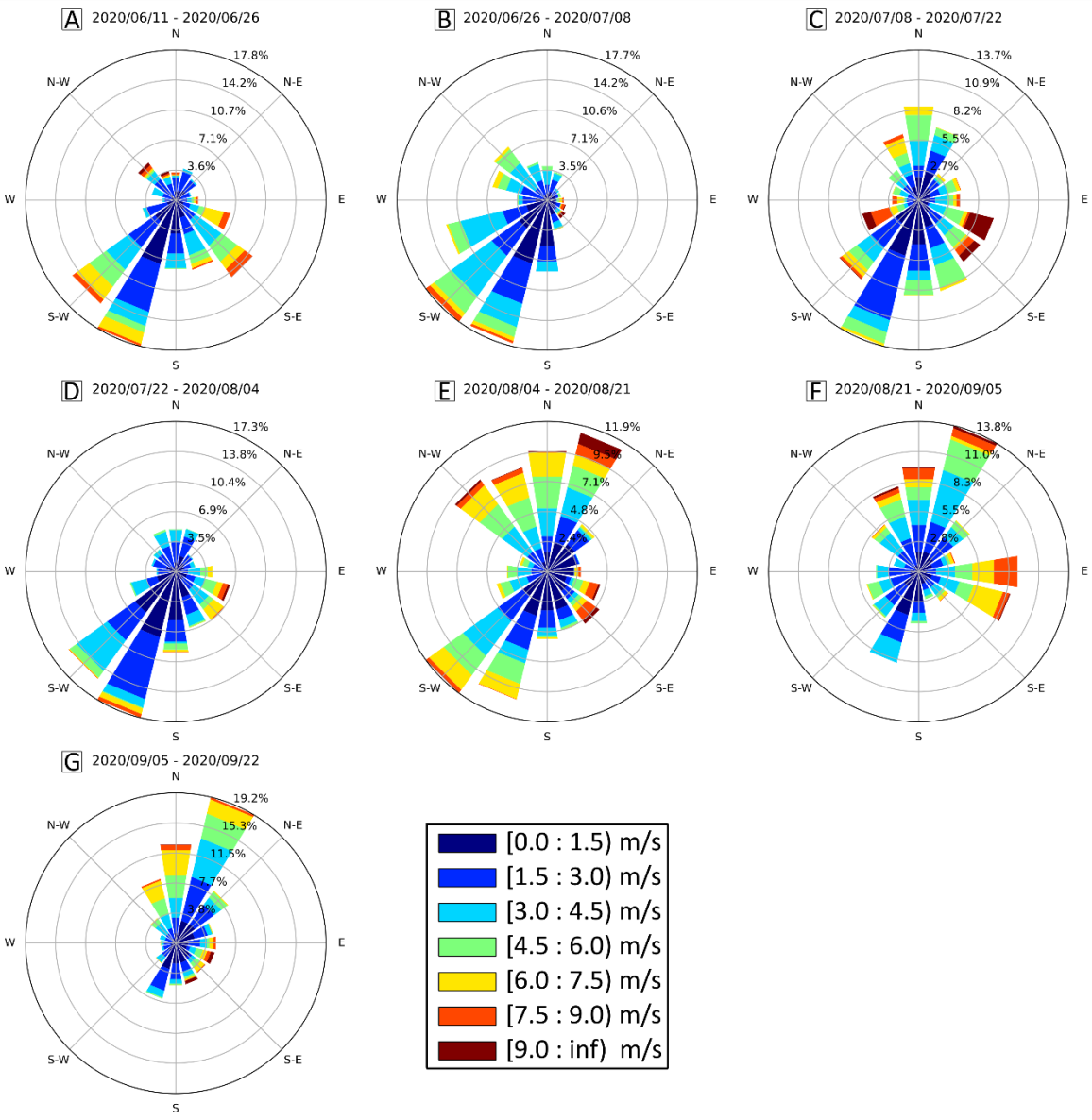

Figure 19. Wind rose data corresponding to the reflectance sampling periods, 10-minute averaged data measured at 10 m AGL at the standalone wind mast, from 11/06/2020 to 01/10/2020.

Figure 19 reveals that the wind preferentially blows from the north-north-east (NNE) or from the south-south-west (SSW) directions, which becomes clear by looking at the composite wind rose for the entire period given in Appendix C. A peak wind is defined here as a wind having a speed equal to or above 6 m/s at 10 m AGL, which occurs roughly 18 % of the time during the period considered.

3.3.3 Reflectance measurements

The results from the reflectance measurement campaign are presented in Figure 20. Only results from the reflectors at 60° are shown here as the soiling for the reflectors at 30° follows similar trends, except with more intense soiling as expected (see Appendix D). The maximum measurement uncertainty observed is 3.2 %, with an average uncertainty being 1.3 %, which is acceptable. The standard deviation from the averaged reflectance of each reflector set is used as a proxy for uncertainty.

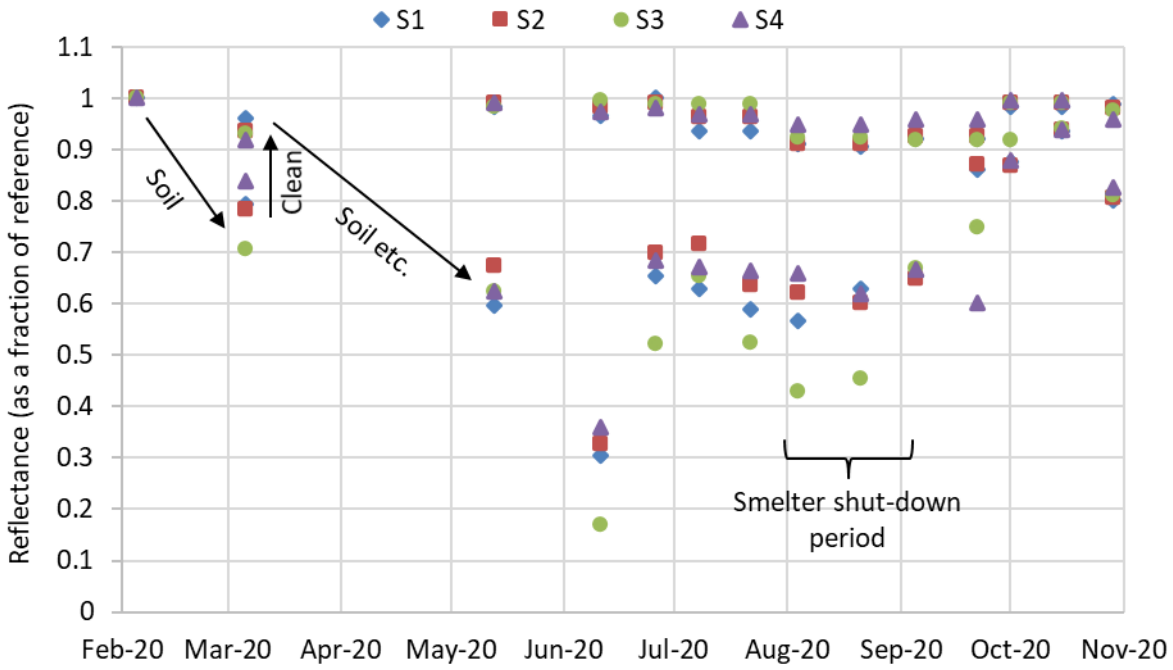

Figure 20. Reflectance of the 60° elevation reflectors for all sampling sets (S1 to S4), from 05/02/2020 to 29/10/2020, showing consecutive soiling and cleaning cycles.

The reflectance of all mirrors starts off at unity, and soiling reduces the value. The goal was to take samples every 14 days, but this was not always possible. Notably, the second soiling period (06/03/2020 – 13/05/2020) was 68 days, corresponding to a nationwide lockdown due to the COVID-19 pandemic. The reflectance loss during this period was an average of 32.7 % across the four reflector sets for the 68-day period, which is markedly less than the averaged reflectance losses experienced over the consecutive 14-day sampling periods of 32.6 % during the dry season (26/06/2020 – 22/09/2020). These reflectance losses, whilst high, are not uncommon in the arid regions of the world. The differences in soiling for sampling sets S1-to-S4 are also larger in the dry season.

When considering the rainfall data in Figure 18 together with the soiling results in Figure 20, a decrease in soiling losses is seen to coincide with the fall of the first rains in the region around the end of September and the start of October 2020. The rain reduces the levels of dust in the atmosphere, thereby decreasing the potential for soiling, and washes off collected dust on the reflectors if enough rain falls before measurements are made.

Additionally, a smelter shutdown period is noted for the month of August, which is not seen to significantly impact measured reflectance on any of the reflector sampling sets. This seems to be in contradiction to the findings of the dust characterization presented earlier that point towards the furnace emissions product being a major dust source and to those made by Davourie *et al.* (2017), who cited furnace processes and stack emissions as contributing a large percentage of total plant dust emissions. Here it is hypothesised that these two pieces of information can be reconciled if it is considered that a large fraction of the furnace ground level and stack emissions largely settle out of the airstream near their origin, resulting in a dust ‘reservoir’ everywhere in close proximity to the major dust emission sources. This can lead to the observed behaviour, that even though the plant is not operating, dust still spreads almost as usual because it is swept up from these reserves of dust around the plant area. This implies that dust emission source control can be effective only if the existing dust ‘reservoirs’ have been suppressed as well.

The mean daily reflectance loss (MDRL), or rate of change in reflectance for that period, is calculated from the data presented in Figure 20. The results are displayed in Figure 21.

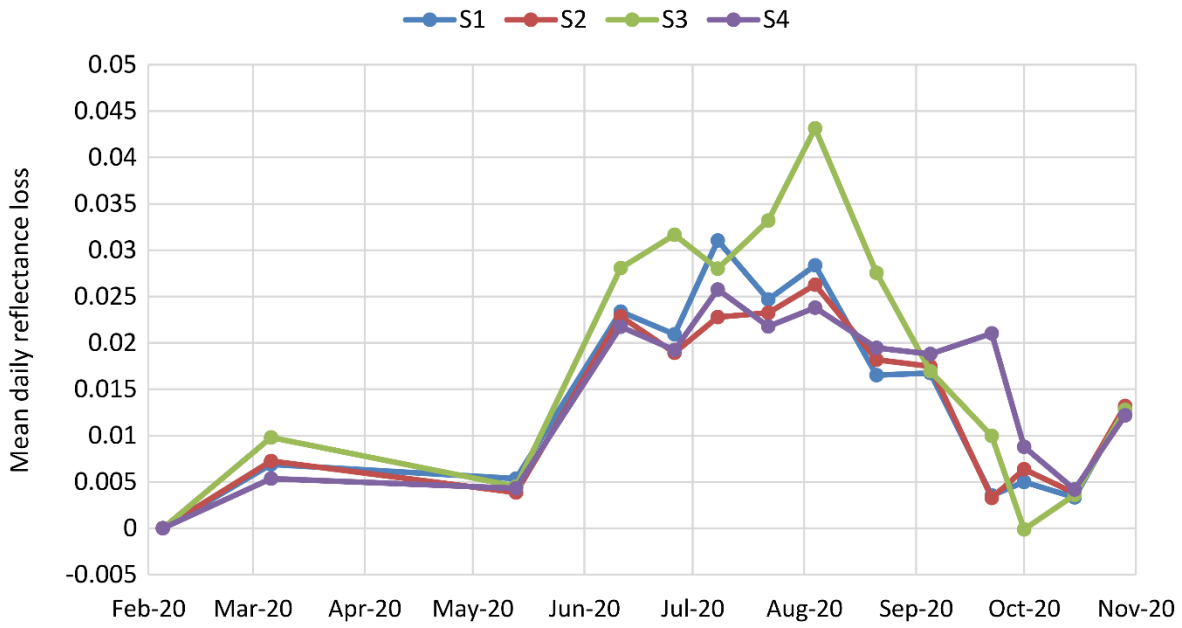

Figure 21. MDRL of the 60° elevation reflectors for all four sampling sets (S1 to S4), from 05/02/2020 to 29/10/2020.

It is noted here that the MDRL rates measured outside of the dry season, or peak soiling season, are in the range of 0.8 % per day, which is an acceptable design estimate given (Wang, 2019a).

3.3.4 Analysis of wind and soiling data

It is noted that background dust concentrations and levels of activity on the plant play a role, but the strongest influence on levels of soiling is assumed to come from the plant area based on the presented dust characterization analysis.

A first inspection of Figure 21 shows that S3 consistently experiences higher levels of soiling in comparison to the other three reflector sets during the dry season. The noticeable changes for the reflector sampling sets from one period to the next show that there are factors that influence soiling apart from proximity, but the location of S3 is clearly such that the proximity to source outweighs these other factors when soiling is more intense. The worst soiling is observed during the height of the dry season in *Period-D* (22/07/2020 – 04/08/2020), in the beginning of August just before the season starts changing and the most dust is present in the atmosphere. S3 experienced a significantly higher soiling rate with an MDRL of 0.043, in comparison to soiling rates at S1 and S2 with MDRLs of 0.028 and 0.026 respectively. It is noted here that the weakest winds of the entire sampling period are observed during this time when the highest soiling rates are observed.

Upon closer inspection of the wind data and the soiling data, some interesting trends emerge. Taking *Periods A* and *B* into consideration (11/06/2020 – 26/06/2020 and 26/06/2020 – 08/07/2020 respectively), the wind data appears to be very similar, yet the soiling rates experienced by the sampling sets are different for these two periods. The highest soiling rate observed for *Period-A* occurs at S3 with an MDRL of 0.032, and the second-highest at S1 with an MDRL of 0.021, a notable difference. *Period-B* sees the highest soiling rate observed for S1 with an MDRL of 0.031 and the second highest at S3 with an MDRL of 0.028. Both *Periods A* and *B* have predominantly SW and SSW winds, except for the SE tertiary wind reaching peak speeds for a short while in *Period-A*.

Period-C is now considered. The highest soiling rate is experienced at S3 with an MDRL of 0.033, the second-highest at S1 with an MDRL of 0.025. The winds of *Period-C* consist of a predominant SSW wind, but with no clear candidates for secondary or tertiary winds, noting that the ESE, SE, and WSW directions all have shorter duration peak winds.

Clear changes in the MDRL patterns for the different reflector sets are observed for *Periods E* to *G*. A decrease of soiling rates, in general, are noted, with the winds starting to blow more intensely from *Period-E* onwards and the first rains falling towards the end of September. Roughly equal MDRLs are observed for all reflector sets in *Period-F* as a result of the winds blowing from all of the directions needed to soil all four reflector sets. *Period-F* signifies a turning point coinciding with the change of season, with S3 no longer experiencing the worst soiling on a consistent basis. Predominant NNE/N winds blow alone for the first time in *Period-G*, causing S4 to experience a significantly higher soiling rate than the other three sets with an MDRL of 0.021; in contrast with the winds from *Period-E* where there are NNE/N winds but the wind signals from the south are still strong enough to cause S3 to experience the highest soiling rate, with S4 the second highest.

To summarise the performance of the different reflector sampling sets during the considered dry season, the averaged MDRL is given alongside a simple scoring system, with one point assigned if the set experienced the highest MDRL for the considered period and four points assigned if the set experienced the lowest MDRL for the considered period. Points are assigned for each *Period A*-to-*G* and results are displayed in Table 4.

Table 4. Reflector set performance scoring for the considered dry season, periods A-to-G, with higher being better.

Reflector set	Averaged MDRL	Score
S1	0.0203	18
S2	0.0186	23
S3	0.0272	11
S4	0.0214	18

This analysis leads to the conclusion that, even though the predominant wind direction over a given period mainly determines where soiling will be most intense, shorter duration peak winds can disproportionately influence experienced soiling rates at a given location, especially if the location is closer to the source. This shows that merely considering predominant wind directions might not be enough if there is a clear point source such as a dust emitting EII close to a planned CST site. The data also reveal that S3 is poorly situated, experiencing much higher soiling rates than the other three sampling locations throughout the dry season. If S3 is excluded from the discussion, then S4 and S1 performed similarly with averaged MDRLs of 0.0214 and 0.0203 respectively, with S2 performing the best during the selected period with an averaged MDRL of 0.0186. This represents a 13.1 % lower averaged MDRL for the period considered when moving from the worst location of S4 to the best location S2.

3.3.5 Dependence of reflector soiling rate on reflector location

Figure 22 shows dust source strength coming from different regions of the plant, based on the presented dust characterization, observations made throughout the campaign, and informal discussions with staff on-site.

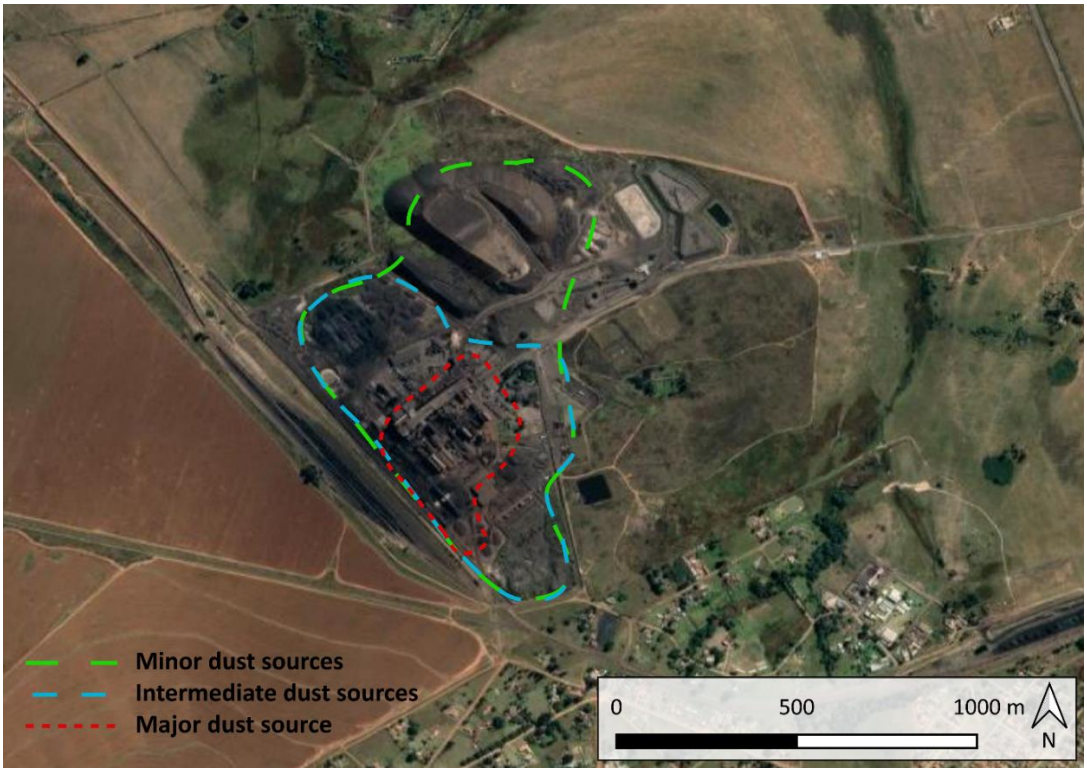

Figure 22. Smelter plant divided into categories of dust sources according to observed strength.

The three different strength category regions are described as follows:

- Major strength dust sources – dust from the baghouse endpoints, furnace emissions, metal tapping and casting zones; all adding to the hypothesised dust reservoir
- Intermediate strength dust sources – raw materials handling and screening of raw materials
- Minor strength dust sources – slag heaps and general area

A cause-and-effect relationship emerges when looking at the soiling data and the wind direction data, for the same sampling periods. This relationship becomes most visible during the dry season. Figure 23 shows images collected by the reflectometer of two different sampling sets, one pair taken during the dry season and the other when the rains have started falling.

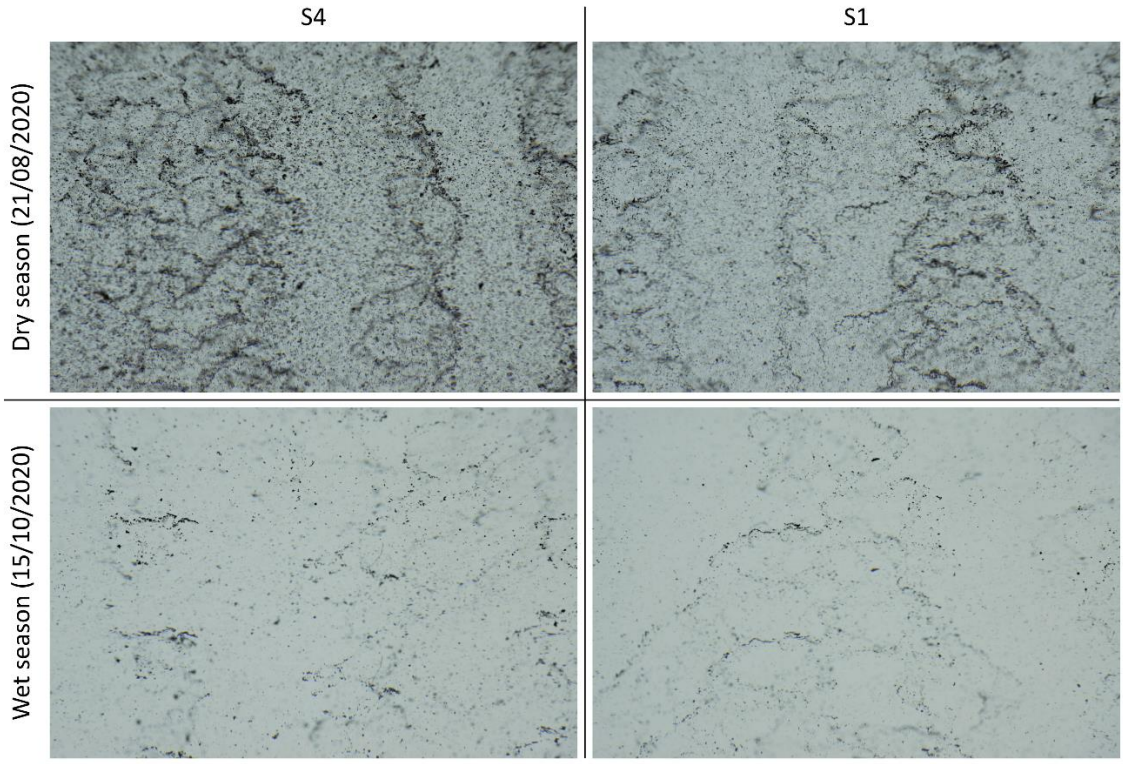

Figure 23. Comparison of captured image data from the reflectometer for a reflector in S1 and S4, each for the dry and wet season.

Figure 23 clearly shows the difference between soiling experienced in the dry and wet seasons. The examples of S1 and S4 were chosen to show the difference between soiling at different locations over the same period because they are only about 500 m apart, and yet there is a clear difference in the amount of dust seen on the surface regardless of the season. The images of S1 and S4 during the dry season in Figure 23 correspond to *Period-E* in Figure 19, with predominant and peak winds blowing from NW-to-NNE, sending more dust in the direction of S4. An illustration of the effect of wind direction and dust source area has on the experienced soiling rates at a given set is shown in Figure 24.

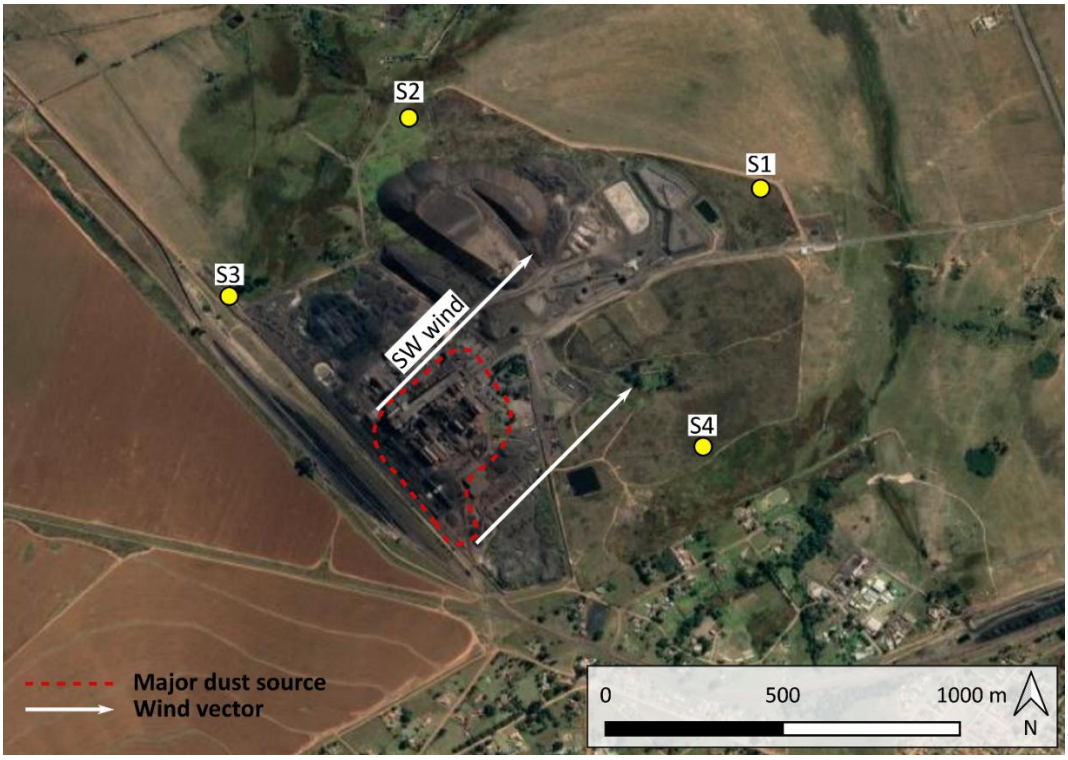

Figure 24. Illustration of the cause-and-effect relationship between wind direction, dust source, and reflector location.

In the example given in Figure 24, S1 is most likely to experience the highest soiling rate, given predominantly SW wind with some peak winds included. In this scenario, all other sampling sets are bypassed in the only source is the 'Major strength dust source' as outlined. Of course, in reality, the situation is more complex.

3.4 Summary and implication of experimental results

An average reflectance loss for all sampling sets of 32.6 % is observed for the 14-day sampling periods during the dry season if all reflector sampling sets are included in the calculation. If, however, the overtly poorly sited reflector set S3 is excluded from the calculation, then an average reflectance loss of 22.6 % is observed.

It was found that the relative position of the reflector sets to the plant area, together with the wind direction, does determine where soiling will be most intense for a given period. A 44.8 % difference in MDRL for the worst period (in terms of soiling) was observed because of where the two different reflector sets were located relative to the plant area. It was also found that peak winds (> 6 m/s) can disproportionately impact where the most soiling occurs, even if they do not represent the dominant wind direction. The worst soiling period also coincided with the period where the weakest winds were observed, which suggests that 'wind washing' does help to limit soiling to some extent during dry dusty periods.

The dust characterisation revealed that 90 % of all particles found on the reflector surfaces are less than 98 µm, with the majority sampled being 31.5 µm. The main components are Si, Al, Fe, S, O and Mn. The phases found were SiO_2, Fe_2SiO_4, $Al_2O_3.SiO_2$, and $Al_9Fe_2Si_2$, none of which are expected to have particularly adverse effects on the reflectors' useful lifetime. The SEM micrographs also revealed that the particle morphology found in the region is not particularly abrasive and is therefore not expected to

pose a serious risk of enhanced mechanical wear on a reflector's surface when washing. The field experiment did not last long enough to draw a conclusion regarding reflector material degradation resulting from the environment over lifetime use.

There are a number of well-known and novel interventions in the area of solar reflector soiling prevention and mitigation that can be derived from the study. Simply by changing location relative to the source, a 13.1 % lower soiling rate is observed at the reflector sampling set S2 relative to the location S4. At the reflector set S2 with the lowest averaged MDRL of 0.0186 during the considered dry season period, it is conceivable that by adding other interventions such as anti-soiling coatings, an acceptable soiling rate can be achieved. It is recommended that any soiling mitigation technique, including prevention of soiling by choosing a proper location relative to the source, should be optimised to work best during the season when the most soiling is expected.

4 CFD Model Description and Validation

4.1 Introduction

By studying the reflector soiling at various locations around the smelter, we have learned that soiling varies depending on the location around the plant and the wind conditions. The four sampled locations give valuable information about the soiling potential of different locations, but the experimental campaign is not run for a long enough time (i.e., a few seasonal cycles) to be able to say with confidence that the location that showed the least soiling potential in the study will remain so in the long run. The other shortfall of the experimental campaign is that the sampling locations only represent four points around the plant, and whilst the soiling potential at other locations can be inferred, it remains unknown. For these reasons, it could be valuable to develop a method based on numerical analysis that is able to provide more complete information with regards to the soiling potential of different areas around the smelter, and that can be used to get this information over a much shorter time. This chapter develops and validates the CFD simulation approach that is able to reproduce realistic flow scenarios at and around the Transalloys smelter complex, to be discussed in more detail in the following chapters.

The dust dispersion that originates from the Transalloys smelter complex is a result of winds crossing the smelter area, entraining dust, and transporting it downstream. The winds are characterised by a unique boundary layer for each wind speed, wind direction and atmospheric condition combination. To realistically predict dust dispersion at Transalloys, a realistic approximation needs to be made of the ABL flow. To achieve this, it is required to model the ABL for a distance upstream and downstream of the smelter complex, such that the ABL profile has developed characteristics representing reality by the time it encounters the smelter complex. An illustration of this is given in Figure 25.

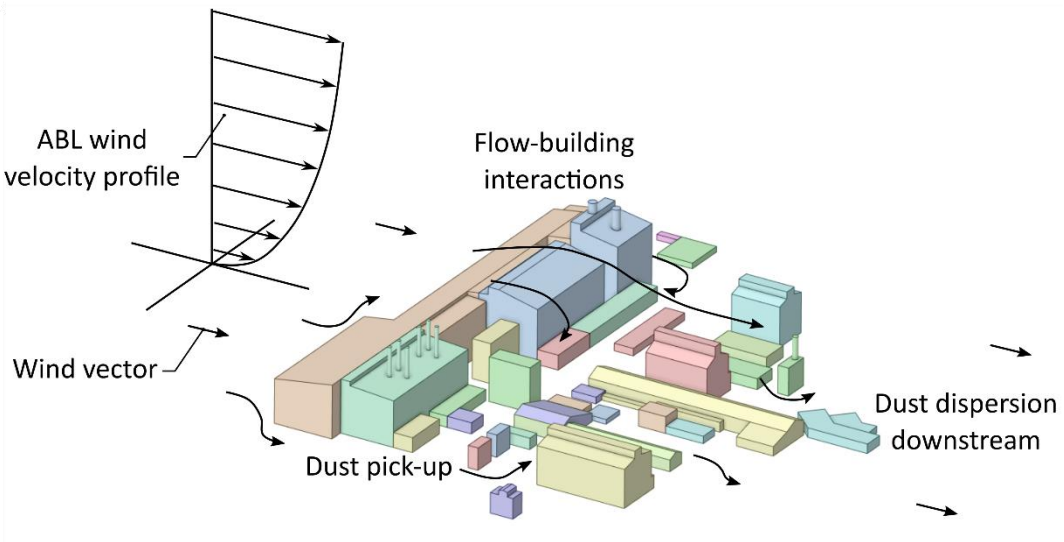

Figure 25. Illustration of the ABL velocity profile approaching the Transalloys smelter building complex and the complex flow-building interactions that are expected to occur.

Figure 25 illustrates the flow scenario that is expected to occur at Transalloys, namely that the ABL velocity profile will encounter the smelter complex buildings and complex flow-building and dispersion interactions will follow. It is self-evident that different velocity boundary layer profiles will result in different flow scenarios around the smelter buildings, and this must be accounted for.

This problem presents many uncertainties with regards to natural and man-made geometries, the surface roughness of the various areas of the flow domain, boundary conditions and the relevant forces; because of this, the *COST Action 732 (COST732) Best Practice Guidelines for CFD of Urban Flows* (Franke *et al.*, 2007) are consulted.

4.2 Modelling ABL flow

Non-standard boundary conditions are required to model ABL flows since the free shear flow of wind over terrain deviates from shear flow over a flat plate in a few important ways. The two main differences are the sustained driving forces that winds have, and the roughness they encounter at the surface that is far greater than that of flow over a flat plate. As described in literature Section 2.4, the *k-ϵ* turbulence model is typically used for modelling neutral stability ABL flow, but a few important modifications are proposed by various authors. All of the proposed modifications are introduced using a user-defined function (UDF) within ANSYS Fluent, given in Appendix E. All simulations are performed using ANSYS Fluent 2021R1

4.2.1 Richards and Hoxey approach

Richards and Hoxey (1993) (RH) proposed the following set of boundary conditions (BCs), appropriate for modelling neutral two-dimensional ABL flows:

$$U = \frac{u_*}{\kappa} ln\left(\frac{z' + z_0}{z_0}\right) \quad \text{Eq. 31}$$

$$k = \frac{u_*^2}{\sqrt{C_\mu}} \quad \text{Eq. 32}$$

$$\epsilon = \frac{u_*^3}{\kappa(z' + z_0)} \quad \text{Eq. 33}$$

which satisfy the standard *k-ϵ* turbulence model conservation equations only if

$$\sigma_\epsilon = \frac{\kappa^2}{(C_{\epsilon 2} - C_{\epsilon 1})\sqrt{C_\mu}} \quad \text{Eq. 34}$$

For the above to be satisfied if $\kappa = 0.4$, then $\sigma_\epsilon = 1.11$ must be enforced. Furthermore, a constant shear stress τ, is also assumed in the vertical direction such that,

$$\mu_t \frac{\partial u}{\partial z} = \tau = \rho u_*^2 \quad \text{Eq. 35}$$

This constant shear stress must be applied as a driver at the top BC. A constant velocity BC can be equally applied at the top BC location.

4.2.2 Comprehensive approach

ANSYS Fluent makes use of a dimensionless sand-grain roughness height k_s models developed mainly for engineering type flows. Engineering type flows are flows over generally 'smooth' surfaces such as channel flows or flows over aerofoils. The sand-grain roughness approach is inherently not well suited to ABL flows, where the implicitly modelled roughness elements are typically tree canopies, suburban areas or grassy fields, as an example. Blocken, Stathopoulos and Carmeliet (2007) discuss the shortfalls

of the standard wall function for ABL flow and propose an alternative way of calculating the wall roughness value for a fully-rough wall; the roughness value is still entered into ANSYS Fluent as the sand-grain roughness, as shown by Eq. 36.

$$k_s = \frac{E z_0}{C_s} \quad \text{Eq. 36}$$

where the empirical constant E = 9.793 and the roughness constant C_s = 0.5. Parente *et al.* (2011) take the roughness-modified wall function a step further such that it can accommodate a roughness height that is larger than the first cell height (i.e., $k_s > z_p$), shown in Eq. 37.

$$\frac{U_p}{u_*} = \frac{1}{\kappa} ln\left(\tilde{E}\tilde{z}^+\right) \quad \text{Eq. 37}$$

with

$$\tilde{E} = \frac{\nu}{z_0 u_*} \quad \text{Eq. 38}$$

and

$$\tilde{z}^+ = \frac{(z + z_0)u_*}{\nu} \quad \text{Eq. 39}$$

where $\tilde{z}^+$ is the non-dimensional distance from the wall shifted by the aerodynamic roughness (Parente and Benocci, 2010). Furthermore, the friction velocity is not kept constant at the wall but varies horizontally instead, with the variation given by,

$$u_{*,wall} = C_\mu^{0.25} k^{0.5} \quad \text{Eq. 40}$$

The use of Eq. 37 preserves the velocity profile but not the turbulence quantities. To address this, Parente *et al.* (2011) propose using the inlet profile described by Richards and Hoxey (1993) as a wall function, with a variable C_μ value given by,

$$C_\mu(z) = \frac{u_*^4}{k(z)^2} \quad \text{Eq. 41}$$

The turbulent kinetic energy profile is no longer kept constant either, as shown by

$$k(z) = C_1 \ln(z + z_0) + C_2 \quad \text{Eq. 42}$$

Eq. 42 reduces back to what RH specifies if $C_1 = 0$. Lastly, either the requirement set by Eq. 34 must be enforced, or a source term S_ϵ must be added to the TDR Eq. 12. The source term is specified by

$$S_\epsilon(z) = \frac{\rho u_*^4}{(z + z_0)^2}\left(\frac{(C_{\epsilon 2} - C_{\epsilon 1})\sqrt{C_\mu}}{\kappa^2} - \frac{1}{\sigma_\epsilon}\right) \quad \text{Eq. 43}$$

At this point, it can be noted that the varying turbulent kinetic energy profile proposed by Parente *et al.* (2011) has two constants which can only be determined by fitting the equation to measured wind profile data. If, however, there are no measurements available, the following empirical Eq. 44, derived by Brost and Wyngaard (1978), can be used. This approach is termed the Alt. comprehensive approach in the following section.

$$k(z) = \frac{u_*^2\left[8.7 - \frac{6(z+z_0)}{h}\right]}{2} \qquad \text{Eq. 44}$$

where h is based on the Coriolis parameter, f, for the local latitude, and the friction velocity:

$$h = \frac{0.33u_*^2}{f} \qquad \text{Eq. 45}$$

The Coriolis parameter for mid latitudes is $f = 0.0001$.

4.2.3 Varying terrain inlet BC

Another challenge faced by wind engineers is that inlet and outlet BCs cross uneven terrain. This is usually sidestepped by extending the domain extents and smoothing the uneven terrain to an even level so that the sides of the domain are all the same height, thus making it easier to prescribe profiles. This approach remains a workaround and does not represent the reality of the complex terrain that the flow encounters. A solution to this is proposed by Hargreaves, Porter and Wright (2006), whereby the reduced scalar transport equation,

$$\nabla^2\varphi = -1 \qquad \text{Eq. 46}$$

is solved, with $\varphi = 0$ at all walls in the domain. The normal distance from the closest wall to any cell is then calculated using,

$$z' = -|\nabla\varphi| + \sqrt{|\nabla\varphi|^2 + 2\varphi} \qquad \text{Eq. 47}$$

At the inlets, z' represents the height AGL. Figure 26 shows the height AGL as calculated using the described method. The vertical slice is taken at an arbitrary location in the computational domain used for the real Transalloys case exposed in chapter 5.

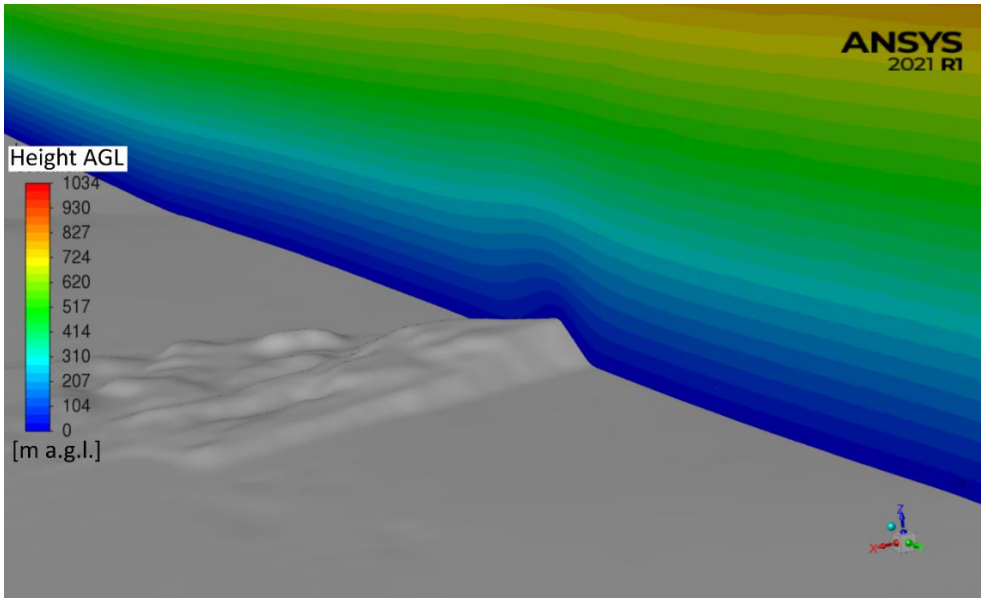

Figure 26. Varying height AGL using the Hargreaves et al. (2006) method for an arbitrary vertical slice over uneven terrain.

The variation in height yielded by the described method fits the terrain well close to the ground and becomes smoothed out further up because of the nature of the diffusion equation used.

4.3 Simulation Settings

The ANSYS Fluent double-precision pressure-based solver is used for all simulations from here onwards. All flows are considered steady-state. The iterative scheme used is the SIMPLE algorithm. Second-order upwind spatial discretisation is used for the momentum and turbulence equations. The standard spatial discretisation is used for pressure interpolation. Gradients and derivatives are computed using a least-squares cell-based method. For this section, where numerical models and settings are compared, the solutions are considered converged when all residuals reach 10^{-12}. The default properties of air were kept for the following horizontal homogeneity and CEDVAL case, that is, air density ρ_{air} = 1.225 kg/m^3, and air viscosity μ_{air} = 1.789e-05 kg/(m s). A reference pressure of P_{ref} = 101325 Pa is used. Importantly, the viscosity ratio limiter also needs to be increased to 10^{11} (from the default 10^6) to account for the large viscosity ratios that exist in atmospheric flows.

4.4 Horizontal Homogeneity Test

The different BCs described above are tested here for their ability to maintain flow profiles in an empty rectangular domain, also known as a horizontal (flow-profile) homogeneity test. A 125,000-cell mesh is applied to an empty rectangular domain, a schematic of which is shown in Figure 27.

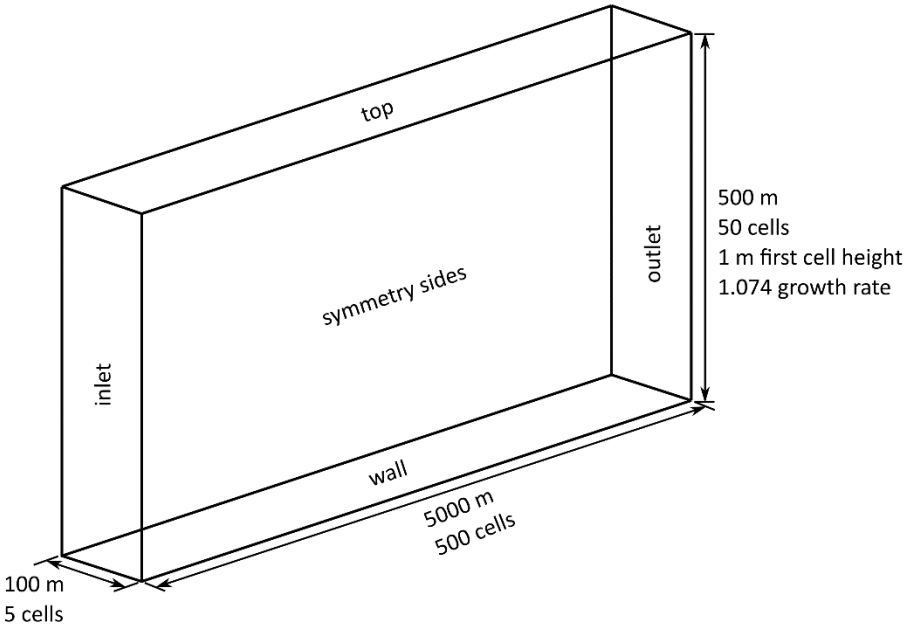

Figure 27. Empty rectangular domain schematic.

An aerodynamic roughness length of z_0 = 0.1 m is used, with a first cell height of 1 m purposely chosen such that $k_s > z_p$. The inlet conditions prescribed for each test are summarised in Table 5.

Table 5. Horizontal homogeneity test input summary.

Case name	U_{ref}	H_{ref}	z_0	$k(z)$	κ	u_*	C_1	C_2	C_μ	f
RH	5	10	0.1	Eq. 32	0.4	0.4334	n/a	n/a	0.0435	n/a
RH + Wall Function	5	10	0.1	Eq. 32	0.4	0.4334	0	0.9	Eq. 41	n/a
Comprehensive	5	10	0.1	Eq. 42	0.4	0.4334	-0.04	1.1	Eq. 41	n/a
Alt. Comprehensive	5	10	0.1	Eq. 44	0.4	0.4334	n/a	n/a	Eq. 41	0.0001

The resulting inlet profiles prescribed for the test cases are shown in Figure 28 for turbulent kinetic energy and velocity, respectively. To ensure that the different cases have comparable inputs, the u_* is kept the constant, therefore C_μ and f are adjusted for the RH and alternative comprehensive cases, respectively, resulting in similar turbulent kinetic energy profiles. The ability of the different cases to sustain inlet profiles is tested by taking line samples in the centre plane of the domain at 2000 m and 4000 m downstream of the inlet.

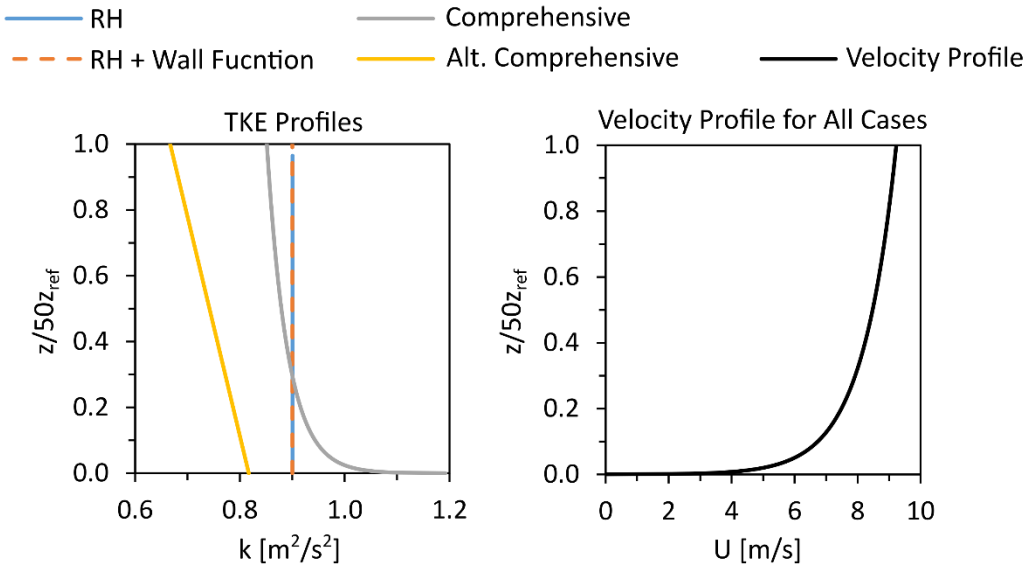

Figure 28. Prescribed turbulent kinetic energy (left) and velocity (right) profiles for empty domain tests.

The resulting turbulent kinetic energy profiles for the four cases are reported in Figure 29.

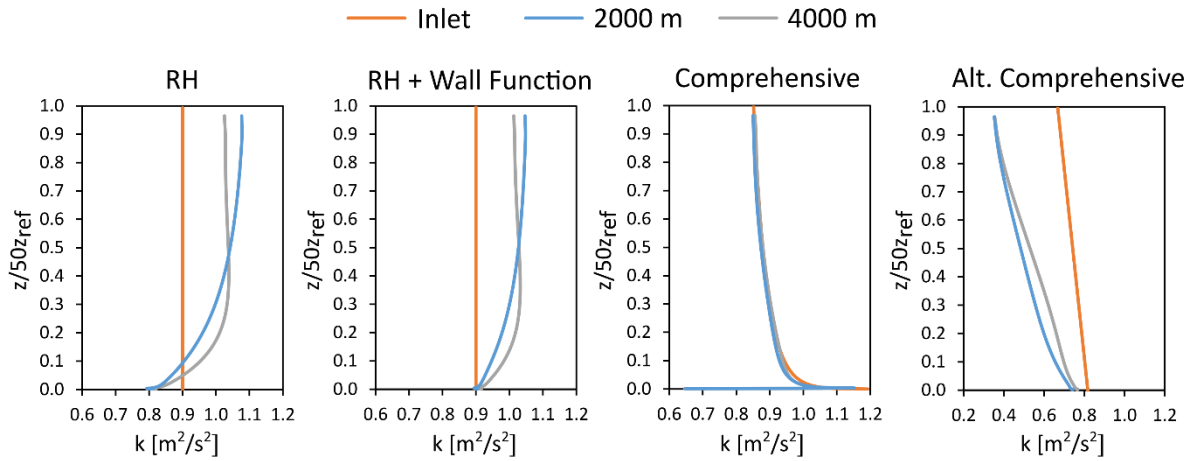

Figure 29. Development of turbulent kinetic energy profiles through an empty domain for different input profiles and solution methods.

Figure 29 reveals a few important details. The RH approach alone is not able to sustain turbulent kinetic energy profiles. The 'RH + Wall Function" approach does not change much for the development of the turbulent kinetic energy profiles, which is expected because the modified wall function must be implemented in conjunction with the full comprehensive approach for profiles to be sustained. The "Comprehensive" approach shows that when feeding the domain with a more realistic decaying profile for turbulent kinetic energy and applying all the conditions required for the comprehensive approach, that the profiles are sustained throughout the length of the domain almost without variation except for the first couple of meters above the ground wall of the domain. The "Alt. Comprehensive" approach is

fed with a linearly decaying profile that is not sustained, but it develops to something approximating a logarithmically decaying profile of the comprehensive approach. A similar test is performed for the identical input velocity magnitude profiles, with the results displayed in Figure 30.

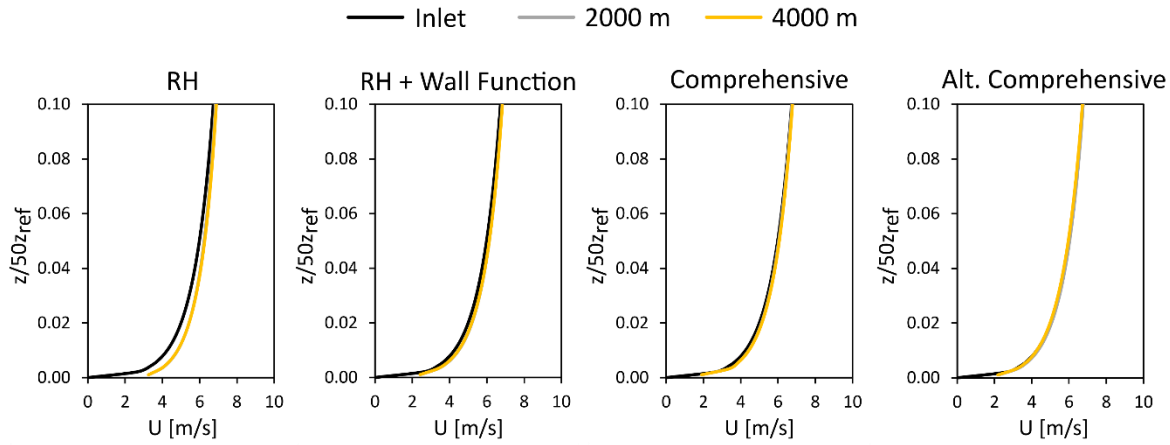

Figure 30. Development of velocity profiles through an empty domain for different solution methods.

From Figure 30, it is clear that all approaches, except the RH approach, are able to sustain the input velocity profiles. The velocity is seen to speed up close to the bottom of the domain for the RH approach, but not for the approaches using the modified wall function. The issue of velocity speed up when $k_s > z_p$ is known (Blocken, Stathopoulos and Carmeliet, 2007).

From the empty domain tests performed, it has been shown that the proposed "Comprehensive approach" achieves horizontal homogeneity for the given input velocity and turbulent kinetic energy profiles.

4.5 CEDVAL Validation Case

In lieu of validation against a sufficient density of full-scale wind profile data in the area of influence of the Transalloys smelter complex buildings, the high-quality data from the CEDVAL case A1-1 (Leitl, 1996) are used to validate that the chosen solution method can reproduce ABL flow interactions with a building. Validation of discrete phase dispersion is difficult because of a general lack of reliable validation data (Schatzmann and Leitl, 2011). The main reason for this lack is that it is difficult to create repeatable particle dispersion experiments in wind tunnels, and impossible to create them at full scale.

4.5.1 CEDVAL A1-1 description

The CEDVAL wind tunnel experiment was conducted in the BLASIUS wind tunnel at the Meteorological Institute of the University of Hamburg, using modified Standen-Spires and uniform Lego-roughness suitable for modelling the ABL at 1:200 scale. The A1-1 case measures flow around a rectangular structure (building). Its geometry is shown in Figure 31, with H = 25 m in the full-scale case as shown, and H = 0.125 m in the scaled-down wind tunnel model setup and current CFD model.

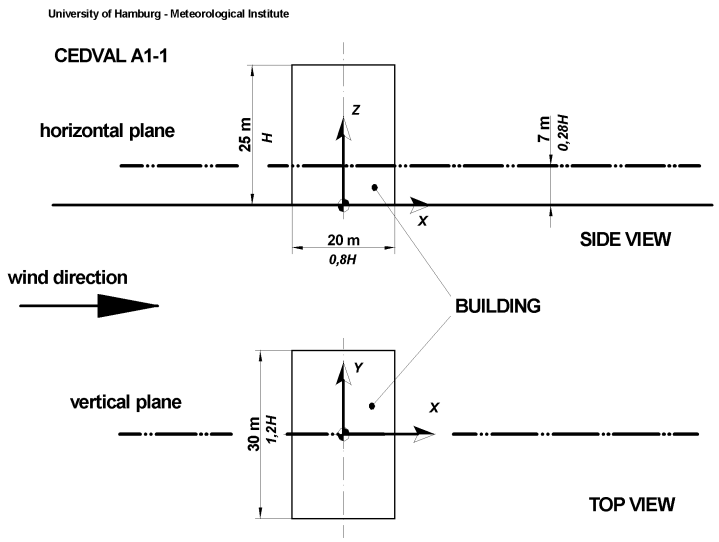

Figure 31. CEDVAL A1-1 case geometry schematic with full-scale dimensions being shown.

To model this, a half-symmetrical rectangular domain is used, with a symmetry condition applied. Figure 32 shows the applied mesh, with the domain extending 1 m upstream of the building because this is where approach flow profiles are measured in the wind tunnel. The domain is then extended 1 m upwards, 0.75 m laterally to match the dimensions of the wind tunnel, and 3m downstream to allow the valid application of a zero-pressure gradient boundary condition with no reverse flow. A fine mesh is used for the computational domain, with the smallest cells concentrated at the building being ~ 1 mm-sized squares. No mesh refinement study was performed for this case. Mesh refinement is deferred to Chapter 5 for the Transalloys smelter application.

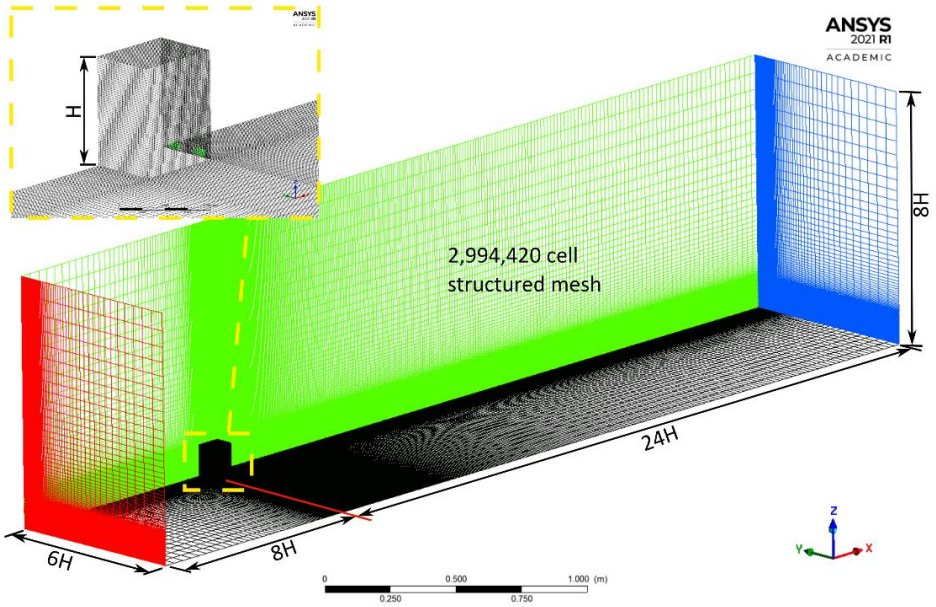

Figure 32. CEDVAL A1-1 case block-structured hex mesh.

The different boundary conditions are colour coded in Figure 32, with red the velocity inlet, blue the zero-pressure outlet, green the symmetry plane, black the wall boundaries. The cut-away faces are smooth no-slip wall boundaries.

4.5.2 Boundary conditions for flow study

The boundary conditions used are all obtained from the experimental data package (Leitl, 1996), and are summarised as follows:

1. Velocity inlet condition using a power-law profile with a reference velocity U_{ref} = 6 m/s at H_{ref} = 0.66 m, and a power law exponent α = 0.21
2. The turbulent kinetic energy profile is determined by curve fitting Eq. 42 to the experimental data points, with C_1 = -0.07 and C_2 = 0.53. The turbulent dissipation rate profile is determined using Eq. 33
3. The friction velocity is given by u_* = 0.377 m/s
4. The vertical plane down the centre of the wind tunnel is taken as a symmetry plane
5. The building, side, and top walls are all smooth no-slip walls (i.e., zero-surface roughness)
6. The ground wall has an aerodynamic roughness length of z_0 = 0.0007 m, resulting in a sand-grain roughness k_s = 0.014 according to Eq. 36
7. A zero-pressure gradient outlet is applied where the flow exits the domain

The inflow profiles for velocity and turbulent kinetic energy are shown in Figure 33.

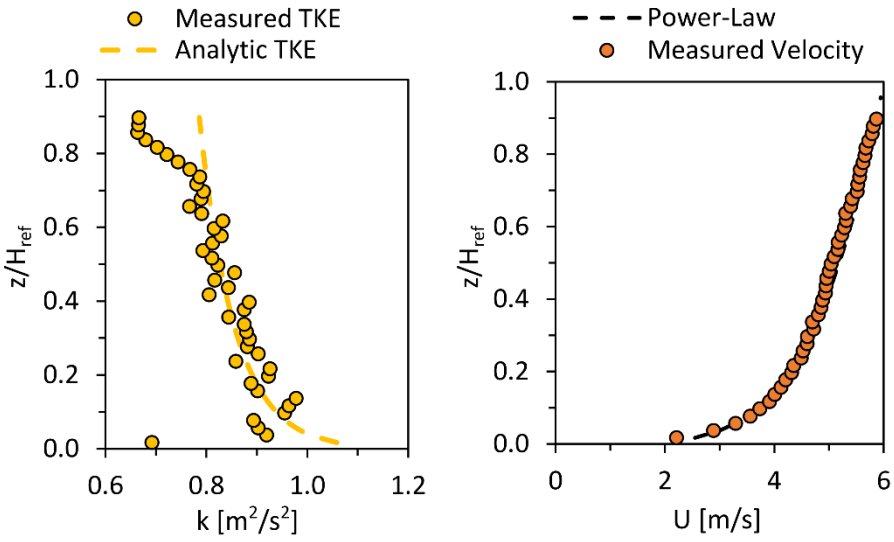

Figure 33. Measured and analytical inlet flow profiles for CEDVAL A1-1.

Figure 33 confirms that a good match is achieved between the experimental and prescribed analytical profiles.

4.5.3 Results for flow field validation

The development of the turbulent kinetic energy and the velocity flow profiles is shown in Figure 34 and Figure 35, respectively.

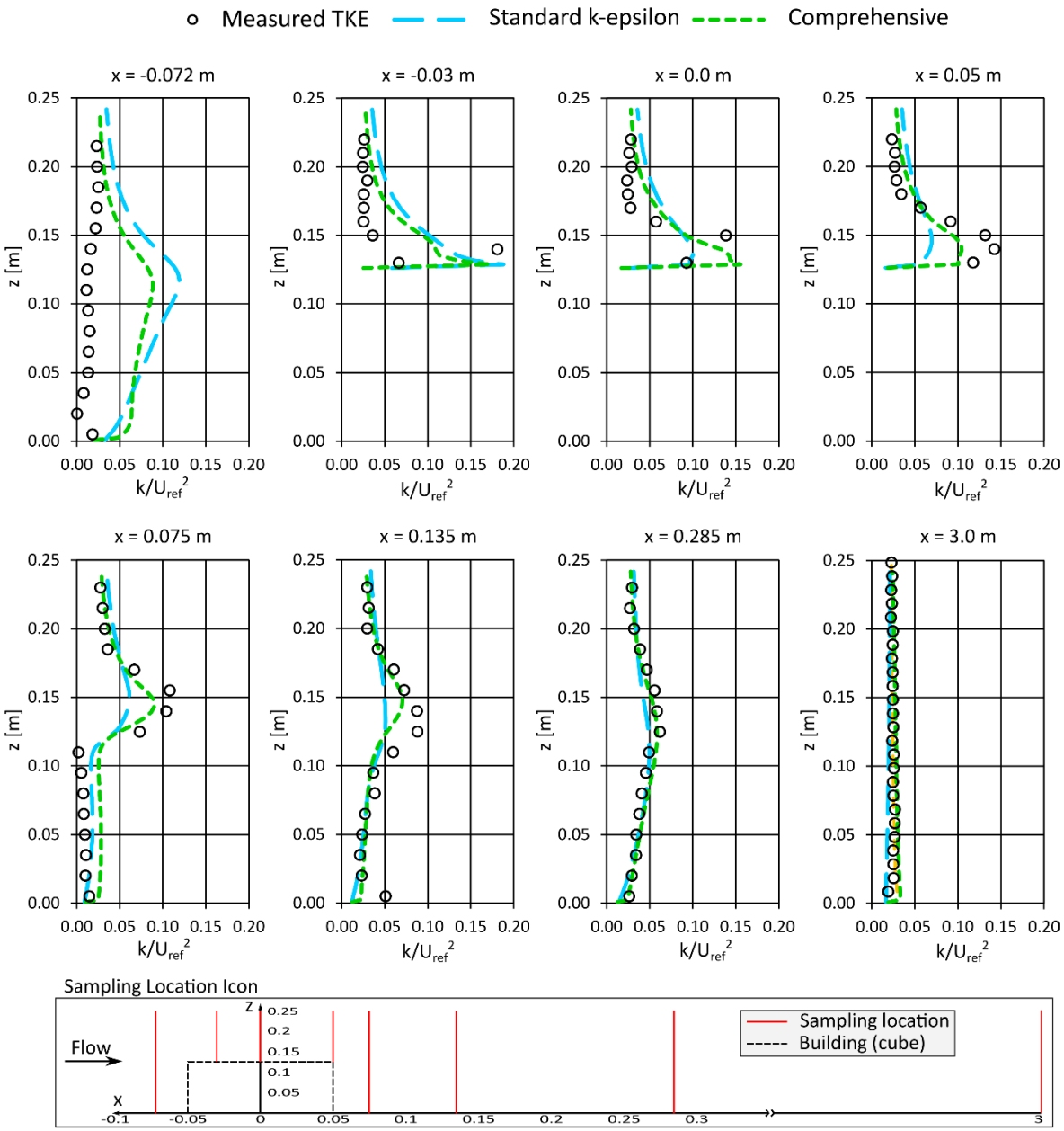

Figure 34. Turbulent kinetic energy (TKE) profile comparison between measured and numerical results, at different locations along the x-axis at y = 0 m, for the CEDVAL A1-1 case. The bottom of the figure features an insert showing the sampling location relative to the cuboid.

Figure 34 shows that both solution methods overpredict the turbulence in the stagnation region just upstream of the building. Both models are not expected to perform too well in the flow separation region on top of the building, but they do not yield results outside of reason, with the comprehensive approach performing slightly better. In the immediate building wake region, both models capture the correct trend in the turbulence profile, although slightly off the experimental results. Further downstream of the building, both models perform well, with the comprehensive approach showing slightly better performance.

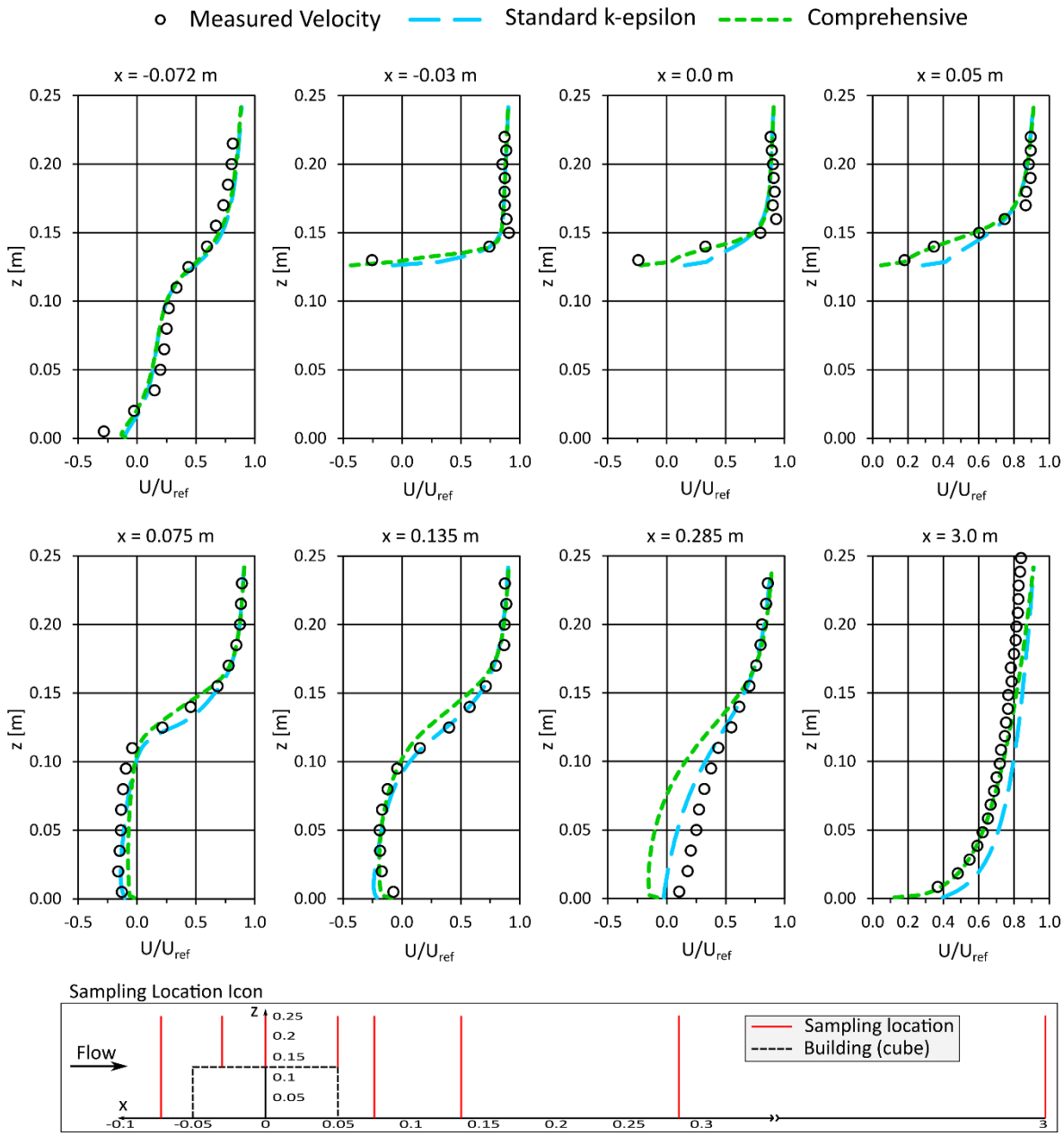

Figure 35. Velocity profile comparison between measured and numerical results, along the x-axis at y = 0 m, for the CEDVAL A1-1 case. The bottom of the figure features an insert showing the sampling location relative to the cuboid.

Figure 35 shows that the velocity is well predicted by both the standard and comprehensive turbulence models at all of the sampled locations. Both models slightly under-predict velocity at x = 0.285 m downstream, just before the end of the building wake. It is also noted that the comprehensive approach is able to recover the velocity profile at the domain exit, whereas the standard turbulence model does not.

4.6 Summary and Limitations of Approach

This chapter has seen the implementation of the solution methods that are required to reproduce realistic neutral ABL flow, which is evidenced by the reproduction of the velocity and turbulence flow profiles along the length of the domain to a reasonable degree of accuracy. The comprehensive turbulence

modelling approach is favoured because of its ability to sustain a decreasing turbulent kinetic energy profile along the length of the domain, which is a closer representation of reality than the profile proposed by (Richards and Hoxey, 1993). With the numerical solution method developed and validated, it is appropriate to move on to the simulation of the actual Transalloys dispersion case in question.

These models do not account for any atmospheric stability other than the neutral class. This is deemed acceptable if the goal of the simulation is to look at qualitative trends, such as in this case. If, however, the goal of the simulation is to try and predict dust loadings accurately, then stability cannot be neglected as the dispersion of dust particles can be enhanced or dampened depending on the given condition.

5 CFD Investigation of Neutral ABL Flow at the Transalloys Smelters

This chapter applies the CFD model, validated in Chapter 4, to simulate neutral ABL flow in the region of the Transalloys smelter. This chapter includes a description of the simulation domain, meshing strategies, sensitivity analyses, identification of priority simulation cases, and validation with prevailing winds and exposition of flow field results.

5.1 CFD simulation goals

Proper simulations can only be performed if the desired outcomes are known. The simulation goals are listed here:

- Build a suitably large mesh independent computational domain
- Identify priority wind conditions to be simulated based on experimental wind data
- Validate the computational domain against experimental wind data for the prevailing wind case
- Discuss some of the obtained results for the flow field to develop a 'feel' for the localised flow phenomena

The *COST732* guidelines (Franke *et al.*, 2007) are consulted as a starting point for all decisions that are made. All simulations and post-processing are performed with ANSYS Fluent 2021R1.

5.2 Priority winds cases

The dustiest period observed (11/06/2020 – 01/10/2020) during the soiling study occurred in the dry season, as identified in Chapter 3. Sampling *Period-D* (as labelled in Figure 19) is the ideal candidate to test the proposed approach because it represents the peak of the dry period with the heaviest mirror soiling measured. The wind rose for *Period-D* is repeated in Figure 36, along with its corresponding wind direction histograms and wind speed probability density functions.

Wind speed typically follows a Weibull distribution (Landberg, 2016), which is why the fit is overlayed onto the wind speed probability distribution in Figure 36. The Weibull shape parameter for the wind speed of *Period-D* is $\beta = 1.5$ and the scale parameter is $\eta = 2.7$. The probabilities provided by the Weibull fit are used to calculate the weighting factors for the simulation results. The fitted function values are used, but the actual values could have been equally used.

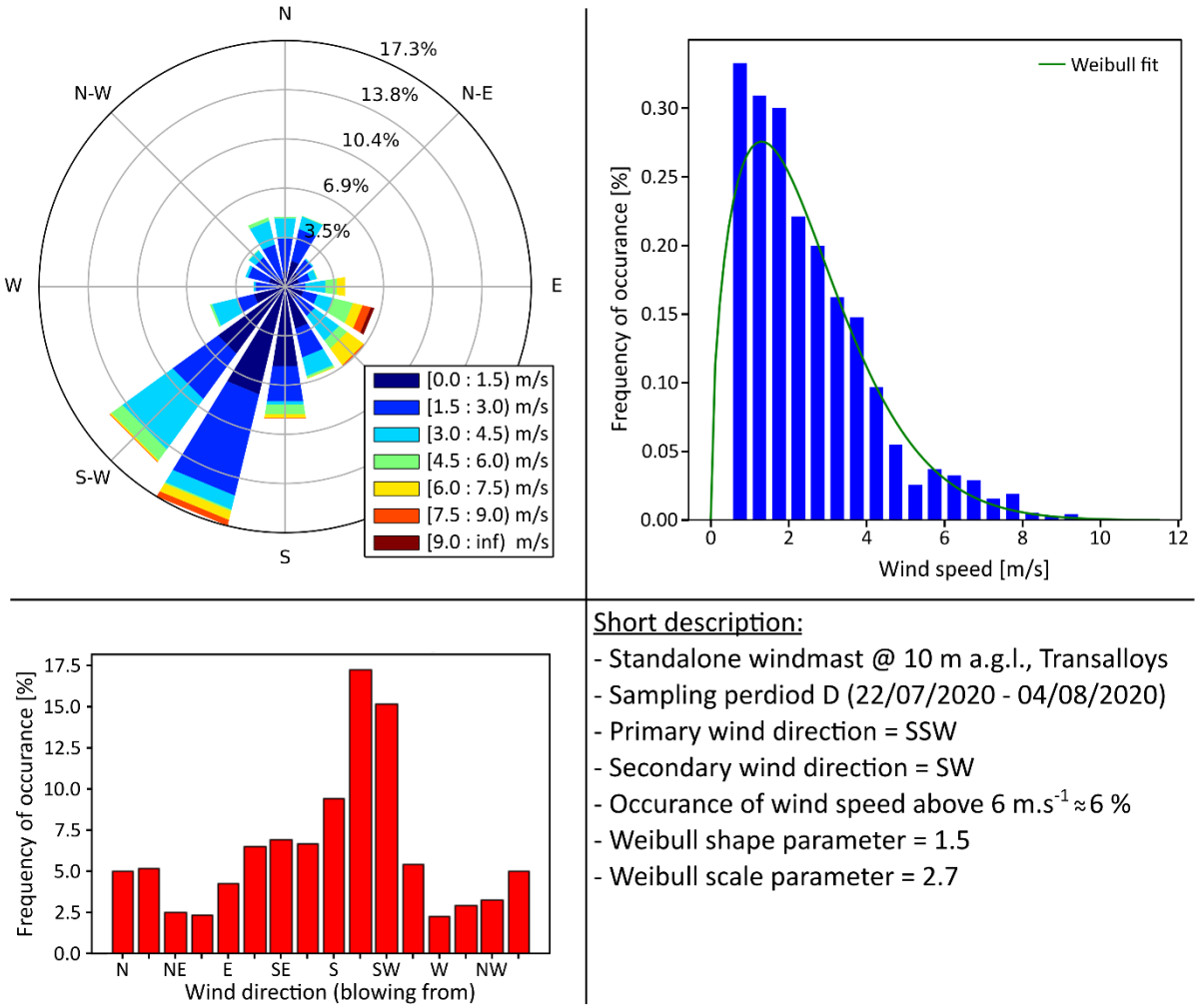

Figure 36. Wind rose data decomposition for mirror reflectance sampling period D, including wind rose (top left), wind speed probability density function (top right), wind direction histogram (bottom).

5.2.1 Priority wind directions

To limit the number of simulations that need to be performed, only the top seven most frequently occurring wind directions for *Period-D* will be used to set up simulation cases. This is a reasonable strategy for *Period-D* specifically because the top seven most frequent wind directions include the dominant winds as well as the less-frequent peak ESE winds exceeding 9 m/s.

5.2.2 Priority wind speeds

Just as the entire wind rose's distribution of wind speeds follows a Weibull distribution, so too can the wind speeds of each wind direction be assumed to follow a Weibull distribution. Once again, to limit the number of required simulations, two representative wind speeds are selected to represent 'low' and 'high' wind speeds for each wind direction. The selected high and low wind speeds are based on the fluid (static) threshold friction velocity required to initiate saltation, and thus emission, for different particle sizes, based on Eq. 27. To calculate these thresholds, the particles are all assumed to be silica-oxide (SiO_2) with density ρ_{SiO_2} = 2200 kg/m^3, and the inter-particle force scaling parameter set to $\gamma = 3.3 \times 10^{-4}$ N/m. The low-wind speed condition selected is U_{low} = 3 m/s, resulting in a fluid threshold friction velocity u_{*ft} = 0.26 m/s, which initiates saltation for particle diameters in the range 60 µm < D_p < 200 µm, accounting for roughly 17 % of particles in the PSD collected from the mirrors (Chapter 3). The high-wind speed condition selected is U_{high} = 6 m/s, resulting in a fluid threshold friction

velocity u_{*ft} = 0.52 m/s, which initiates saltation for particle diameters in the range 13 µm < D_p < 900 µm, accounting for roughly 82 % of particles in the PSD collected from the mirrors. The fluid threshold saltation friction velocities and the corresponding SiO_2 particles that will saltate are summarised in Figure 37.

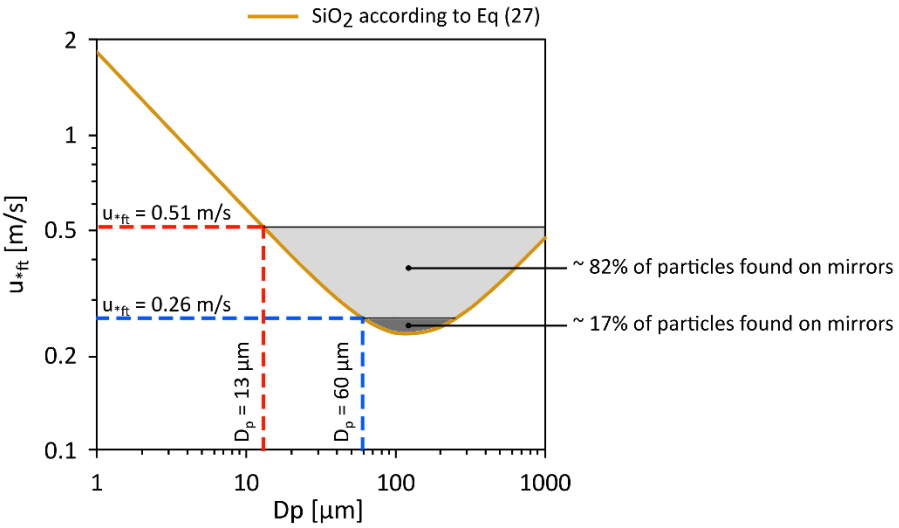

Figure 37. Fluid threshold (static threshold) friction velocity for saltation initiation for a range of SiO_2 particle sizes based on the semi-empirical relationship given by Shao and Lu (2000).

5.2.3 Simulation cases

The test cases are summarised in Table 6, giving the case name containing the wind speed, wind direction (measured clockwise from North as is convention), wind speed, and other required simulation parameters. Appendix F shows the full set of values required to generate appropriate BCs for each case.

Table 6. *Period-D* test cases summary of experimentally determined BC inputs, wind data from the standalone wind mast at 10 m height AGL

Case name	WD	U_{ref} at 10 m AGL	u_*	Weighting factor based on frequency of occurrence
	[°]	[m/s]	[m/s]	
SSW-3	202.5	3	0.26	0.17001
SSW-6	202.5	6	0.52	0.00306
SW-3	225	3	0.26	0.14803
SW-6	225	6	0.52	0.00422
S-3	180	3	0.26	0.09242
S-6	180	6	0.52	0.00159
SE-3	135	3	0.26	0.05332
SE-6	135	6	0.52	0.01612
SSE-3	157.5	3	0.26	0.06646
SSE-6	157.5	6	0.52	0.00032
ESE-3	112.5	3	0.26	0.04294
ESE-6	112.5	6	0.52	0.02170
WSW-3	247.5	3	0.26	0.05365
WSW-6	247.5	6	0.52	0.00084

5.3 Validation case and data

In an ideal scenario, data from a wind mast at some distance away from the area of interest (AOI) would be used to derive the inlet BC flow profiles. Measured data from wind masts close to the AOI would then be used to provide data for validation. In this case, the standalone wind mast data must be used to derive inlet BCs and to provide data for validation since it is the only wind mast that provides reliable data.

To ensure that the data used for deriving inlet conditions and for validation are representative of the wind blowing from a given direction at a given speed, only wind directions fluctuating less than $\pm 5°$ about a given direction are considered (Van Hooff and Blocken, 2010). Similarly, wind speeds can also not fluctuate more than 0.6 m/s about the sought mean reference velocity. Only if the sampled 10-minute wind data points meet both these criteria for more than an hour, are the specific data included in the calculation of the mean values used to derive flow profiles. It should be noted that the wind mast was not on site for long enough to collect enough data to satisfy the above criteria for all wind directions as well as the high and low wind speed categories; in these cases, the criteria are relaxed slightly.

The most frequent wind direction for sampling *Period-D* is the SSW wind direction. The *SSW-6* case will thus be used for validation of the flow field. An hour of continuous wind direction data from the standalone wind mast (Figure 11) used to derive inlet flow profiles for the *SSW-6* case is depicted in Figure 38 (see Appendix H for the data excerpt)**.** Data from the weather station wind mast (Figure 11), which is in the wind shadow of the slag heap for an SSW wind, are shown for the same hour period. Data from both masts are plotted in Figure 38 to illustrate the difference between them.

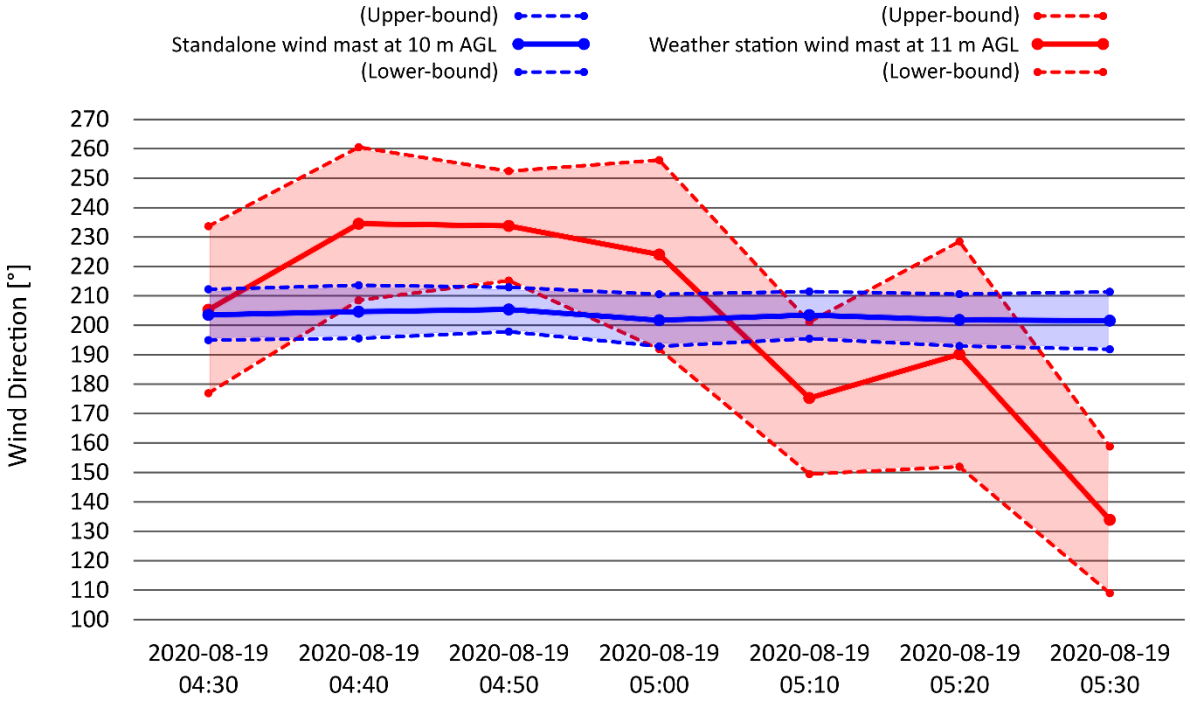

Figure 38. An hour excerpt of wind direction data for an SSW wind as measured at the standalone wind mast, contrasted with wind direction data measured at the weather station wind mast for the same period.

Figure 38 makes the difference in flow stability clear between the two wind mast locations. The variation in wind direction with time, as well as the difference in the standard deviation of the wind direction, shows us that the wind direction in the wake region of the slag heap is sensitive to the

upstream wind direction and that small changes in upstream direction can lead to a significant change of mean wind direction behind the heap. The flow meanders in the wind shadow of the smelter building complex and slag heap. This result highlights the importance of proper wind mast placement relative to any potential flow obstacles. Refer back to Figure 11 for wind mast and smelter site layout.

Considering the data presented in Figure 38, it is noted again that any characteristic component of the wind in the immediate wake region of any obstacle, in and around the smelter complex, is not a reliable source of information and should not be used to draw conclusions about the accuracy or usefulness of the simulation results.

5.4 Simulation settings

Most of the simulation settings specified in section 4.3 are kept the same, with some material property changes to account for the height above sea level of the smelter location.

The smelter complex, and computational domain, centre point is taken to be x = 712,085 m east, y = 7,134,141 m south, height above sea level (ASL) z_{ASL} = 1539 m. The coordinates are given in EPSG:32735 UTM35S projected format, allowing easy translation between real-world coordinates and mesh coordinates going forward.

A summary of the inputs for all the simulations from here onwards is given in Table 7. The material properties of the standard atmosphere (NASA, 1976) at the height of 1550 m ASL are used where applicable.

Table 7. CFD simulation settings for full-scale Transalloys case.

Setting	**Value**
Solver	Double precision pressure-based
Iterative scheme	SIMPLE
Turbulence model	$k-\epsilon$ (modified)
Momentum and turbulence equations	Second-order upwind discretisation
Pressure equations	Standard discretisation
Gradients and derivatives	Least-squares based
Residual convergence criteria	10^{-3} at least
Density of air	ρ_{air} = 1.053 kg/m^3
Viscosity of air	μ_{air} = 1.761e-05 kg/(m s).
Reference pressure	P_0 = 84,038 Pa
Inlet BC type	Velocity inlet with *x* and *y* components
Outlet BC type	Zero static pressure outlet, no reverse flow
Top BC type	Velocity inlet with *x* and *y* components
Terrain wall BC	z_0 = 0.1 m (roughly open)
Building wall BCs	Smooth

A roughness height of z_0 = 0.1 m corresponding to roughly open terrain (see Appendix A) is selected. This is based on observations and on the land use classification data presented in Figure 8, showing that Transalloys is situated in a grassland biome with agricultural lands and mining activities surrounding it. Assigning one aerodynamic roughness height value to the entire terrain BC is a simplification made in this investigation. If more accuracy is required, then this simplification might need to be revised.

5.5 Computational domain description

The input data used in the construction of the computational domain are discussed in this section.

5.5.1 Domain layout section

The layout of the computational domain is shown in Figure 39. Two velocity inlet BCs and two pressure outlet BCs are assigned to the sides of the domain (N-E-S-W) depending on the horizontal wind vector components.

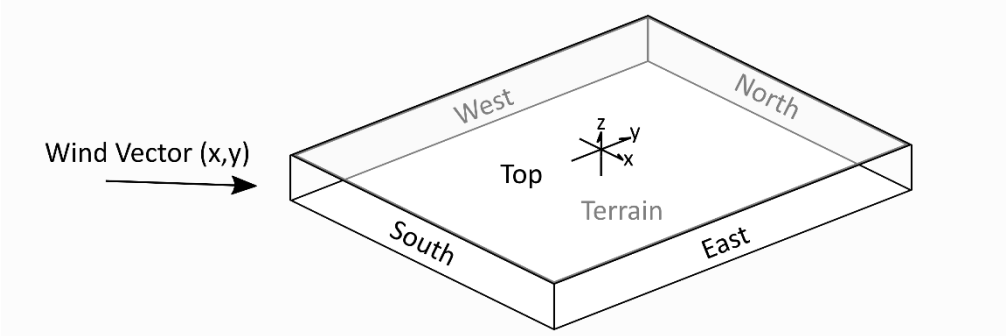

Figure 39. Computational domain layout schematic.

In the case of the illustration in Figure 39, the south and west faces would be velocity inlets, and the east and north faces would be pressure outlets. The top face is always a velocity inlet with the same components as the side velocity inlet conditions. The terrain is always a fully rough wall where the comprehensive approach wall function is assigned. The illustrated domain layout allows for wind from all directions to be simulated by simply assigning inlet and outlet faces accordingly. The assignment of BCs is implemented in an ANSYS Fluent journal file, see Appendix G.

5.5.2 Terrain

The terrain that ABL flow encounters directly influences the local flow characteristics, especially close to the ground. The representation of the terrain also determines how the vertical velocity and turbulence profiles develop. It is, therefore, essential to have a good enough mesh representation of the terrain that stretches a sufficient length upstream and downstream of the area of interest (AOI). If the study's focus height is closer to the ground, then it may be more important to have a fine resolution of the terrain, whereas if the study is focusing on flow-field characteristics further away from the ground, a coarser resolution may suffice. There is a well-known 30 m horizontal resolution digital terrain model (DTM) dataset made available by NASA (Farr *et al.*, 2007). However, in order to have the flexibility available to represent the terrain in more detail, a higher resolution is sought. To this end, a 2 m horizontal resolution DTM dataset (GeoSmart, 2019) was obtained, shown in Figure 40. It is large enough to allow an upstream and downstream computational domain length of 8 km from the AOI if desired.

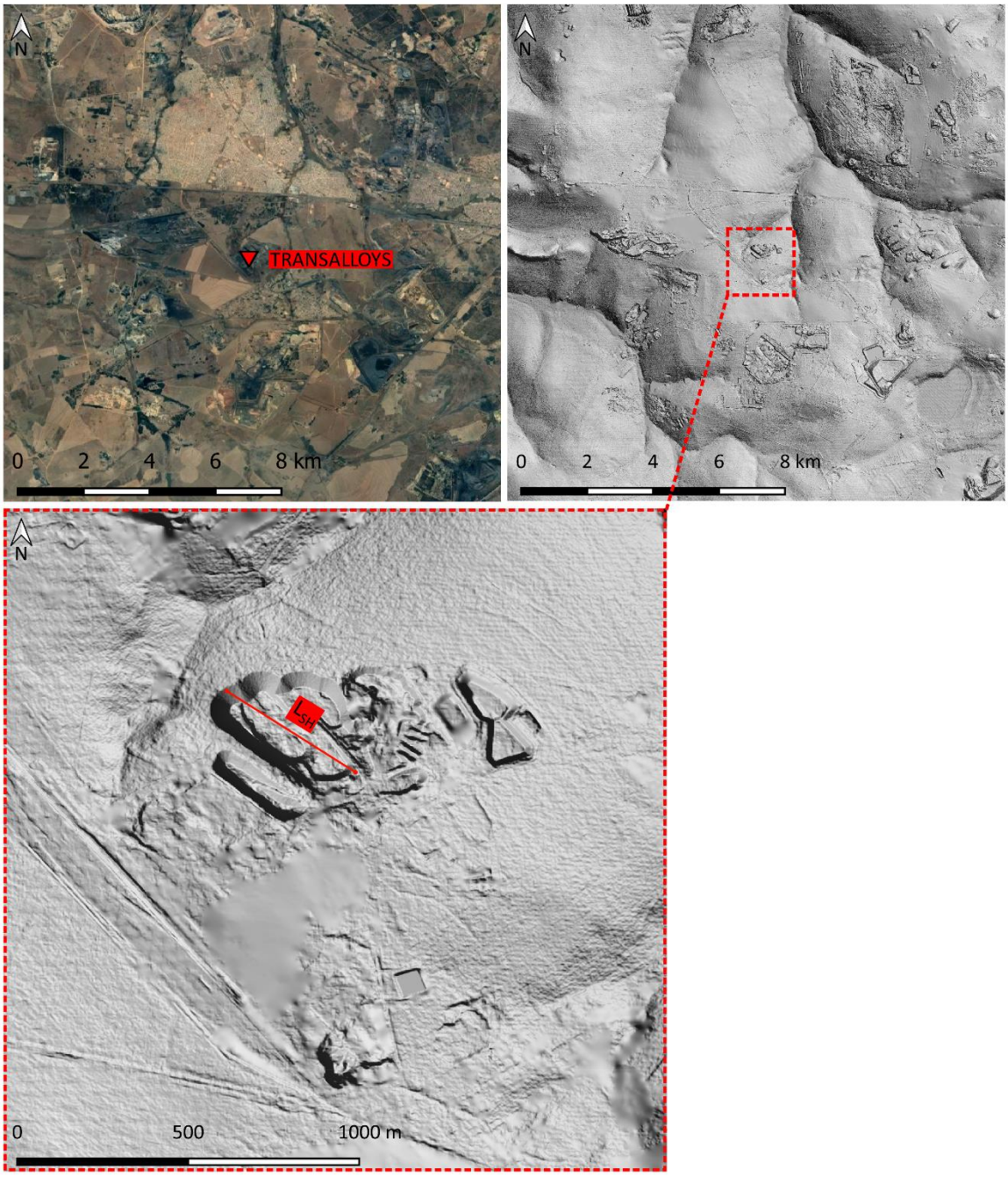

Figure 40. High resolution 2 m digital terrain model of 16×16 km^2 area centred on Transalloys. Google Earth 16×16 km^2 satellite image (top left), DEMSA2 16×16 km^2 hillshade (top right), DEMSA2 2×2 km^2 hillshade showing the characteristic length of the slag heap (bottom). DEMSA2 source: (GeoSmart, 2019).

The bottom section of Figure 40 shows a close-up of the AOI. The DTM data do not include the smelter building complex or any other buildings in the area. The smelter buildings are important to the local flow in the AOI and are re-introduced in section 5.5.3. The characteristic length of the slag heap is taken to be $L_{SH} \approx 460$ m and indicated in the bottom part of Figure 40. The characteristic length of the slag heap is used to help determine the required downstream length of the domain since it is the largest single obstacle that the flow encounters.

To get a better feel for the topographical features of the terrain, further analysis of the DTM was done using QGIS's built-in raster tools. The results of the terrain slope and aspect analysis of the terrain data

are shown in Figure 41, where slope indicates the rate of change or steepness of terrain and aspect indicates in which direction the terrain is facing.

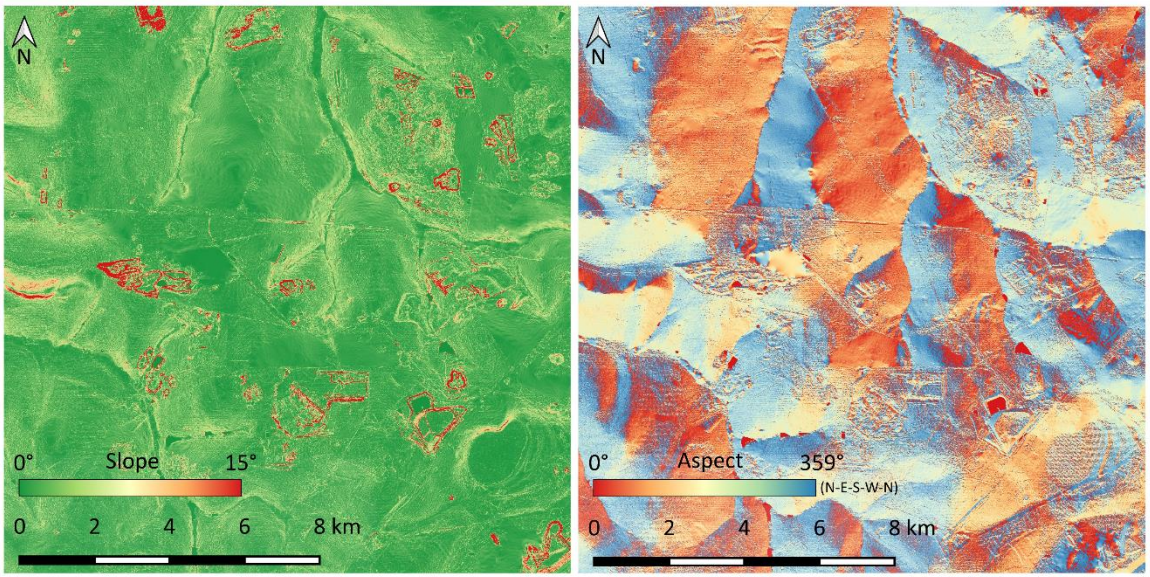

Figure 41. Slope (left) and aspect (right) of terrain surrounding Transalloys, derived from the 16×16 km^2 DEMSA2.

The slope and aspect of the terrain shown in Figure 41 helps better understand where and how the terrain is likely to influence the wind flow.

The DTM data are made available in GeoTIFF file format, which needs to be converted to a format that is readable by the ANSYS Fluent meshing tool, such as the stereolithography (STL) file format. The DTM data are reprojected to the UTM35S coordinate system and converted to STL format, using an open-source python library *phstl* (available at https://github.com/anoved/phstl.git). Thereafter, the STL terrain is easily handled by the ANSYS Fluent parallel meshing tool.

5.5.3 Transalloys plant bluff model

The construction of plant building geometries as bluff bodies was made possible from images and existing computer-aided design (CAD) models. These simplifications can be made because the flow field a few building heights downstream of the building obstacle is not so sensitive to geometry details but rather to the bulk flow displacements by projected area. Partial CAD models of the smelter building complex were obtained from Transalloys. The CAD models were converted into simpler bluff bodies, and rough approximations of missing buildings were added based on on-site observations and satellite imagery. The semi-detailed CAD to bluff-model conversion is shown in Figure 42.

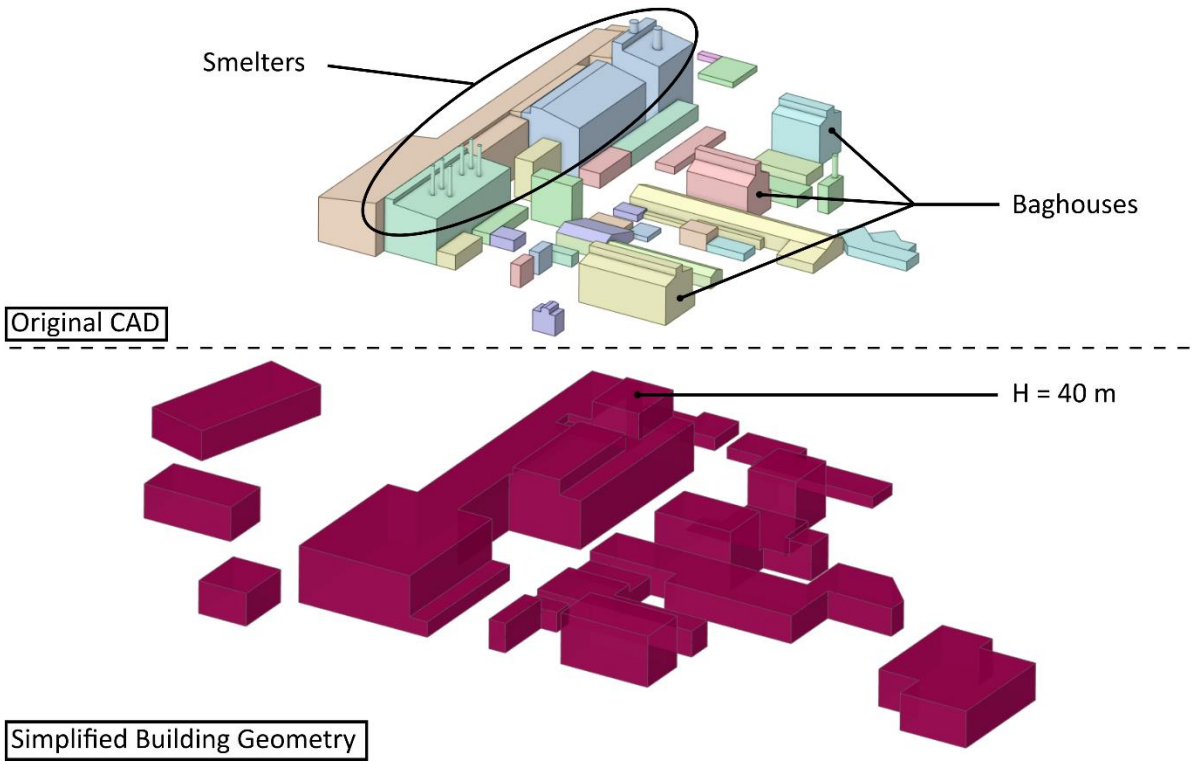

Figure 42. Smelter building complex geometry simplification, with the addition of a few buildings that are not present in the original CAD geometries.

Figure 42 indicates the characteristic height of the tallest building is H = 40 m, with the characteristic length not specified as the close-by slag heap's length is greater and will have a larger impact on the flow. The indicated building is also the tallest object in the smelter complex.

5.6 Computational mesh

A poor computational mesh will yield inaccurate results since the numerical solution is only as appropriate as the mesh allows it to be. Because of this, proper care must be taken when developing a mesh for further use. Here, a meshing strategy is defined, followed by a determination of the domain extent requirements, and finally, a mesh refinement study.

5.6.1 Meshing strategy

The generation of a suitable mesh is complicated because of the large difference between the smallest (~ 1 m) and largest (~ 500 m) length scales in the domain. In most cases, structured or body-fitted grids are preferred because they usually allow faster convergence towards a solution if the grid is flow-aligned and the resolution and cell sizes can be precisely controlled in all areas of the solution domain. A bottom-up surface mesh extrusion approach showing a good example of body-fitted mesh generation in an urban environment exposed to the wind is detailed by Van Hooff and Blocken (2010), where the interactions between ABL flow and indoor ventilation are investigated. This approach is easier to take when the terrain is relatively flat and contains obstacles (e.g., buildings in a city) or when a more complex terrain with no obstacles (e.g., open hilly terrain) is being considered; it is not so easy to follow when the domain of interest consists of complex terrain with obstacles (a smelter plant in hilly terrain, as considered here).

Alternatively, a more automatic mesh generation approach can be followed to yield a completely unstructured mesh with selected regions of refinement in the zones of interest. In the case of Transalloys smelter, the flow will be guided by the hilly terrain, and multiple wind directions will be considered. It would therefore be advantageous to have one mesh that can be used for all cases. The benefits of using a more structured mesh are diminished if the mesh is not aligned with the flow, whereas an unstructured mesh will perform equally with all wind directions. The universality and more automatic nature of the unstructured meshing approach is therefore favoured here.

The meshing strategy and basic cell parameters are summarised by the following:

- Polyhedral cells will be used to generate the unstructured mesh
- Wall perpendicular grid lines are required at the walls, meaning that only prismatic cells (inflation layers) should be used at and close to the walls
- A grid stretching ratio of no more than 1.2 is used
- Two nested body(s)-of-influence (BOIs) are used to refine the mesh in the 1.4 km radius region surrounding the smelter, with the finest cells located on and around the smelter building complex
- A maximum building face cell size of 2 m, which is small enough to capture bulk flow features in the areas of the buildings
- A domain height is chosen such that the height above the building complex is ~ 900 m, which is consistent with a neutral ABL, yielding a blockage ratio of 3.9 %

The domain used will be a square and centred on the smelter complex, with two BCs being inlets and the other two being outlets depending on the flow direction.

The ANSYS Fluent parallel meshing tool is used to perform the terrain and building geometry intersections and the subsequent meshing. An example of the steps used for the automated meshing procedure is shown in a journal file in Appendix G.

5.6.2 Mesh extents

It is difficult to determine the best domain size in the case of a complex terrain simulation since all of the upstream obstacles have an influence on the flow, and naturally, the closer the obstacle is to the AOI, the higher its impact is on the flow in the AOI. This is also reflected in the *COST732* guidelines (Franke *et al.*, 2007), where it is suggested that a building with height *H* has an influence on its surrounding flow up to a distance of 6-10*H*. This implies that if an obstacle or building falls outside of this distance from the AOI, it can be crudely represented or excluded from the domain entirely. It is for this reason that it is necessary to include the Transalloys smelter building complex explicitly, and safe to exclude all other buildings from surrounding plants.

To prevent artificial flow acceleration around the AOI, a ratio of projected obstacle area to the free-flow cross-section is defined, known as the blockage ratio, with the recommendation to keep this under 3 %. To keep below the recommended blockage ratio, the *COST732* guidelines recommend minimum domain extents, which typically results in the requirement being met. The vertical domain extent of $5H_{max}$ is recommended, with lateral extents of $5H_{max}$ recommended, while acknowledging that the influence of lateral boundaries on the flow is case-dependent and that two different setups should be tested. The extent of the domain in the flow direction is $8H_{max}$ if the inlet flow profiles are known and much longer if they are not to allow for flow development. The minimum downstream distance to allow

for flow recovery in the wake of the obstacle is $15H_{max}$. All these recommendations are made for the case of a single obstacle and are usually allowed to be reduced in the case of many obstacles (e.g., the buildings of a city).

The Transalloys smelter building complex next to the slag heap form multiple flow obstacles with different qualities. The buildings have sharp protruding edges, where the slag heap is more like an abrupt hill, and although the slag heap is not as tall as the tallest building, it presents a large obstacle to flow, being a continuous obstacle that the flow must travel over or around. The selected vertical domain extent of 1 km above the AOI results in a vertical blockage of 4 %. The downstream length is the focus of the domain extent because the fetch length will be made the same to create a square domain. The slag heap's characteristic length is used to estimate what distance the wake needs to recover since it is the largest solid obstacle to the flow. According to the recommendation of $15H_{max}$, the downstream distance needs to be $15L_{SH}$ = 6900 m. Figure 43 illustrates the three options for horizontal domain extents that are considered (2500 m, 5000 m and 7500 m).

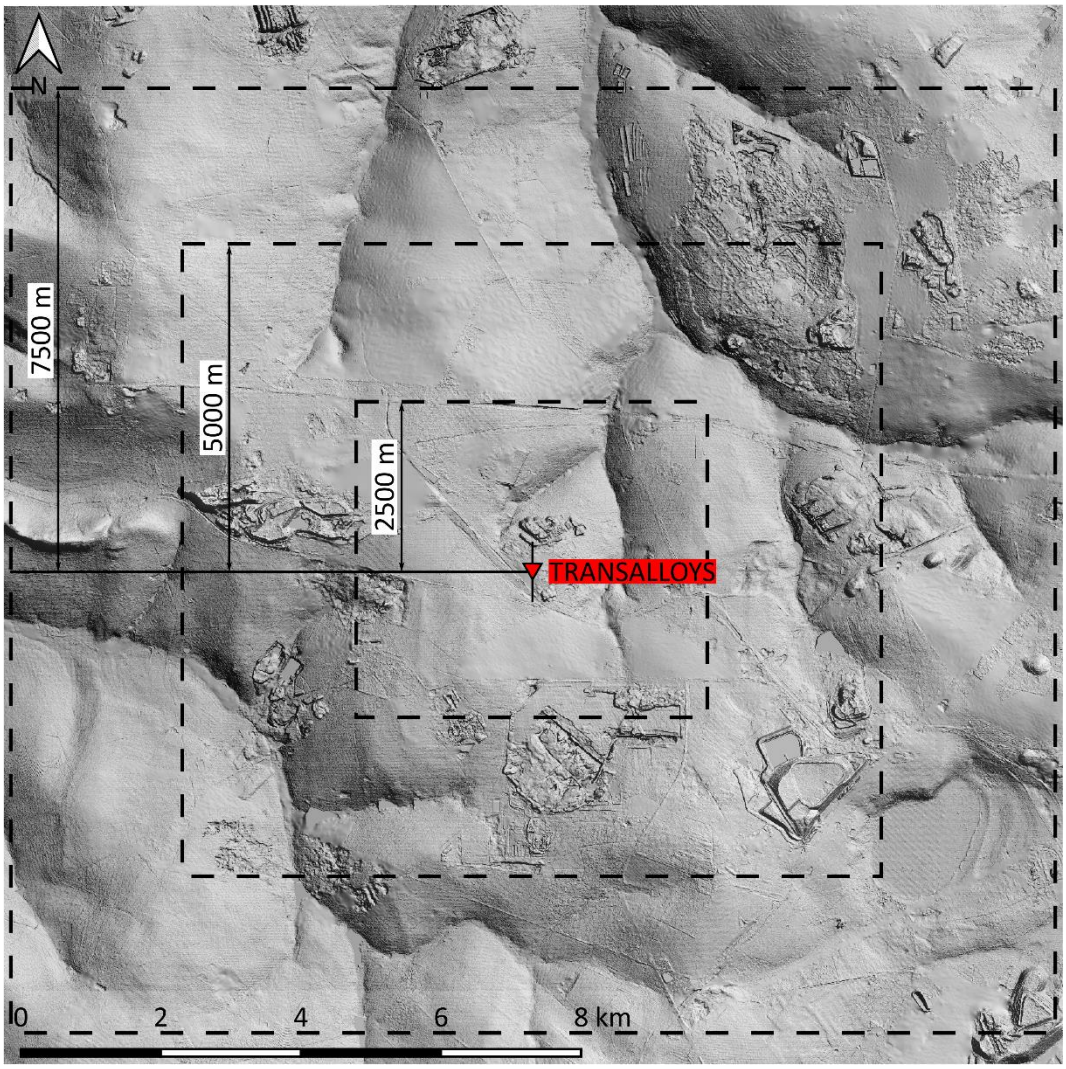

Figure 43. Three square domain sizes considered for the computational domain.

The extent of 2500 m is included as a domain size as a test even though it is much smaller than the estimated 6900 m extents required, simply because a smaller domain size could result in faster computation. The three different domain sizes are meshed using the described baseline meshing strategy and simulated using the priority SSW wind direction with the higher wind speed category of U_{high} = 6

m/s as the BCs. Simulation of the 2500 m extent domain did not converge to the stated residual level because the domain outlet boundary sits in the wake region of the smelter complex as predicted, whereas simulation of the $5000\,m$ extent domain did converge, implying that the flow in the wake region recovers sooner than expected or to an acceptable level. The extent of 7500 m did not converge either, contrary to initial estimation, but upon closer inspection, this makes sense since the bottom right corner of the boundary crosses a large materials pile which causes instability at the domain boundary dominating the equations' residuals. The conclusion that can be drawn from these results is that undulating terrain at the outlet boundary location is not an issue, but care must be taken when selecting the extent such that it does not cross a large obstacle that can result in instabilities at the boundary location.

5.6.3 Mesh refinement

The purpose of a mesh independence study is to result in a mesh that does not have a significant influence on the results, meaning that as the mesh gets finer, values measured at the same location should converge towards a single value or be in the asymptotic range. One way of checking whether the simulation results are becoming independent of the mesh is by comparison to experimental results at a given location. The relative change in results between one mesh to the next should also become smaller with each successive refinement. The refinements made relative to the baseline mesh are shown in Table 8 in the form of cell counts. The baseline mesh is the first guess at a good mesh, based on the good practice guidelines and other atmospheric flow CFD literature.

Table 8. Cell counts for the coarse, baseline, intermediate, and fine meshes.

Mesh number	Cell count
Coarse	4,552,755
Baseline	7,887,224
Intermediate	13,317,763
Fine	42,462,708

The scale of the computational domain means that refinements should be focused in and around the areas of interest in the simulation. The important refinements are thus made in the two BOIs, on the building walls and on the terrain wall. The baseline mesh generated for the 5000 m extent simulation is shown in Figure 44 as an example. The clustering of the mesh in the vicinity of the smelter buildings is clearly illustrated.

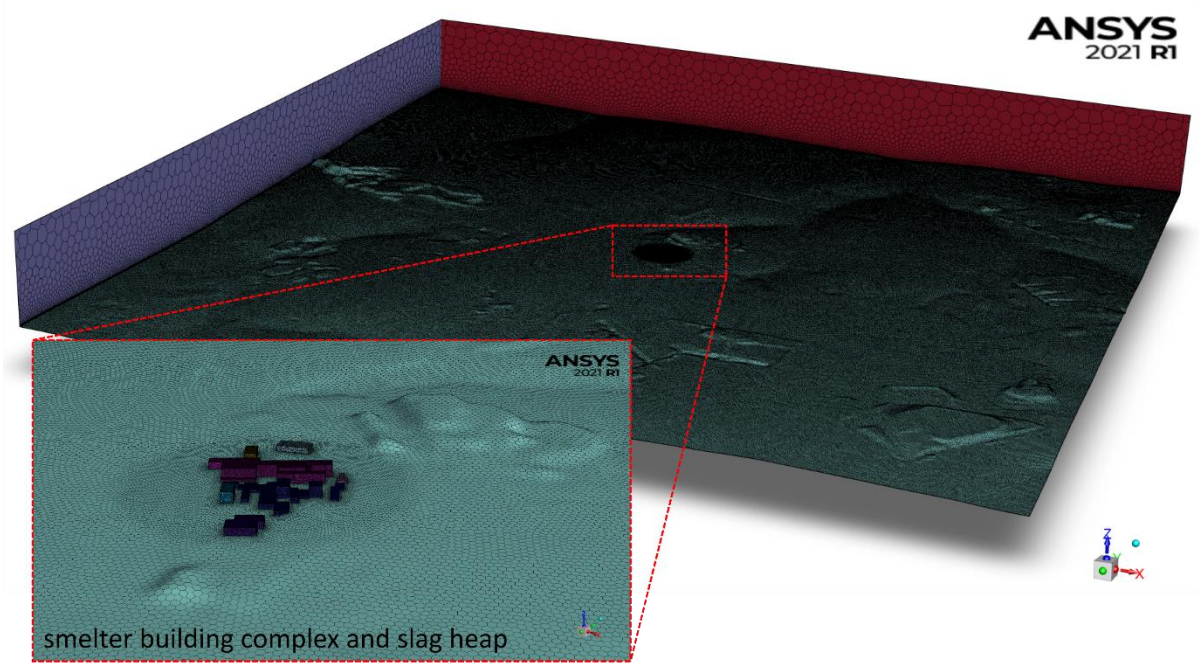

Figure 44. Overview and close-up view of a representative 5 km extent polyhedral mesh used for independence study.

A sectioned view of the mesh is given in Figure 45 to highlight the cylindrical BOI refinement regions centred of the smelter building complex. Also evident is the stretching of the mesh in the vertical direction, away from the region of interest.

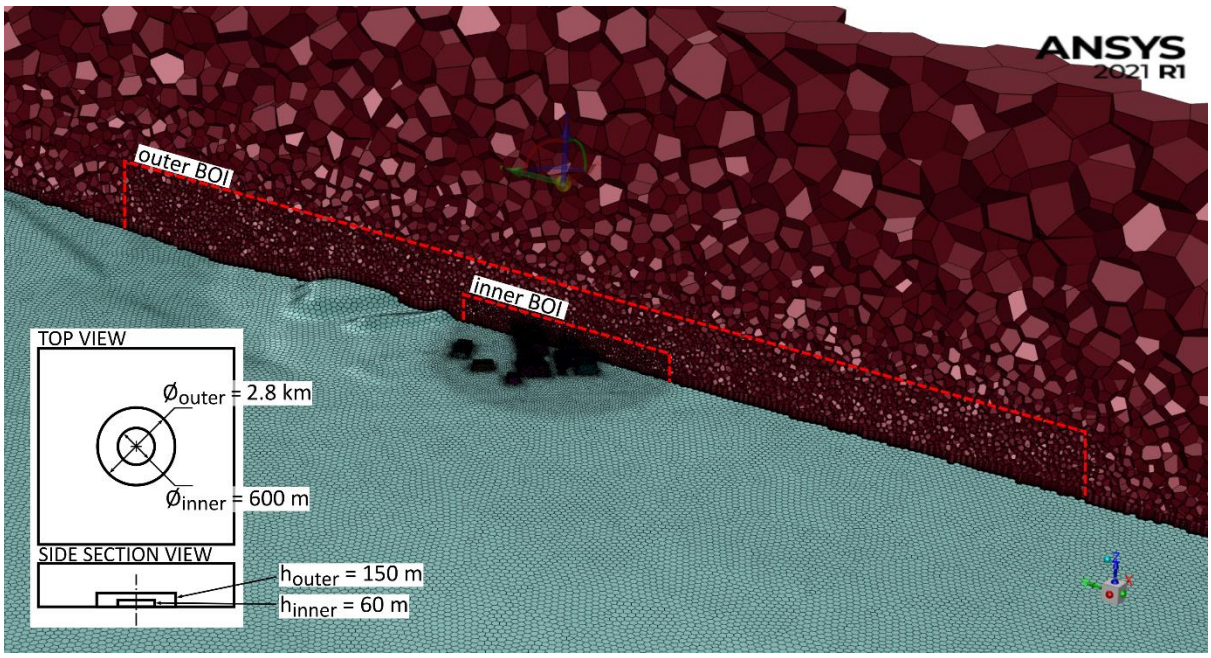

Figure 45. Sectioned view of mesh showing polyhedral cell layer and refinement zones around the smelter building complex, accompanied by schematic showing the refinement regions' (BOIs) sizes.

Simulations were performed for the sequentially refined meshes. The sampled results for velocity magnitude and turbulent kinetic energy are shown together with the experimentally measured wind mast values in Figure 46. The experimental turbulent kinetic energy was estimated from the standalone wind mast data, an example of which is given in Appendix H.

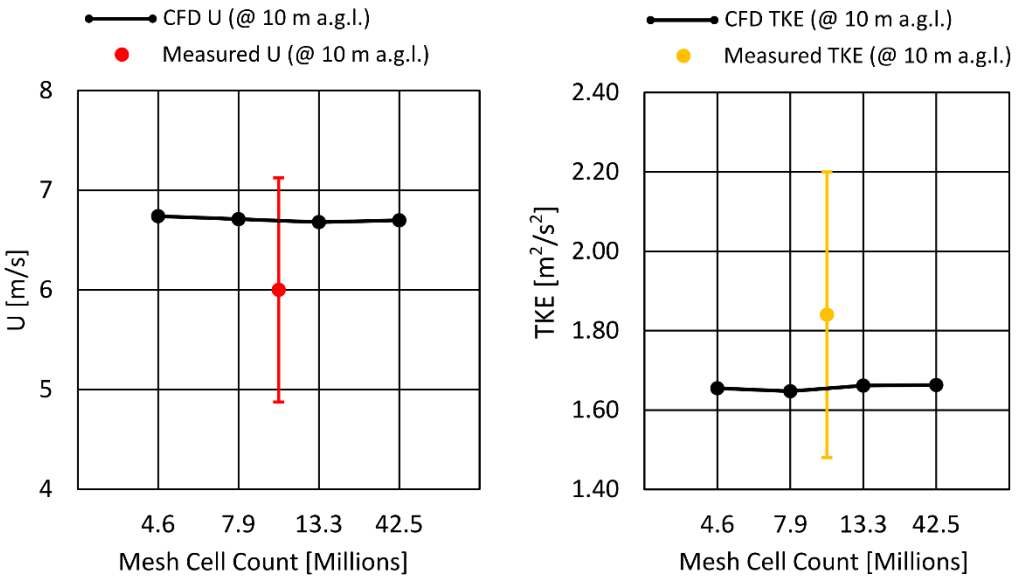

Figure 46. Velocity magnitude (U) and turbulent kinetic energy (TKE) at the standalone wind mast location for consecutive mesh refinements.

Figure 46 shows that the mesh produces reasonable results within the estimated experimental range, with a velocity increase being observed when compared to the mean experimental value. A streamwise terrain height increase is believed to cause the slight wind velocity increase from the inlet to the standalone wind mast measurement location. It is reiterated here that the domain inlet conditions are derived from the wind mast data that were not measured at the inlet location, so it is to be expected that the profiles will develop from there and that the flow conditions simulated at the wind mast location would not match the experimental data.

The two graphs in Figure 46 show that the location of the standalone wind mast in the computational domain is not very sensitive to the consecutive mesh refinements, with the tracked variables changing only slightly with increased cell counts, although they do converge for the final two finer meshes. This is not surprising considering that the main refinements occur in the BOIs, with only slight refinement of terrain cell sizes upstream of the standalone wind mast for the test direction used. The weather station wind mast is located in the outer BOI, making it an appropriate location to evaluate the flow field response to consecutive mesh refinements. That being said, its location is in the wind shadow of the smelter building complex and the exact produced values should not be relied on too much. Figure 47 presents the profiles of wind velocity magnitude and turbulent kinetic energy of the four meshes considered.

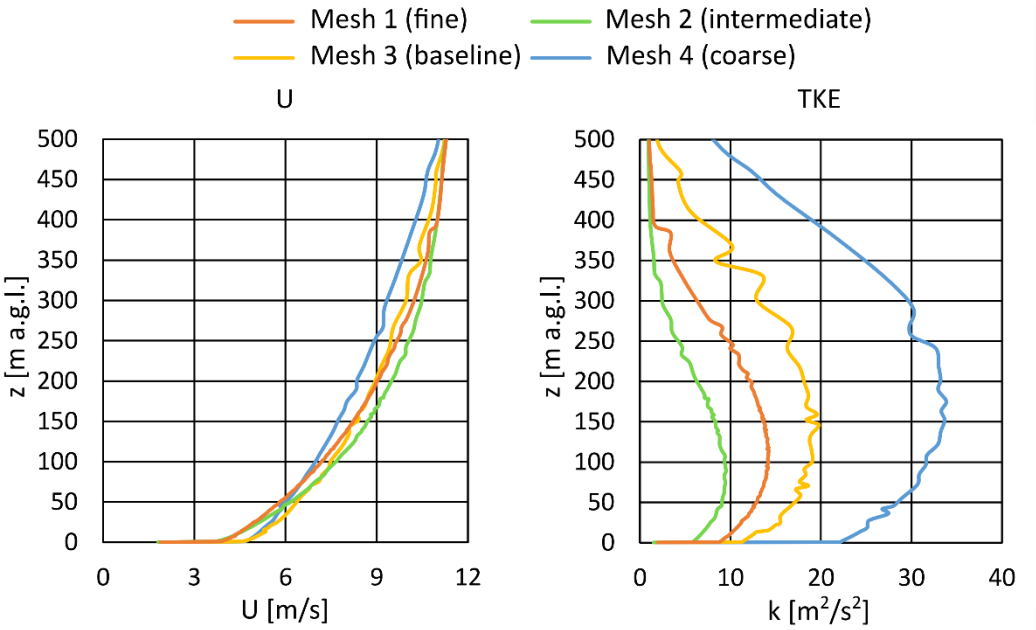

Figure 47. Profiles of simulated wind speed and turbulent kinetic energy in the outer BOI, located in the wake region of the smelter complex, for consecutive mesh refinements.

The velocity profiles in Figure 47 are all very similar and appear to be converging as the mesh is refined, whereas the profiles of turbulent kinetic energy show larger leaps with consecutive refinements of the mesh. From the results presented in Figure 46 and Figure 47, it can be concluded that consecutive mesh refinements mostly impact the regions of the domain where complex flows appear, with the bulk flows already being resolved with a relatively coarse mesh.

The intermediate mesh (Mesh 2) is selected as the mesh going forward based on the presented results. Apart from the difference between the turbulent kinetic energy profiles that the intermediate and fine meshes produce in the outer BOI smelter complex wake region, there is not much difference between the intermediate and the fine meshes. The results yielded by the two finest meshes are shown to yield realistic approach flow profiles (as sampled at the standalone-wind mast location), and the resulting velocity profiles in the smelter complex wake region appear to converge towards a mesh independent result. The intermediate mesh also allowed better convergence relative to the other meshes that were tested. The intermediate mesh is used going forward, with the caveat that turbulence kinetic energy values in the immediate wake region of large obstacles should not be relied upon too heavily.

5.7 Solution strategy

5.7.1 Building influence area (BIA)

Residual convergence below 10^{-3} is not possible without some modification to the computational space because of the application of the variable C_μ in the Comprehensive approach, which is intended for use only where the ABL flow is undisturbed (Parente *et al.*, 2011). This was ignored in the CEDVAL validation section in Chapter 4 because the flow only encounters one isolated cube; but it cannot be ignored in the current full-scale application. Convergence issues were picked up during the first few full-scale simulation cases when the solution diverged because of erratic and unrealistic growth of μ_t, resulting from the variable C_μ in the flow surrounding the buildings. To counter this effect, Gorlé, van Beeck and Rambaud (2010) demonstrated the so-called building influence area (BIA) approach based on the work of Beranek and Van Koten (1979), where a constant C_μ is set for the BIA while the variable

C_μ is enforced elsewhere. This approach is implemented in the current study by specifying a fixed region of 1.6H (based on the 1.76H used by Beranek and Van Koten (1979)) away from all the faces of the building in question, which in this case will be taken as 1.6H away from the perimeter and height of all the buildings in the smelter building complex. The cylindrical region that encloses the smelter building complex with a 1.6H gap in all directions is shown in Figure 48 (i.e., H + 1.6H = 104 m, where H = 40 m, the height of the tallest building)**.**

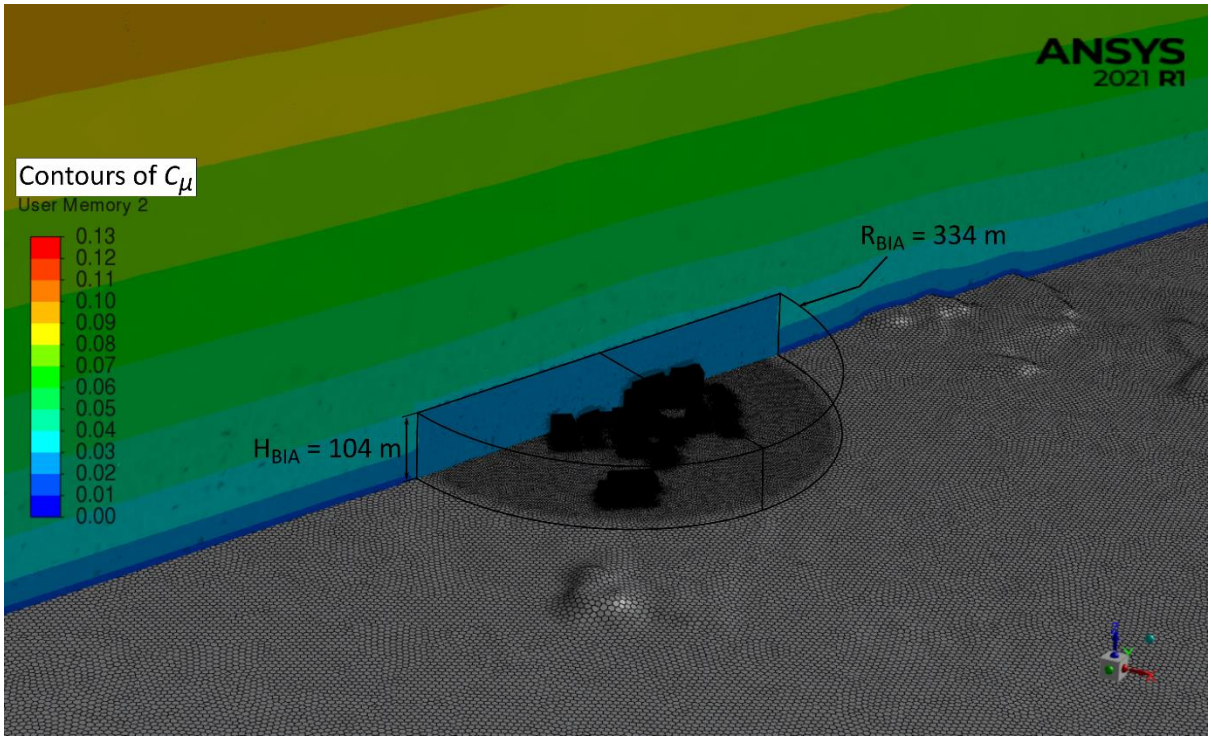

Figure 48. Variation of *Cμ* in the vertical axis, showing the BIA cylindrical region of constant *Cμ*.

The value of C_μ in this BIA region is set to $C_\mu = 0.03$, which approximates the average of the vertically varying C_μ from the terrain to the top of the buildings. The variable C_μ is incorporated into the simulation by performing the turbulent viscosity calculation in the UDF, see Appendix E.

5.7.2 Solution steps

There are many methods to implement that are non-standard in ANSYS Fluent. The solution is therefore reached by performing a series of steps based on inputs from a Fluent journal file that calls UDF functions when needed. User-defined scalars (UDS) and user-defined memory (UDM) slots are created and used along the way to store information required for calculations elsewhere in the solution procedure. The steps are outlined as follows:

- The first step is to generate a valid mesh as outlined in section 5.6
- Set up the computational domain with the desired BC and numerical methods
- Specify a UDS in ANSYS Fluent and turn off the turbulence and momentum solution equations
- Calculate the height AGL with the approach specified in section 4.2.3, for this, a user-defined scalar (UDS) and user-defined memory (UDM) slots need to be defined within ANSYS Fluent
- Calculate the BIA area as specified in section 5.7.1

- Turn the scalar equation off and turn the turbulence and momentum equations back on within ANSYS Fluent
- Initialise the computational domain by extrapolating BCs inwards using an on-demand function specified for initialising in the UDF, built-in hybrid initialisation procedures cannot be used as they will clear the UDS information already stored for the domain
- Limit wild fluctuations between initial solution iterations by using a solution 'spin-up approach; the 'spin-up approach down-adjusts the under-relaxation factors for all flow variables (i.e., pressure, momentum, turbulent kinetic energy, turbulent dissipation rate and turbulent viscosity) for the first few iterations, then returns them to their default values gradually as the solution progresses in a stepwise manner
- Once residual fluctuation between iterations are relatively stable, and under-relaxation factors are back to their original values, iterate the solution until all residual values are at least 10^{-3} or less

The above steps outline what the solution procedure journal files in Appendix G encode.

5.8 Flow field results

The validation in the previous section was done for the *SSW*-6 case. Additional flow simulations are performed for the top seven most frequent wind directions of sampling *Period-D*. An overview of the flow field for the *SSW-6* and *SSW-3* cases is given in this section. Results are provided at the 10 m height AGL to show the characteristic of the wind field at the standalone-wind mast sensor height, at 2 m height AGL to show the wind movements at the height of the dust and mirror samplers, and in the first computational cell above the terrain to show the friction velocity variation for the two different wind speed categories. Cell-centred values are displayed in all cases and the colour maps are clipped and binned in a manner that makes the different features in the flow stand out. The *SSW-6* case is discussed first because it was the case used for validation.

5.8.1 SSW-6 validation case

This subsection shows four results taken from the *SSW-6* validation case. Here, figures depicting velocity magnitude, turbulent kinetic energy and friction velocity are shown, each followed by interpretation guiding descriptions.

Figure 49 shows the wind speed at 10 m height AGL for the high-wind reference velocity case. A close-up of the smelter complex is shown with the reflector soiling sampling locations and standalone wind mast location indicated. The first point to make is the wind velocity speed-up that occurs over large parts of the domain relative to the inlet reference velocity condition of U_{ref} = 6 m/s at 10 m height AGL.

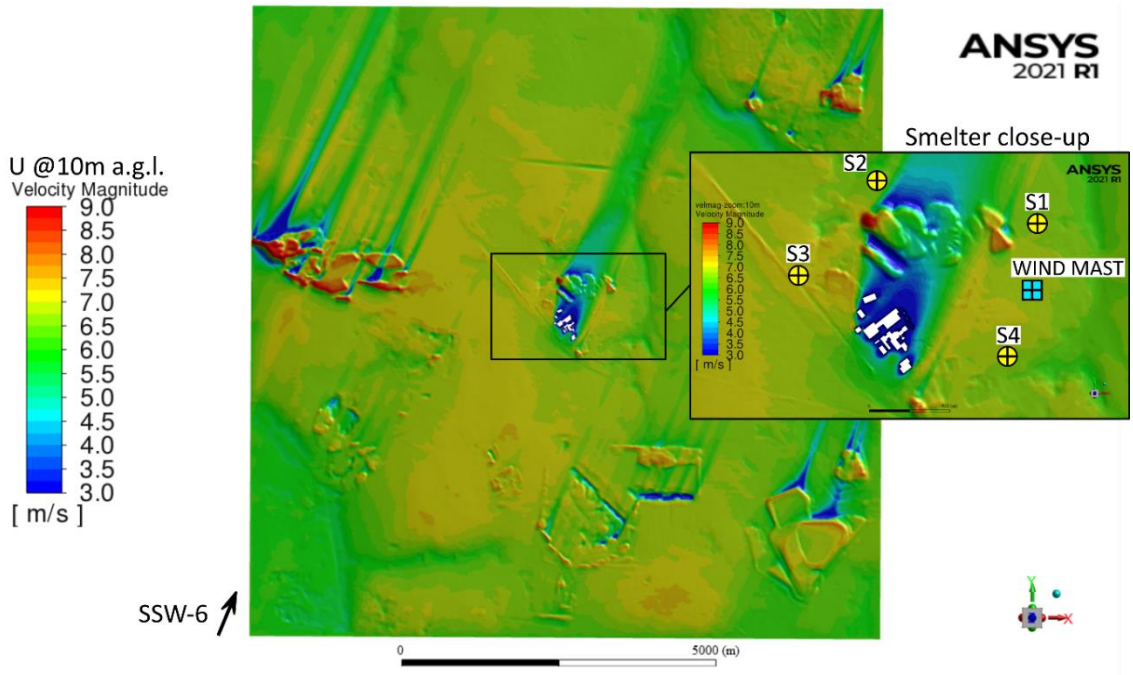

Figure 49. Velocity magnitude (U) at 10 m height AGL over the entire domain for the SSW-6 case. A close-up of the smelter complex is shown with the soiling sampling set and standalone wind mast locations as labelled in Chapter 3.

The observed speed-up happens because of the slight upwards inclination of the terrain in the flow direction, which accounts for the difference seen in the measured wind mast data for the *SSW-6* case and the numerical result for wind speed at the same location. If the goal of the simulation was to reproduce measured conditions, then the inlet velocity could be 'tuned' lower to account for the relative speed up such that the numerical output at the wind mast location matches the measured data, but this is not the objective of this investigation and is thus left as is.

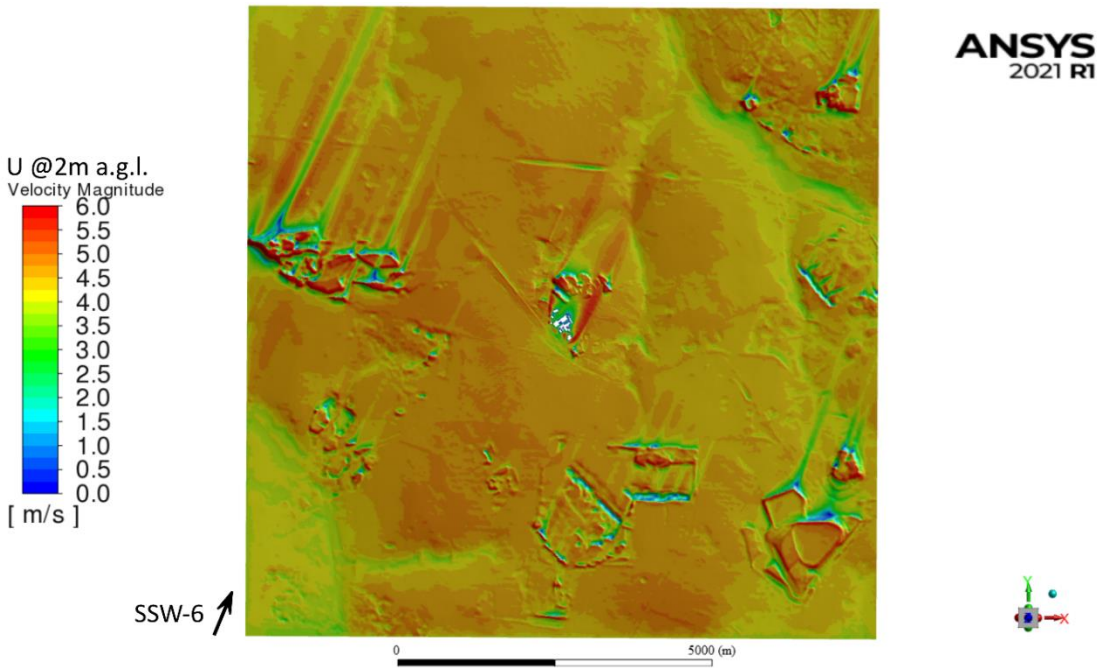

Figure 50. Velocity magnitude (U) at 2 m height AGL over the entire domain for the SSW-6 case.

Figure 50 shows the wind speed at 2 m height AGL for the high reference wind speed case. The same general trends are observed as at 10 m height AGL, except that the general velocity is slower closer to the terrain surface. A phenomenon that is more visible closer to the ground, in this case, is the wind diversion and subsequent relative flow speed-up that occurs as the flow moves around the outer parts of the smelter complex buildings. This speed-up is more noticeable closer to the ground because the buildings present a larger cross-section closer to the ground, forcing the flow laterally and upwards to bypass the building complex.

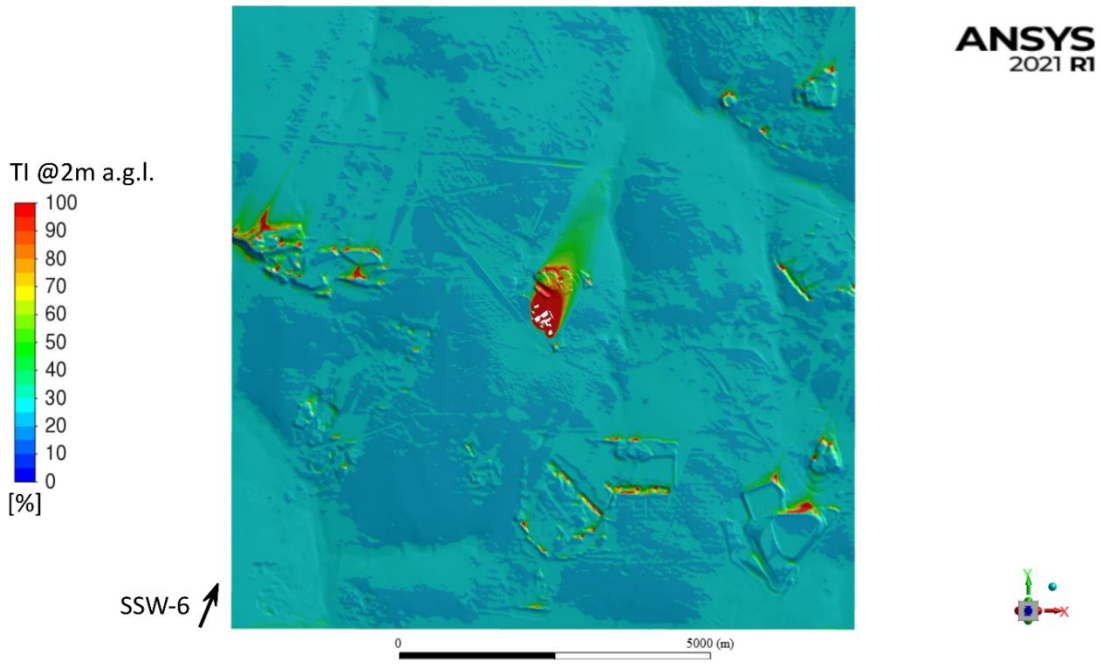

Figure 51. Turbulence Intensity (TI) at 2 m height AGL over the entire domain for the SSW-6 case.

The turbulence intensity, *TI*, is used in Figure 51 to display the levels of turbulent fluctuation in the flow at 2 m height AGL. Turbulence intensity is used instead of the turbulent kinetic energy because percentages are easier to interpret than the turbulent kinetic energy values, even though the same pattern would be observed. The *TI* is calculated using Eq. 48 with the local cell velocity magnitude, U_{local}, this has to be done because the *TI* is calculated with U = 1 m/s by default.

$$TI = \frac{TI_{ref=1m/s}}{U_{local}} \qquad \text{Eq. 48}$$

The turbulence intensity map immediately reveals the high velocity fluctuation that the bluff bodies of the building complex cause in the flow. There is also an extended wake region where large velocity fluctuations occur. Even though some of the slag heaps or materials piles in the periphery of the domain rival the smelter buildings in height, they do not have the same effects on the flow because they are characterised by smooth gradients, whereas the buildings present sharp edges to the flow. The rest of the domain shows comparatively lower levels of turbulence at this height.

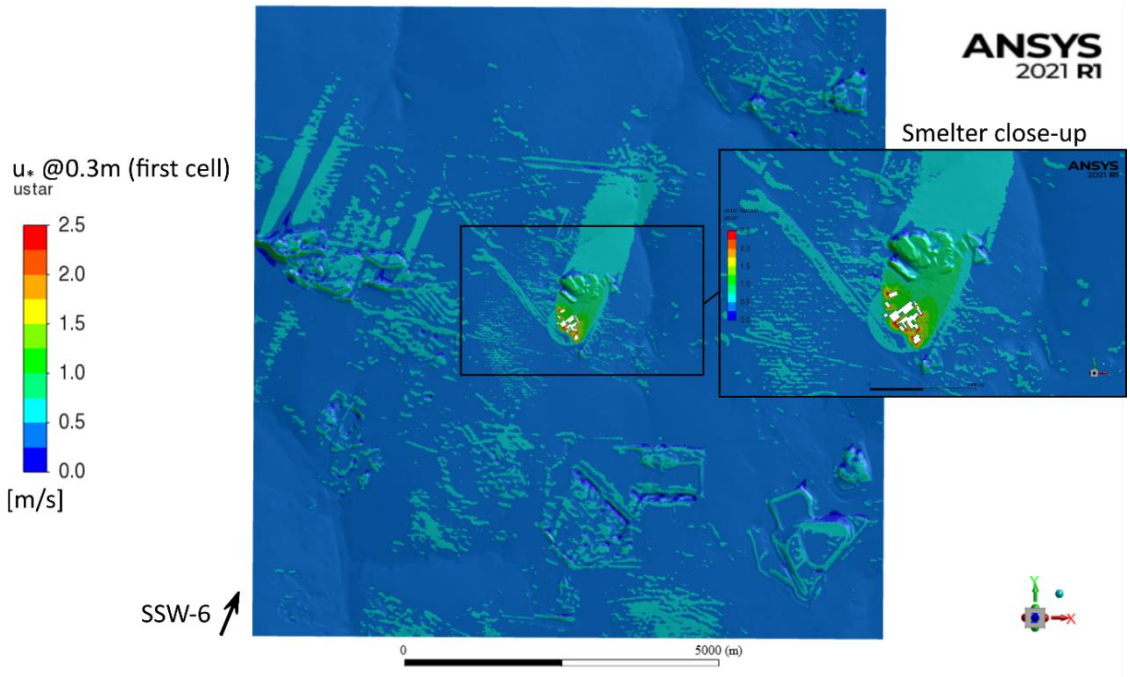

Figure 52. Friction velocity at 0.3 m height AGL (the first cell centroid) above the terrain for the SSW-6 case.

The friction velocity is displayed in Figure 52 in the first cell centroid above the terrain at 0.3 m for the high reference wind speed case. The friction velocity is of interest because it indicates the steepness of the velocity gradient at ground level and thus also the wall shear stress to which it is proportional in a quadratic sense, all of which can affect dust erosion. Taking a closer look at the friction velocity in the area of the smelter building complex as highlighted in the zoomed area of Figure 52, a circular shape becomes apparent where the friction velocity is slightly higher upstream of the building compared to the surrounding upstream flow. This circular region directly corresponds to the BIA region where C_μ is kept fixed to prevent solver instabilities. The friction velocity is expected to be slightly higher because the fixed C_μ in the BIA region, which means that the turbulent viscosity is also expected to be slightly higher relative to the directly surrounding flow, resulting in an increased wall shear stress and hence friction velocity. This effect is not of concern, however, because it is marginal and is not expected to have a significant bearing on the outcomes of the dispersion study.

5.8.2 SSW-3 case

This subsection shows the corresponding *SSW-3* low reference wind speed case to the *SSW-6* case presented in the preceding section. The results are presented with less discussion since some of the noteworthy phenomena are similar.

Figure 53 presents a different flow-field when compared to Figure 49, which presented the case for a higher reference velocity. The same general speed-up of flow is observed over the central part of the domain, but the relative velocity speed-up is less pronounced when compared to the *SSW-6* case. The velocity deficits in the wake regions of obstacles, especially the materials piles, are not as pronounced when compared to the higher reference velocity case.

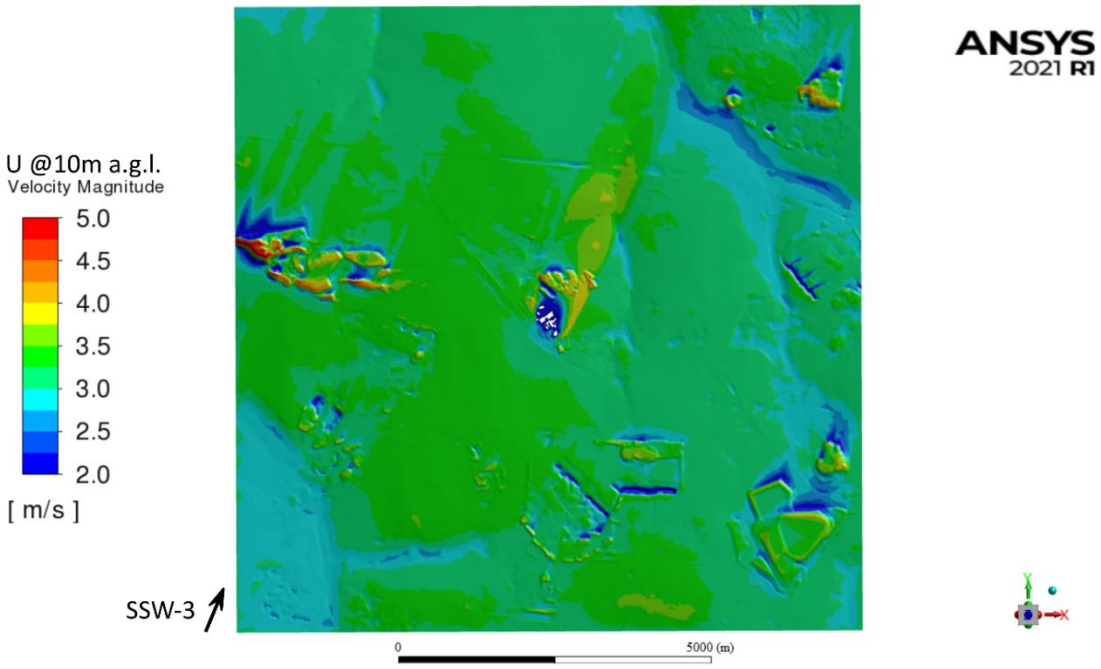

Figure 53. Velocity magnitude (U) at 10 m height AGL over the entire domain for the SSW-3 case.

A flow stagnation region in front of the smelter building complex also becomes more visible for this low reference velocity case. In this case, there are two yellowed regions downstream of the smelter complex that have a relatively higher velocity than the surrounding flow, visible in Figure 53. These are attributed to the variation in terrain height at those locations and the height difference of the buildings and slag heap that the flow is presented with.

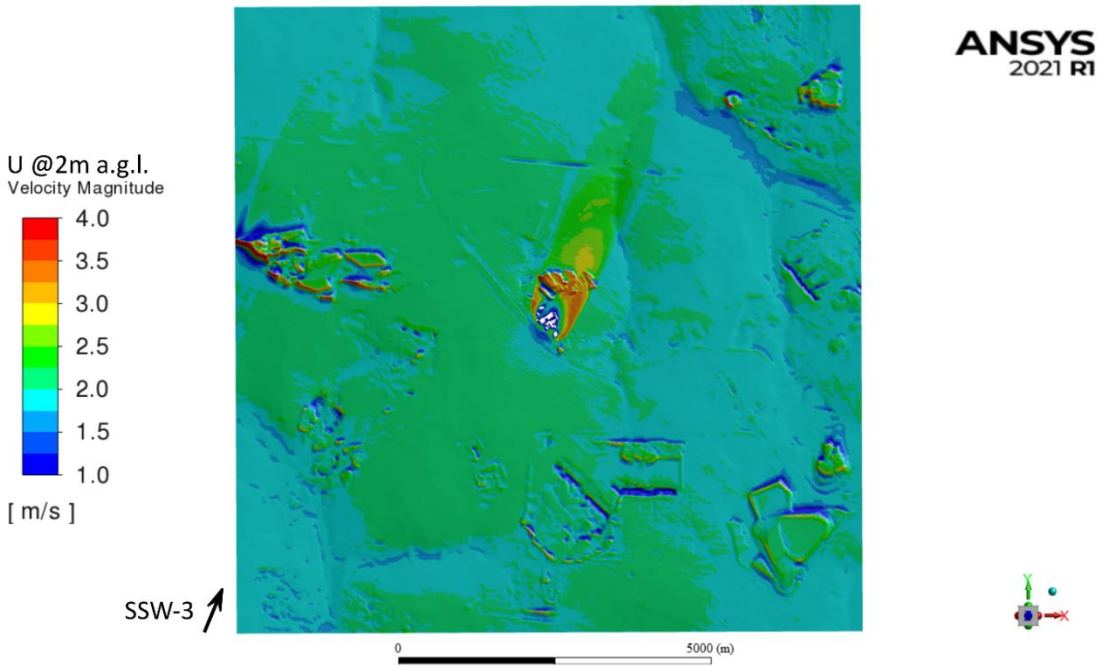

Figure 54. Velocity magnitude (U) at 2 m height AGL over the entire domain for the SSW-3 case.

Figure 54 presents the wind velocity magnitude at 2 m height AGL. Like Figure 53, an uneven velocity distribution is observed in the wake region but is less pronounced because it is closer to the ground, where flow retarding surface effects are stronger.

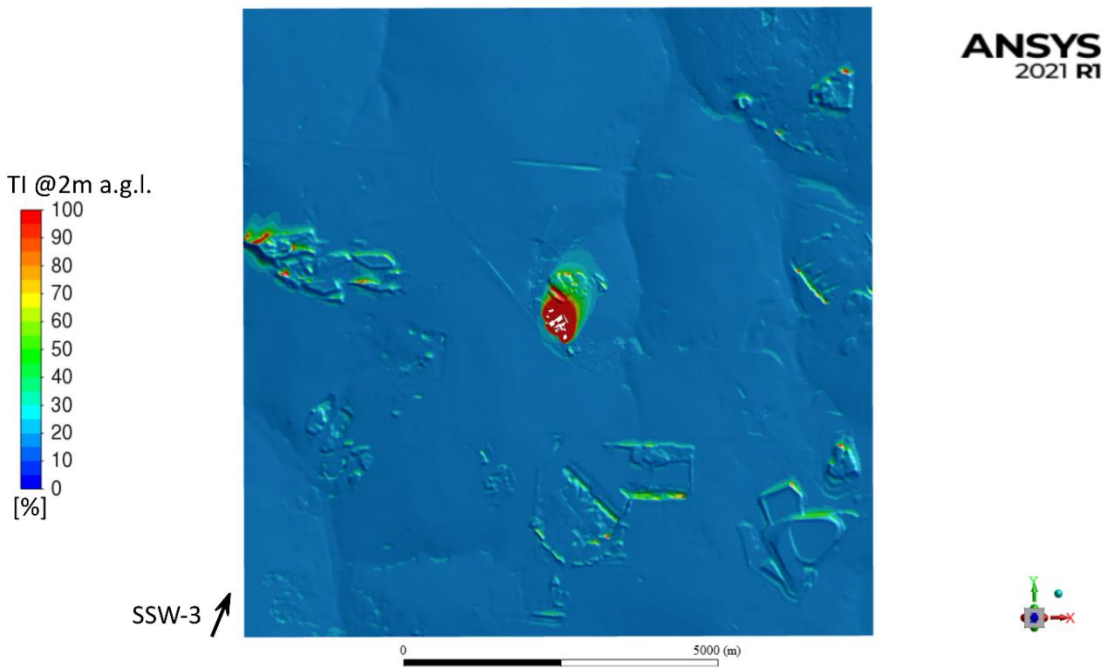

Figure 55. TI at 2 m height AGL over the entire domain for the SSW-3 case.

Figure 55 shows that the *TI* is generally lower for the low reference velocity case (i.e., (20-to-25) % for the high wind speed case, versus (10-to-15) % for the low wind speed case).

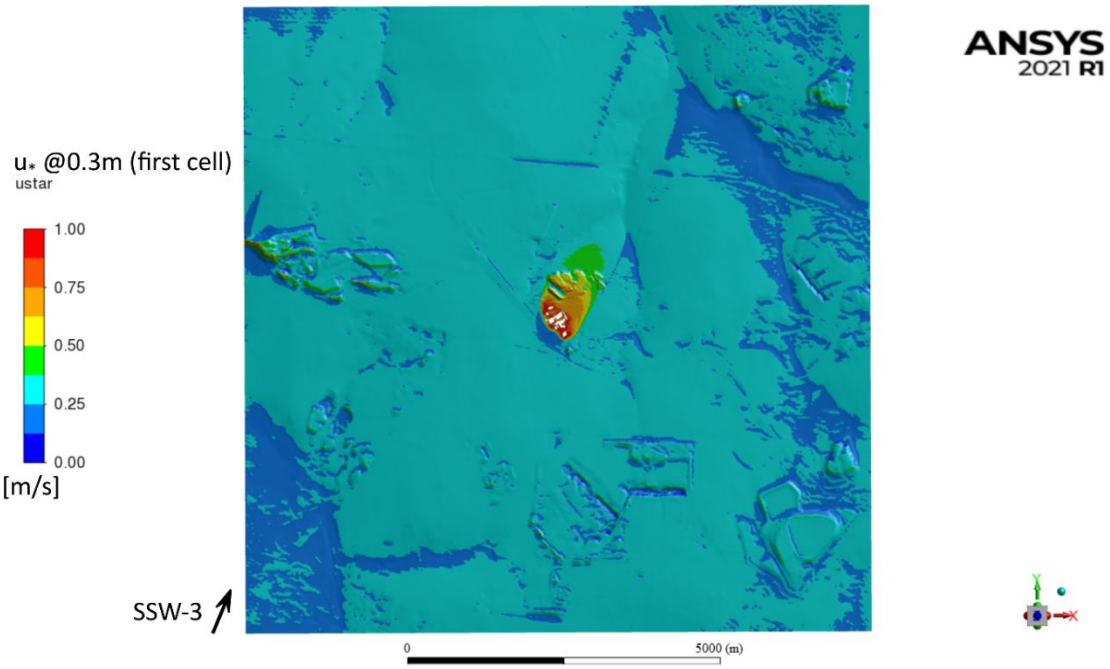

Figure 56. Friction velocity at 0.3 m height AGL (the first ell centroid) above the terrain for the SSW-3 case.

Figure 56 shows the friction velocity in the first cell above the terrain. The effect of the constant C_μ in the BIA region discussed for the high wind speed case in Figure 52, is much less visible for the low-wind speed case.

5.8.3 General comments on flow-fields for high and low reference velocities

The high reference velocity validation case *SSW-6* was presented first, followed by the low reference wind speed case *SSW-3* for the same wind direction. The different flow patterns that emerge from the two cases are a confirmation that the specific choices of high and low reference velocity values are good choices because the flow-fields are sufficiently different, representing sufficiently different scenarios.

The results indicate that the dispersion simulations to be presented in the next chapter are not expected to yield straightforward, uniform dispersion and deposition distributions because of the unique influence that the upstream terrain, smelter buildings and slag heap has on the local flow. Furthermore, the dust dispersion distribution is expected to be wider in the high wind speed case because of the increased levels of turbulence.

The results presented for these two cases, *SSW-6* and *SSW-3*, are an example of the results obtained from the simulation of all the other wind direction and reference velocity cases mentioned in Table 6. The outcomes of the other cases are used for the following chapter in a weighted sense, but the results are not directly displayed in the interest of space.

5.9 Summary

The neutral ABL k-ϵ RANS turbulence model modifications have been implemented, validated, and demonstrated for priority wind speed and direction cases. The atmospheric flow has been simulated for all of the identified cases, and some results have been highlighted. These CFD results can now be used to feed the dust dispersion simulations of the following chapter.

6 Dust Dispersion at the Transalloys Smelters

The dust dispersion simulations are performed using a Lagrangian stochastic DPM approach as presented in Chapter 2, which is based on the outcomes of the steady-state flow field results obtained in Chapter 5. This chapter describes the dust dispersion simulation setup, evaluates the behaviour and validates the dust dispersion models, and shows the results for dust dispersion and accumulation for a chosen period around the smelter.

6.1 Dust dispersion simulation goals

- Derive appropriate dust dispersion simulation parameters from experimental dust characterisation data
- Validate the Lagrangian stochastic DPM method against dust characterisation data of soiled mirror dust samples
- Simulate dust dispersion and accretion patterns around the Transalloys smelter corresponding to one reflectance sampling period
- Combine the accretion results for the priority test cases in such a way as to represent the accretion pattern corresponding to the chosen mirror reflectance sampling period
- Evaluate the performance of the demonstrated CFD-DPM approach against experimental soiling data

All DPM simulations are performed using ANSYS Fluent 2021R1, with some of the post-processing being performed in earlier versions of ANSYS CFD-Post. The dust deposition maps were post-processed in ParaView-5.10.0-RC1.

6.2 Validation of dispersion model

This section validates the use of the Lagrangian stochastic DPM, as described in Section 2.5, against the dust data measured at the Transalloys site.

6.2.1 Boundary conditions and setup

DPM simulations require the specification of additional BCs and input parameters. The choice of available BCs to be made at existing BCs are the trap, reflect or escape BCs (ANSYS Inc., 2021) pertaining to the particles. The BCs of relevance to this investigation are the trap condition specified on the terrain, the reflect condition specified on the building faces and the escape condition specified on the inlets and outlets of the computational domain. The assumption is made that these BCs are perfect and ideal, i.e., 100 % trapping and reflection is enforced on the respective boundaries. This combination of BCs allows for the calculation of the dust particle deposition downstream of the injection surface, the reflection of particles off the building faces, and the escape of tiny particles that remain in the airstream.

An injection point or surface must also be specified from which the particles are introduced into the domain. In this case, it is appropriate to specify an injection surface with relevant injection parameters. Relevant injection parameters can be derived from the dust characterisation data collected from the dust deposition samplers during the experimental campaign at the Transalloys site (as described in Chapter 3). ANSYS Fluent can take a distribution of particle sizes in the form of a Rosin-Rammler (RR)

distribution (ANSYS Inc., 2021). Thus, the measured dust data are put into the appropriate form, and an RR distribution equation is fit to the measured data. More detail of this process can be found in Appendix I.

6.2.2 Validation simulations

A random-walk (stochastic) method is used to perturb a particle track in such a way as to mimic the path that a particle is likely to travel in a turbulent air stream. To illustrate this effect, two simulations were performed using an arbitrarily specified upstream particle injection surface. The results are displayed in Figure 57 as an illustration of the difference between the random-walk particle tracking and the default deterministic approach.

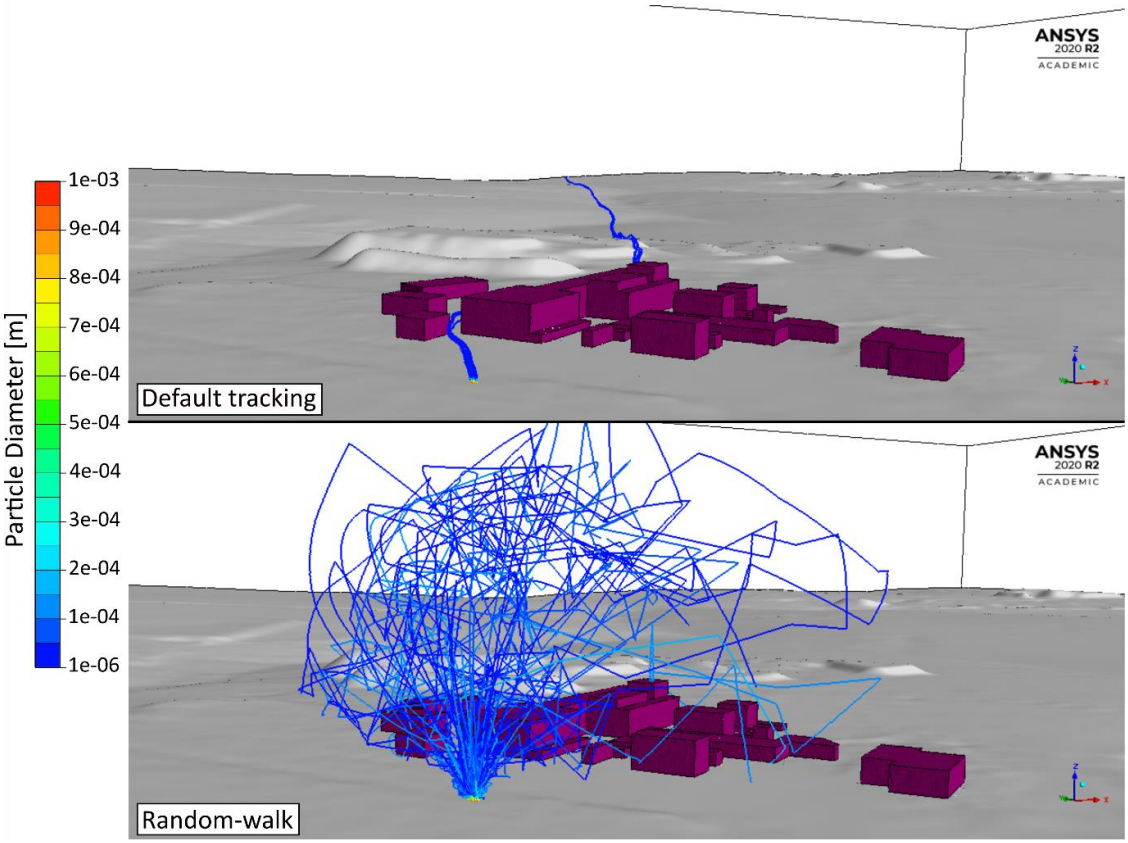

Figure 57. Comparison of default particle tracking and random-walk particle tracking method for the SSW-6 case.

Figure 57 shows that the random-walk method is likely to represent a particle in a turbulent air stream more realistically than that of the default tracking approach, which follows the streamlines of the flow for the most part and settles out in a deterministic fashion based on the forces acting on it. Particle dispersion is stochastic by nature and the random-walk method works for this. A good approach is, therefore, to perform a sufficient number of particle releases (tries) so that meaningful statistics can be drawn from the simulated sample size.

Figure 58 shows the behaviour of the particle plume after injection at two different arbitrary locations upstream of the building complex. The one location is just before the flow stagnation region in front of the building complex, already exposed in Figure 57, and the other is placed such that the particles will not directly cross the BIA region. The two different tracks eventually develop similar plume widths given enough downstream travel, but the increased turbulence intensity and flow re-direction in the BIA

region speeds up the lateral and vertical dispersion significantly (i.e., by roughly 1900 m, as shown in Figure 58).

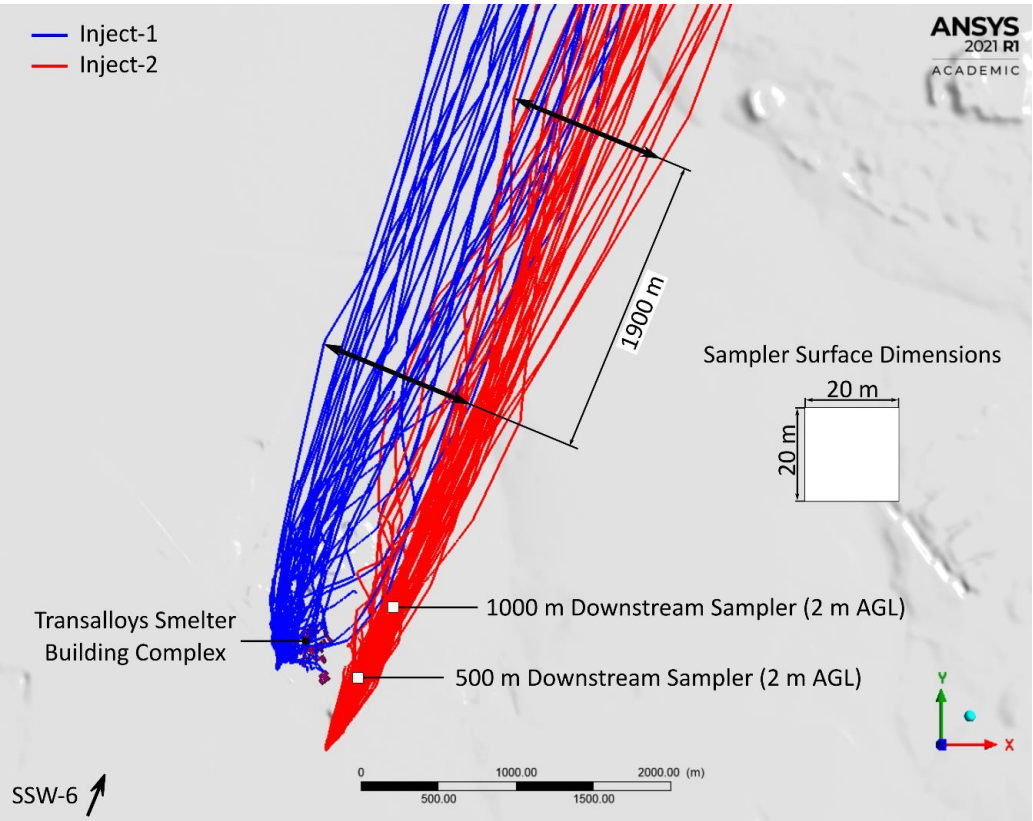

Figure 58. Effect of an obstacle immediately downstream of an injection compared to that of a relatively undisturbed particle stream.

The particle traces shown by the injections in Figure 58 are accompanied by the calculation of an accretion (deposition) trail, where the particles deposit on the terrain. A mean accretion trail is created in ANSYS Fluent by internal averaging of particle accretion rates for each stochastic release. This accretion trail can be used as an indicator for solar field soiling potential, as will be illustrated later.

An important step in the validation of the DPM modelling is to determine how many stochastic tries will result in a sufficient number of particles being transported to a region of interest to achieve the desired outcome. In this case, it is important to recover a realistic representation of the measured dust PSD (500 to 1000) m downstream of the dust injection location. Therefore, to find the appropriate number of releases or tries, two sampling surfaces are specified 500 m and 1000 m downstream of *Inject-2* as shown in Figure 58, both at the same height AGL as the reflectors in the reflector sampling sets (i.e., 2 m height AGL). The samplers are horizontally oriented and have a selected size of 20 m by 20 m. The sampler size implies that the validation will only be valid down to a horizontal resolution of 20 m, which is deemed to be sufficiently accurate given that a CST plant's heliostat field will be at least 100 m across (see solar field size indication in Chapter 7).

One stochastic try injects a certain number of particles, depending on the injection mass and the injection surface area. For *Inject-2*, e.g., 500 particles are released per try. The number of tries is increased systematically from 10 tries to 640,000 tries. A tabulated form of the sequential particle injections and sampled result summaries is given in Appendix J, and the graphs representing these are given here. Figure 59 shows the number of tries together with the mean of the sampled particles.

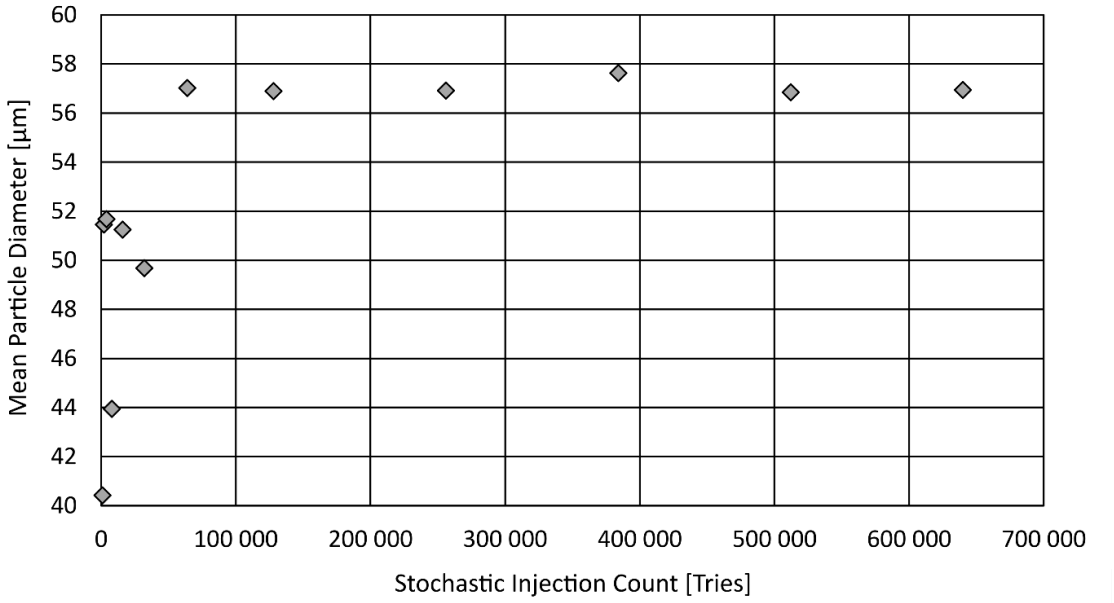

Figure 59. Resulting sampled particle mean diameter from an increasing number of stochastic tries, released from 'Inject-2' and sampled at 1000 m downstream.

Figure 59 shows that, from 64,000 tries onwards, the sampled mean particle diameter passing through the 20×20 m^2 sampler area at 1000 m downstream does not change much. However, the mean is a good first indicator but does not give an indication whether the desired distribution of particle sizes are present at the sampling location. Figure 60 displays the sampled results for 16,000 tries onwards to illustrate how the distribution varies with an increasing number of stochastic injection tries.

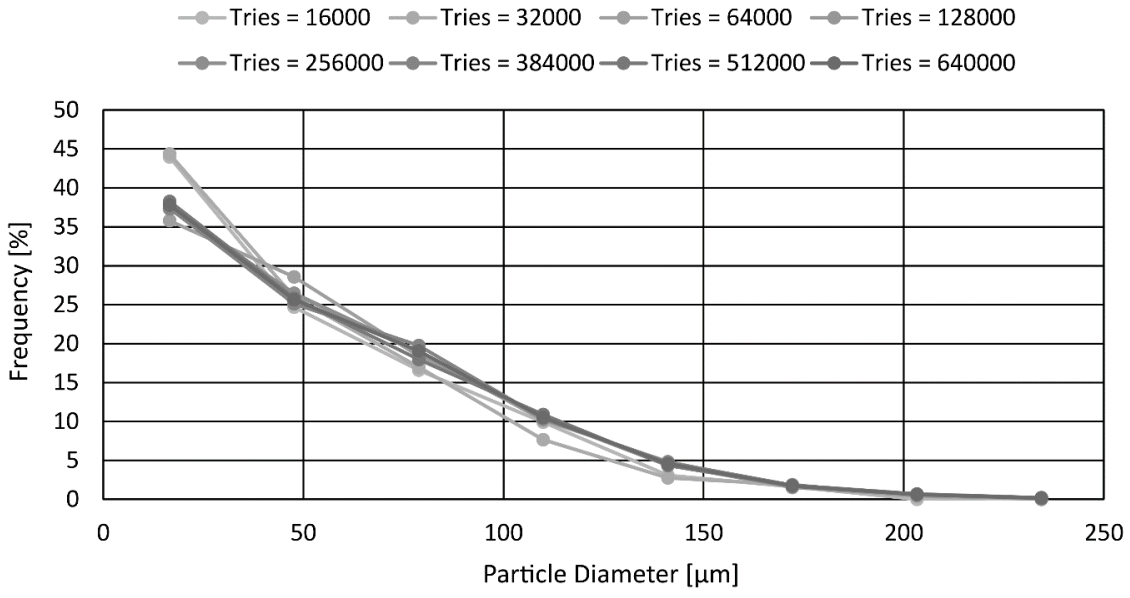

Figure 60. Probability densities of particle sizes sampled at 1000 m downstream of 'Inject-2' for an increasing number of stochastic tries.

Figure 60 shows that the PSD for the number of tries converge towards a distribution and is taken to be converged from 128,000 tries and upwards. As a result, 128,000 tries are used going forward in this subsection.

It is expected that a change in reference velocity (3 m/s vs. 6 m/s) will result in different PSDs when sampled at given distances downstream of an injection point; this is illustrated by Figure 61.

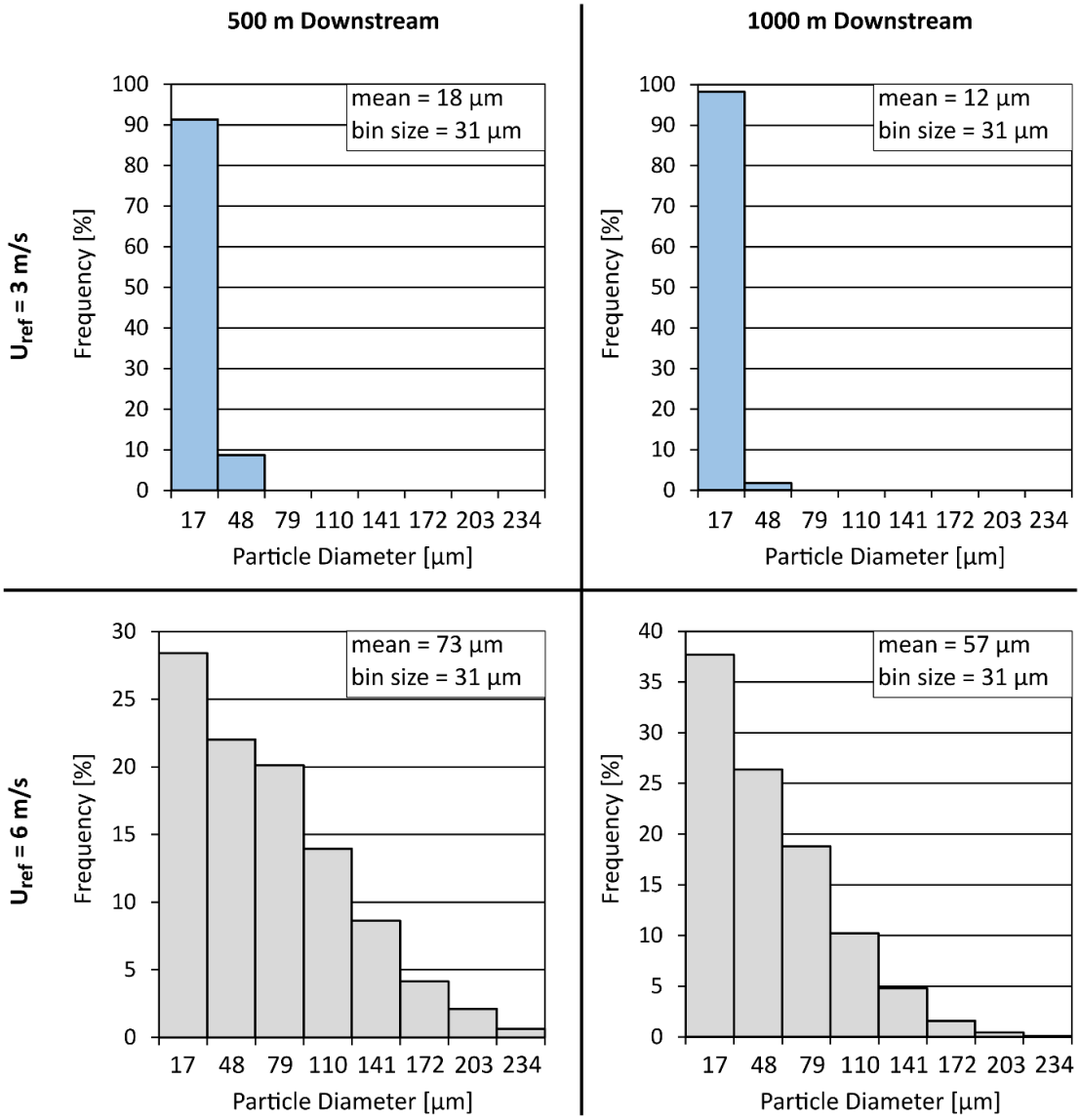

Figure 61. Particle diameter distributions sampled at 500 m and 1000 m downstream of 'Inject-2', at the two different reference velocities of 3 m/s and 6 m/s.

Figure 61 shows the comparison of PSD sampled at 500 m and 1000 m downstream of *Inject-2* for the two chosen reference velocities. It can be seen that a reference velocity of 3 m/s is not able to transport any particles larger than ~ 80 µm, whereas a reference velocity of 6 m/s results in the transportation of particles up to ~ 250 µm. The difference is also reflected in the mean particle diameters and distributions for the various samples, noting that the change in sampled PSD with distance downstream is more pronounced for the higher reference velocity than for the lower reference velocity (as emphasised by the vertical-axis scaling).

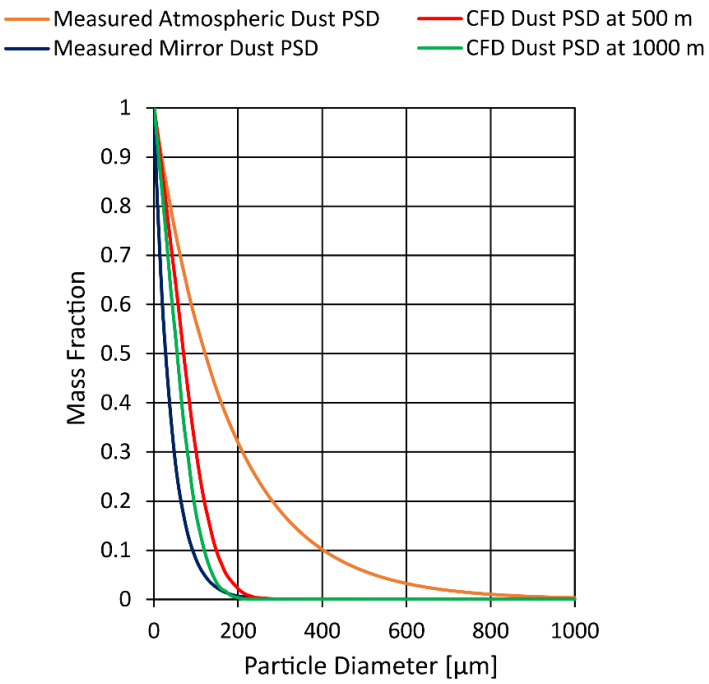

Figure 62. Comparison of experimentally collected dust PSDs for mirror and dust deposition samplers, and numerically sampled dust PSDs at 500 m and 1000 m downstream of Inject-2, for the SSW-6 case. PSDs are displayed in Rosin-Rammler distribution format.

Figure 62 shows that the injected PSD of *Inject-2*, the RR-fit to the atmospheric dust PSD data, is not retrieved at the 500 m downstream sampler nor the 1000 m downstream sampler. This result implies that wind speeds higher than that produced by the high reference velocity case (U_{ref} = 6 m/s) are responsible for spreading the larger particles or that the larger particles present in the experimental sample are less dense than the numerically simulated SiO_2 particles. The retrieved PSDs at both samplers do however approximate the PSD of the experimentally collected mirror dust data, showing that the injection method and parameters are valid for further use in this case. If the goal were to recover a PSD approximating that of the total atmospheric dust sample, then more simulations would be required, including other particle densities or higher wind reference velocity cases. A comparison of the effects of particle density on numerically sampled PSD is given in Appendix K for completeness.

6.3 Dust Accretion Corresponding to one Reflectance Sampling Period at Transalloys

With the behaviour of dust dispersion using a Lagrangian stochastic DPM method in ANSYS Fluent now validated for use in the case of dispersing dust at the Transalloys site as it relates to solar reflector soiling, the validated method can now be used to assess cumulative dispersion and accretion for the different simulation cases listed in Table 6.

This section describes the case setup for the dispersion scenario of interest, followed by an additional sensitivity study, ending with the cumulative weighted dust accretion corresponding to soiling sampling *Period-D*.

6.3.1 Setup of case

The dust reservoir region, hypothesised in Section 3.4, loosely overlapping with the *Major-Source* area specified in Figure 22, is used as the dust particle injection surface for this case since it was identified

that the dust reservoir is the most likely source of most of the dust. The dust reservoir is specified as a horizontally-oriented surface in the immediate area of the central buildings in the smelter building complex (highlighted in salmon orange in Figure 63), at an average height of ~ 1 m above the ground. The created surface is shown in a top view of the smelter building complex along with the terrain surface mesh in Figure 63.

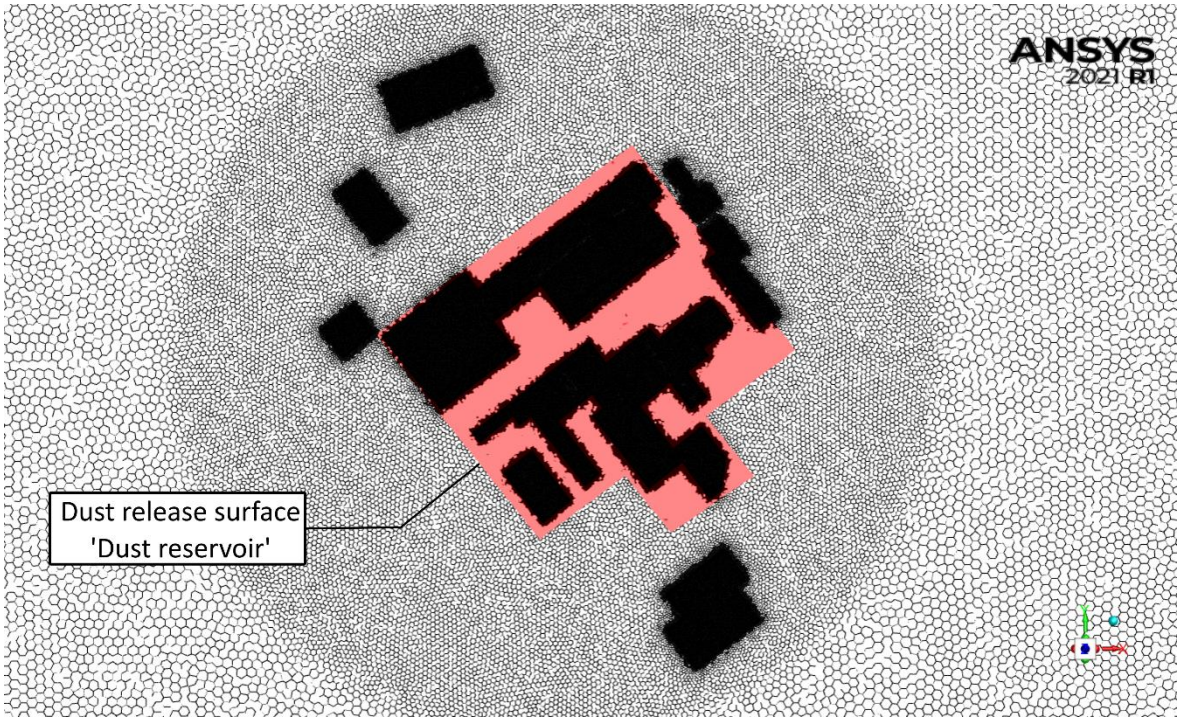

Figure 63. Top view of the smelter building complex with dust reservoir particle injection surface shown in red, located ~ 1 m height AGL.

Since the PSDs of the experimentally collected mirror dust samples are recovered up to 1000 m downstream of the test injection, *Inject-2*, it stands to reason that a similar distribution will be recovered for the following 1000 m downstream as well, skewing towards more smaller particles as the distance downstream increases. A sampling band of interest is defined radially around the smelter complex based on the following reasoning: locating a CST plant closer than 500 m to the smelter complex would result in untenable amounts of reflector soiling. Additionally, locating a CST plant further than ~ 1500 m downstream can result in unacceptable heat losses (i.e., see Gobereit *et al.* (2015) who propose transporting the heated particles using a system of containers over ~ 1000 m distances).

To simplify the simulation further and to lessen the computational load, only the PSD recovered for the mirror dust data is used to define the particle injection from the dust reservoir surface since the larger particles are not transported into the donut-shaped band of interest. The injection is summarised in Appendix L.

6.3.2 Accretion pattern sensitivity study

It has already been shown that, given the correct DPM inputs, the desired dust PSD can be achieved, but it takes many stochastic tries to achieve this. It may not, however, require as many stochastic tries to find the general accretion pattern that emerges as a result of the dispersion simulations. The large area of the dust reservoir surface results in the release of many more particles per try when compared to *Inject-2*; e.g., 60 stochastic injections from the dust reservoir surface results in the same number of particles tracked when doing 128,000 injections from *Inject-2*. The dust accretion rate is therefore

sampled for an increasing number of stochastic tries starting at 60 tries to assess how the dust accretion pattern changes with the number of stochastic injections. It is advantageous to find the lowest number of tries that produce suitable results because the computational cost goes up in proportion to the number of particles tracked. Figure 64 shows the result of four accretion samples on the band terrain area of interest surrounding the smelter complex. The sampling region takes the shape of a donut ring centred on the smelter with attention being paid downstream of the SSW wind direction.

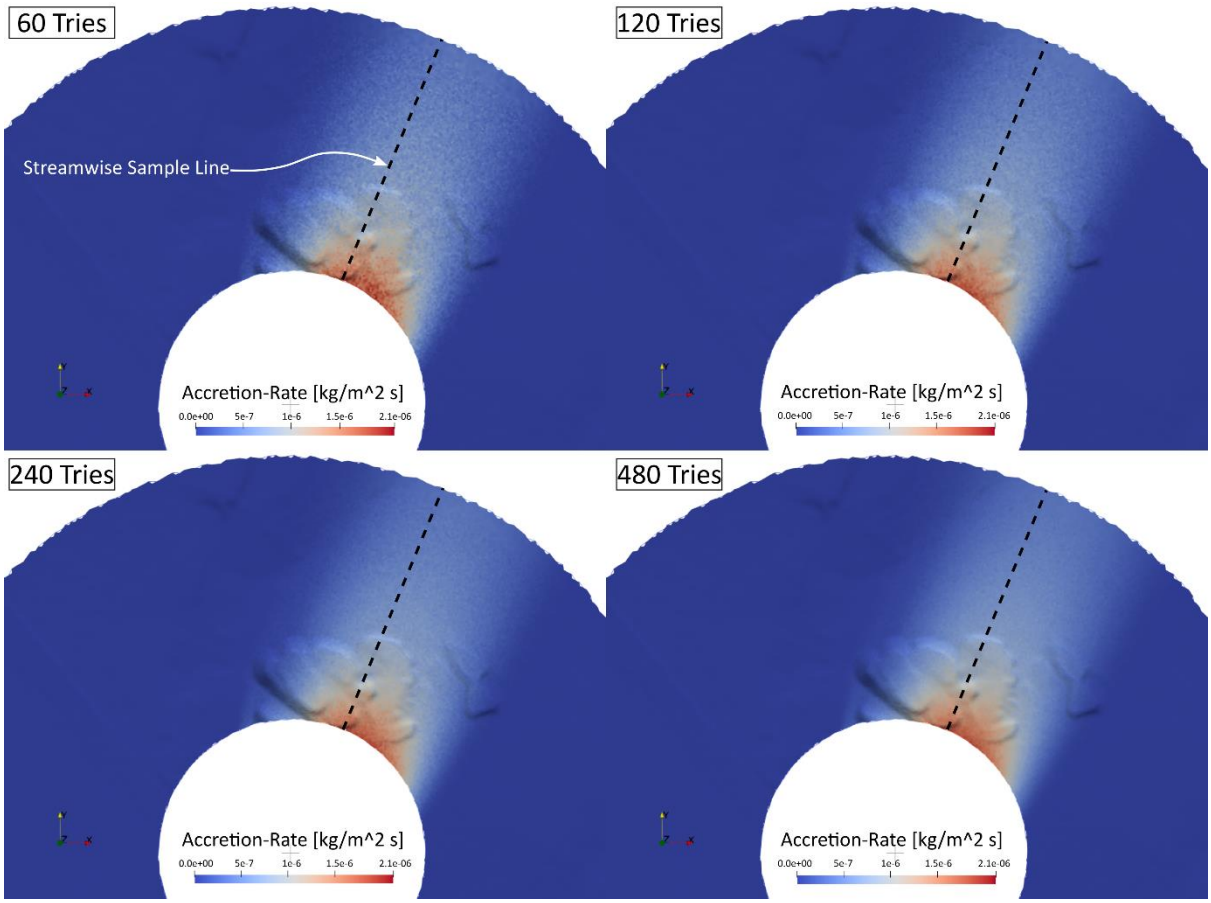

Figure 64. Dust accretion heat map sensitivity to an increasing number of stochastic tries for the SSW-6 case.

Figure 64 shows that the dust accretion pattern is already captured by 60 tries, becoming smoother with an increasing number of tries. A sample is taken along the line indicated in Figure 64 to quantitatively illustrate the dust accretion sensitivity to an increasing number of tries, the results of which is shown in Figure 65.

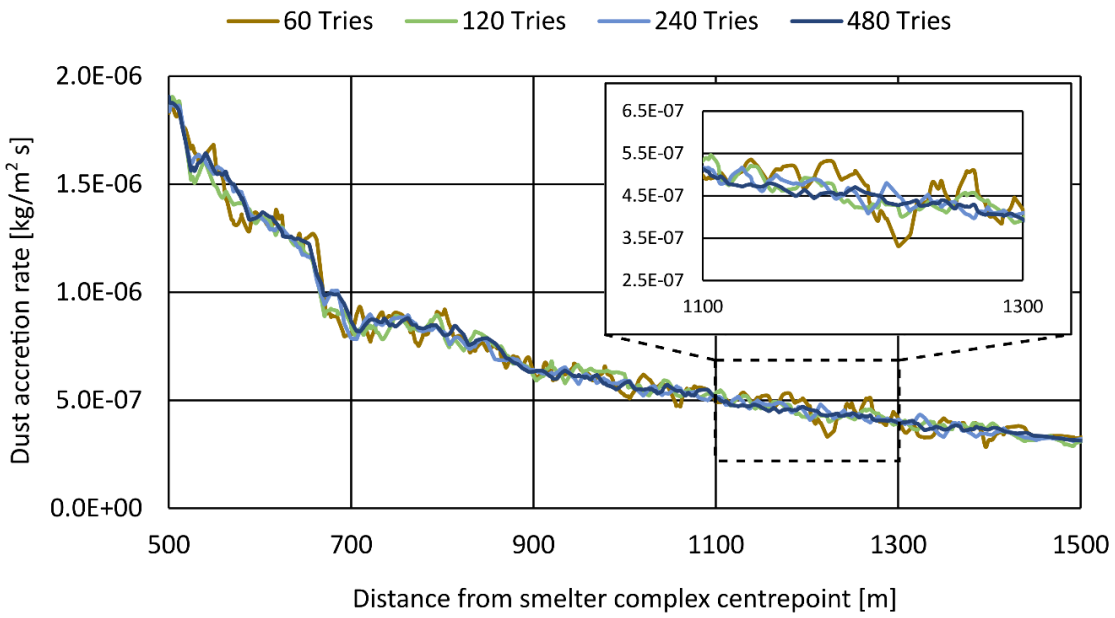

Figure 65. Dust accretion sensitivity to an increasing number of stochastic tries sampled along a streamwise line along the terrain for the SSW-6 case.

Figure 65 shows that the dust accretion trend clearly converges, with an acceptable level of smoothness achieved with 240 stochastic tries. Thus, all DPM simulations performed for the test cases of interest use 240 stochastic tries. The 240 tries result in the release of 157,291,200 particles, of which 92 % are trapped on the terrain and used for the accretion rate calculation, 7.7 % escape, and 0.3 % remain incompletely tracked (i.e., stuck in a building recirculation zone). An additional note to make is that the dust accretion rate decreases with a power-law profile with distance away from the dust reservoir source.

6.3.3 Dust accretion results

The weighting process of the accretion results for the different cases is illustrated in Figure 66 using the *SSW-3* and *SSW-6* cases, then combining the results with the weighting factors based on the frequency of occurrence for the seven wind directions of *Period-D*, specified in Table 6.

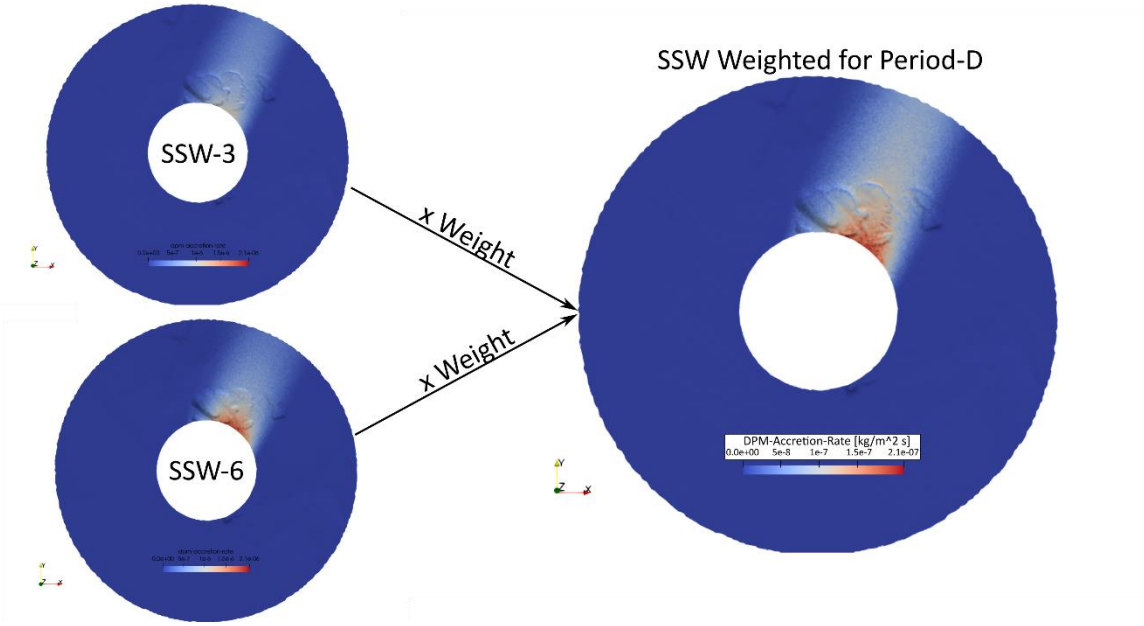

Figure 66. Illustration of result weighting for high and low wind speed categories of SSW wind direction for Period-D. Only 2 of 14 cases in Table 6 are shown on the left of figure as an illustration.

The dust accretion results for each case specified in Table 6 are combined as illustrated in Figure 66 above and presented in Figure 67. It can be seen that the highest accretion rate occurs due to the dominant wind directions, SSW and SW, as expected from Figure 36, however, significant accretion rates are also observed due to the ensemble of south to south-eastern winds in the north-west quadrant where the S3 sampling location is situated. Proximity of the samplers to the smelter complex is also highlighted, with accretion rates diminishing with distance as expected.

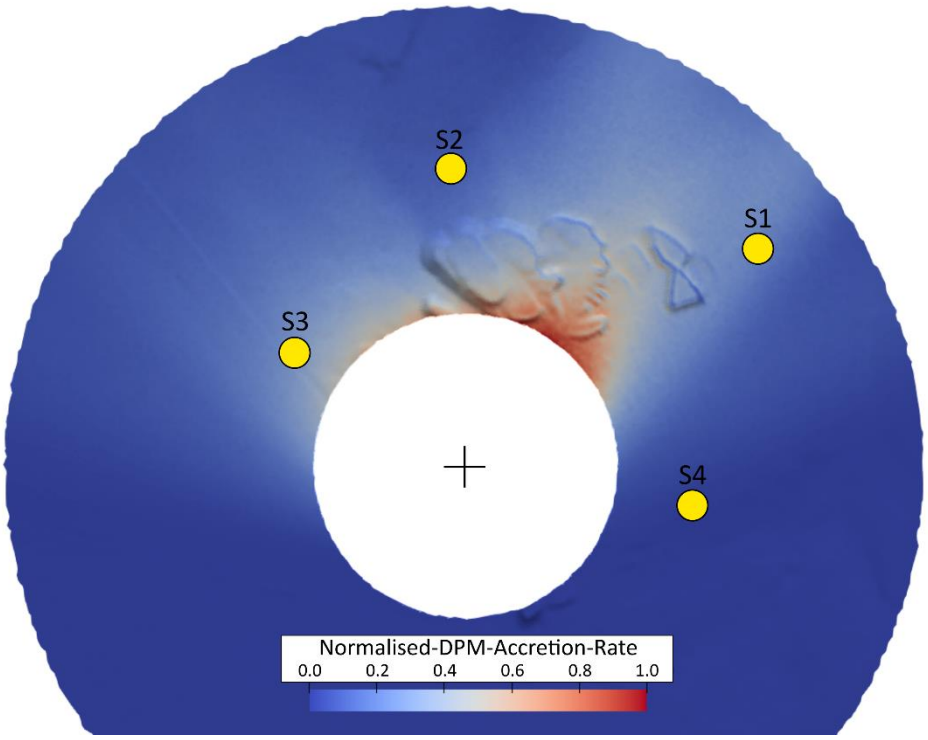

Figure 67. Combined weighted accretion rate (normalised) map for 14 cases in Period-D, for wind speeds 3 and 6 m/s and wind directions WSW, SW, SSW, S, SSE, SE and ESE.

Figure 67 does not contain any results from cases with winds blowing from the northern side of the wind rose. However, in reality, there are minor winds blowing from northern directions, therefore some dust deposition will be present on the southern side. Nevertheless, as a validation exercise, the simulated combined dust accretion map for *Period-D* is sampled at the locations of the sampling sets one, two and three, and then compared to the experimentally determined mirror set soiling rates in a non-dimensional way, the results of which are presented in Figure 68. The simulated accretion rate for sampling set S4 is zero since no northern winds are simulated, thus, only the experimental MDRL is seen.

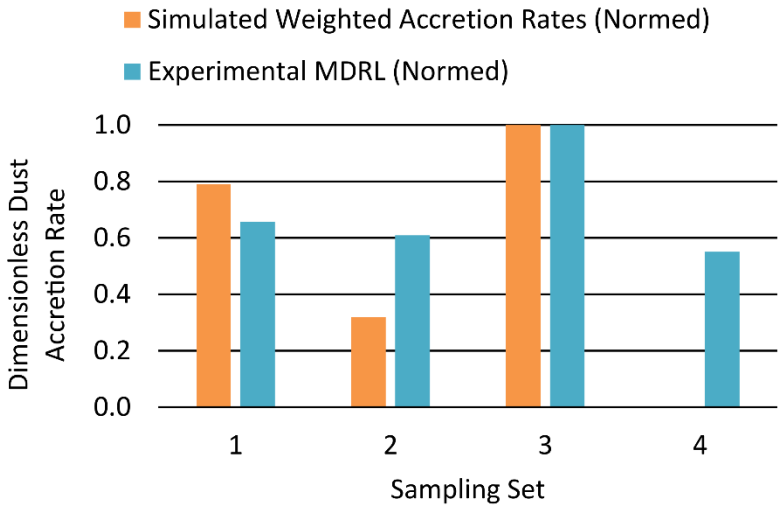

Figure 68. Comparison of normalised experimental and CFD-DPM accretion rates for Period-D.

As evidenced by Figure 68, the outcomes from the dust accretion for *Period-D* closely resemble the experimentally observed soiling trend. Even though the same trends are observed, there is a discrepancy

in the relative closeness of the simulated accretion rate magnitudes of set S1 and S2 when compared to that of the experimental results. Discrepancies are to be expected since the simulation approach only accounts for two wind speeds for any given direction. Another way of displaying the accretion trends is by drawing sampling lines radially outwards from the smelter complex centre through the soiling sampling set locations; this is shown in Figure 69.

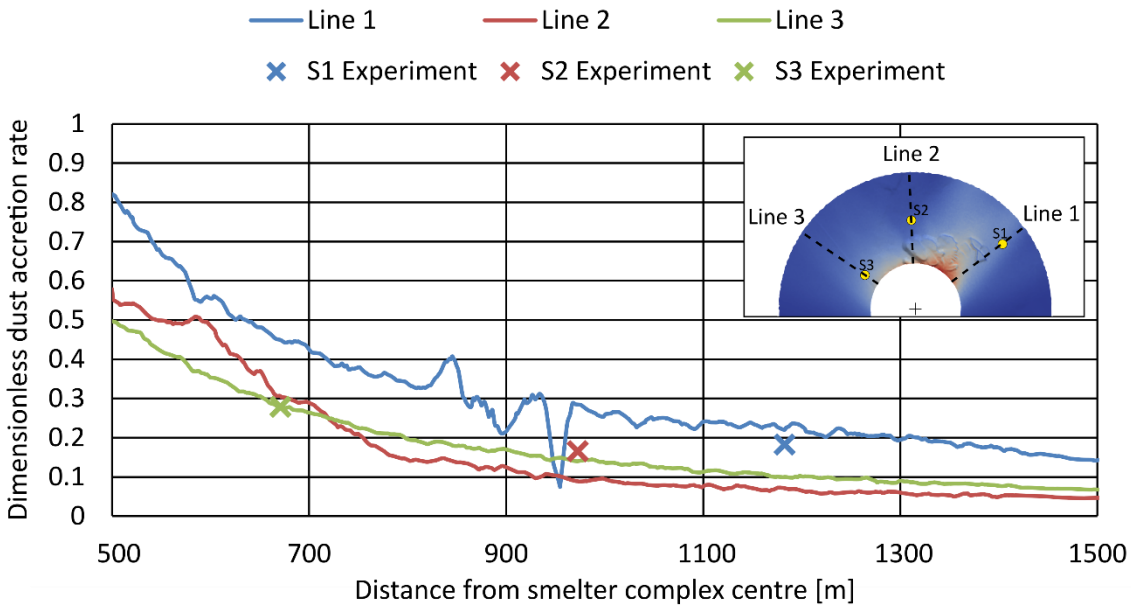

Figure 69. Comparison of radially sampled dust accretion rates (normed) to experimental reflector soiling rates (normed) for Period-D.

The line sample results shown in Figure 69 shows that *Line 1*, which is roughly aligned with the primary and secondary wind directions (i.e., SSW and SW), does, in fact, experience the most dust accretion. Sampling *Line 3* starts off with much lower dust accretion rates but still shows the highest accretion rate when sampled closer to the source relative to the other sampling sets. These displayed results clearly demonstrate the interplay between the sampling location's radial location relative to the dust source and the proximity of the sampling location to the dust source and how this affects the simulated and measured soiling rates.

The local effects of the slag heap can also be seen by looking at *Line 1*. The local peak at 850 m, followed by a local dip at 950 m, respectively, is where the terrain inclination fluctuates sharply. The sudden increase in accretion is seen on the smelter-facing side of the material pile and the sudden drop in accretion is in the wake region of the pile. Interestingly, a closer look at *Line 2* reveals a possible reason for the discrepancy in relative accretion magnitude when comparing the simulated results to the measured results in Figure 68. The location of sampling set S2 is in the wake region of the largest section of the slag heap, which means that most of the dust is expected to blow over in the *S**-*6* case, and most of the dust is expected to deposit on the smelter-facing side of the slag heap in the *S**-*3* case, leaving the dust accretion in the general location of S2 underpredicted. This could potentially be remedied by running additional wind speed cases for the southerly wind direction. Finally, it should also be noted that the simulation results are being compared to only three experimental data points.

It would be advantageous to perform more comparisons of experimental and numerical results since the experimental soiling data do exist. There are two ways in which more comparison could be drawn between numerical and experimental results. The first way would be to follow the demonstrated CFD-

DPM simulation approach for more periods since the soiling data for each of these periods are already captured.

6.4 Summary

Fourteen CFD simulations were performed for the identified priority simulation cases. The outcomes of the CFD simulation were then used to simulate dust dispersion and accretion at the Transalloys smelter complex. The simulation procedures used were validated for the sought outcomes at each step of the way to ensure fit-for-purpose results were obtained. The accretion rates were sampled on a band of interest surrounding the Transalloys smelter where a prospective heliostat field could be placed. It was shown that, when considering the cumulative dust dispersion and accretion over a given time period, that there will be regions of lower soiling potential relative to regions of higher soiling potential. Importantly, it was demonstrated that these regions of high and low soiling potential could be predicted using a CFD-DPM approach.

There is room for improvement in the simulation approach. For instance, given enough time, it would be ideal to simulate all wind directions with at least two reference wind speeds so that a complete picture of the cumulative accretion around the plant can be formed. Using the specified approach against another period of wind and soiling data would also be required to see if the method holds for cases where the soiling was not as extreme as seen for *Period-D* that was investigated.

The total CPU-hours spent on the simulation work at the CHPC was ~ 65,000 hours, on eight nodes with 24 cores each (192 cores total). About 80 % of the time went to setup, validation and testing. Only about 20 % of the CPU-hours spent went to the final runs, which translates to about 13,000 CPU-hours. The final runs comprise of the CFD and DPM simulations that yielded the presented results, each contributing to time spent in roughly equal parts. The CFD runs took 35 real hours (or walltime) and the DPM runs took 42 real hours.

7 Demonstration of CST Site Selection

This chapter serves the practical purpose of demonstrating how to identify candidate CST site(s) in the vicinity of a ferromanganese smelter or any dust-producing EII, for that matter. The site selection method might also be used by any industrial plant that is looking to build a solar PV plant to provide electricity for its operations. The long-term performance of the PV plant will also benefit from proper site selection with regard to solar panel soiling potential.

7.1 Discussion

This dissertation proposes that a key factor in the mitigation of dust at a potential CST plant site (or any solar dependent plant), is to prevent as much soiling from occurring in the first place. This 'design philosophy' is more applicable in situations where there is a suspected 'point' dust source, rather than in a situation where the solar plant is to be sited in an arid region, inside the dust source. The site selection process could be straightforward when considering a site where the wind pattern has a clear, year-round, dominant wind direction and perhaps a secondary direction; in other words, a simple wind rose. However, for a case where the year-round wind patterns are more complicated, such as the investigated site of the Transalloys smelter, the proposed approach could be useful.

Dust source control is an excellent way of reducing the potential of soiling of a solar field, and particularly the source control of smaller PM size fractions which disperse more readily. It is also suggested that the source control first targets the stronger emission source, such as the smelter emissions and the identified dust reservoir in the studied case.

Preventative action can be taken for the dust that does end up being emitted. A realistic approximation of neutral ABL flow can be simulated using steady-state CFD methods, with modified k-ϵ turbulence models. Since the near-field dust dispersion is of interest, looking only at neutral ABL stability conditions is a reasonable simplification. The results of the CFD can then be used in a one-way coupling to simulate dust particle dispersion using a Lagrangian stochastic DPM. It is up to the discretion of the designer how many wind direction and wind speed cases to simulate. At least 12 wind directions are recommended with at least two wind speed cases for each direction, as demonstrated in this study. Furthermore, if a more realistic representation of the dust PSD needs to be obtained further downstream, particularly for larger-sized particles, then a higher reference wind speed as informed by available wind roses needs to be included in the CFD simulation cases. The outcomes of the dust accretion study can then be combined into one accretion map by weighting the different case outputs by the frequency of occurrence of the specific wind speed and direction. The combined weighted dust accretion map for the chosen period can then be used to make an informed decision regarding the best location to site a prospective CST plant.

When using a simulation-based approach, the availability of quality experimental validation data is very important, especially if the model outcomes will be used to make real-world design decisions. In the case of solar field site selection based on soiling potential, on-site wind and dust data for at least one year are required, the former which can be correlated with longer term data at nearby locations, if available. Based on the outcomes of the experimental work in this study, it is recommended that dust data be gathered at different locations around the potential dust source and all sampling locations at an equal distance from the dust source. This will remove proximity to the source as a factor and isolate the directional soiling signal. The case explored in this work used reflectance measurements from mirror samples as a proxy for dust data because of the knowledge that reflectance loss rates are important. If reflectance loss rates are not required for some reason, dust deposition data using sampling buckets can

equivalently be gathered and used. At least one wind mast is required on-site with two different wind measurement heights so that the boundary layer profile and friction velocity can be inferred for the different wind directions. The on-site wind data can be used for validation data and can also be used to derive input boundary conditions for the CFD simulations and provide an estimate of turbulence intensity. Experimental data should be gathered according to the relevant standards.

7.2 Demonstration

A CST plant large enough to sustain an ore pre-heating operation for a 30 MWe ferromanganese smelter is expected to have a heliostat field diameter of ~ 260 m, or a total solar field area of 57,008 m^2, according to work done by Mckechnie, McGregor and Venter (2020) as a part of the PREMA project. A potential heliostat field would ideally not be located closer than ~ 500 m to the smelter complex (dust source), neither can it be located further than ~ 1500 m away; intense soiling and excessive heat losses give rise to these two design limitations.

The cumulative weighted dust accretion map created for the two-week *Period-D*, shown in Figure 67, is considered for this method demonstration. The region south of the smelter is excluded since no northern wind directions were simulated. The reader is reminded that there are various other factors that need to be considered, besides soiling potential, when siting a solar field; these include evenness of terrain, availability of land, existing servitudes due to the operation of the plant, and so on. However, taking only solar field soiling potential and the acceptable distance range away from the smelter into account, and neglecting all other factors, Figure 70 presents three candidate locations for the siting of a CST reflector field.

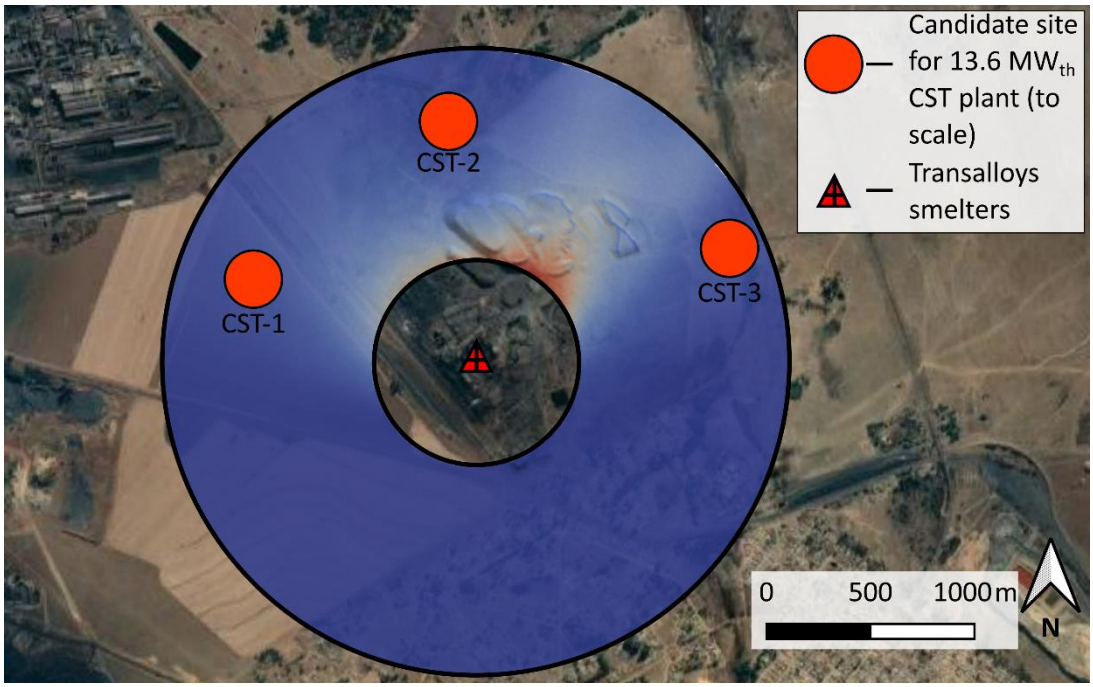

Figure 70. Candidate CST site locations based on outcomes of CFD-DPM simulations, excluding the southern side of the plant for consideration.

Of the three candidate CST sites, each will have their own characteristics. Site *CST-1* has the advantage of being close to an existing railway which could be used to transport the hot particles to the smelter area. The drawback of *CST-1* is that it is closer to a steel plant in the NW corner of the figure, which has not been factored into the investigations and could cause soiling under certain wind conditions. Site

CST-2 is in the wind shadow of the slag heap and is close to the experimental sampling site S2, which was found to experience the least soiling on average throughout the peak soiling season (see Table 4). Site *CST-3* is out of the path of the most serious soiling and on a north-facing slope, adding it to the sites to be considered. If site *CST-1* were ruled out, the choice between *CST-2* and *CST-3* needs to be made based on other factors besides soiling.

This concludes the demonstration of CST, or solar field, site selection based on the outcomes of the CFD-DPM simulation work. It is expected that when all the wind direction and speed cases are considered for the period of an entire year, in addition to all other influential factors, that a clear best candidate solar field site will emerge.

7.3 Applications in industry

The demonstrated heliostat soiling potential CST solar field site selection approach can be added to designers' toolbelts. It is emphasised that the demonstrated approach only considers solar field soiling potential and distance away from the smelter complex as design parameters, however, in reality a CST plant designer will look at numerous other factors when considering where best to site the plant.

When considering supplying solar thermal heat to an energy-intensive metallurgical process, the approach taken will be different when considering the development at greenfield (new) or brownfield (existing) sites. The approach taken at a brownfield site will resemble the approach demonstrated in this work, where the Transalloys smelter was considered as the EII that needs to be supplied with solar thermal heat. In the brownfield case, data about the plant's operations, experimental dust and meteorological data, and data about the surrounding terrain will be most valuable.

For a greenfield site in particular, even more factors would be considered. Let us consider, for example, the development of a new metallurgical beneficiation plant situated close to the mining operation that will supply it, in South Africa. Additionally, this metallurgical plant could benefit greatly from solar thermal process heat. The macro-drivers for the site selection would be the mineral resource and the solar resource. Hockaday (2019) presented a map of the DNI solar resource in South Africa, overlayed with an indication of where the primary mineral fields in South Africa are to be found, as displayed in Figure 71.

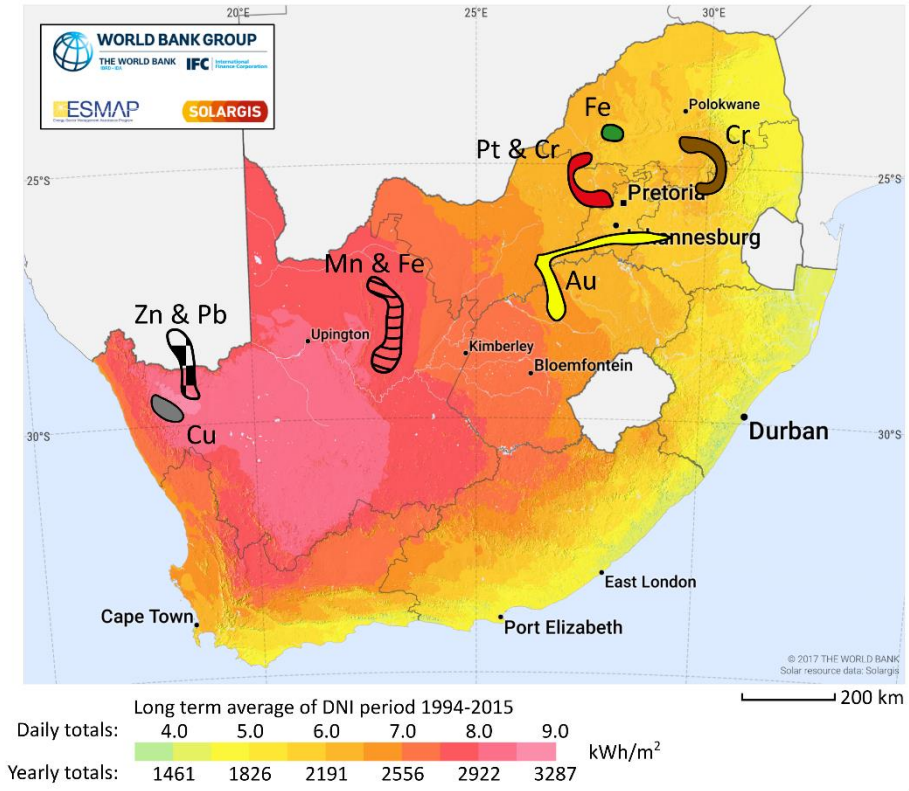

Figure 71. South African DNI solar resource overlaid with rough indication of primary mineral resources. Reproduced from Lina Hockaday (2019) with permission, based on data from Voster and Dixon (2005) and SolarGIS (2019).

Once an appropriate site has been selected, then the approach demonstrated in this work can be followed. Wind and solar data will need to be gathered at the proposed site. It can be assumed that there will be regional dust and that the new minerals beneficiation plant will also produce its own dust, as observed at the Transalloys site. Since the site is only in planning, the designer will not be able to collect the metallurgical dust data required as part of the input to the CFD-DPM simulation models. In this case, it is recommended that the designer gather sample dust data at a similar beneficiation plant and use it as a stand-in for the dust that will actually be produced by the new plant once operational.

This demonstrated solar field site selection approach can be applied to site, or consider the impacts of industrial dust on any solar field or activity that is expected to be sensitive to dust, in the vicinity of an industrial dust source.

8 Conclusions and Recommendations

8.1 Conclusions

The purpose of this research was to investigate the unknowns related to heliostat soiling at a ferromanganese smelter. A two-pronged experimental and numerical approach was adopted to conduct this research.

The experimental work consisted of an 8-month mirror soiling campaign (mirrors used as proxies for heliostats), dust characterisation work of samples collected from the soiled mirrors and from dust deposition gauges, and sampling of on-site wind and rain conditions through a wind mast and a weather station. The outcomes of the experimental work led to the following conclusions:

- A cause-and-effect relationship between wind direction and speed and dust dispersion direction and intensity was observed
- Dust characterisation confirmed that the primary dust source is indeed the smelter
- 90 % of all particles analysed from the soiled mirror samples were smaller than about 100 μm in diameter
- The proximity of the mirror sampling location and the consideration of the relative positioning of the sampling location to the dust source and the prevailing wind direction are both factors in determining where the most soiling will occur
- Mirror soiling is more intense during the dry season; any dust prevention and mitigation approaches should therefore be targeted to work best for the time of year when peak soiling is expected at the given site
- By changing the location relative to the smelter source, a 13 % lower soiling rate was observed at sampling set S2 relative to sampling set S4 averaged over the peak soiling period

A set of large-scale atmospheric flow CFD simulations was conducted for the relevant wind conditions at the Transalloys smelter. A steady-state RANS approach was used, and care was taken to modify, and validate, the standard k-ϵ turbulence model to be suitable for modelling neutral ABL flow. The outcomes of the CFD simulations were used to feed into a Lagrangian stochastic DPM simulation to simulate dust particle dispersion and accretion around the Transalloys smelter site. The accretion rates were used as an indicator of mirror soiling potential for a given location, thus allowing the comparison of experimentally measured soiling rates and simulation accretion rate outputs. The outcomes of the simulation work led to the following conclusions:

- The cumulative accretion pattern produced by the CFD-DPM approach fitted the experimental soiling rate data well for the studied period, with some minor discrepancies in relative magnitude
- The demonstrated CFD-DPM approach made the major simplifying assumption of only simulating two reference wind speeds for each wind direction case and still yielded results comparable to the experimental data, showing that a smart simulation approach is worth pursuing

- The advantage of using a CFD-based approach is that it can provide a complete picture of the flow field and accompanying dispersion-and-accretion patterns, whereas the experimental data obtained could only provide information about specific points in the field of interest
- On-site wind data are required to produce reliable ABL flow simulations

The unknowns posed in the introduction are explicitly answered here:

- What are heliostat soiling rates like in the vicinity of a ferromanganese smelter, and given these soiling rates, would it be feasible to locate a heliostat field in the vicinity of a ferromanganese smelter?

The performance of the different reflector sampling sets over the identified peak soiling period (11/06/2020 – 01/10/2020) was evaluated by assigning performance scores. Sampling set S2 achieved the best score, with a period averaged MDRL of 1.9 %. The 1.9 % observed by S2 is higher than the typical daily performance loss of 0.8 % cited in the literature. It is hard to make statements regarding feasibility purely based on the measured reflectance performance losses. The potential is there to lower the on-site MDRL values by applying existing measures such as the application of anti-soiling coatings. Furthermore, the simulation work outcomes suggest that there are locations around the Transalloys smelter that would experience less soiling on average, given the wind conditions at the site. It is, therefore, safe to say that more work is needed to conclude outright feasibility, but the results of the performed work are auspicious.

- Are there any particulates present in the atmosphere immediately surrounding a ferromanganese smelter that could result in enhanced physical degradation of a heliostat?

The main elemental components found on the mirror samples were confirmed to originate from the ferromanganese smelter. The primary elements (Si, Al, Fe, O, Mn) and the primary mineral phases (SiO_2, $FeSiO_4$, $Al_2O_3.SiO_2$, and $Al_9Fe_2Si_2$) found on the soiled mirror samples do not indicate that there would be a greater potential for heliostat reflective surface degradation when compared to a desert-like region where the main mineral is the sand of the region.

- Is there a location around the smelter complex that will have a lower heliostat soiling potential in comparison to other locations around the smelter?

The combined outcomes of the experimental campaign and the CFD-DPM simulation work showed that there are locations with lower soiling potential relative to locations with higher soiling potential. Furthermore, the approach followed demonstrates that CFD modelling of the ABL coupled with DPM modelling of the dust dispersion can be successfully used to identify these regions with the least soiling potential, with minimal on-site experimental measurements required for validation.

8.2 Recommendations

The demonstrated approach has its limitations. Appropriate experience with CFD tools is required to follow the approach in a time frame typically allotted for a feasibility assessment of the type of CST-EII integration project investigated by PREMA. A shortcoming of the simulation work is that it only investigates a period corresponding to one reflectance sampling period and then compares the experimental and simulation results. More experimental-to-numerical comparisons are needed to assess whether the demonstrated approach is suitable for predicting dust soiling patterns throughout a typical wind year. Furthermore, the approach only considers two reference wind speed conditions for each wind direction, and while this simplifies the study and has its advantages in terms of computational cost

savings, this is also the possible cause of some identified discrepancies between the experimental and simulation results.

In general, the wind mast was not located on-site long enough to get a true representation of the ABL flow profiles. Future work will benefit from wind data gathered over a period longer than one year. The mirror soiling samplers were not located at equal distances from the primary dust source, which means that the wind direction and sampler proximity to source variables could not be isolated properly. Future work should thus endeavour to locate any dust or soiling samplers roughly equal distances away from the plant dust source.

Bibliography

Anfossi, D. *et al.* (2010) 'A new Lagrangian particle model for the simulation of dense gas dispersion', *Atmospheric Environment*, 44(6), pp. 753–762. doi:10.1016/j.atmosenv.2009.11.041.

ANSYS Inc. (2020) 'ANSYS Fluent Theory Guide (2021 R1)'. ANSYS Inc.

ANSYS Inc. (2021) 'ANSYS Fluent User's Guide (2021 R1)'. ANSYS Inc.

Bataille, C. *et al.* (2018) 'A review of technology and policy deep decarbonization pathway options for making energy-intensive industry production consistent with the Paris Agreement', *Journal of Cleaner Production*, 187, pp. 960–973. doi:10.1016/j.jclepro.2018.03.107.

Beranek, W. and Van Koten, H. (1979) 'Visual techniques for the determination of wind environment', *Journal of Wind Engineering and Industrial Aerodynamics*, 4(3–4), pp. 295–306.

Berg, R.S. (1977) 'Survey of mirror-dust interactions', in. United States. Available at: https://www.osti.gov/biblio/7089188.

Berg, R.S. (1978) *Heliostat dust buildup and cleaning studies*. United States. doi:10.2172/6867834.

Blackmon, J.B. and Curcija, M. (1978) 'Heliostat Reflectivity Variations Due To Dust Buildup Under Desert Conditions.', in, pp. 169–183.

Blocken, B., Stathopoulos, T. and Carmeliet, J. (2007) 'CFD simulation of the atmospheric boundary layer: wall function problems', *Atmospheric Environment*, 41, pp. 238–252. doi:10.1016/j.atmosenv.2006.08.019.

Brooks, M.J. *et al.* (2015) 'SAURAN: A new resource for solar radiometric data in Southern Africa', *Journal of Energy in Southern Africa*, 26, pp. 2–10.

Brost, R. and Wyngaard, J. (1978) 'A model study of the stably stratified planetary boundary layer', *Journal of Atmospheric Sciences*, 35(8), pp. 1427–1440.

Buck, R. and Giuliano, S. (2019) 'Solar tower system temperature range optimization for reduced LCOE', in. *SOLARPACES 2018: International Conference on Concentrating Solar Power and Chemical Energy Systems*, Casablanca, Morocco, p. 030010. doi:10.1063/1.5117522.

Celles, S. *et al.* (2020) *Windrose*. Available at: https://github.com/python-windrose/windrose.git.

Costa, S.C.S. *et al.* (2016) 'Dust and soiling issues and impacts relating to solar energy systems: Literature review update for 2012-2015'. doi:10.1016/j.rser.2016.04.059.

Costa, S.C.S., Diniz, A.S.A.C. and Kazmerski, L.L. (2018) 'Solar energy dust and soiling R&D progress: Literature review update for 2016', *Renewable and Sustainable Energy Reviews*, 82, pp. 2504–2536. doi:10.1016/j.rser.2017.09.015.

Davourie, J. *et al.* (2017) 'Evaluation of particulate matter emissions from manganese alloy production using life-cycle assessment', *NeuroToxicology*, 58, pp. 180–186. doi:10.1016/j.neuro.2016.09.015.

DMRE (2021) *Renewable Energy IPP Procurement Programme (REIPPPP) Bid Window 5: Announcement of the Preferred Bidders*. South Africa: Department of Mineral Resources.

Ebert, M. *et al.* (2018) 'First On-Sun Tests of a Centrifugal Particle Receiver System', in *ASME 2018 12th International Conference on Energy Sustainability*. *ASME 2018 12th International Conference on Energy Sustainability collocated with the ASME 2018 Power Conference and the ASME 2018 Nuclear Forum*, Lake Buena Vista, Florida, USA: American Society of Mechanical Engineers, p. V001T11A002. doi:10.1115/ES2018-7166.

Ebert, M. *et al.* (2019) 'Operational experience of a centrifugal particle receiver prototype', in. *SOLARPACES 2018: International Conference on Concentrating Solar Power and Chemical Energy Systems*, Casablanca, Morocco, p. 030018. doi:10.1063/1.5117530.

European Commission (2020) *Proposal for a regulation of the European parliament and of the council establishing the framework for achieving climate nuetrality and amending Regulation (EU) 2018/1999 (European Climate Law)*. EU law COM(2020) 80 final. European Commission.

Farr, T.G. *et al.* (2007) 'The Shuttle Radar Topography Mission', *Reviews of Geophysics*, 45(2), pp. RG2004–RG2004. doi:10.1029/2005RG000183.

Fernández-García, A. *et al.* (2014) 'Study of Different Cleaning Methods for Solar Reflectors Used in CSP Plants', *Energy Procedia*, 49, pp. 80–89. doi:10.1016/J.EGYPRO.2014.03.009.

Fernández-García, A. *et al.* (2017) 'Equipment and methods for measuring reflectance of concentrating solar reflector materials', *Solar Energy Materials and Solar Cells*, 167, pp. 28–52. doi:10.1016/J.SOLMAT.2017.03.036.

Fernández-García, A. *et al.* (2019) 'Durability testing of a newly developed hydrophilic anti-soiling coating for solar reflectors', in. *SOLARPACES 2018: International Conference on Concentrating Solar Power and Chemical Energy Systems*, Casablanca, Morocco, p. 160002. doi:10.1063/1.5117665.

Franke, J. *et al.* (2007) *Best practice guideline for the CFD simulation of flows in the urban environment, COST action*, p. 52. Available at: http://cat.inist.fr/?aModele=afficheN&cpsidt=23892111%5Cnhttp://scholar.google.com/scholar?hl=en&btnG=Search&q=intitle:Best+practice+guideline+for+the+CFD+simulation+of+flows+in+the+urban+environment#0.

Freese, J.M. (1979) 'Effects of Outdoor Exposure on the Solar Reflectance Properties of Silvered Glass Mirrors.', in *Electric Power Research Institute (Report) EPRI EA*, pp. 1340–1344.

GeoSmart (2019) '2 m Digital Elevation Model of South Africa (DEMSA2)'. Available at: https://geosmart.space/products/dsmsa2.html.

Ghazi, S., Sayigh, A. and Ip, K. (2014) 'Dust effect on flat surfaces – A review paper', *Renewable and Sustainable Energy Reviews*, 33, pp. 742–751. doi:10.1016/j.rser.2014.02.016.

Gillette, D.A., Blifford, I.H. and Fryrear, D.W. (1974) 'The influence of wind velocity on the size distributions of aerosols generated by the wind erosion of soils', *Journal of Geophysical Research*, 79(27), pp. 4068–4075. doi:10.1029/JC079i027p04068.

Gobereit, B. *et al.* (2015) 'Cost Analysis of Different Operation Strategies for Falling Particle Receivers', in *Volume 1: Advances in Solar Buildings and Conservation; Climate Control and the Environment; Alternate Fuels and Infrastructure; ARPA-E; Combined Energy Cycles, CHP, CCHP, and Smart Grids; Concentrating Solar Power; Economic, Environmental, and Policy Aspects of Alternate Energy; Geothermal Energy, Harvesting, Ocean Energy and Other Emerging Technologies; Hydrogen Energy Technologies; Low/Zero Emission Power Plants and Carbon Sequestration; Micro and Nano Technology Applications and Materials*. *ASME 2015 9th International Conference on*

Energy Sustainability collocated with the ASME 2015 Power Conference, the ASME 2015 13th International Conference on Fuel Cell Science, Engineering and Technology, and the ASME 2015 Nuclear Forum, San Diego, California, USA: American Society of Mechanical Engineers, p. V001T05A010. doi:10.1115/ES2015-49354.

Gorlé, C. *et al.* (2009) 'CFD modelling of small particle dispersion: The influence of the turbulence kinetic energy in the atmospheric boundary layer', *Atmospheric Environment*, 43(3), pp. 673–681. doi:10.1016/j.atmosenv.2008.09.060.

Gorlé, C., van Beeck, J. and Rambaud, P. (2010) 'Dispersion in the Wake of a Rectangular Building: Validation of Two Reynolds-Averaged Navier–Stokes Modelling Approaches', *Boundary-Layer Meteorology*, 137(1), pp. 115–133. doi:10.1007/s10546-010-9521-0.

Gorlé, C., Van Beeck, J. and Rambaud, P. (2009) 'RANS CFD modelling of particle dispersion behind a rectangular building in the atmospheric boundary layer', in *5th European and African Conference on Wind Engineering, EACWE 5, Proceedings*.

Griffith, D.J., Vhengani, L. and Maliage, M. (2014) 'Measurements of Mirror Soiling at a Candidate CSP Site', *Energy Procedia*, 49, pp. 1371–1378. doi:10.1016/j.egypro.2014.03.146.

Hanna, S. *et al.* (2011) 'Comparisons of JU2003 observations with four diagnostic urban wind flow and Lagrangian particle dispersion models', *Atmospheric Environment*, 45(24), pp. 4073–4081. doi:10.1016/j.atmosenv.2011.03.058.

Hargreaves, D., Porter, T. and Wright, N. (2006) 'Consistent inlet boundary conditions in Computational Fluid Dynamics modelling of wind flow over terrain', in *Proc. 7th UK Conference on Wind Engineering, Glasgow, UK*, pp. 47–50.

Heimsath, A. and Nitz, P. (2019) 'The effect of soiling on the reflectance of solar reflector materials - Model for prediction of incidence angle dependent reflectance and attenuation due to dust deposition', *Solar Energy Materials and Solar Cells*, 195, pp. 258–268. doi:10.1016/j.solmat.2019.03.015.

Hewitt, C.N. and Jackson, A.V. (eds) (2020) *Atmospheric science for environmental scientists*. Second edition. Hoboken: Wiley-Blackwell.

Hockaday, L. (2019) 'Solar thermal applications in minerals processing in South Africa', in *Proceesings of the 6th South African Solar Energy Conference. SASEC2019*, East London, p. 8.

Hockaday, Lina (2019) 'Solar Thermal Applications in Minerals Processing in South Africa', in *Proceedings of the 6th South African Solar Energy Converence*. *SASEC2019*, East London, p. 8. Available at: https://www.sasec.org.za/papers2019/76.pdf (Accessed: 31 March 2020).

IEA (2017) *Energy Technology Perspectives 2017*. Paris: OECD/IEA.

IEA (2021) *World Energy Outlook 2021*. Paris. Available at: https://www.iea.org/reports/world-energy-outlook-2021.

IEA and Philibert, C. (2017) *Renewable Energy for Industry*. Paris: IEA. Available at: https://www.iea.org/reports/renewable-energy-for-industry.

Ilse, K.K. *et al.* (2018) 'Comprehensive analysis of soiling and cementation processes on PV modules in Qatar', *Solar Energy Materials and Solar Cells*, 186, pp. 309–323. doi:10.1016/j.solmat.2018.06.051.

Intergovernmental Panel on Climate Change *et al.* (eds) (1990) *Climate change: the IPCC scientific assessment*. Cambridge ; New York: Cambridge University Press.

IPCC (2018) *An IPCC Special Report on the impacts of global warming of 1.5°C above pre-industrial levels and related global greenhouse gas emission pathways, in the context of strengthening the global response to the threat of climate change, sustainable development, and efforts to eradicate poverty*. Geneva, Switzerland: World Meteorological Organization, p. 32 pp.

IPCC *et al.* (eds) (2021) *Contribution of Working Group I to the Sixth Assessment Report of the Intergovernmental Panel on Climate Change*. Switzerland: Intergovernemntal Panel on Climate Change (Summary for Policy Makers. In: Climate Change: The Physical Science Basis).

Jain, R.K., Cui, Z. "Cindy" and Domen, J.K. (2016) 'Mitigation Measures and Control Technology for Environmental and Human Impacts', in *Environmental Impact of Mining and Mineral Processing*. Elsevier, pp. 229–269. doi:10.1016/B978-0-12-804040-9.00007-3.

Jones, W.P. and Launder, B.E. (1972) 'The prediction of laminarization with a two-equation model of turbulence', *International Journal of Heat and Mass Transfer*, 15(2), pp. 301–314. doi:10.1016/0017-9310(72)90076-2.

Joseph, G.M.D., Lowndes, I.S. and Hargreaves, D.M. (2018) 'A computational study of particulate emissions from Old Moor Quarry, UK', *Journal of Wind Engineering and Industrial Aerodynamics*, 172, pp. 68–84. doi:10.1016/j.jweia.2017.10.018.

Kazmerski, L.L., Diniz, A.S.A.C. and Costa, S.C.S. (2020) 'Dust in the wind: An historical timeline of soiling R&D for solar technologies', in *Proceedings of the ISES Solar World Congress 2019 and IEA SHC International Conference on Solar Heating and Cooling for Buildings and Industry 2019*. doi:10.18086/swc.2019.54.01.

Kok, J.F. *et al.* (2012) 'The physics of wind-blown sand and dust', *Reports on Progress in Physics*, 75(10), p. 106901. doi:10.1088/0034-4885/75/10/106901.

Landberg, L. (2016) *Meteorology for wind energy: an introduction*. Chichester, West Sussex: Wiley.

Leitl, B. (1996) *CEDVAL at Hamburg University, Compilation of Experimental Data for Validation of Microscale Dispersion Models*. Available at: http://www.mi.uni-hamburg.de/cedval.

Lotter, M.C. (2010) *MBSP Landcover 2010 [Vector] 2010*. Mpumalanga Tourism and Parks Agency. Available at: Available from the Biodiversity GIS http://bgis.sanbi.org/SpatialDataset (Accessed: 15 September 2020).

Lovegrove, K. and Pye, J. (2012) '2 - Fundamental principles of concentrating solar power (CSP) systems', in Lovegrove, Keith and Stein, W. (eds) *Concentrating Solar Power Technology*. Woodhead Publishing, pp. 16–67. doi:10.1533/9780857096173.1.16.

Mckechnie, T., McGregor, C. and Venter, G. (2020) 'Concentrating Solar Thermal Process Heat for Manganese Ferroalloy Production: Plant Modelling and Thermal Energy Storage Dispatch Optimization', in *ASME 2020 14th International Conference on Energy Sustainability*. *ASME 2020 14th International Conference on Energy Sustainability*, Virtual, Online: American Society of Mechanical Engineers, p. V001T14A001. doi:10.1115/ES2020-1635.

Meroney, R.N. (2008) 'Protocol for CFD prediction of cooling-tower drift in an urban environment', *Journal of Wind Engineering and Industrial Aerodynamics*, 96(10), pp. 1789–1804. doi:10.1016/j.jweia.2008.02.029.

Merrouni, A.A. *et al.* (2017) 'Measurement, comparison and monitoring of solar mirror's specular reflectivity using two different Reflectometers', *Energy Procedia*, 119, pp. 433–445. doi:10.1016/J.EGYPRO.2017.07.045.

Meyen, S. *et al.* (2018) 'Guidelines: parameters and method to evaluate the solar reflectance properties of reflector materials for concentrating solar power technology', *SolarPACES* [Preprint], (June).

Morsi, S.A. and Alexander, A.J. (1972) 'An investigation of particle trajectories in two-phase flow systems', *Journal of Fluid Mechanics*, 55(02), p. 193. doi:10.1017/S0022112072001806.

Moukalled, F., Mangani, L. and Darwish, M. (2016) *The Finite Volume Method in Computational Fluid Dynamics: An Advanced Introduction with OpenFOAM® and Matlab*. Cham: Springer International Publishing (Fluid Mechanics and Its Applications). doi:10.1007/978-3-319-16874-6.

Nabernegg, S. *et al.* (2017) 'The Deployment of Low Carbon Technologies in Energy Intensive Industries: A Macroeconomic Analysis for Europe, China and India', *Energies*, 10(3), p. 360. doi:10.3390/en10030360.

NASA (1976) *U.S. Standard Atmosphere*. Technical Memorandum N77-16482. National Aeronautics and Space Administration, p. 241.

Nieuwstadt, F.T.M., Westerweel, J. and Boersma, B.J. (2016) *Turbulence: Introduction to Theory and Applications of Turbulent Flows*. Cham: Springer International Publishing. doi:10.1007/978-3-319-31599-7.

Orlanski, I. (1975) 'A Rational Subdivision of Scales for Atmospheric Processes', *Bulletin of the American Meteorological Society*, 56(5), pp. 527–530.

Parente, A. *et al.* (2011) 'Improved k–ε model and wall function formulation for the RANS simulation of ABL flows', *Journal of Wind Engineering and Industrial Aerodynamics*, 99(4), pp. 267–278. doi:10.1016/j.jweia.2010.12.017.

Parente, A. and Benocci, C. (2010) 'On the RANS simulation of neutral ABL flows', in *Proceedings of the Fifth International Symposium on Computational Wind Engineering (CWE2010) Chapel Hill, North Carolina, USA, May*, pp. 23–27.

Petavratzi, E., Kingman, S. and Lowndes, I. (2005) 'Particulates from mining operations: A review of sources, effects and regulations', *Minerals Engineering*, 18(12), pp. 1183–1199. doi:10.1016/j.mineng.2005.06.017.

Pettit, R.B. and Freese, J.M. (1980) 'Wavelength Dependent Scattering Caused By Dust Accumulation on Solar Mirrors.', in *Solar energy materials*, pp. 1–20. doi:10.1016/0165-1633(80)90046-5.

Pettit, R.B., Freese, J.M. and Arvizu, D.E. (1978) 'Specular Reflectance Loss of Solar Mirrors Due To Dust Accumulation.', in, pp. 164–168.

Picotti, G. *et al.* (2020) 'Optimization of cleaning strategies for heliostat fields in solar tower plants', *Solar Energy*, 204, pp. 501–514. doi:10.1016/j.solener.2020.04.032.

QGIS.org (2021) *QGIS Geographic Information System*. QGIS Association. Available at: http://www.qgis.org.

Rabinovich, E. and Kalman, H. (2007) ‘Pickup, critical and wind threshold velocities of particles’, *Powder Technology*, 176(1), pp. 9–17. doi:10.1016/j.powtec.2007.01.033.

Randerson, D. (1976) ‘Overview of regional-scale numerical models’, *Bulletin of the American Meteorological Society*, 57(7), pp. 797–804. doi:10.1175/1520-0477(1976)057<0797:OORSNM>2.0.CO;2.

Reichart, M. *et al.* (2021) ‘Numerical Assessment of Packing Structures for Gas-Particle Trickle Flow Heat Exchanger for Application in CSP Plants’, in *ASME 2021 15th International Conference on Energy Sustainability*. To be published soon.

Richards, P.J. and Hoxey, R.P. (1993) ‘Appropriate boundary conditions for computational wind engineering models using the k-ϵ turbulence model’, *Journal of Wind Engineering and Industrial Aerodynamics*, 46–47(C), pp. 145–153. doi:10.1016/0167-6105(93)90124-7.

Ringdalen, E. (2018) *PREMA*. Available at: https://www.spire2030.eu/prema (Accessed: 17 February 2020).

Roth, E.P. and Pettit, R.B. (1980) ‘The effect of soiling on solar mirrors and techniques used to maintain high reflectivity’, in *Solar Materials Science*, pp. 199–227. doi:10.1016/b978-0-12-511160-7.50013-2.

SANS 1137:2012 and ASTM D1739:1998 (2012) *SANS 1137:2012, ASTM D1739:1998, South African national Standard, Standard test method for collection and measurement of dustfall (settleable particulate matter)*. 978-0-626-26763–6. doi:10.1520/D1739-98R04.

Sarver, T., Al-Qaraghuli, A. and Kazmerski, L.L. (2013) ‘A comprehensive review of the impact of dust on the use of solar energy: History, investigations, results, literature, and mitigation approaches’, *Renewable and Sustainable Energy Reviews*, 22, pp. 698–733. doi:10.1016/j.rser.2012.12.065.

Scargiali, F. *et al.* (2005) ‘Heavy Gas Dispersion Modelling Over a Topographically Complex Mesoscale: A CFD Based Approach’, *Process Safety and Environmental Protection*, 83(3), pp. 242–256. doi:10.1205/psep.04073.

Schatzmann, M. and Leitl, B. (2009) ‘Evaluation of numerical flow and dispersion models for applications in industrial and urban areas’, *Chemical Engineering and Technology*, 32(2), pp. 241–246. doi:10.1002/ceat.200800578.

Schatzmann, M. and Leitl, B. (2011) ‘Issues with validation of urban flow and dispersion CFD models’, *Journal of Wind Engineering and Industrial Aerodynamics*, 99(4), pp. 169–186. doi:10.1016/j.jweia.2011.01.005.

Schlecht, M. and Meyer, R. (2012) ‘4 - Site selection and feasibility analysis for concentrating solar power (CSP) systems’, in Lovegrove, K. and Stein, W. (eds) *Concentrating Solar Power Technology*. Woodhead Publishing, pp. 91–119. doi:10.1533/9780857096173.1.91.

Schlünzen, K.H. *et al.* (2011) ‘Joint modelling of obstacle induced and mesoscale changes—Current limits and challenges’, *Journal of Wind Engineering and Industrial Aerodynamics*, 99(4), pp. 217–225. doi:10.1016/j.jweia.2011.01.009.

Scire, J.S., Strimaitis, D.G. and Yamartino, R.J. (2000) *A User’s Guide for the CALPUFF Dispersion Model (Version 5.0)*. Concord, MA 01742: Earth Tech, Inc.

Shao, Y. and Lu, H. (2000) ‘A simple expression for wind erosion threshold friction velocity’, *Journal of Geophysical Research: Atmospheres*, 105(D17), pp. 22437–22443. doi:10.1029/2000JD900304.

Shao, Y., Raupach, M.R. and Findlater, P.A. (1993) ‘Effect of saltation bombardment on the entrainment of dust by wind’, *Journal of Geophysical Research*, 98(D7), p. 12719. doi:10.1029/93JD00396.

SolarGIS (2019) ‘Solar resource maps and GIS data for 200+ countries’. (SolarGIS Resources). Available at: https://solargis.com/maps-and-gis-data/overview/ (Accessed: 27 February 2020).

Strong, J. *et al.* (2010) ‘Development and application of a Lagrangian model to determine the origins of ozone episodes in the UK’, *Atmospheric Environment*, 44(5), pp. 631–641. doi:10.1016/j.atmosenv.2009.11.019.

Stull, R.B. (ed.) (1988) *An Introduction to Boundary Layer Meteorology*. Dordrecht: Springer Netherlands. doi:10.1007/978-94-009-3027-8.

Svensson, G. *et al.* (2011) ‘Evaluation of the Diurnal Cycle in the Atmospheric Boundary Layer Over Land as Represented by a Variety of Single-Column Models: The Second GABLS Experiment’, *Boundary-Layer Meteorology*, 140(2), pp. 177–206. doi:10.1007/s10546-011-9611-7.

Swart, M. (2019) ‘Weather station installation at Transalloys finished!’, *PREMA news and events*, August. Available at: https://www.spire2030.eu/prema/New-Event/weather-station-installation-transalloys-finished.

Thomson, D.J. and Wilson, J.D. (2013) ‘History of Lagrangian Stochastic Models for Turbulent Dispersion’, in Lin, J. et al. (eds) *Geophysical Monograph Series*. Washington, D. C.: American Geophysical Union, pp. 19–36. doi:10.1029/2012GM001238.

Van Hooff, T. and Blocken, B. (2010) ‘Coupled urban wind flow and indoor natural ventilation modelling on a high-resolution grid: A case study for the Amsterdam ArenA stadium’, *Environmental Modelling and Software*, 25(1), pp. 51–65. doi:10.1016/j.envsoft.2009.07.008.

Vervoort, R., Blocken, B. and van Hooff, T. (2019a) ‘Reduction of particulate matter concentrations by local removal in a building courtyard: Case study for the Delhi American Embassy School’, *Science of the Total Environment*, 686, pp. 657–680. doi:10.1016/j.scitotenv.2019.05.154.

Vervoort, R., Blocken, B. and van Hooff, T. (2019b) ‘Reduction of particulate matter concentrations by local removal in a building courtyard: Case study for the Delhi American Embassy School’, *Science of the Total Environment*, 686, pp. 657–680. doi:10.1016/j.scitotenv.2019.05.154.

Voster, C.J. and Dixon, E. (2005) *Simplified Geology , Selected Mines and Mineral Deposits South Africa, Lesotho and Swaziland*. Pretoria, South Africa: Council for Geoscience.

Wang, Z. (2019a) ‘Chapter 4 - Design of the Concentration System’, in Wang, Z. (ed.) *Design of Solar Thermal Power Plants*. Academic Press, pp. 225–318. doi:10.1016/B978-0-12-815613-1.00004-3.

Wang, Z. (2019b) ‘Chapter 7 - Site Selection, Power Load, and Power Generation Procedures’, in Wang, Z. (ed.) *Design of Solar Thermal Power Plants*. Academic Press, pp. 417–424. doi:10.1016/B978-0-12-815613-1.00007-9.

Wette, J., Sutter, F. and Fernández-García, A. (2019) 'Evaluation of anti-soiling coatings for CSP reflectors under realistic outdoor conditions', *Solar Energy* [Preprint]. doi:10.1016/j.solener.2019.09.031.

Wieringa, J. (1992) 'Updating the Davenport roughness classification', *Journal of Wind Engineering and Industrial Aerodynamics*, 41(1–3), pp. 357–368. doi:10.1016/0167-6105(92)90434-C.

Wilcox, D.C. (1993) *Turbulence modeling for CFD*. La Cãnada, CA: DCW Industries, Inc.

WMO (2018) *Guide to meteorological instruments and methods of observation*. 2018th edn. Geneva: World Meteorological Organization.

World Bank (1999) *Pollution prevention and abatement handbook, 1998: Toward cleaner production*. The World Bank. doi:10.1596/0-8213-3638-X.

Zakhidov, R.A. and Ismanzhanov, A. (1980) 'Investigation of Abrasive Action of Atmospheric Particles on the Reflectance of Mirrors.', *Applied Solar Energy (English translation of Geliotekhnika)*, 16(6), pp. 39–43.

Zhang, M.H. (2015) *Wind resource assessment and micro-siting: science and engineering*. Singapore: Wiley [u.a.].

Appendix A. – Terrain Surface Roughness Classifications

Table 9 was generated by Wieringa (1992), updating the roughness classifications based on newly available experimental data at the time.

Table 9. Aerodynamic roughness length classifications.

z_0 (m)	Landscape description
0.0002 "Sea"	Open sea or lake (irrespective of the wave size), tidal flat, snow-covered flat plain, featureless desert, tarmac and concrete, with a free fetch of several kilometres.
0.005 "Smooth"	Featureless land surface without any noticeable obstacles and with negligible vegetation; e.g. beaches, pack ice without large ridges, morass, and snow-covered or fallow open country.
0.03 "Open"	Level country with low vegetation (e.g., grass) and isolated obstacles with separations of at least 50 obstacle heights; e.g. grazing land without windbreaks, heather, moor and tundra, runway area of airports.
0.10 "Roughly open"	Cultivated area with regular cover of low crops, or moderately open country with occasional obstacles (e.g., low hedges, single rows of trees, isolated farms) at relative horizontal distances of at least 20 obstacle heights.
0.25 "Rough"	Recently developed "young" landscape with high crops or crops of varying height, and scattered obstacles (e.g., dense shelterbelts, vineyards) at relative distances of about 15 obstacle heights.
0.5 "Very rough"	"Old" cultivated landscape with many rather large obstacle groups (large farms, clumps of forest) separated by open spaces of about 10 obstacle heights. Also, low large vegetation with small interspaces, such as bushland, orchards, young densely-planted forest,
1.0 "Closed"	Landscape totally and quite regularly covered with similar-size large obstacles, with open spaces comparable to the obstacle heights; e.g., mature regular forests, homogeneous cities or villages.
≥ 2 "Chaotic"	Centres of large towns with mixture of low-rise and high-rise buildings. Also, irregular large forests with many clearings.

Appendix B. – Code for Reflectance Calculations

This appendix contains two tables with the python code used to calculate reflectance values and manage the reflectance data frame. Table 10 is the notebook that is used to control the creation and viewing of the reflectance database. Table 11 contains the function definitions that are called in the notebook to build the reflectance data frame for an individual sampling period and to perform the reflectance calculations on the individual mirrors. The code is available at https://github.com/swartmilan/solsurf-image.git.

Table 10. Mirror reflectance monitoring data frame control Jupyter Notebook in '.rst' format.

```
.. code:: ipython3

    import pandas as pd
    import matplotlib as matplt
    from matplotlib import pyplot as plt
    import os
    import pickle as pkl
    from IPython.display import display

    from image_processing_scripts.image_processing_functions import
dataframe_creator

Take User Inputs
~~~~~~~~~~~~~~~~

2020/03/06 is the date when the first samples were taken.

All images are captured using 1/320 exposure length and ISO-100 on a
Nikon D5300 DSLR camera.

Reference mirror (calibration mirror) dates
~~~~~~~~~~~~~~~~~~~~~~~~~~~~~~~~~~~~~~~~~~~

The following lists the date on which the reference photos where taken
and the time period for which those reference measurements are used: \*
20200907 used as reference for (202000205 - )

.. code:: ipython3

    calibration_mirror_df_path = 'F:/Master
Controller/DataStorageActive/df_calibration'
                                  + '_mirror_20200907.pkl'

.. code:: ipython3

    ##Change or append date series as needed, be careful
    dates = pd.Series([
        '2020/03/06',
        '2020/05/13',
        '2020/06/11',
        '2020/06/26',
        '2020/07/08',
        '2020/07/22',
        '2020/08/04',
        '2020/08/21',
        '2020/09/05',
        '2020/09/22',
        '2020/10/01',
        '2020/10/15',
        '2020/10/29'])

.. code:: ipython3

    df_Dates = pd.DataFrame({'Dates':pd.to_datetime(dates, format='%Y/%m/%d'),
```

```
                                'Days Passed':0})
    current_date_string = current_date.strftime(format='%Y%m%d')
    previous_date_string = previous_date.strftime(format='%Y%m%d')
    print("Current date: " + current_date_string)
    print("Previous date: " + str(previous_date_string))
    #calculate time deltas
    df_Dates['Days Passed'] = df_Dates.Dates.diff()
    days_passed = df_Dates.iloc[-1]['Days Passed'].days
    display(df_Dates)
    print(str(days_passed), 'passed since last measurements.')

Checks
^^^^^^

.. code:: ipython3

    print('Have you populated appropriate Image directories ??')
    print('Have you checked the code below ??')

note:
^^^^^

the first time the master_df is initialised and populated is when the
first

calibration/reference mirror is processed

Create Set and Mirror DataFrame for current_date
~~~~~~~~~~~~~~~~~~~~~~~~~~~~~~~~~~~~~~~~~~~~~~~~

This can take longer than an hour.

.. code:: ipython3

    dataframe_creator(current_date_string, calibration_mirror_df_path)
    df_dir = 'F:/Master Controller/DataStorageActive/df_' + current_date_string +
'.pkl'

max_spots = 22.0


print('Max spot count =' + str(max_spots))

Create new DataFrame tracking set values over time
--------------------------------------------------

Load appropriate reference dataframe
^^^^^^^^^^^^^^^^^^^^^^^^^^^^^^^^^^^^

.. code:: ipython3

    df_reference = pd.read_pickle('F:/Master Controller/DataStorageActive/'
                                  + 'df_calibration_mirror_20200907_no1.pkl')
    reference_mean_PI = df_reference.iloc[0]['Mean_PI']
    reference_mean_PI

Load correct month data frame
^^^^^^^^^^^^^^^^^^^^^^^^^^^^^

.. code:: ipython3

    df_dir = 'F:/Master Controller/DataStorageActive/df_' + current_date_string +
'.pkl'
    month_df = pd.read_pickle(df_dir)
    month_df

Load master dataframe
^^^^^^^^^^^^^^^^^^^^^
```

```
.. code:: ipython3

    master_df_file = 'F:/Master Controller/master_df.pkl'
    master_df = pd.read_pickle(master_df_file)

Populating of master_df
^^^^^^^^^^^^^^^^^^^^^^^

MDRL - Mean Daily Reflectance Loss, calculated as (R2-R1)/days_passed

Reflectance is an expression of the reflected average light intensity of
a soiled

mirror divided by the average intensity of the reflected light of that
same mirror

when cleaned.

.. code:: ipython3

    #### NOTE: The subset variability is shown for the M60 subset to give an
indication
    # of how good a representation that mean reflectance value actually is. The
mirrors
    # are spaced 2m apart in all directions, therefore, the variability should be
low.
    Sets = ['S1','S2','S3','S4']
    for s in Sets:

        ####    M30subset    ####
        #current soiled seflectance
        df_M30 = month_df.loc[(month_df['Set']==s) & (month_df['Mirror
Elevation']==30)]
        soiled_reflectance_M30 = df_M30['Soiled Reflectance'].mean()
        #reflectance loss for period -> previous clean reflectance -
        # current soiled reflectance
        previous_reflectance_M30_df =
master_df.loc[(master_df['Date']==previous_date_string)
                                                    & (master_df['Set']==s)]
        previous_reflectance_M30 = previous_reflectance_M30_df.iloc[0]
                                                            ['Clean Reflectance
M30subset']
        reflectance_loss_M30 = previous_reflectance_M30 - soiled_reflectance_M30
        #mean daily reflectance loss
        MDRL_M30 = reflectance_loss_M30 / days_passed
        #current clean reflectance
        clean_reflectance_M30 = df_M30['Clean Reflectance'].mean()

        ####    M60subset    ####
        #current soiled seflectance
        df_M60 = month_df.loc[(month_df['Set']==s) & (month_df['Mirror
Elevation']==60)]
        soiled_reflectance_M60 = df_M60['Soiled Reflectance'].mean()
        #reflectance loss for period -> previous clean reflectance -
        # current soiled reflectance
        previous_reflectance_M60_df =
master_df.loc[(master_df['Date']==previous_date_string)
                                                    & (master_df['Set']==s)]
        previous_reflectance_M60 = previous_reflectance_M60_df.iloc[0]
                                                            ['Clean Reflectance
M60subset']
        reflectance_loss_M60 = previous_reflectance_M60 - soiled_reflectance_M60
        #mean daily reflectance loss
        MDRL_M60 = reflectance_loss_M60 / days_passed
        #current clean reflectance
        clean_reflectance_M60 = df_M60['Clean Reflectance'].mean()
```

```
        #set variability calculation, done using only the subset of mirrors
elevated at
        #60deg, reason being that the 30deg elevation mirror are likely to soil
faster and
        #will cause the variability to be higher eventhough the comparison being
made is
        # not valid
        set_max_soiled_reflectance = df_M60['Soiled Reflectance'].max()
        set_min_soiled_reflectance = df_M60['Soiled Reflectance'].min()
        set_reflectance_range = set_max_soiled_reflectance -
set_min_soiled_reflectance
        # set uncertainty and variability applies to all mirrors in set - ASSUMED
        # pull values from any mirror in sets that is at 60deg
        stats_df = month_df.loc[(month_df['Set']==s) &
(month_df['Mirror']=='M3')]
        uncertainty = stats_df.iloc[0]['Set Measurement Uncertainty %']

        # DataFrame entry
        new_entry = {'Date':current_date_string,
                     'Set':s,
                     'Soiled Reflectance M30subset':soiled_reflectance_M30,
                     'Clean Reflectance M30subset':clean_reflectance_M30,
                     'MDRL M30subset':MDRL_M30,
                     'Soiled Reflectance M60subset':soiled_reflectance_M60,
                     'Clean Reflectance M60subset':clean_reflectance_M60,
                     'MDRL M60subset':MDRL_M60,
                     'Reflectance Variability M60subset':set_reflectance_range,
                     'Measurement Uncertainty %':uncertainty}
        master_df = master_df.append(new_entry, ignore_index=True)

.. code:: ipython3

    master_df

Saving to active and cold storage
^^^^^^^^^^^^^^^^^^^^^^^^^^^^^^^^

.. code:: ipython3

    pd.to_pickle(master_df, master_df_file)
    master_df_file_cold_storage = "F:/Master
Controller/DataColdStorage/MasterDFs/master_df_"
                                  + str(current_date_string) + ".pkl"
    pd.to_pickle(master_df, master_df_file_cold_storage)
    master_df

.. code:: ipython3

    master_df.to_excel('master_spreadsheet.xlsx')
```

Table 11. Function definitions for construction and calculation of reflectance data frame values.

```
#processes the noise corrected 'spot' reflectance on a mirror
def spot_processor(rgb_dark, rgb_light):
    ''' swap betweenn 16383. and 1., depending on whether float
    (range 0-1) or unassigned integer (uint14) format is required
    respectively. The values are read in as uint14 (range 0-16383)
    and put into a 16bit (range 0-65535) array, max value remains
    16383, no rescale needed
    '''
    dark_float  = rgb_dark / 16383.
    light_float = rgb_light / 16383.
    #Subtract noise
    noise_corr_image = light_float - dark_float
```

```
    return noise_corr_image

'''processes a mirror using a series of spots
   first noise correct then process '''
def mirror_processor(mp_filename, current_date):
    import glob
    import rawpy
    import numpy as np

    #get images
    images = glob.glob(mp_filename + '*.NEF')
    n_images = len(images)
    #number of spots, two images per spot, one dark and one light
    N = n_images/2.0
    if not (n_images % 2 == 0):
        print('Must be even number of images in the set - check '
              + mp_filename)
        return

    # empty array creation
    spot_means = []
    #collecting light and dark
    for i in range(0, n_images, 2):
        #collect images
        with rawpy.imread(images[i]) as raw:
            rgb_dark = raw.postprocess(gamma=(1,1),
                                       no_auto_bright=True,
                                       output_bps=16)
        with rawpy.imread(images[i+1]) as raw:
            rgb_light = raw.postprocess(gamma=(1,1),
                                        no_auto_bright=True,
                                        output_bps=16)
        #correct for noise by subtracting dark from light image
        corrected_image = spot_processor(rgb_dark, rgb_light)
        #corrected image (ci) channel means
        ci_channel_means = corrected_image.mean(axis=0).mean(axis=0)
        print(str(ci_channel_means))
        with open("F:/Master Controller/" + str(current_date) +
                  "_logfile.txt", "a") as logfile:
            logfile.write(str(ci_channel_means)+"\n")
        #linear mean of three channel means
        channels_mean = np.mean(ci_channel_means)
        print(channels_mean)
        spot_means.append(channels_mean)

    #mirror statistics
    mean_PI = np.mean(spot_means)
    #the PI is a float (also a percentage)
    #std_dev is thus expressed as precentage
    std_dev =  (np.std(spot_means))*100.0
    return spot_means, mean_PI, std_dev, N


def dataframe_creator(current_date, calibration_mirror_df_path):
    import time
    import pandas as pd
    import _pickle as pickle

    start_time = time.time()
    #reference values
    df_reference = pd.read_pickle(calibration_mirror_df_path)
    reference_mean_PI = df_reference.iloc[0]['Mean_PI']
    #main image folder for current date, contains all sets and mirrors
    image_folder = 'F:/DataFrame Images/' + str(current_date) +'/'
    # DataFrame Initialisation
    df_init = pd.DataFrame(columns=['Date',
                                    'Set',
                                    'Mirror',
```

```
                                    'Mirror Elevation',
                                    'Reference Mean PI',
                                    'Soiled Mean PI',
                                    'Clean Mean PI',
                                    'Soiled Reflectance',
                                    'Clean Reflectance',
                                    'Measurement Uncertainty %',
                                    'Set Measurement Uncertainty %'])
    #store file for regular use
    df_filename = ('F:/Master Controller/DataStorageActive/df_' +
                   str(current_date) + '.pkl')
    pd.to_pickle(df_init, df_filename)

    #Layout of mirror sets specified here, not all the same
    #SET 1 MIRROR LAYOUT
     #  M1~elev.60deg,soiled.cleaned  #  M2~elev.30deg,soiled.cleaned
     #  M3~elev.60deg,soiled.cleaned  #  M4~elev.60deg,soiled.cleaned
     #  M5~elev.30deg,soiled.cleaned  #  M6~elev.60deg,soiled.cleaned
     #  M7~elev.60deg,soiled.cleaned  #  M8~elev.60deg,soiled.cleaned
    S1 = [60,30,60,60,30,60,60,60]
    #SET 2 MIRROR LAYOUT
    #  M1~elev.30deg,soiled.cleaned  #  M2~elev.60deg,soiled.cleaned
    #  M3~elev.60deg,soiled.cleaned  #  M4~elev.60deg,soiled.cleaned
    #  M5~elev.30deg,soiled.cleaned  #  M6~elev.60deg,soiled.cleaned
    #  M7~elev.60deg,soiled.cleaned  #  M8~elev.60deg,soiled.cleaned
    S2 = [30,60,60,60,30,60,60,60]
    #SET 3 MIRROR LAYOUT
    #  M1~elev.30deg,soiled.cleaned  #  M2~elev.60deg,soiled.cleaned
    #  M3~elev.60deg,soiled.cleaned  #  M4~elev.60deg,soiled.cleaned
    #  M5~elev.30deg,soiled.cleaned  #  M6~elev.60deg,soiled.cleaned
    #  M7~elev.60deg,soiled.cleaned  #  M8~elev.60deg,soiled.cleaned
    S3 = [30,60,60,60,30,60,60,60]
    #SET 4 MIRROR LAYOUT
    #  M1~elev.30deg,soiled.cleaned  #  M2~elev.60deg,soiled.cleaned
    #  M3~elev.60deg,soiled.cleaned  #  M4~elev.60deg,soiled.cleaned
    #  M5~elev.30deg,soiled.cleaned  #  M6~elev.60deg,soiled.cleaned
    #  M7~elev.60deg,soiled.cleaned  #  M8~elev.60deg,soiled.cleaned
    S4 = [30,60,60,60,30,60,60,60]
    set_elevations = [S1, S2, S3, S4]

    log_file = open("F:/Master Controller/" +
                    str(current_date) + "_logfile_v3.txt", "a")
    log_file.write('This is the logfile for ' + str(current_date) +
                   '. Logs values that are\'nt make it to the DataFrame.')

    #create DataFrame
    Sets = ['S1', 'S2', 'S3', 'S4']
    #exclude as needed if images are jpeg format or unusable
    Mirrors = ['M1', 'M2', 'M3', 'M4', 'M5', 'M6', 'M7', 'M8']

    df = pd.read_pickle(df_filename)
    for s in Sets:
        #variable initialisation
        set_start_time = time.time()
        set_index = Sets.index(s)
        set_stddev = 0
        #list create
        spot_count_list = []
        standard_deviation_list = []

        for m in range(len(Mirrors)):
            mirror_folder = image_folder + s + '/' + Mirrors[m] + '/'
            #elevation
            elev = set_elevations[set_index][m]
            print(str(elev) + 'deg')
            log_file.write(str(elev) + 'deg\n')
            #'soiled' mirror
            mirror_subfolder = mirror_folder + 'soiled/'
```

```
            start = time.time()
            s_spot_channel_means, s_mean_PI, s_stddev, s_spot_count =
            ............mirror_processor(mirror_subfolder, current_date)
            end = time.time() - start
            #list appends
            spot_count_list.append(s_spot_count)
            standard_deviation_list.append(s_stddev)
            #debug prints
            print('./' + str(current_date) + '/' + s
                  + '/' + Mirrors[m] + '/soiled/' + ':')
            print('timed=' + str(end) + 's, '
                  + 'spot_count=' + str(s_spot_count))
            print(s_spot_channel_means)
            print(s_mean_PI)
            print('++++++++++++')
            #recordkeeping logfile outputs
            log_file.write('./' + str(current_date) + '/' + s
                           + '/' + Mirrors[m] + '/soiled/' + ':\n')
            log_file.write(str(s_spot_channel_means)+'\n')
            log_file.write(str(s_mean_PI)+'\n')
            log_file.write('timed=' + str(end) + 's, '
                           + 'spot_count=' + str(s_spot_count)+'\n')
            log_file.write('++++++++++++\n')
            #'clean' mirror
            mirror_subfolder = mirror_folder + 'clean/'
            start = time.time()
            c_spot_channel_means, c_mean_PI, c_stddev, c_spot_count =
            ............mirror_processor(mirror_subfolder, current_date)
            end = time.time() - start
            #debug prints
            print('./' + str(current_date) + '/' + s
                  + '/' + Mirrors[m] + '/clean/' + ':')
            print('timed=' + str(end) + 's, '
                  + 'spot_count=' + str(c_spot_count))
            print(c_spot_channel_means)
            print(c_mean_PI)
            print()
            #recordkeeping logfile outputs
            log_file.write('./' + str(current_date) + '/'
                           + s + '/' + Mirrors[m] + '/clean/' + ':\n')
            log_file.write(str(c_spot_channel_means)+'\n')
            log_file.write(str(c_mean_PI)+'\n')
            log_file.write('timed=' + str(end) + 's, '
                           + 'spot_count=' + str(c_spot_count) + '\n')
            #Reflectance calculations
            s_reflectance = s_mean_PI / reference_mean_PI
            c_reflectance = c_mean_PI / reference_mean_PI
            #dataframe entry creation
            new_entry = {'Date':current_date,
                         'Set':s,
                         'Mirror':Mirrors[m],
                         'Mirror Elevation':elev,
                         'Reference Mean PI':reference_mean_PI,
                         'Soiled Mean PI':s_mean_PI,
                         'Clean Mean PI':c_mean_PI,
                         'Soiled Reflectance':s_reflectance,
                         'Clean Reflectance':c_reflectance,
                         'Measurement Uncertainty %':s_stddev,
                         'Set Measurement Uncertainty %':set_stddev}
            df = df.append(new_entry, ignore_index=True)

        '''after cycling through mirrors, make set_stdev all sets value
        that was previously zero typical spot count is 10 spots per
        mirror, one mirror per set is chosen at random to sample more
        than 10 spots in order to calculate a representative measurement
        uncertainty for the set max spots count is where s_stddev ==
        set_stddev'''
        max_spots = max(spot_count_list)
```

```
        #print('Max spot count = ' + str(max_spots))
        log_file.write('Maximum spot count' + str(max_spots))
        log_file.write('\n')
        max_spots_index = spot_count_list.index(max_spots)
        set_stddev = standard_deviation_list[max_spots_index]
        df.loc[(df['Date'] == current_date) & (df['Set'] == s) &
               (df['Set Measurement Uncertainty %'] == 0),
               'Set Measurement Uncertainty %'] = set_stddev
        set_time = (time.time() - set_start_time)/60.0
        print('Elapsed Time for Set = ' + str(round(set_time,2))
              + ' <minutes>')
        log_file.write('Elapsed Time for Set = '
                       + str(round(set_time,2)) + ' <minutes>\n')
        log_file.write('\n')

    #save to active storage
    pd.to_pickle(df, df_filename)
    #send same file to cold-storage
    cold_storage = 'F:/Master Controller/DataColdStorage/df_'
                   .... + str(current_date) + '.pkl'
    pd.to_pickle(df, cold_storage)

    elapsed_time = (time.time() - start_time)/60.0
    print('Elapsed Time = ' + str(round(elapsed_time,2)) + ' <minutes>')
    print('DataFrame creation COMPLETE!!!')
    log_file.write('Elapsed Time = ' + str(round(elapsed_time,2)) + '
<minutes>\n')
    log_file.close()
```

Appendix C. – Wind Rose for the Dry Season at the Transalloys Smelters

The wind data presented in Figure 72 corresponds to the identified peak soiling period (or dry season) at the Transalloys smelter. The open-source python library *windrose v1.6.8* was used for all wind data analysis and presentations. The code is available at https://github.com/python-windrose/windrose.git.

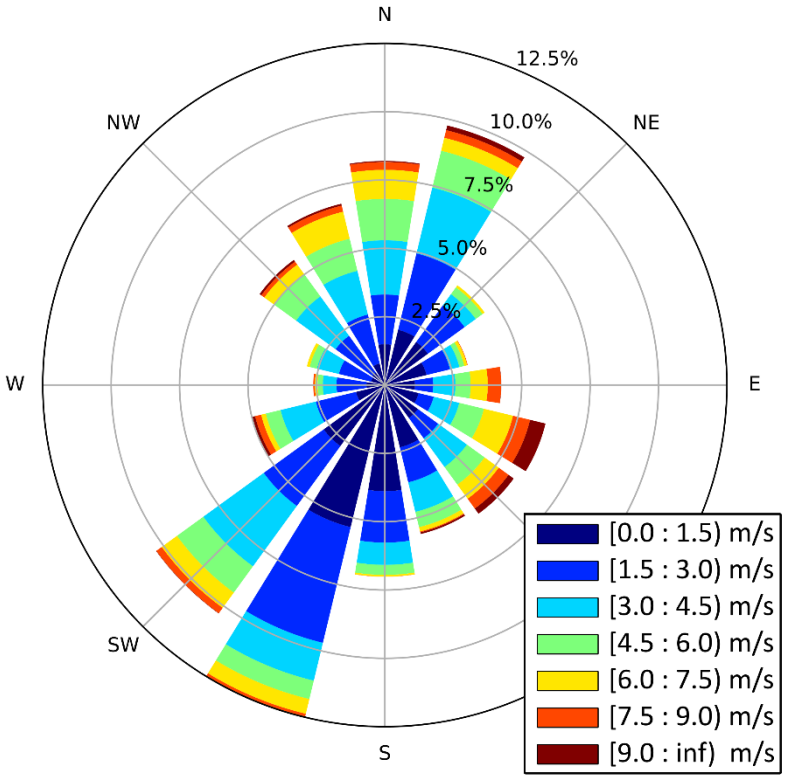

Figure 72. Wind data from the standalone wind mast at 10 m height AGL, corresponding to the period 11/06/2020 to 22/09/2020, located at Transalloys.

Appendix D. – Reflectance Measurement Data for 30° Elevation Reflectors

Figure 73 shows the reflectance trends of the reflectors at 30° elevation over the given time period. This data is excluded from the main text because the 30° elevation reflectors were collocated with the 60° elevation reflectors in order to check if the more horizontal reflector surfaces collect more dust than the more inclined 60° reflectors, which was expected based on literature. The expected trend is confirmed by the presented reflector soiling data.

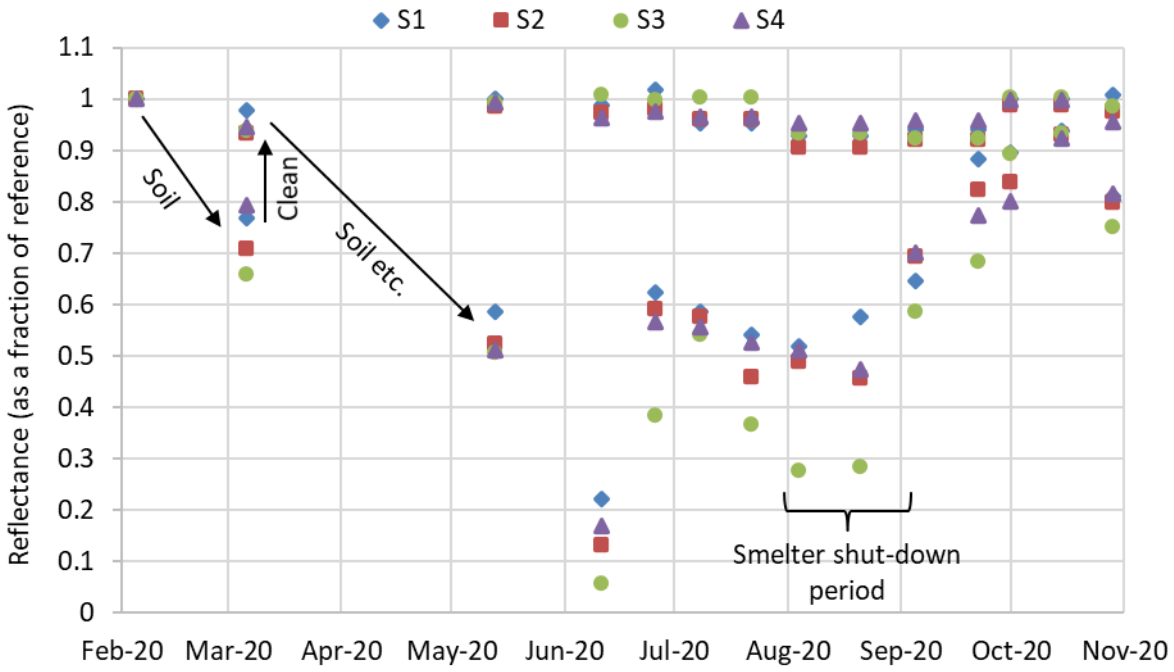

Figure 73. Reflectance of the 30° elevation reflectors for all sampling sets (S1 to S4), from 05/02/2020 to 29/10/2020, showing the consecutive soiling and cleaning cycles.

Appendix E. – ANSYS Fluent User-Defined Function (UDF)

Below is the C-language code used to introduce the appropriate modification into the RANS k-ϵ turbulence models for modelling neutral ABL flow. The modifications include proposals made by: Richards and Hoxey (1993); Hargreaves, Porter and Wright (2006); Gorlé, Van Beeck and Rambaud (2009); Parente *et al.* (2011).

```
/************************************************************************
UDFs for neutral ABL flow. BCs are consistent w/ t/ k-epsilon
turbulence model as shown by Richards & Hoxey (1993). To drive the flow,
the velocity profiles can simply be prescribed to the top boundary of
the flow as well. This UDF also contains three 'on-demand' functions.
The first, calculates the height above ground for every cell in the
domain based on a user-scalar field as first demonstrated by
Hargraeves et al. (2006). The second calculates the Building
Influence Area (BIA) where CMU is fixed in the immediate region of
the buildings according to Gorle et al. (2009).
The third initialises the field with velocity and turbulence
values based on the newly obtained z' field, this prevents solver
failure and/or divergence. The comprehensive k-epsilon approach for
ABL modelling is then specified according to Parente et al. (2011).
************************************************************************/
#include "udf.h"
/* constants */
#define UREF 6.0 /* ref. speed m/s */
#define CMU 0.03 /* turbulent viscocity model constant */
#define VKC 0.4 /*von Karman's constant */
#define ZREF 10.0 /* ref. height */
#define Z0 0.1 /* aerodynamic roughness for 'roughly open' terrain*/
#define USTAR 0.52 /*defined according to uref*vkc/ln((z+z0)/z0) */
#define WD 202.5 /* SW direction the wind is blowing from*/
#define C1EPS 1.44 /* k-eps model constant */
#define C2EPS 1.92 /* k-eps model constant */
#define C1 -0.25 /* constant for tke analytic */
#define C2 2.5 /* constant for tke analytic */
#define SIG_E 1.11
#define SIG_K 1.0
#define NUM_UDM 8

/* all cell faces are identified by 'f' in the face loop, on the
given boundary zone thread 't', sometime 'ft', similarly for cells*/
/* NOTE: when multiple cases are open in a workbench session, enough
UDMs and UDSs must be defined to accommodate all of them. They are
stored in order of creation in Fluent memory */

/************************************************************************
    Height above ground level
************************************************************************/
/* height of face cells of velocity inlets above terrain-wall, this must
be stored in UDS so that the prescribed velocity profile can be
calculated based on a localised height above ground */
/* boundary face heights above ground level */
DEFINE_ON_DEMAND(z_prime)
{
       real phi = 0.0;
       real gradphi = 0.0;
       real height_agl = 0.0;
       /* t *f_t; */
       /* for single phase flow domain(1) is fluid domain */
       Domain *domain = Get_Domain(1);
       cell_t c;
       Thread *ct;

       /* loop over entire domain to compute normal wall distance */
       thread_loop_c(ct,domain)
       {
```

```
            begin_c_loop(c,ct)
            {
                  /* get scalar value as defined in fluent */
                  phi = C_UDSI(c,ct,0);
                  /* gradient of phi in z-axis */
                  gradphi = NV_MAG(C_UDSI_G(c,ct,0));
                  C_UDMI(c,ct,0) = gradphi;
                  /* calculate normal wall distance */
                  height_agl = -gradphi + sqrt(fabs(pow(gradphi,2.0)
                                                      + 2.0*phi));
                  /* store height_agl in memory */
                  /* there are a small number of problematic cells close
                  to buildings or sharp corners that end up having
                  negative heights, for this reason the value is limited
                  to 0.1 which is the ks sandgrain roughness value for
                  the relatively 'smooth' walls of the buildings OR 0.3
                  which is the first cell centroid height*/
                  if (height_agl < 0.25)
                  {
                        C_UDMI(c,ct,1) = 0.3;
                  }
                  else
                  {
                        C_UDMI(c,ct,1) = height_agl;
                  }
            }
            end_c_loop(c,ct)
      }
}

/************************************************************************
    BIA method follows
************************************************************************/
/* sphere OR cylinder distance checking function */
real checker(real cx, real cy, real cz, real x, real y, real z)
{
      real d;
      real x1 = pow((x-cx),2);
      real y1 = pow((y-cy),2);
      real z1 = pow((z-cz),2);
      /*distance between centre and given point*/
      d = x1+ y1; /*+z1;*/
      return d;
}
/* loop over domain to create a marker for whether the point lies inside
or outside a sphere or cylinder centered on the building complex */
DEFINE_ON_DEMAND(cylinder_inside_out)
{
      int ms;
      real cx, cy, cz, x, y, z, r, distance, xc[ND_ND], checker();
      Domain *domain = Get_Domain(1);
      cell_t c;
      Thread *t;

      /* centre of cluster coordinates */
      cx = 712085.0;
      cy = 7134141.0;
      cz = 1539.0;
      /* radius of influence set to r=334m */
      /* a perimeter with radius=270m can be drawn to exactly encompass
      all buildings in the complex, an extra 1.6H is added, where H is
      the height of the tallest building H=40m, the top of the cylinder
      is also clipped so that the volume only extends 1.6H from the,
      top of the tallest building, which coordinate is z = 1557m */
      r = 334.0; /*radius of cylinder in meters */

      /*loop through domain and mark wether a point is inside or outside
      the sphere*/
```

```
        thread_loop_c(t,domain)
        {
                begin_c_loop(c,t)
                {
                        C_CENTROID(xc,c,t);
                        x = xc[0];
                        y = xc[1];
                        z = xc[2];
                        /*distance from centre */
                        distance = checker(cx, cy, cz, x, y, z);
                        if (distance <= (r*r) && z<= 1641)
                        {
                                ms = 0;
                                C_UDMI(c,t,7) = ms;
                        }
                        else
                        {
                                ms =1;
                                C_UDMI(c,t,7) = ms;
                        }
                }
                end_c_loop(c,c)
        }
}

/************************************************************************
    Initialise field after z' has been computed
************************************************************************/
DEFINE_ON_DEMAND(set_field)
{
        real z = 0.0;
        real x_comp, y_comp;
        real calculate_tke();
        cell_t c;
        Thread *ct;
        Domain *d = Get_Domain(1);
        /*calculate ustar*/
        /*ustar = (UREF*VKC)/log((ZREF+Z0)/Z0);*/
        /* calculate velocity components using WD convention */
        x_comp = -cos((90.0-WD)*M_PI/180.0);
        y_comp = -sin((90.0-WD)*M_PI/180.0);
        /*printf("X_COMP: %f\n", x_comp);*/
        /*printf("Y_COMP: %f\n", y_comp);*/
        /* loop over all cell threads in the domain */
        thread_loop_c(ct,d)
        {
                /* loop over all cells */
                begin_c_loop(c,ct)
                {
                        z = C_UDMI(c,ct,1);
                        C_U(c,ct) = x_comp*(USTAR/VKC)*log((z+Z0)/Z0); /*x-velocity*/
                        C_V(c,ct) = y_comp*(USTAR/VKC)*log((z+Z0)/Z0); /*y-velocity*/
                        C_W(c,ct) = 0.0; /*z-velocity*/
                        C_K(c,ct) = calculate_tke(z); /*k*/
                        C_D(c,ct) = pow(USTAR,3.0)/(VKC*(z+Z0)); /*epsilon*/
                        C_P(c,ct) = 0.0; /*pressure*/
                }
                end_c_loop(c,ct)
        }
}

/************************************************************************
    Boundary Conditions
************************************************************************/
/* Define velocity BCs using their cartesian components. This
is for the x-velocity component which defaults to +ve 1 at WD
is zero on a polar plot (i.e., in an Easterly direction);
axis transformation has to be done to ensure the correct signs
```

```
are assigned to the velocity vectors.
Y-X are positive in the North-East directions*/
/* x-velocity component */
DEFINE_PROFILE(x_vel_comp,ft,i)
{
       /* variable declarations */
       real z = 0.0;
       real x_comp, velX; /* x[ND_ND] pos. vector of cell centroid */
       face_t f;
       cell_t c0;
       Thread *t0 = THREAD_T0(ft); /* cell thread pointer for cell c0 */
       /*calculate ustar*/
       /*ustar = (UREF*VKC)/log((ZREF+Z0)/Z0);*/
       /* calculate x-component using WD convention */
       x_comp = -cos((90.0-WD)*M_PI/180.0);
       /* 'begin_f_loop' loops through all cell faces for the
          boundary zone */
       begin_f_loop(f,ft)
       {
              c0 = F_C0(f,ft); /* index of face's neighbouring c0 cell*/
              /* face memory and cell memory use same location*/
              /*F_UDMI(f,ft,1) = C_UDMI(c0,t0,1);*/
              z = C_UDMI(c0,t0,1);
              velX = x_comp*(USTAR/VKC)*log((z+Z0)/Z0);
              F_PROFILE(f,ft,i) = velX;
       }
       end_f_loop(f,ft)
}

/* y-velocity component */
DEFINE_PROFILE(y_vel_comp,ft,i)
{
       /* variable declarations */
       real z = 0.0;
       real y_comp, velY;
       face_t f;
       cell_t c0;
       Thread *t0 = THREAD_T0(ft); /* cell thread pointer for cell c0 */
       /*calculate ustar*/
       /*ustar = (UREF*VKC)/log((ZREF+Z0)/Z0);*/
       /* calculate y-component using WD convention */
       y_comp = -sin((90.0-WD)*M_PI/180.0);
       /* 'begin_f_loop' loops through all cell faces for the
          boundary zone */
       begin_f_loop(f,ft)
       {
              c0 = F_C0(f,ft); /* index of face's neighbouring c0 cell*/
              /* face memory and cell memory use same location*/
              /*F_UDMI(f,ft,1) = C_UDMI(c0,t0,1);*/
              z = C_UDMI(c0,t0,1);
              velY = y_comp*(USTAR/VKC)*log((z+Z0)/Z0);
              F_PROFILE(f,ft,i) = velY;
       }
       end_f_loop(f,ft)
}

/* turbulent kinetic energy profile */
DEFINE_PROFILE(k_profile,t,i)
{
       real z = 0.0;
       face_t f;
       cell_t c0;
       Thread *t0=THREAD_T0(t); /* cell thread pointer for cell c0 */
       real calculate_tke();

       /* 'begin_f_loop' loops through all cell faces for the
          boundary zone */
       begin_f_loop(f,t)
```

```
    {
                    c0 = F_C0(f,t); /* index of face's neighbouring c0 cell*/
                    /*F_UDMI(f,t,1) = C_UDMI(c0,t0,1);*/
                    z = C_UDMI(c0,t0,1);
                    F_PROFILE(f,t,i) = calculate_tke(z);
    }
      end_f_loop(f,t)
}

/* turbulence dissipation profile */
DEFINE_PROFILE(dissip_profile,t,i)
{
      real z = 0.0;
      face_t f;
      cell_t c0;
      Thread *t0 = THREAD_T0(t); /* cell thread pointer for cell c0 */
      /*calculate ustar*/
      /*ustar = (UREF*VKC)/log((ZREF+Z0)/Z0);*/
      /* 'begin_f_loop' loops through all cell faces for the
         boundary zone */
      begin_f_loop(f,t)
      {
                      c0 = F_C0(f,t); /* index of face's neighbouring cell*/
                      /*F_UDMI(f,t,1) = C_UDMI(c0,t0,1);*/
                      z = C_UDMI(c0,t0,1);
            F_PROFILE(f,t,i) = pow(USTAR,3.0)/(VKC*(z+Z0));
      }
      end_f_loop(f,t)
}

/* velocity components for TOP INLET BC, assigned as a fixed value,
calculated by using the average height above ground of the
top boundary */
DEFINE_PROFILE(top_x_vel,ft,i)
{
      real z = 0.0;
      real fcount = 0.0;
      real z_avg = 0.0;
      real x_comp; /* x[ND_ND] pos. vector of cell centroid */
      face_t f;
      cell_t c0;
      Thread *t0 = THREAD_T0(ft); /* cell thread pointer for cell c0 */
      /* calculate x-component using WD convention */
      x_comp = -cos((90.0-WD)*M_PI/180.0);
      /* calculate average height above ground */
      begin_f_loop(f,ft)
      {
            fcount += 1.0;
            c0 = F_C0(f,ft); /* index of face's neighbouring c0 cell*/
            /* face memory and cell memory use same location*/
            z += C_UDMI(c0,t0,1);
      }
      end_f_loop(f,ft)
      z_avg = z/fcount;
      /* 'begin_f_loop' loops through all cell faces for the
         boundary zone */
      begin_f_loop(f,ft)
      {
            F_PROFILE(f,ft,i) = x_comp*(USTAR/VKC)*log((z_avg+Z0)/Z0);
      }
      end_f_loop(f,ft)
}
/* The same as above is done here for the y-velocity component */
DEFINE_PROFILE(top_y_vel,ft,i)
{
      /* variable declarations */
      real z = 0.0;
      real fcount = 0.0;
```

```
        real z_avg = 0.0;
        real y_comp;
        face_t f;
        cell_t c0;
        Thread *t0 = THREAD_T0(ft); /* cell thread pointer for cell c0 */
        /* calculate y-component using WD convention */
        y_comp = -sin((90.0-WD)*M_PI/180.0);
        /* calculate average height above ground */
        begin_f_loop(f,ft)
        {
                fcount += 1.0;
                c0 = F_C0(f,ft); /* index of face's neighbouring c0 cell*/
                /* face memory and cell memory use same location*/
                z += C_UDMI(c0,t0,1);
        }
        end_f_loop(f,ft)
        z_avg = z/fcount;
        /* 'begin_f_loop' loops through all cell faces for the
           boundary zone */
        begin_f_loop(f,ft)
        {
                F_PROFILE(f,ft,i) = y_comp*(USTAR/VKC)*log((z_avg+Z0)/Z0);
        }
        end_f_loop(f,ft)
}

/* TOP BCs for TKE */
DEFINE_PROFILE(top_k_profile,t,i)
{
        real z = 0.0;
        real fcount = 0.0;
        real z_avg = 0.0;
        face_t f;
        cell_t c0;
        Thread *t0=THREAD_T0(t); /* cell thread pointer for cell c0 */
        real calculate_tke();
        /* calculate average height above ground */
        begin_f_loop(f,t)
        {
                fcount += 1.0;
                c0 = F_C0(f,t); /* index of face's neighbouring c0 cell*/
                /* face memory and cell memory use same location*/
                z += C_UDMI(c0,t0,1);
        }
        end_f_loop(f,t)
        z_avg = z/fcount;
        /* 'begin_f_loop' loops through all cell faces for the
           boundary zone */
        begin_f_loop(f,t)
    {
                        F_PROFILE(f,t,i) = calculate_tke(z_avg);
    }
        end_f_loop(f,t)
}

/* TOP BCs for TDR */
DEFINE_PROFILE(top_dissip_profile,ft,i)
{
        real z = 0.0;
        real fcount = 0.0;
        real z_avg = 0.0;
        face_t f;
        cell_t c0;
        Thread *t0 = THREAD_T0(ft); /* cell thread pointer for cell c0 */
        /* calculate average height above ground */
        begin_f_loop(f,ft)
        {
                fcount += 1.0;
```

```
            c0 = F_C0(f,ft); /* index of face's neighbouring c0 cell*/
            /* face memory and cell memory use same location*/
            z += C_UDMI(c0,t0,1);
      }
      end_f_loop(f,ft)
      z_avg = z/fcount;
      /* 'begin_f_loop' loops through all cell faces for the
         boundary zone */
      begin_f_loop(f,ft)
      {
            F_PROFILE(f,ft,i) = pow(USTAR,3)/(VKC*(z_avg+Z0));
      }
      end_f_loop(f,ft)
}

/*****************************************************************
    Wall function described by comprehensive approach specified here
*****************************************************************/
DEFINE_WALL_FUNCTIONS(user_wall_function, f, t, c0, t0, wf_ret,
                      yPlus, Emod)
{
      /*************************************************************
                SIMULATION DEPENDENT PARAMETERS - CHANGE !
      *************************************************************/
      int n_smooth_walls = 9;
      int smooth_walls[9] = {162854,
                             162853,
                                    162852,
                                    162849,
                                    162851,
                                    162850,
                                    162848,
                                    162847,
                                    162846};
      /*************************************************************/
      int i;
      int type_wf = 0;
      int zone_ID;
      int flag = 0;
      real wf_value = 0.0;
      real yPlus_prime = 0.0;
      real E_prime = 0.0;
      real zp = 0.3;
      real ustar_ground = 0.0;
      real dx_mag;
      real xf[ND_ND], xc[ND_ND], dx[ND_ND];
      real Cmu = CMU;
      real calculate_Cmu();
      real mu = C_MU_L(c0,t0);
      real k = C_K(c0,t0);
      real rho = C_R(c0,t0);
   zone_ID = THREAD_ID(t);

      /* first cell centroid height from ground face centroid */
      /*F_CENTROID(xf,f,t);
      C_CENTROID(xc,c0,t0);
      dx[0] = xc[0]-xf[0];
      dx[1] = xc[1]-xf[1];
      dx[2] = xc[2]-xf[2];
      dx_mag = NV_MAG(dx);
      zp = dx_mag;*/
      zp = C_UDMI(c0,t0,1);

      /*cylinder_inside_out BIA flag*/
      flag = C_UDMI(c0,t0,7);
      if (flag == 0)
      {
            Cmu = CMU;
```

```
        }
        else
        {
                Cmu = calculate_Cmu(zp);
        }

    if (n_smooth_walls != 0)
    {
                for (i = 0; i < n_smooth_walls-1; i++)
         {
                    if (zone_ID == smooth_walls[i])
              {
                            type_wf = 1.0;
                    }
            }
    }
        if (type_wf != 1)
        {
                /* u_start is not kept constant in longitudinal
                   direction but calculated locally */
                ustar_ground = pow(k,0.5)*pow(Cmu,0.25);
                /*ustar_ground = USTAR;*/
                E_prime = (mu/rho) / (Z0*ustar_ground);
                yPlus_prime = (zp+Z0) * ustar_ground / (mu/rho);
                /* calculate dissipation at wall adjacent cell */
                /*C_D(c0,t0) = (pow(Cmu,0.75)*pow(k,1.5)) / (VKC*(zp+Z0));*/
                C_D(c0,t0) = (pow(Cmu,0.5)*k*ustar_ground) / (VKC*(zp+Z0));
                C_UDMI(c0,t0,5) = yPlus_prime;
        }

        switch (wf_ret)
        {
                case UPLUS_LAM:
                        wf_value = yPlus;
                        break;
                case UPLUS_TRB:
                        /*
                        Message(" ** ID = %lf \n", dx_mag);
                        Message(" ** ID = %d \n", zone_ID);
                        Message(" ** yPlus_mine = %lf \n", yPlus_mine);
                        */
                        if (n_smooth_walls != 0)
                        {
                                for (i = 0; i <= n_smooth_walls-1; i++)
                                {
                                        if (zone_ID == smooth_walls[i])
                                        {
                                                type_wf = 1; /* Smooth wall */
                                        }
                                }
                        }
                        if (type_wf == 1)
                        {
                                wf_value = log(Emod*yPlus) / VKC; /*Smooth WF*/
                        }
                        else
                        {
                                wf_value = log(E_prime*yPlus_prime) / VKC; /*Rough
WF*/
                        }
                        C_UDMI(c0,t0,6) = wf_value;
                        break;
                        case DUPLUS_LAM:
                                wf_value = 1;
                                break;
                        case DUPLUS_TRB:
                        if (n_smooth_walls != 0)
                        {
```

```
                        for (i = 0; i <= n_smooth_walls-1; i++)
                        {
                                if (zone_ID == smooth_walls[i])
                                {
                                        type_wf = 1; /* Smooth wall */
                                }
                        }
                }
                if (type_wf == 1)
                {
                        wf_value = 1.0 / (VKC*yPlus); /* Smooth WF */
                }
                else
                {
                        wf_value = 1.0 / (VKC*yPlus_prime); /* Rough WF */
                }
                break;
                case D2UPLUS_TRB:
                if (n_smooth_walls != 0)
                {
                        for (i = 0; i <= n_smooth_walls-1; i++)
                        {
                                if (zone_ID == smooth_walls[i])
                                {
                                        type_wf = 1; /* Smooth wall */
                                }
                        }
                }
                if (type_wf == 1)
                {
                        wf_value = -1.0 / (VKC*yPlus*yPlus); /* Smooth wall WF
*/
                }
                else
                {
                        wf_value = -1.0/(VKC*yPlus_prime*yPlus_prime);/*Rough
WF*/
                }
                break;
        default:
                printf("Wall function return value unavailable\n");
        }
        return wf_value;
}

/*****************************************************************************
    in-script functions
*****************************************************************************/
/* variable tke */
real calculate_tke(real z_loc)
{
        real tke;
        tke = C1 * log(z_loc+Z0) + C2;
        return tke;
}
/* variable cmu */
real calculate_Cmu(real z_loc)
{
        real tke;
        real calculate_tke();
        real Cmu;

        tke = calculate_tke(z_loc);
        Cmu = pow(USTAR,4) / pow(tke,2);
        return Cmu;
}
```

```
/* Turbulent Viscosity - implementation of the
variable cmu in turbulence model */
DEFINE_TURBULENT_VISCOSITY(user_mu_t, c, t)
{
       int flag;
       real mu_t = 1.0;
       real mu = C_MU_L(c,t);
       real k = C_K(c,t);
       real d = C_D(c,t);
       real rho = C_R(c,t);
       real z = 0.0;
       real Cmu = 0.0;
       real calculate_Cmu();
       real visc_ratio = 0.0;
       /* BIA cylinder_inside_out falg */
       /* if in the building area, use default values, else
              use variable values */
       flag = C_UDMI(c,t,7);
       if (flag == 0)
       {
              Cmu = CMU;
       }
       else
       {
              /*C_CENTROID(x,c,t);*/
              z = C_UDMI(c,t,1);
              /* calc modified  Cmu */
              Cmu = calculate_Cmu(z);
       }
       C_UDMI(c,t,2) = Cmu; /* stores Cmu for post-processing */
       /* calc of modified (or unmodified) turbulent viscosity */
       mu_t = rho * Cmu * pow(k,2) / d;
       /* limiter needs to be manually implemented to prevent
          unrealistic values, especially in solution spin-up stage*/
       if (mu == 0.0)
       {
              mu = 1.78E-05;
       }
       /* visc ratio limiter needs to be implemented here,
          otherwise solution diverges */
       visc_ratio = mu_t / mu;
       if (visc_ratio > 1E+11)
       {
              mu_t = 1000000;
       }
       C_UDMI(c,t,3) = mu_t;
       return mu_t;
}

/************************************************************
    EITHER PRANDTL OR SOURCE, THEY HAVE SAME EFFECT
************************************************************/
/* User TDR prandtl number to be consistent with chosen VKC */
DEFINE_PRANDTL_D(user_pr_d, c, t)
{
       int flag;
       real z = 1.0;
       real pr_d = 1.0;
       real Cmu = CMU;
       real calculate_Cmu();

       /* BIA cylinder_inside_out falg */
       /* if in the building area, use default values, else use
          variable values */
       flag = C_UDMI(c,t,7);
       if (flag == 0)
       {
              Cmu = CMU;
```

```
        }
        else
        {
                /*C_CENTROID(x,c,t);*/
                z = C_UDMI(c,t,1);
                /* calc modified  Cmu */
                Cmu = calculate_Cmu(z);
        }

        pr_d = VKC * VKC / ((C2EPS-C1EPS)*sqrt(Cmu));
        return pr_d;
}

/* Dissipation source */
DEFINE_SOURCE(e_source, c, t, dS, eqn)
{
        int flag;
        real source_eps, z_z0_2, z, m1, f1, f2, rho;
    real Cmu, calculate_Cmu();

    m1 = f1 = f2 = 0.0;
    rho = C_R(c,t);

    z = C_UDMI(c,t,1);
        z_z0_2 = pow((z+Z0),2);

        m1 = rho * pow(USTAR,4) / z_z0_2;

        /* BIA cylinder_inside_out falg */
        /* if in the building area, use default values, else use
           variable values */
        flag = C_UDMI(c,t,7);
        if (flag == 0)
        {
                Cmu = CMU;
        }
        else
        {
                /*C_CENTROID(x,c,t);*/
                z = C_UDMI(c,t,1);
                /* calc modified  Cmu */
                Cmu = calculate_Cmu(z);
        }

        f1 = pow(Cmu,0.5) * (C2EPS-C1EPS) / pow(VKC,2);
        f2 = -1.0 / SIG_E;
        /* Source term */
        source_eps = m1 * (f1+f2);
        dS[eqn] = 0;
        C_UDMI(c,t,4) = source_eps;
        return source_eps;
}
```

Appendix F. – CFD Input Variables for Priority Simulation Cases

Table 12 shows the input variables for the priority simulation cases. Constants C_1 and C_2 are obtained by curve fitting to wind data extracted from the wind mast data, as demonstrated by Figure 33.

Table 12. Input variables for priority simulation cases.

Case name	WD	U_{ref}	z_{ref}	z_0	κ	u_*	C_1	C_2	C_μ
SSW-3	202.5°	3	10	0.1	0.4	0.26	-0.02	0.19	Eq. 41
SSW-6	202.5°	6	10	0.1	0.4	0.52	-0.25	2.5	Eq. 41
SW-3	225°	3	10	0.1	0.4	0.26	-0.009	0.07	Eq. 41
SW-6	225°	6	10	0.1	0.4	0.52	-0.25	2.5	Eq. 41
S-3	180°	3	10	0.1	0.4	0.26	-0.1	1.25	Eq. 41
S-6	180°	6	10	0.1	0.4	0.52	-0.3	2.8	Eq. 41
SE-3	135°	3	10	0.1	0.4	0.26	-0.02	0.35	Eq. 41
SE-6	135°	6	10	0.1	0.4	0.52	-0.21	1.7	Eq. 41
SSE-3	157.5°	3	10	0.1	0.4	0.26	-0.13	1.1	Eq. 41
SSE-6	157.5°	6	10	0.1	0.4	0.52	-0.23	1.7	Eq. 41
ESE-3	112.5°	3	10	0.1	0.4	0.26	-0.05	0.59	Eq. 41
ESE-6	112.5°	6	10	0.1	0.4	0.52	-0.2	1.5	Eq. 41
WSW-3	247.5°	3	10	0.1	0.4	0.26	-0.01	0.13	Eq. 41
WSW-6	247.5°	6	10	0.1	0.4	0.52	-0.25	2.5	Eq. 41

Appendix G. – ANSYS Fluent Journal Files

The computational domain creation and meshing ANSYS Fluent journal file scripts are given in Table 13, Table 14, and Table 15.

Table 13. Journal file to generate the computational mesh.

```
/file/set-tui-version "21.1"

; File import options
/file/import/cad-options/one-object-per part
/file/import/cad-options/strip-file-name-extension-from-naming? yes
/file/import/cad-options/strip-path-prefix-from-names? yes

; Importing files
/file/import/cad-geometry yes "C:/geom_5000m_fetch.scdoc" yes m cad-faceting no
/file/import/cad-geometry yes "C:/emalahleni_DEMSA2_stl_utm35s_terrain.stl"
 yes m cad-faceting no

; Renaming objects
/objects/rename-object f-domain-5000m-square-fetch fetch
/objects/rename-object emalahleni_DEMSA2_stl_utm35s_terrain terrain
/objects/rename-object refinement-region-300m-radius refinement_inner
/objects/rename-object refinement-region-1400m-radius refinement_outer

;if model consists of different parts, merge all of them - several in this case
/objects/merge bluffmodel* bluffmodel* bluffmodel* bluffmodel* bluffmodel* ()
buildings

; Intersect objects with each other to define the edges
/objects/create-intersection-loops collectively fetch terrain buildings ()

; Define fluid volume region
/material-point/create-material-point atmozone 712085 7134141 1700

; Sizing controls
; All boundaries that surround the fluid-region MUST be given size controls ...
; otherwise, the octree refinement algorithm used in shrink-wrap method doesn't
work, ...
; ... it needs to be fully defined
/size-functions/set-global-controls 1 200 1.2
/scoped-sizing/create terrain_size soft face-zone yes no *terrain 16 1.2
/scoped-sizing/create bounds-size proximity face-zone-labels yes no fetch
 "north east south west" 1 200 1.2 3 face-face yes yes
/scoped-sizing/create top_size soft face-zone yes no top 200 1.2
/scoped-sizing/create buildings_size hard face-zone yes no bluffmodel* 1 1.15
/scoped-sizing/create boi_inner boi object-faces-and-edges yes no
refinement_inner 4 1.15
/scoped-sizing/create boi_outer boi object-faces-and-edges yes no
refinement_outer 8 1.2

;Compute size field
/scoped-sizing/compute

; Create surface mesh - face zone labels inherited from parent parts
/objects/wrap/wrap (fetch terrain buildings) collectively flow_field shrink-wrap
 atmozone hybrid 1

; Delete problematic mesh object labels for compute step below
/objects/labels/delete flow_field (atmozone fetch)

; Compute volumetric region
/objects/volumetric-regions/compute flow_field yes (atmozone)

; Quality control settings (default is aspect ratio)
/diagnostics/quality/general-improve objects (flow_field) skewness 0.85 30 10 yes
```

```
; Generate volume mesh
; Prisms/inflation layers
/mesh/scoped-prisms/create prism-layer uniform 0.6 12 1.2 flow_field fluid-
regions
 selected-labels terrain
/mesh/scoped-prisms/create prism-layer2 uniform 0.6 12 1.05 flow_field fluid-
regions
 selected-labels buildings
/mesh/poly/controls/cell-sizing size-field
; Create POLY volume mesh
/mesh/auto-mesh flow_field no scoped pyramids poly yes

; Prepare for solve
/mesh/prepare-for-solve yes
; Write
/file/write-mesh "F:/meshes-transalloys/mesh2-5000mfetch.msh.gz"
```

After meshing journal is complete, switch to Fluent solution mode. The Fluent case setup and solve procedure for the flow simulations are given here. Table 14 shows the journal file used to initialise all CFD cases on a local machine.

Table 14. Journal file to initialise the CFD case on a local machine.

```
/file/set-tui-version "21.1"

/file/read-case "F:/meshes-transalloys/mesh2-5000mfetch.msh.gz"

; Declare UDS and UDMs depending on how many is called in UDF
/define/user-defined/user-defined-scalars 1 yes no yes "none"
/define/user-defined/user-defined-memory 8
; Interpret or load pre-compiled UDF
/define/user-defined/compiled-functions load "F:/meshes-transalloys/libudf"

; Define variable for wind direction WD and assign BCs accordingly
; NOTE if 0<WD<90, then N&E(BC faces)=>inlets and S&W=>outlets ...
; ... and if WD==0 then N=>inlet, S=>outlet, E&W=>symmetry ...
; ... similarly for other three 90deg sectors
; WD=202.5 (SSW) ... CHANGE FOR EVERY CASE!
; Boundary Conditions
; Inlet
/define/boundary-conditions/zone-type (south top west) velocity-inlet
/define/boundary-conditions/velocity-inlet south no yes yes no 0 yes yes yes
"udf" "x_vel_comp::libudf" yes yes "udf" "y_vel_comp::libudf" no 0 yes yes yes
"udf" "k_profile::libudf" yes yes "udf" "dissip_profile::libudf" yes no 0
/define/boundary-conditions/velocity-inlet west no yes yes no 0 yes yes yes "udf"
"x_vel_comp::libudf" yes yes "udf" "y_vel_comp::libudf" no 0 yes yes yes "udf"
"k_profile::libudf" yes yes "udf" "dissip_profile::libudf" yes no 0
/define/boundary-conditions/velocity-inlet top no yes yes no 0 yes yes yes "udf"
"top_x_vel::libudf" yes yes "udf" "top_y_vel::libudf" no 0 yes yes yes "udf"
"k_profile::libudf" yes yes "udf" "top_dissip_profile::libudf" yes no 0
; Outlet
/define/boundary-conditions/zone-type (north east) pressure-outlet
/define/boundary-conditions/set/pressure-outlet (north east) prevent-reverse-
flow? yes q
; Building walls
/define/boundary-conditions/wall *terrain , , no no no 1.97 no 0.5 no yes no 0
/define/boundary-conditions/wall bluffmodel-sld1 no no no 0.1 no 0.5 no yes no 0
/define/boundary-conditions/wall bluffmodel-sld2 no no no 0.1 no 0.5 no yes no 0
/define/boundary-conditions/wall bluffmodel-sld3 no no no 0.1 no 0.5 no yes no 0
/define/boundary-conditions/wall bluffmodel-sld4 no no no 0.1 no 0.5 no yes no 0
/define/boundary-conditions/wall bluffmodel-sld5 no no no 0.1 no 0.5 no yes no 0
/define/boundary-conditions/wall bluffmodel-sld6 no no no 0.1 no 0.5 no yes no 0
/define/boundary-conditions/wall bluffmodel-sld7 no no no 0.1 no 0.5 no yes no 0
/define/boundary-conditions/wall bluffmodel-sld8 no no no 0.1 no 0.5 no yes no 0
/define/boundary-conditions/wall bluffmodel-sld9 no no no 0.1 no 0.5 no yes no 0
```

```
; Material diffusivity per UDS and cell zone condition UDS source of 1
;/define/materials/change-create air air no no no no no no yes defined-per-uds 0
constant 1 0 constant 1 -1 no
/define/boundary-conditions/fluid atmozone no yes 0 0 0 0 0 0 1 yes 1 no no no 0
no 0 no 0 no 0 no 0 no 1 no no no no no

; Model setup
/define/models/steady? yes
/define/models/viscous/ke-standard? yes
/define/models/viscous/user-defined "user_mu_t::libudf" "none"
"user_pr_d::libudf"
/define/models/viscous/near-wall-treatment/user-defined yes
"user_wall_function::libudf"

; Solver settings
; solver p-v coupling scheme (20:SIMPLE, 21:SIMPLEC, 22:PISO, 24:Coupled,
25:FractionalStep)
/solve/set/p-v-coupling 20
; discretisation schemes (0:FOUpwind, 1:SOUpwind, 3:CentralDiff, 4:QUICK, 12:SO)
/solve/set/discretization-scheme/pressure 10
/solve/set/discretization-scheme/mom 1
/solve/set/discretization-scheme/k 1
/solve/set/discretization-scheme/epsilon 1
/solve/set/discretization-scheme/uds-0 1

; Convergence criteria (one for each equation including UDS)
/solve/monitors/residual/convergence-criteria 1e-06 1e-06 1e-06 1e-06 1e-06 1e-06
1e-04

; Solution control limits
/solve/set/limits 1 5e10 1e-14 1e-20 1e11

; Solve UDS first by turning off other flow eqns
/solve/set/equations/flow no
/solve/set/equations/ke no
/solve/set/equations/uds-0 yes

; Initialise
/solve/initialize/hyb-initialization
; Solve
/solve/iterate 200

; Solve for height above ground by calling UDF functions
/define/user-defined/execute-on-demand "z_prime::libudf"
/define/user-defined/execute-on-demand "sphere_inside_out::libudf"
/define/user-defined/execute-on-demand "set_field::libudf"

; SOLVE FLOW EQUATIONS by turning off UDS and turn others on
/solve/set/equations/flow yes
/solve/set/equations/ke yes
/solve/set/equations/uds-0 no

; Under relaxation factors - sequential approach (spin-up) followed to limit
effects of wild initial fluctuations
; Divergence tends to occur in unproperly initialised, larger >6mil cells, such
as this one
/solve/set/under-relaxation pressure 0.1
/solve/set/under-relaxation mom 0.2
/solve/set/under-relaxation k 0.2
/solve/set/under-relaxation epsilon 0.2
/solve/set/under-relaxation turb-viscosity 0.4
/solve/iterate 10

/define/user-defined/compiled-functions unload "F:/meshes-transalloys/libudf"
/file/write-case "F:/hpc_upload/ssw6.cas.h5"
```

After setup on local machine, upload the case to the CHPC and solve. Table 15 shows the ANSYS Fluent journal file used on the CHPC cluster.

Table 15. Fluent CFD journal file for iteration on the CHPC cluster.

```
/file/set-tui-version "21.1"

/define/user-defined/compiled-functions load "libudf"
; Read case and data file
/file/read-case-data "/mnt/lustre/users/mswart/masters/SSW/ssw6.cas.h5"
/define/user-defined/compiled-functions load "libudf"

;reduce reporting interval to speed up iteration intervals
/solve/set/reporting-interval 10
/solve/set/limiter-warnings? no

; output backups in case cluster falls over
/file/auto-save/retain-most-recent-files yes
/file/auto-save/root-name "/mnt/lustre/users/mswart/masters/SSW/ssw6"
/file/auto-save/case-frequency each-time
/file/auto-save/data-frequency 5000

; Under relaxation factors - sequential approach (spin-up) followed to limit
effects of wild initial fluctuations
/solve/set/under-relaxation pressure 0.1
/solve/set/under-relaxation mom 0.2
/solve/set/under-relaxation k 0.2
/solve/set/under-relaxation epsilon 0.2
/solve/set/under-relaxation turb-viscosity 0.4
/solve/iterate/90

/solve/set/under-relaxation pressure 0.2
/solve/set/under-relaxation mom 0.5
/solve/set/under-relaxation k 0.5
/solve/set/under-relaxation epsilon 0.5
/solve/set/under-relaxation turb-viscosity 0.7
/solve/iterate/900

; default under-relaxation factors restored
/solve/set/under-relaxation pressure 0.3
/solve/set/under-relaxation mom 0.7
/solve/set/under-relaxation k 0.8
/solve/set/under-relaxation epsilon 0.8
/solve/set/under-relaxation turb-viscosity 1.0

/solve/iterate 8000

;WriteCaseAndData
/define/user-defined/compiled-functions unload "libudf"
/file/write-case-data "/mnt/lustre/users/mswart/masters/SSW/ssw6_it%i.cas.h5"
exit y
```

Appendix H. – Sample Wind Data and Flow Profile Fit

Table 16 contains values for an hour of wind data sampled that satisfy the conditions for validation wind validation data laid out in Section 5.3. The data shown are isolated for the *SSW-6* validation case. The reader is reminded that the wind data are gathered using two-component 4 Hz ultrasonic anemometers. Wind data are gathered at 4 Hz, then averaged out over 1-minute interval and sent to the end-user in 10-minute averaged intervals. This means that one data point in Table 16 is the aggregate of 2400 samples. The TKE values are calculated from the sigma (or fluctuating velocity component) by making a local isotropic assumption for turbulence (i.e., $k = 3u'^2/2$). Turbulence intensity (i.e., Eq. 48) could have equally been calculated instead of turbulence kinetic energy.

Table 16. Wind data snippet used for profile and validation data for the SSW-6 case, taken from the standalone wind mast at 10 m AGL, on 2020-08-19.

Time	WS	WD	Sigma	TKE	WS	WD	Sigma	TKE
[hh:mm:ss]	[m/s]	[°]	[m/s]	[m²/s²]	[m/s]	[°]	[m/s]	[m²/s²]
	4 m AGL				10 m AGL			
04:30:00	4.79	197.7	1.12	1.88	5.89	203.6	1.17	2.05
04:40:00	4.76	199.7	1.39	2.89	5.92	204.6	1.16	2.00
04:50:00	4.44	201.7	1.01	1.52	5.88	205.4	1.05	1.64
05:00:00	4.07	198.3	0.93	1.29	5.21	201.7	0.98	1.43
05:10:00	4.62	197.5	1.11	1.85	5.96	203.5	1.18	2.08
05:20:00	4.69	193.6	1.27	2.43	6.00	201.8	1.25	2.33
05:30:00	4.25	196.9	1.16	2.03	5.54	201.6	0.96	1.38
Average	4.52	197.9	1.14	1.98	5.77	203.2	1.10	1.84

The data are used to derive inlet flow profile BCs for velocity and turbulent kinetic energy as shown in Figure 74. The profiles for U and TKE are obtained using Eq. 31 and Eq. 42, respectively. The relevant variables are $C1$ = -0.25, $C2$ = 2.5, z_0 = 0.1 m, U_{ref} = 6 m/s, z_{ref} = 10 m, κ = 0.4 and u_* = 0.52.

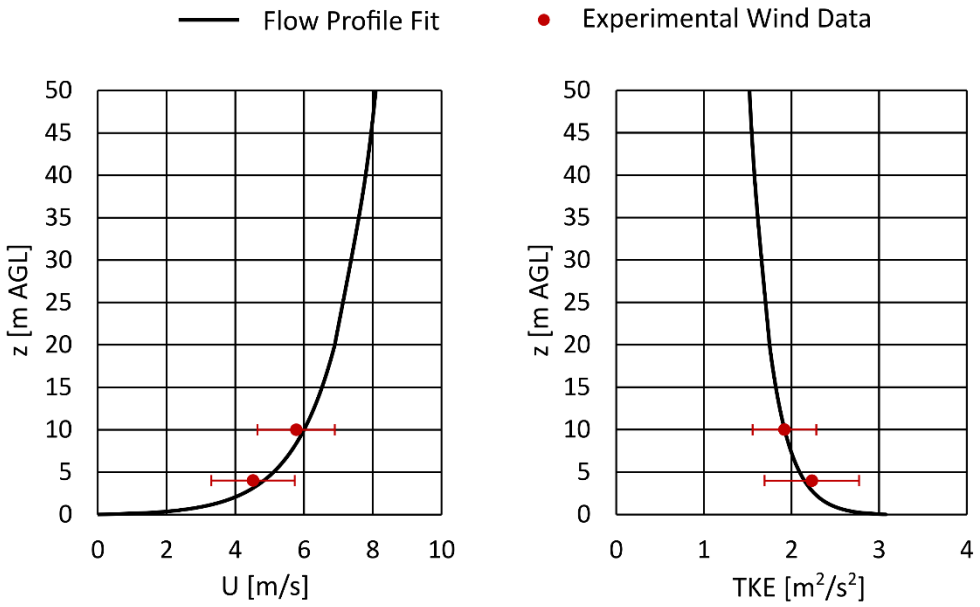

Figure 74. Flow profile fits to experimental standalone wind mast data, for wind velocity magnitude (U) and for turbulent kinetic energy (TKE).

Appendix I. – Rosin-Rammler (RR) Fit to Dust Data

The RR fit is a way of representing particle size distribution data in terms of mass fraction (ANSYS Inc., 2021). The experimental dust data collected from the dust deposition buckets and the mirrors at the Transalloys site need to be converted to RR format. The conversion allows the experimental data to be used as input and for comparison with the dust dispersion simulations performed in ANSYS Fluent.

The RR distribution function assumes an exponential relationship between particle diameters *d*, and the mass fraction of the particles Y_d, given by

$$Y_d = e^{-(d/\bar{d})^n} \qquad \text{Eq. 49}$$

where the exponent *n* is given by

$$n = \frac{\ln(-\ln Y_d)}{\ln(d/\bar{d})} \qquad \text{Eq. 50}$$

The experimentally collected dust data's volume density distribution is directly transformed to a mass fraction, assuming that there is a one-to-one relationship between dust particle volume and mass. The dust data for the atmospheric and mirror dust are presented in Figure 75, with the RR distribution curves fit through.

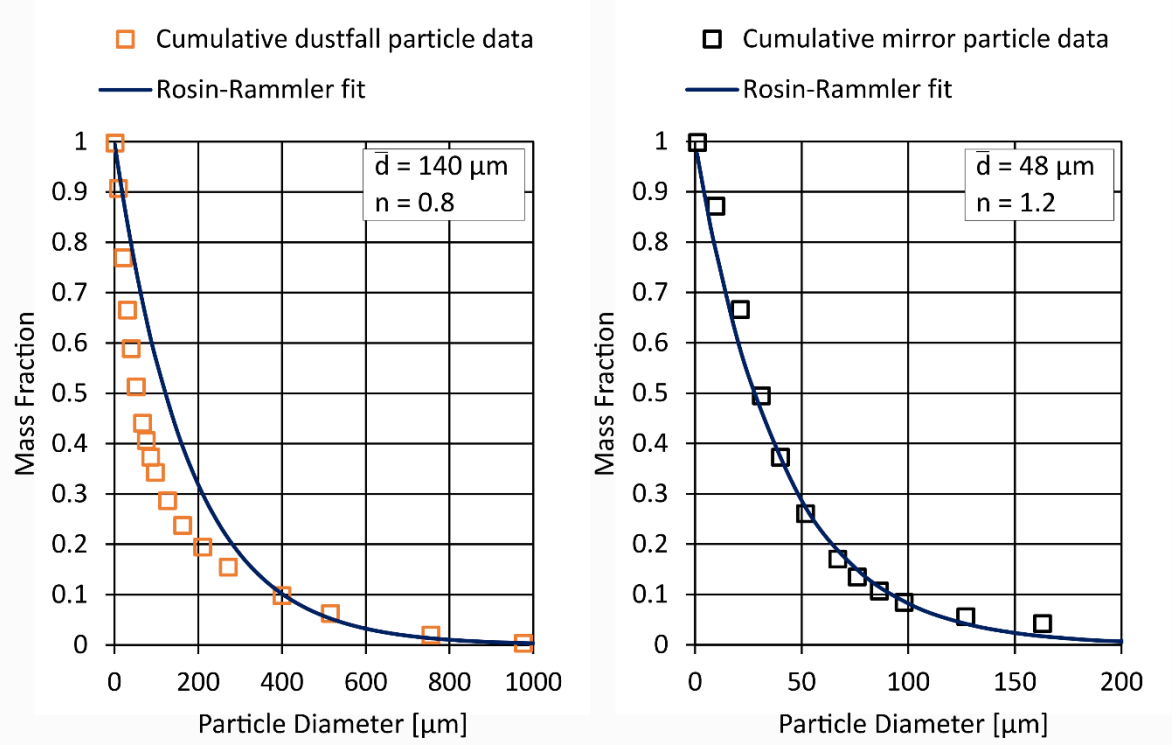

Figure 75. Rosin-Rammler distribution curve fit through experimental dust data collected at Transalloys smelter.

The mean particle diameter, in each case, is where $Y_d \approx 0.37$.

Appendix J. – Change in Numerically Sampled Dust Particle Mean Diameter with Number of Stochastic Tries

Table 17 shows the dust particle mean diameters sampled at the 1000 m downstream sampler, as labelled in Figure 58, along with other values not plotted in Figure 59. The internal statistical calculations that ANSYS Fluent DPM solver performs are evidenced in Table 17, with the number of particles sampled and total mass sampled increasing along with the number of tries, but the sampled mean levels out.

Table 17. Particle statistics sampled 1000 m downstream of Inject-2 for an increasing number of released particles.

Tries	Particles Tracked	Sampled Number of Particles	Total Sampled Mass [kg]	Particle Mean Diameter [µm]	Min. Particle Diameter [µm]	Max. Particle Diameter [µm]
1000	500,000	32	1.29E-03	40.4	1	250
2000	1,000,000	71	3.65E-03	51.5	1	250
4000	2,000,000	136	7.02E-03	51.7	1	250
8000	4,000,000	258	1.13E-02	43.9	1	250
16,000	8,000,000	555	2.84E-02	51.3	1	250
32,000	16,000,000	1019	5.06E-02	47.7	1	250
64,000	32,000,000	1635	9.32E-02	57.0	1	250
128,000	64,000,000	3144	1.79E-01	56.9	1	250
256,000	128,000,000	6253	3.56E-01	56.9	1	250
384,000	192,000,000	9644	5.56E-01	57.6	1	250
512,000	256,000,000	12,578	7.15E-01	56.9	1	250
640,000	320,000,000	15,891	9.04E-01	56.9	1	250

Appendix K. – Effect of Dust Particle Density on Numerically Sampled PSD

Figure 76 shows the effects of particle density on the numerically sampled PSDs at downstream distances of 500 m and 1000 m from *Inject-2*, for a U_{ref} = 6 m/s at a reference height of 10 m AGL.

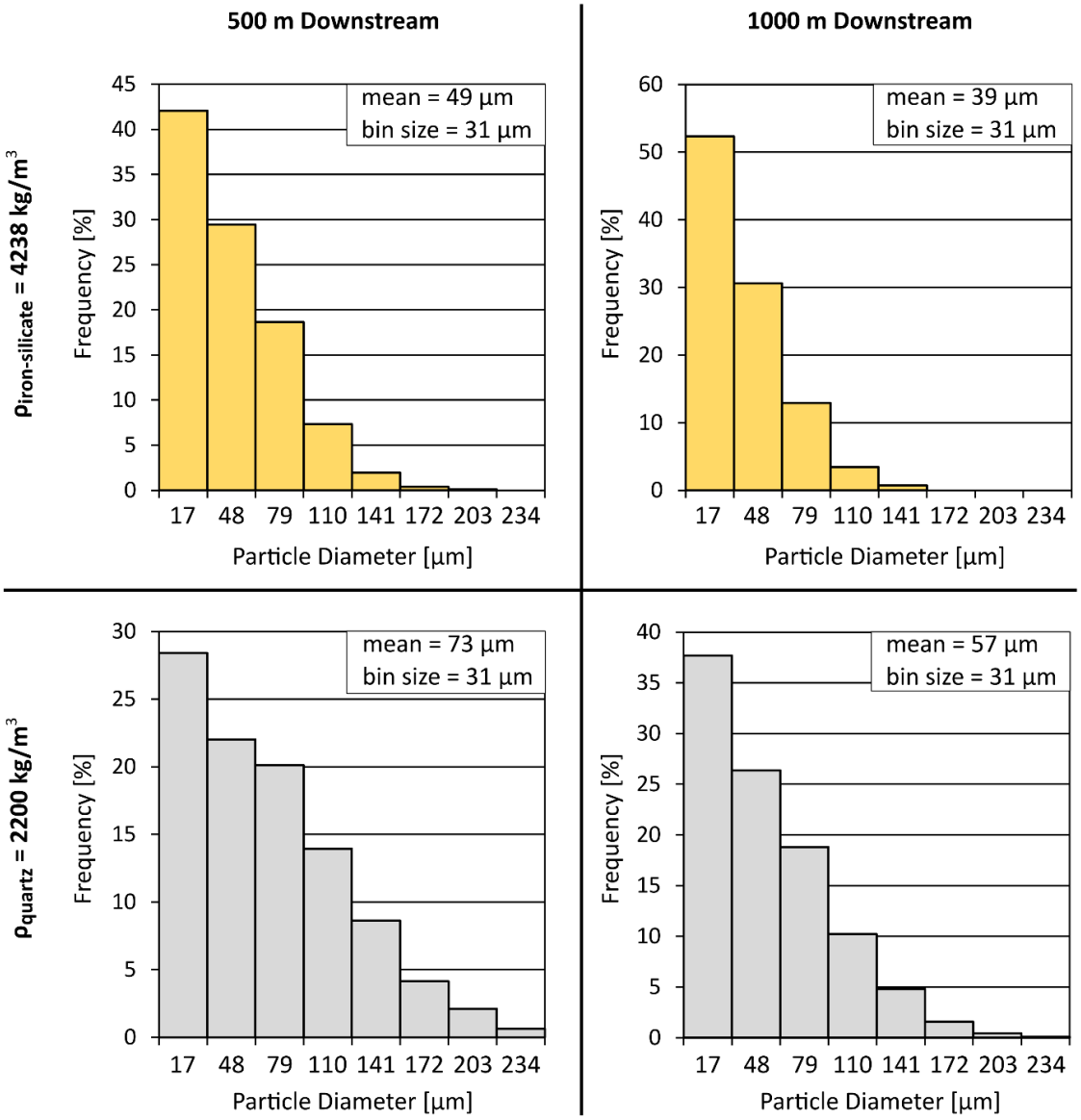

Figure 76. PSDs numerically sampled at 500 m and 1000 m downstream of 'Inject-2', for two different particle densities, at the same reference velocity.

The Figure 76 shows that particle density influences the likelihood of a larger particle travelling further downstream, where a denser particle is less likely to travel further downstream than a less dense particle. The change in dust particle density results in a narrowing of the PSD distribution as density is increased.

Appendix L. – DPM Injection Properties for the Dust Reservoir Surface

Table 18 summarises the values and settings used to specify the dust particle injection properties for the dust reservoir surface. The z-velocity and the total injection mass are arbitrarily chosen.

Table 18. DPM settings and injection properties for particles tracked from 'dust reservoir' surface.

Parameter	**Value**
Number of steps	8000
Length scale	2 m
Particle type	Inert
Material	SiO_2
Density	ρ_{SiO2} = 2200 kg/m^3
Diameter distribution	Rosin-Rammler fit
Z-velocity	0.5 m/s
Total mass	10 kg
Min. diameter	1 μm
Max. diameter	200 μm
Mean diameter	48 μm
Spread parameter (exponent n)	1.2
Number of diameters	20
Stochastic tracking	Discrete random walk model
Number of tries	240
Time scale constant (default)	0.15
Particles tracked	157,291,200